

Disruption of Ribosome Biogenesis and Induction of Nucleolar Stress by Platinum(II)-
based Chemotherapeutics

by

Matthew Vincent Yglesias

A dissertation accepted and approved in partial fulfillment of the
requirements for the degree of
Doctor of Philosophy
in Chemistry

Dissertation Committee:

Michael J. Harms, Chair

Victoria J. DeRose, Advisor

Michael D. Pluth, Core Member

David M. Garcia, Institutional Representative

University of Oregon

Fall 2024

© 2024 Matthew Vincent Yglesias
This work is openly licensed via CC BY 4.0.



DISSERTATION ABSTRACT

Matthew Vincent Yglesias

Doctor of Philosophy in Chemistry

Title: Disruption of Ribosome Biogenesis and Induction of Nucleolar Stress by Platinum(II)-based Chemotherapeutics

Platinum(II) metal complexes—cisplatin, carboplatin, and oxaliplatin—represent a major class of antineoplastic agents used in a majority of cancer treatment regimens throughout the world. Despite their ubiquitous use, the precise mechanisms and targets responsible for cancer cell death are not fully understood. Overcoming these deficiencies will be necessary to address the limitation associated with current Pt-based chemotherapeutics in the clinical setting. Current literature has revealed, unlike cisplatin and carboplatin, oxaliplatin primarily kills cells through disruption of ribosome biogenesis. Ribosome biogenesis is intimately connected to the nucleolus, a phase-separated nuclear condensate, which also functions as a central hub for sensing and coordinating cellular stress response through nucleolar stress response.

This work provides insight on the relationship between Pt(II) compounds and disruptions in ribosome biogenesis, and the impact on nucleolar structure. Chapter I summarizes the significance and current understanding of Pt-based chemotherapeutics in the context of ribosome biogenesis and the nucleolus. Chapter II identifies structural and chemical properties of Pt(II) compounds necessary for nucleolar stress induction through a novel immunofluorescence imaging approach for quantifying nucleolar stress. Chapter III applies this framework to a subset of monofunctional Pt(II) compounds which are also shown to induce nucleolar stress. Chapter IV examines spatiotemporal differences in nucleolar stress induced by Pt(II) compounds identified in previous studies—ruling out connections with intracellular accumulation and DNA binding. Chapter V discusses current progress on elucidating the molecular mechanisms for inhibition of rRNA synthesis by oxaliplatin by adapting a ChIP-based sequencing techniques to map the occupancy of RNA Polymerase I machinery along rDNA. Chapter VI provides a comprehensive review on the coordination metal ions with nucleic acids, highlighting recent examples of NMR and x-ray crystallography structures from the literature. This dissertation includes published and unpublished co-authored material.

CURRICULUM VITAE

NAME OF AUTHOR: Matthew Vincent Yglesias

GRADUATE AND UNDERGRADUATE SCHOOLS ATTENDED:

University of Oregon, Eugene
University of Texas, Austin
University of Texas, San Antonio

DEGREES AWARDED:

Doctor of Philosophy, Chemistry, 2024, University of Oregon
Bachelor of Science, Biochemistry, 2014, University of Texas at Austin

AREAS OF SPECIAL INTEREST:

Platinum Chemotherapeutics
Ribosome Biogenesis
Immunofluorescence Imaging
Chromatin Immunoprecipitation High-throughput Sequencing

PROFESSIONAL EXPERIENCE:

Graduate Employee, University of Oregon, 2018-2024
Graduate Research Fellow, University of Texas at San Antonio, 2015-2016
Academic Laboratory Technician, Palo Alto College, 2015

GRANTS, AWARDS, AND HONORS:

Molecular Biology and Biophysics Training Program NIH Training Grant,
University of Oregon, 2020-2022
University of Oregon Promising Scholar Award, University of Oregon, 2018

PUBLICATIONS:

Pigg, H. C.; **Yglesias, M. V.**; Sutton, E. C.; McDevitt, C. E.; Shaw, M.; DeRose, V. J. Time-Dependent Studies of Oxaliplatin and Other Nucleolar Stress-Inducing Pt(II) Derivatives. *ACS Chem. Biol.* **2022**, *17* (8), 2262–2271. DOI: [10.1021/acscchembio.2c00399](https://doi.org/10.1021/acscchembio.2c00399).

- DeRose, V. J.; **Yglesias, M. V.** Metal Ion Interactions With DNA, RNA, and Nucleic Acid Enzymes. In *Comprehensive Coordination Chemistry III*; Elsevier, 2021; pp 968–993. DOI: [10.1016/B978-0-08-102688-5.00112-4](https://doi.org/10.1016/B978-0-08-102688-5.00112-4).
- Sutton, E. C.; McDevitt, C. E.; **Yglesias, M. V.**; Cunningham, R. M.; DeRose, V. J. Tracking the Cellular Targets of Platinum Anticancer Drugs: Current Tools and Emergent Methods. *Inorganica Chimica Acta* **2019**, *498*, 118984. DOI: [10.1016/j.ica.2019.118984](https://doi.org/10.1016/j.ica.2019.118984).
- Sutton, E. C.; McDevitt, C. E.; Prochnau, J. Y.; **Yglesias, M. V.**; Mroz, A. M.; Yang, M. C.; Cunningham, R. M.; Hendon, C. H.; DeRose, V. J. Nucleolar Stress Induction by Oxaliplatin and Derivatives. *J. Am. Chem. Soc.* **2019**, *141* (46), 18411–18415. DOI: [10.1021/jacs.9b10319](https://doi.org/10.1021/jacs.9b10319).
- McDevitt, C. E.; **Yglesias, M. V.**; Mroz, A. M.; Sutton, E. C.; Yang, M. C.; Hendon, C. H.; DeRose, V. J. Monofunctional Platinum(II) Compounds and Nucleolar Stress: Is Phenanthriplatin Unique? *J Biol Inorg Chem* **2019**, *24* (6), 899–908. DOI: [10.1007/s00775-019-01707-9](https://doi.org/10.1007/s00775-019-01707-9).
- Deng, Y.; **Yglesias, M. V.**; Arman, H.; Doyle, M. P. Catalytic Asymmetric Synthesis of Cyclopentyl β -Amino Esters by [3+2] Cycloaddition of Enecarbamates with Electrophilic Metalloenolcarbene Intermediates. *Angew Chem Int Ed* **2016**, *55* (34), 10108–10112. DOI: [10.1002/anie.201605438](https://doi.org/10.1002/anie.201605438).

ACKNOWLEDGMENTS

I would like to sincerely thank my advisor Dr. Victoria DeRose for her guidance and support over the years. None of this would have been possible without her help and dedication. I would like to thank my committee chair Dr. Michael Harms as well as my other committee members Dr. Michael Pluth, for and Dr. David Garcia, for their support and interest in my work and for fostering such a collaborative environment.

I would also like all the members of the DeRose lab I've had the chance to work with. I would like to thank former members, Dr. Rachael Cunningham, Dr. Emily Sutton, and Dr. Christine McDevitt for being inspiring mentors, collaborators, and friends; and our current lab members—Hannah Pigg, Dillon Willis, Andres Guerrero, Ethan Kimmett, Katelyn Alley, Chris Griffin, Leif Lindberg—for their advice on experiments, random discussions about research, notes on presentation, group meeting snacks, and keeping up a positive lab environment. I would also like to thank all the rotation students and undergraduates I've had the opportunity to work with, everyone from my cohort who started this out with me, and all of the friends and colleague I've gotten to know over the years for all their support, and camaraderie. I would also like to thank Anna Bartuska for leading the graduate writing circles over the summer and fall, which was incredibly helpful in preparing this document. I would also like to acknowledge my former Dr. Michael Doyle and mentor Dr. Yongming Deng, for helping me gain the skills to get to graduate school.

Lastly, I would like to thank my family, especially my mom, dad, aunt and sister for their unrelenting love and support over these many years, who made something like pursuing a PhD even possible for me.

This work benefited from access to the University of Oregon high performance computing cluster, Talapas. This investigation was supported in part by a National Institutes of Health Training Grant from Molecular Biology and Biophysics Training Program, T32GM007759 and by grants from the National Science Foundation, CHE 1710721 and CHE 2109255, to Dr. Victoria J. DeRose at the University of Oregon.

TABLE OF CONTENTS

Chapter	Page
I. INTRODUCTION	16
Background.....	16
Cellular uptake and Accumulation of Pt(II) Drugs	19
Cellular Effects of Pt Chemotherapeutics.....	20
Non-canonical Pt Based Chemotherapeutics.....	21
Ribosome Biogenesis and the Nucleolus	22
The nucleolus as a sensor for cellular stress.....	25
Ribosome biogenesis and Pol I transcription as a chemotherapeutic target	27
Conclusion	28
Bridge to Chapter II.....	29
II. NUCLEOLAR STRESS INDUCTION BY OXALIPLATIN AND DERIVATIVES.....	30
Nucleolar Stress Induction by Oxaliplatin and Derivatives.....	30
Bridge to Chapter III	38
III. MONOFUNCTIONAL PLATINUM(II) COMPOUNDS AND NUCLEOLAR STRESS: IS PHENANTHRIPLATIN UNIQUE?	40
Introduction.....	40
Results and discussion.....	42
Oxaliplatin and phenanthriplatin cause NPM1 relocalization	42
Picoplatin does not cause NPM1 relocalization	44
NPM1 relocalization is not a general property of monofunctional platinum compounds.....	44
Steric bulk is not sufficient to predict NPM1 relocalization.....	46
Hydrophobicity is not sufficient for predicting NPM1 relocalization	47
Conclusions.....	48
Bridge to Chapter IV	50
IV. TIME-DEPENDENT STUDIES OF OXALIPLATIN AND OTHER NUCLEOLAR STRESS-INDUCING PT(II) DERIVATIVES	52
Introduction.....	52
Results and discussion.....	55
Differences in Kinetics of Nucleolar Stress Induction by Pt(II) Compounds	55

Chapter	Page
Pentaplatin Induces Lower Inhibition of rRNA Transcription.....	58
Whole Cell and Nuclear Platinum Accumulation Do Not Correlate with Nucleolar Stress Induction by Pt(II) Compounds	60
Pt(II)-DNA Binding In Vitro and in Cell Does Not Correlate with Nucleolar Stress Induction.....	62
Chirality of Pt(II) Compounds Influences the Degree of Nucleolar Stress	63
Conclusions.....	66
Bridge to Chapter V.....	68
V. INFLUENCE OF NUCLEOLAR STRESS INDUCING COMPOUNDS ON THE INTERACTION OF POLYMERASE I TRANSCRIPTION MACHINERY WITH RIBOSOMAL DNA	70
Introduction.....	70
Results.....	73
BMH-21 and oxaliplatin induce reorganization of FC components	73
ChIP-based occupancy assay of Pol I transcription of rDNA.....	76
BMH-21 induces Pol I stalling along rDNA.....	79
Pol I and UBF occupancy does not correlate to relative rDNA GC- content	81
Discussion.....	82
Bridge to Chapter VI	85
VI. METAL ION INTERACTIONS WITH DNA, RNA, AND NUCLEIC ACID ENZYMES.....	87
Introduction.....	87
Background: Roles of Metals in DNA and RNA Structure and Function.....	87
Nucleic Acids as Ligands	89
Overview of DNA /RNA Structure	89
Ligand Properties of Bases, Nucleosides, and Nucleotides	93
Metal Interactions with RNA and DNA Biopolymers.....	95
Properties of Metal Interactions with Oligonucleotides	95
Scope of Review	97
Monovalent Cations: Group I and Thallium(I)	98
Sodium.....	100
Potassium, Thallium.....	101

Chapter	Page
Rubidium, Cesium.....	102
Group IIA: Magnesium/Calcium/Strontium/Barium	102
Transition Metals	104
Chromium.....	106
Manganese	107
Iron	108
Cobalt.....	108
Nickel.....	110
Copper	110
Zinc, Cadmium	110
Transition Metals: Second and Third Row.....	112
Molybdenum, Ruthenium, Rhodium, Palladium	114
Silver	114
Platinum and Palladium.....	115
Platinum	115
Palladium	123
Tungsten, Rhenium, Iridium, Osmium, Gold, and Mercury	123
Tungsten, Rhenium, Iridium, Osmium	123
Gold.....	124
Mercury	124
Lead	126
Lanthanides	127
Concluding Remarks.....	128
Bridge to Chapter VII.....	129
VII. CONCLUDING REMARKS.....	130
Summary	130
Future Directions	131
APPENDICES.....	133
A. SUPPLEMENTARY MATERIALS FOR CHAPTER II.....	133
Supplementary Figures and Tables	133
Materials and Methods	138
B. SUPPORTING INFORMATION FOR CHAPTER III	146
Materials and Methods	146

Chapter	Page
Supplemental Figures	150
C. SUPPLEMENTARY MATERIALS FOR CHAPTER IV	151
Methods.....	151
Supplemental Figures	157
Synthesis of Pt(II) Compounds.....	159
D. SUPPLEMENTARY MATERIALS FOR CHAPTER V.....	161
Materials and Methods.....	161
Supplemental Figures	165
REFERENCES CITED	167

LIST OF FIGURES

Figure	Page
1.1. Chemical structure of Pt (II)-based chemotherapeutics approved worldwide for the treatment of cancer	16
1.2 The mechanism of action for cell death induced by cisplatin.....	17
1.3 Chemical structure of monofunctional Pt(II) compounds with demonstrated anticancer properties	22
1.4 Ribosome biogenesis in mammalian cells.....	23
1.5 Nucleolar organization in mammalian cells.....	24
1.6 Organization of rDNA genes in humans	25
1.7 Disruption of early ribosome biogenesis induces characteristic ‘nucleolar cap’ stress morphology	27
2.1. Compounds tested for inducing nucleolar stress via NPM1 relocalization.....	32
2.2. Nucleolar stress induced by Pt(II) compounds.....	33
2.3. Quantification of NPM1 relocalization, by Pt(II) compounds.....	34
2.4. Size and hydrophobicity correlate with stress induction	36
2.5. Computed distance measurements and volume representations.....	37
3.1. Platinum compounds used in this study.....	41
3.2. NPM1 relocalization.....	45
3.3. Two ring structural isomers related to phenanthriplatin	47
3.4. Optimized structures of the platinum(II) compounds.....	48
4.1. Pt(II) compounds used in this study	53
4.2. Quantification of NPM1 relocalization induced by Pt(II) compounds at various time points	57
4.3. Metabolic labeling to measure rRNA synthesis and processing at 3 h treatment.....	59
4.4. Metabolic labeling to measure rRNA synthesis and processing at 5 h treatment.....	60
4.5. Platinum content in whole cell, nuclear, and DNA samples measured by ICP-MS	61
4.6. Pt(II) compounds used in isomer-specific NPM1 relocalization studies	64
4.7. Quantification of NPM1 relocalization induced by pentaplatin isomers	64
4.8. Quantification of NPM1 relocalization induced by DACHplatin isomers.....	65
4.9. Lowest-energy conformations of pentaplatin, 1 <i>S</i> ,2 <i>S</i> - and 1 <i>R</i> ,2 <i>R</i> -configurations	66

Figure	Page
5.1 Oxaliplatin and BMH-21 induce nucleolar caps containing UBF	74
5.2. Oxaliplatin and BMH-21 induce condensation of Pol I	76
5.3. Effect of platinum and BMH-21 treatment on rDNA occupancy of Pol I.....	77
5.4. Relative Pol I ChIP-seq signal mapped at defined regions of rDNA	78
5.5. Influence of platinum and BMH-21 treatment on UBF-rDNA occupancy.....	79
5.6. Relative UBF ChIP-seq signal mapped at defined regions of rDNA.....	80
5.7. BMH-21 induces Pol I stalling at the 47S promoter	80
5.8. BMH-21 induces Pol I stalling downstream of TTF1 binding sites	81
5.9. Pol I and UBF occupancy does not correlate with relative rDNA GC- content.....	82
6.1. Metal binding sites of nucleic acids.....	90
6.2. Canonical A- and B-form helices adopted by double-stranded RNA and DNA.....	91
6.3. Predicted influence and distribution of Mg ²⁺ ions on folding of the SAM-1 riboswitch	92
6.4. Metal nanostructure templated by DNA origami substrate	93
6.5. Classes of cation interactions and influence on nucleic acid structure	97
6.6. Na ⁺ ion in Hammerhead ribozyme canonical “A9” metal site bound directly to N7 G	100
6.7. Metal sites modeled in crystal structures of a 16-nt RNA duplex	101
6.8. Mg-F cluster in a 52-nt fluoride-sensing riboswitch from <i>T. petrophila</i>	104
6.9. Crystal structure of <i>L. lactis</i> Mn-sensing riboswitch.....	108
6.10. Crystal structure of NiCo riboswitch from <i>E. bacterium</i> bound to Co(II)	109
6.11. Ultrahigh-resolution structure of Z-DNA in complex with Zn ²⁺	111
6.12. Observed binding modes of Cd(II) in <i>ykoY</i> -aptamer domain crystal structures	112
6.13. Crystal structure of RNA duplex containing C-Ag(I)-C base pair.....	115
6.14. The 2.5 Å crystal structure of DNA Pol β complexed to monofunctional platinum-carbazole conjugate.....	117
6.15. Pt-bound sites observed in 2.8 Å structure of 50S ribosome from <i>T.</i> <i>Thermophilus</i>	122
6.16. Crystal structure of HIV-1 Subtype B DNA duplex bound to Au(III)	124
6.17. DNA duplex containing unexpected C-Hg(II)-T metallobase pairing.....	125
6.18. High-resolution crystal structure of Pb(II) bound to DNA quadruplex.....	127

Figure	Page
6.19. Crystal structure of octameric RNA duplex in complex with Tb(III).....	128
A.1. Additional images for compounds tested.....	134
A.2. Quantification of nucleolar stress induction for Pt(II)-free ligands and solvents used.....	135
A.3. Histograms showing NPM1 intensity within a single nucleus in stressed and unstressed cells.	136
A.4. DFT-optimized structures of compounds.....	137
B.1. Concentration dependence of nucleolar stress induced by monofunctional Pt(II) compounds.....	150
C.1. Model oligonucleotide DNA-Pt(II) adduct assays.....	157
C.2. Representative cell images of A549 cells treated with 1 <i>S</i> ,2 <i>S</i> - and 1 <i>R</i> ,2 <i>R</i> -pentaplatin at given treatment times.....	158
C.3. Representative cell images of A549 cells treated with 1 <i>S</i> ,2 <i>S</i> - and 1 <i>R</i> ,2 <i>R</i> -DACHplatin at given treatment times.	158
D.1. ChIP-seq mapping of Pol I (RPA194) occupancy along rDNA gene in U2OS cells.....	165
D.2. ChIP-seq mapping of UBF occupancy along rDNA gene in U2OS cells.....	166

LIST OF TABLES

Table	Page
3.1. Steric bulk measurements for platinum compounds	47
3.2. Gibbs free energy of transfer between octanol and water.....	49
6.1 Nucleic acid structures with thallium, rubidium and cesium.....	99
6.2 Nucleic acid structures with first-row transition metals	105
6.3 Nucleic acid structures with second and third row transition metals, lead, and terbium.....	113
6.4 Nucleic acid structures containing Pt-nucleic acid adducts.....	118
A.1. IC ₅₀ values in A549 cells for selected compounds at 24 hours.....	137
A.2. IC ₅₀ values in A549 cells for selected compounds at 48 hours.....	137
A.3. Volume and hydrophobicity data	138

LIST OF SCHEMES

Scheme	Page
A.1. NPM1 assay and quantification scheme.....	133

Background

Platinum (Pt) metal complexes represent an important and distinct class of anti-tumor compounds routinely used in chemotherapeutic regimens today. To date three Pt(II)-based chemotherapeutics have been approved worldwide for the treatment of cancers; cisplatin, carboplatin and oxaliplatin (**Figure 1.1**) (Riddell & Lippard, 2018).

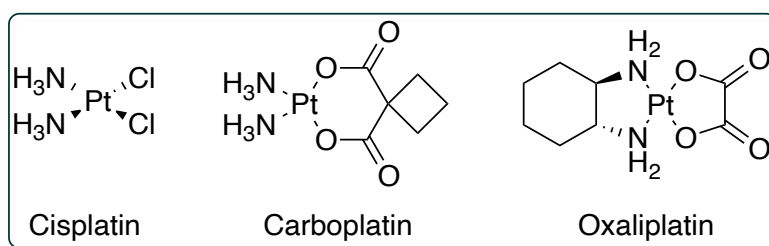


Figure 1.1. Chemical structure of Pt (II)-based chemotherapeutics approved worldwide for the treatment of cancer.

The first of these Pt(II) complexes, cisplatin [*cis*-diamminedichloroplatinum(II)], was first described in 1844 by chemist Michele Peyrone (Rottenberg et al., 2021). The cytotoxic and antiproliferative effects of cisplatin were not known until 120 years later when they were unexpectedly discovered by Barnett Rosenberg and Loretta Van Camp, who noticed a distinct inhibition of cell division when studying the effects of electric fields on *E. coli* utilizing platinum electrodes (Rosenberg et al., 1965; Rottenberg et al., 2021). Subsequent studies identified several Pt compounds generated *in situ*, including cisplatin, as the causative agent (Rosenberg et al., 1969). Soon after this discovery cisplatin was demonstrated as a potent anti-tumor compound, eventually leading to its approval for medical use in 1978 as the first metal organic coordination complex for the treatment of cancer. Cisplatin is currently used to treat a broad range of cancers including head and neck, lung, breast, cervical, and ovarian, but has been particularly successful in the treatment of testicular cancer where it has improved survival rates from 55% to over 90% (Ghosh, 2019; Wexselblatt et al., 2012).

Like many chemotherapeutic agents, cisplatin has a narrow therapeutic range that is primarily limited by patient tolerance to well-known toxic side effects such as nephrotoxicity, ototoxicity, and neurotoxicity (Ghosh, 2019). Despite these limitations, the

initial success of cisplatin spurred extensive research into characterizing the cellular mechanisms behind Pt-induced cell death. Early investigation into the mechanism of action for cisplatin quickly identified nuclear DNA as the primary cellular target responsible for the cytotoxic effects, characterizing cisplatin as an alkylating agent (Rottenberg et al., 2021). These efforts culminated into a generalized mechanism of action defined by four key steps: (i) cellular uptake, (ii) activation, (iii) DNA binding, and (iv) cellular response leading to cell death (**Figure 1.2**) (Johnstone et al., 2016; Riddell & Lippard, 2018).

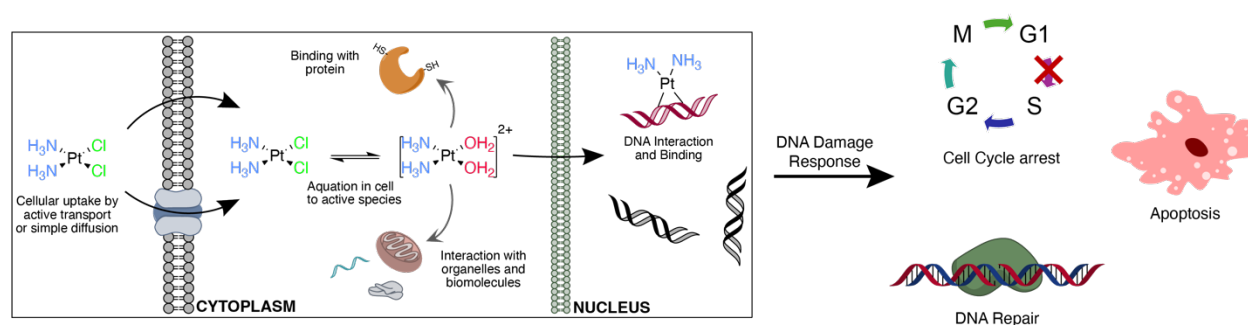


Figure 1.2. The mechanism of action for cell death induced by cisplatin. Following uptake into the cell, cisplatin undergoes aquation to form an active cationic species where it may bind to biomolecules present in the cytoplasm or nucleus. Inside the nucleus, a small percentage of cisplatin forms adducts with genomic DNA and trigger the DNA damage response (DDR), which activates several downstream repair and stress pathways.

Upon treatment, cisplatin can enter the cell via active transport or simple diffusion. Once inside the cell, the relatively lower $[Cl^-]$ concentration inside the cell drives aquation of the two *cis*-labile chloride ligands to form the active cationic complex *cis*- $[Pt(NH_3)_2(OH_2)_2]^{2+}$ (Ghosh, 2019). This active aquation species can react with a wide variety of biomolecules, most importantly genomic DNA where it shows affinity towards adjacent guanine nucleobases by forming 1,2-intrastrand crosslinks, 1,2-d(GpG), at the N7 position (Ghosh, 2019; Wexselblatt et al., 2012). The non-labile ligands on Pt-DNA adducts induce distortions in genomic DNA that disrupt DNA function, which eventually trigger the DNA damage response (DDR) in an effort to repair DNA damage (Rottenberg et al., 2021; Wexselblatt et al., 2012). Rapidly dividing cancer cells—which often lack fully functional DNA repair mechanisms—are less able to cope with the extensive DNA damage during replication, eventually leading to DDR activation of cell arrest or apoptosis pathways (Rottenberg et al., 2021). Much of the mechanistic work into

cisplatin helped define a structure-activity-relationship (SAR) for Pt chemotherapeutics¹ which was followed in the design of second generation compounds: carboplatin and oxaliplatin (Johnstone et al., 2016; Kelland, 2007).

Carboplatin, [*cis*-diammine(cyclobutane-1,1-dicarboxylate)platinum(II)], was initially developed to mitigate the toxic side effects observed in cisplatin treatments. Compared to the dichloro ligands of cisplatin, the less labile bidentate dicarboxylate ligand of carboplatin reduces intracellular aquation rates, effectively limiting off-target binding responsible for the undesirable side effects in cisplatin treatments (Johnstone et al., 2016; Kelland, 2007).

The most recently Pt(II) chemotherapeutic to achieve FDA-approval, oxaliplatin, [(1,2-diaminocyclohexane)oxalatoplatinum(II)] was intended to further address toxic side effects in cisplatin treatments and improve efficacy in cisplatin resistant cancers (O'Dowd et al., 2023; Rottenberg et al., 2021). Oxaliplatin maintains a square-planer geometry around the Pt center which is coordinated between a bidentate oxalate ligand and a bidentate 1*R*,2*R*-diaminocyclohexane (DACH) ligand (Johnstone et al., 2016; Rottenberg et al., 2021). The labile oxalate ligand improves the water solubility in comparison to the dichloro [Pt(DACH)Cl₂] species, while maintaining effective aquation rates (O'Dowd et al., 2023). The 1*R*,2*R*-DACH enantiomer was found to be more effective than the 1*S*,2*S*-DACH enantiomer *in vitro* and *in vivo*. This chirality effect is proposed to be partially due to favorable hydrogen bonding between the NH of 1*R*,2*R*-DACH and O6 of 3'-dG in 1,2-d(GpG) crosslinks (Johnstone et al., 2016; O'Dowd et al., 2023). Oxaliplatin has a distinct activity profile compared to cisplatin and carboplatin and is more effective in a distinct subset of cancers, such as gastrointestinal and colorectal cancers. Chemotherapy regimens commonly use oxaliplatin in combination with antimetabolites 5-fluorouracil (5-FU) and folinic acid (FOL), which interfere with DNA synthesis (O'Dowd et al., 2023; Rottenberg et al., 2021).

¹ The SAR for Pt chemotherapeutics describes a general structural and chemical component responsible for the cytotoxic and anticancer effects of Pt compound: a neutral square-planer metal complex coordinated to two *cis*-oriented non-labile ligands (such as amines), and two *cis* labile ligands (Wexselblatt et al., 2012).

Cellular uptake and accumulation of Pt(II) drugs

The apparent differences in efficacy, resistance, and side effect profiles, between Pt(II) chemotherapeutics observed in the clinical setting have been widely studied in the context of cellular uptake² or accumulation of Pt. Decreased cellular accumulation of Pt is shown to correlate with increased resistance in cisplatin, carboplatin, and oxaliplatin, treatments and is considered one of the primary mechanisms by which cells acquire resistances to Pt drugs (Hall et al., 2008; Riddell & Lippard, 2018).

Pt(II) compounds move across the cell membrane by a combination of passive diffusion and protein-mediated/active transport. Cisplatin and carboplatin are believed to primarily enter cells through passive diffusion, while oxaliplatin is thought to depend more heavily on active transport mechanisms (O'Dowd et al., 2023; Riddell & Lippard, 2018). However, there is still an incomplete understanding of both modes of transport, (Riddell & Lippard, 2018) and the cellular mechanisms which confer resistance are less well understood (Rottenberg et al., 2021).

Several proteins involved in the active transport of organic and/or metal cations, have been reported to interact with Pt and influence intracellular Pt accumulation, many of which belong to the solute carrier (SLC) family of transporters such as, copper transporter 1 (CTR1; SLC31A), organic cation transporters (OCTs; SLC22A) OCT1-3, and multidrug and toxin extrusion antiporters (MATEs; SLC47) MATE1 and MATE2-K. CTR1 expression is shown to correlate with intracellular Pt accumulation and has been implicated in cisplatin resistance mechanisms. CTR1 is downregulated in response to cisplatin treatments and decreased expression is associated with cisplatin resistance in tumor cell lines (Hall et al., 2008; Riddell & Lippard, 2018). However, more recent studies suggest CTR1 may not play a direct role in a Pt uptake (O'Dowd et al., 2023; Riddell & Lippard, 2018). OCT1-3 are bidirectional polyspecific transporters for small organic cations that are differentially expressed among several tissue-types. OCTs promote Pt uptake and are linked to several tissue-specific side effects associated with Pt(II) chemotherapeutics. OCT2 expression in kidney and cochlear hair cells is a key determinant of nephrotoxicity and ototoxicity in cisplatin treatments, which was found to

² In the literature 'cellular uptake' is commonly used to describe flux in/out of the cell, as well as total intracellular amounts (Hall et al., 2008). To avoid this ambiguity, we focus on cellular accumulation—the net amount of drug or analyte within the cell at a given point in time—and limit 'cellular uptake' to mean an influx, or movement of drug into the cell.

be a better substrate for OCT2 compared to carboplatin or oxaliplatin (Hall et al., 2008; Riddell & Lippard, 2018). OCT3 has been observed to transport oxaliplatin, but not cisplatin, and is hypothesized to promote sensitivity of colon cancer to oxaliplatin due to its high expression in the GI tract (Riddell & Lippard, 2018).

P-type ATPases, ATP7A and ATP7B, are responsible for sequestering and extruding excess copper in the cell and have been shown to promote Pt efflux. Increased levels of ATP7B in particular are strongly associated with Pt resistance and used as a prognostic marker for oxaliplatin treatment of colorectal cancers (Riddell & Lippard, 2018). MATE1 and MATE2-K are cation efflux transporters associated with Pt efflux mechanisms. MATE2-K, which is expressed in the kidneys, shows strong substrate specificity for oxaliplatin in comparison to cisplatin, and is hypothesized to cause the reduction in nephrotoxicity observed in oxaliplatin treatments (O'Dowd et al., 2023; Riddell & Lippard, 2018). ATP-binding cassette transporters, multidrug resistance proteins (MRP), MRP1, MRP2, and MRP4, have also been shown to transport Pt(II) chemotherapeutics and Pt metabolites. MRP2, which is expressed in the liver and kidneys, is widely implicated in oxaliplatin efflux and its expression is linked to a decrease in accumulation and cytotoxicity (O'Dowd et al., 2023).

Cellular uptake and accumulation mechanisms have provided strong insight into Pt sensitivity/resistances mechanisms and demonstrate clear differences in how Pt compounds are handled by the cell. Nevertheless, seemingly contradictory findings highlight how these mechanisms are not fully elucidated, and do not provide a sufficient explanation on their own for the dissimilar efficacies observed in the clinic.

Cellular effects of Pt chemotherapeutics

From initial research on cisplatin, Pt drugs are understood to be inherently non-specific and have been shown to interact with a broad range of biomolecules including RNAs, proteins, mitochondrial DNA, and sufficiently nucleophilic metabolites (O'Dowd et al., 2023), the biological impacts of which are still poorly understood.

The traditional paradigm for Pt chemotherapeutics centers around DDR pathways, and has revealed some differences in the molecular mechanisms of oxaliplatin and cisplatin. The DDR encompasses several mechanisms for the recognition and repair of DNA damage, many of which share overlapping function. Nucleotide excision repair

(NER), the primary repair mechanism for processing interstrand crosslinks, is not influenced by the non-labile ligands bound to Pt in DNA adducts. However, mismatch repair (MMR) pathways which can repair cisplatin crosslinks do not detect oxaliplatin crosslinks (O'Dowd et al., 2023; Riddell & Lippard, 2018). Double strand break (DSBs) repair pathways involving homologous recombination (HR) are implicated as a key factor in cisplatin resistance, but deficiencies in HR show little influence on oxaliplatin sensitivity. Similarly, defects in base excision repair (BER) pathways result in sensitivity to cisplatin, but not oxaliplatin (Riddell & Lippard, 2018).

Strikingly, RNAi-based genetic analysis revealed that oxaliplatin and phenanthriplatin, but not cisplatin, induce cell death primarily through a disruption of ribosome biogenesis (Bruno et al., 2017). Although both cisplatin and oxaliplatin have been previously demonstrated to induce disruptions in early ribosome biogenesis and inhibit rRNA synthesis, these effects were thought to result downstream of DDR or off-target effects caused by high treatment concentrations (Burger et al., 2010; Hamdane et al., 2015). However, subsequent experiments showed lower Pt accumulation in oxaliplatin treatments compared to cisplatin, which resulted in fewer DSBs when measured by marker γ H2AX (Bruno et al., 2017; Schoch et al., 2020). This seminal work led to a paradigm shift for Pt chemotherapeutics (particularly oxaliplatin) towards ribosome biogenesis, and its deeply connected process of nucleolar stress where there has been renewed interest in elucidating the molecular interactions involved in these cell death mechanisms.

Non-canonical Pt based chemotherapeutics

Pt compounds which fall outside of the traditional SAR are continually investigated in mechanistic studies and drug development. Among these, monofunctional Pt(II) complexes have shown promise as potential anticancer compounds. Unlike bifunctional *cis*-coordinated Pt(II) chemotherapeutics which can form both monofunctional and bifunctional adducts with DNA, monofunctional Pt(II) compounds contain only one labile ligand which expectedly forms a single bond with DNA (Johnstone et al., 2016). Initial studies found monofunctional Pt(II) compounds such as $[\text{Pt}(\text{dien})\text{Cl}]^+$ (dien = diethylenetriamine) and $[\text{Pt}(\text{NH}_3)_3\text{Cl}]^+$ did not display significant anticancer activity, which fell in agreement with traditionally defined SAR. However,

monofunctional Pt(II) compounds following the structure $cis-[Pt(NH_3)(Am)Cl]^+$ (Am = aromatic *N*-heterocyclic amine), pyriplatin (Am = pyridine) and phenanthriplatin (Am = phenanthridine) (**Figure 1.3**), were later found to be potent anticancer agents, and shown to form covalent bonds and intercalate with duplex DNA (Johnstone et al., 2016; Wexselblatt et al., 2012). Both pyriplatin and phenanthriplatin are strongly up-taken by the cell, and are thought to work through pathways distinct from cisplatin (Johnstone et al., 2016; Park et al., 2012). Phenanthriplatin was identified to be more similar to oxaliplatin by primarily inducing cell death through a disruption of ribosome biogenesis (Bruno et al., 2017).

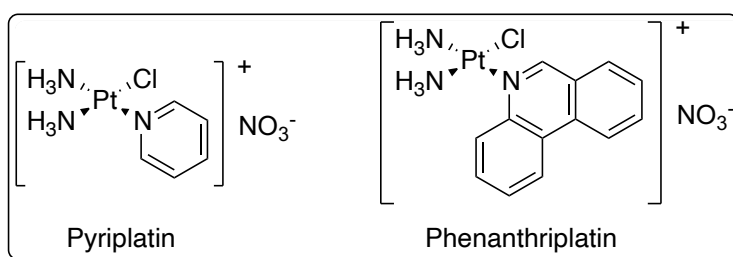


Figure 1.3. Chemical structure of monofunctional Pt(II) compounds with demonstrated anticancer properties. Phenanthriplatin has been shown to disrupt ribosome biogenesis and induce nucleolar stress.

Ribosome biogenesis and the nucleolus

Ribosome Biogenesis is the highly conserved and essential process of synthesizing and regulating the production of ribosomes. In eukaryotes, ribosomes are constructed from four ribosomal RNAs (rRNA) in combination with dozens of ribosomal proteins. These are organized into two primary subunits; a large subunit containing the 28S, 5S, and 5.8S rRNA, and a small subunit containing the 18S rRNA (González-Arzola, 2024; Pitts & Laiho, 2022). Ribosome biogenesis primarily takes place in the nucleolus, a non-membrane bound organelle, or biomolecular condensate, within the nucleus (**Figure 1.4**) (González-Arzola, 2024; Lafontaine et al., 2021). Ribosome biogenesis begins with the rate-limiting transcription of rRNA genes (rDNA) by RNA polymerase I (Pol I) to generate a single pre-rRNA (47S rRNA) containing the 18S, 5.8S, and 28S rRNAs. The 5S rRNA is concomitantly transcribed outside of the nucleolus by RNA polymerase III (González-Arzola, 2024; Pitts & Laiho, 2022). These pre-rRNAs then further cleaved and processed to generate mature rRNA transcripts, which are then assembled with ribosomal proteins to form the two pre-ribosomal subunits (Peña et al., 2017). These pre-

ribosomal subunits translocate into the nucleoplasm where they undergo several maturation steps before being exported to the cytoplasm (Peña et al., 2017). Here, they undergo “functional proof reading” maturation where they combine to form a fully functional ribosome (González-Arzola, 2024; Peña et al., 2017).

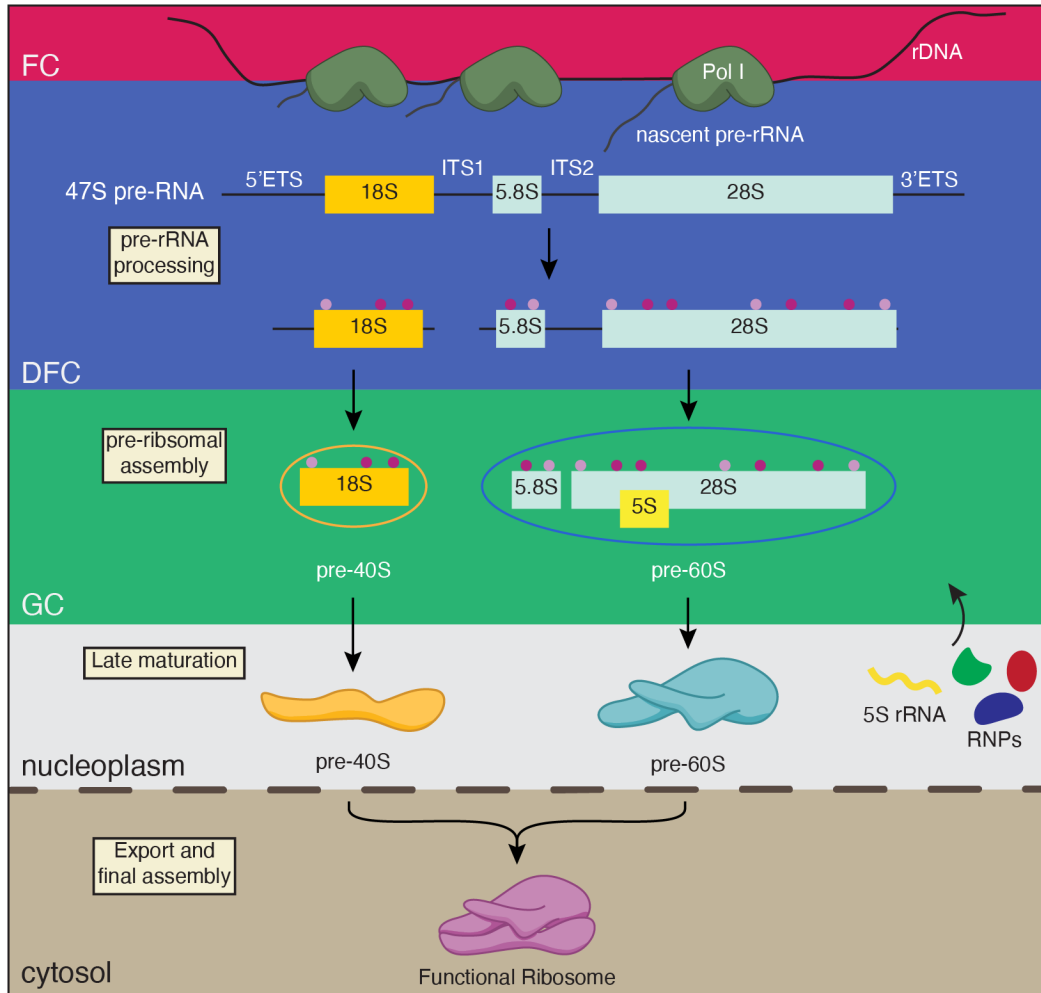


Figure 1.4. Ribosome biogenesis in mammalian cells. Ribosome biogenesis begins with the initial transcription of 47S pre-rRNA by Pol I, which occurs at the interface of the fibrillar center and dense fibrillar component (FC-DFC) allowing for nascent pre-rRNA to be co-transcriptionally processed. In the DFC, pre-rRNA undergoes further processing and modification. In the granular component (GC) pre-rRNAs are combined with the 5S rRNA and essential ribosomal proteins (RNPs) to assembly the pre-40S and pre-60S ribosomal subunit. Pre-ribosomal subunits undergo further late stage maturation in the nucleoplasm before final export into the cytosol where they combine to form a functional ribosome.

The nucleolus is organized in a nested tripartite structure containing three distinct sub-nucleolar compartments which reflect the transcription, processing, and assembly steps of ribosome biogenesis (**Figure 1.5**) (González-Arzola, 2024; Lafontaine et al., 2021). At the core is the fibrillar center (FC), which is highly enriched in with rRNA

transcription machinery and related essential cofactors. Surrounding the FC is the dense fibrillar component (DFC), where pre-rRNA processing occurs (González-Arzola, 2024; Lafontaine et al., 2021). It is generally accepted that pre-rRNA transcription occurs at or near the border of the FC and DFC, which allows for nascent pre-rRNA to be co-transcriptionally processed as it enters the DFC (Hori et al., 2023; Lafontaine et al., 2021). The FC and DFC form a functional module contained within the granular component (GC), where assembly of mature rRNAs with ribosomal proteins takes place, making up the largest component of the nucleolus which demarcates the nucleolus from the nucleus (González-Arzola, 2024; Lafontaine et al., 2021).

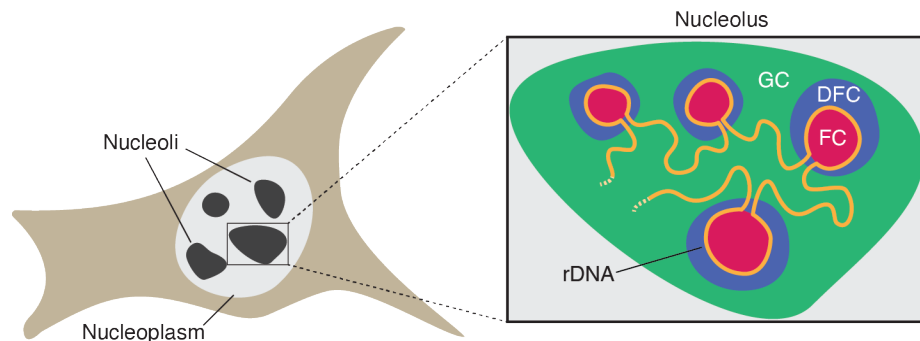


Figure 1.5. Nucleolar organization in mammalian cells. Multiple complete nucleoli which organize around NORs may be present within the nucleus. The three sub compartments of the nucleolus, the fibrillar center (FC, red), dense fibrillar component (DFC, blue), and granular component (GC, green) are maintained through liquid-liquid phase separation. Multiple FC-DFC modules exist within a single GC sub-compartment. At the interface of each FC-DFC module are ribosomal rRNA genes (rDNA, orange) under active transcription.

A single GC may contain dozens of FC-DFC modules, which form around transcriptionally active rDNA repeats (González-Arzola, 2024; Pitts & Laiho, 2022). These clusters of rDNA repeats, known as nucleolar organizer regions (NORs), are arranged in tandem repeat arrays containing hundreds of copies of rDNA (**Figure 1.6**) (Pitts & Laiho, 2022). In humans, NORs are located on the short arms of acrocentric chromosomes 13, 14, 15, 21, and 22 (Nurk et al., 2022). The number of repeats can vary substantially between species and individuals, the maintenance and regulation of which is not well understood in mammalian cells (Hori et al., 2023; Pitts & Laiho, 2022). The human genome contains between 200–600 copies of rDNA (Nurk et al., 2022), which can vary between 20–100 copies per NORs (Hori et al., 2023). However, only a fraction of these rDNA repeats are active at any point in time (González-Arzola, 2024; Hori et al., 2023).

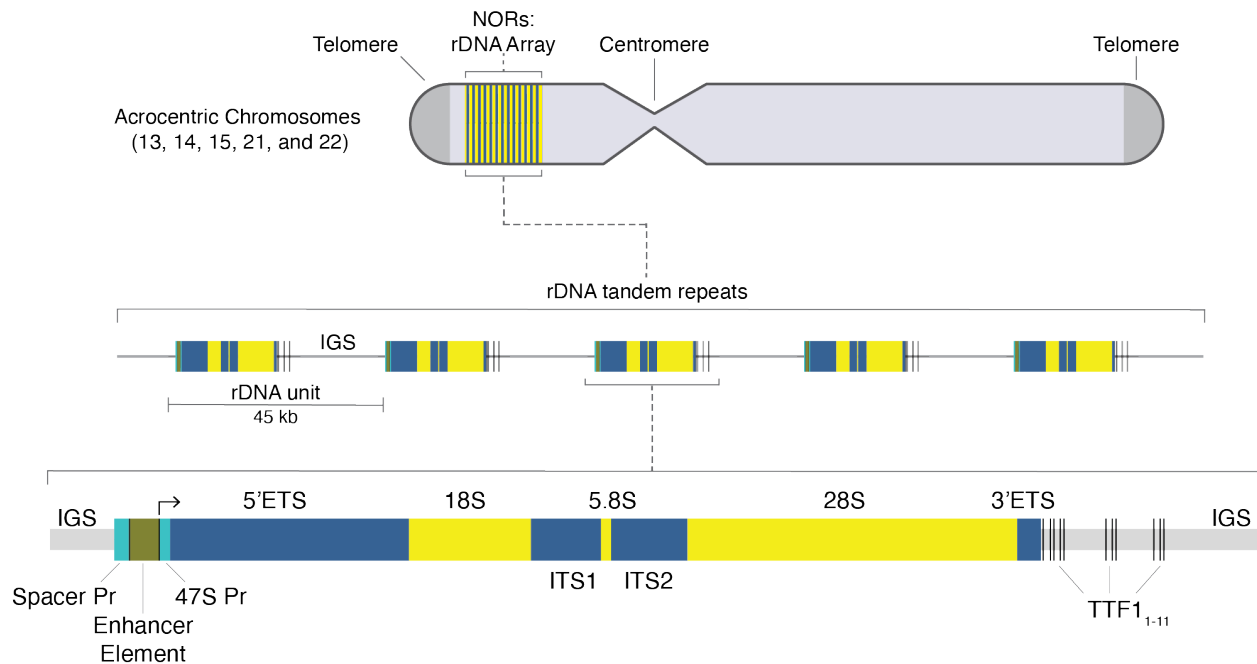


Figure 1.6. Organization of rDNA genes in humans. rDNA arrays are found in nucleolar organizer regions (NORs) located on the short arm of acrocentric chromosomes. rDNA arrays are organized into tandem repeats of rDNA units, each containing a transcribed region encoding for the 47S pre-rRNA and a non-transcribed intergenic spacer (IGS) region. The IGS contains the spacer promoter (Spacer Pr), enhancer element, 47S promoter (47S Pr) and transcription termination sites (TTF1) for adjacent repeats. External transcribed spacers (5'ETS and 3'ETS) flank each coding region; rDNA genes are separated by internal transcribed spacers (ITS1 and ITS2)

The nucleolus as a sensor for cellular stress

In more recent decades, the nucleolus has come to be understood as a multifaceted organelle, which not only directly facilitates ribosome biogenesis but is deeply involved in the cellular processes surrounding its regulation. The production of ribosomes is essential and highly coordinated with cell growth and division (González-Arzola, 2024). Perhaps consequently, the nucleolus plays an important role in coordinating cell signaling involved in cell cycle progression, proliferation, and apoptosis. (Yang et al., 2018). More uniquely, the nucleolus functions as sensor of cellular stress through a nucleolar stress response. A broad range of cellular insults can induce nucleolar stress which is defined as a disruption in nucleolar structure or function that leads to activation of downstream cellular stress-response pathways³ (González-Arzola, 2024; Yang et al., 2018). Canonically, nucleolar stress is induced by either rDNA specific DNA damage or

³ Prior to nucleolar stress being understood as a general cell stress sensing phenomenon, the term 'nucleolar stress' was often used synonymously with 'disruption of ribosome biogenesis', since this was only known function of the nucleolus (González-Arzola, 2024).

disruption in ribosome biogenesis homeostasis. Other factors which can induce nucleolar stress include nonspecific DNA damage, inhibition in RNA transcription or protein translation, and general stress conditions which can lead to p53 activation (Yang et al., 2018).

An important aspect of nucleolar stress is the apparent relocalization of nucleolar proteins which often reflect the inherent relationship between ribosome biogenesis and nucleolar structure. Several nucleolar proteins, such as NPM1, ARF, RPL11, and RPL5, translocate from the nucleolus into the nucleoplasm and cytosol where they have been demonstrated to aid in stabilizing p53 by inhibiting murine double minute 2 (MDM2, HDM2 in humans), causing activation of p53-dependent apoptosis or cell-cycle arrest pathways (Penzo et al., 2019). NPM1 and ARF are also linked to activation of downstream stress response pathways independent of p53. Both NPM1 and ARF can bind the transcription factor c-Myc within the nucleolus, disrupting c-Myc activation of oncogenes involved in cell growth and proliferation (Weeks et al., 2019). ARF has been shown to activate the DDR through ATM (ataxia-telangiectasia mutated)/ATR (ATM- and Rad3-Related) signaling pathways, leading to cell cycle arrest, senescence, or apoptosis (González-Arzola, 2024; Weeks et al., 2019). Translocation of NPM1 from the GC to the nucleoplasm is a well characterized early hallmark of nucleolar stress, although additional distinct nucleolar stress morphologies are observed when nucleolar stress results from disruptions in ribosome biogenesis (Yang et al., 2018). Inhibitors of RNA pol I transcription, such as actinomycin D (ActD) and BMH-21, have been shown to cause segregation of nucleolar subcomponents leading to the formation of 'nucleolar caps', where the FC and DFC phase separate and then condense around the periphery of the GC (**Figure 1.7**) (Lafontaine et al., 2021; Yang et al., 2018). The function and mechanisms which govern nucleolar restructuring during nucleolar stress are poorly understood, but are thought to depend heavily on the composition and liquid-liquid phase separation properties of the resulting nucleolar condensates (Lafontaine et al., 2021). Another overlooked aspect of nucleolar stress is the kinetics and robustness of nucleolar relocalization, which has been shown to vary significantly among small molecule inhibitors of ribosome biogenesis and in some cases even be reversible (Lu et al., 2018; Pigg et al., 2022).

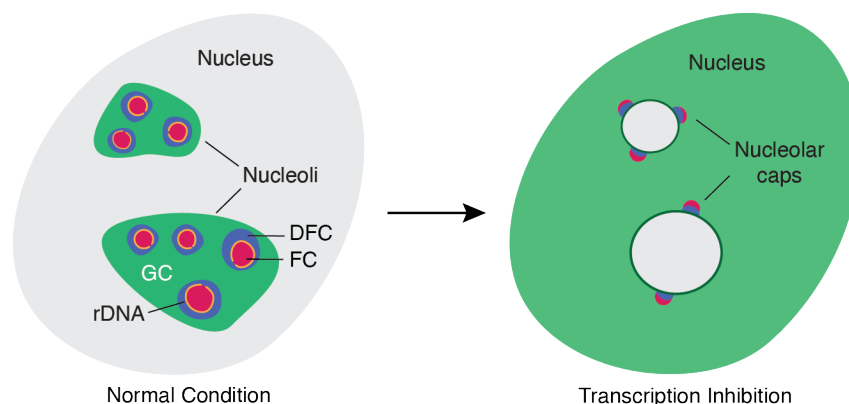


Figure 1.7. Disruption of early ribosome biogenesis induces characteristic 'nucleolar caps' stress morphology. Inhibition of rRNA transcription leads to the formation of 'nucleolar caps'.

Ribosome biogenesis and Pol I transcription as a chemotherapeutic target

In recent years inhibition of ribosome biogenesis, and more specifically rRNA transcription, has emerged as a potential chemotherapeutic strategy for selectively targeting cancer cells. It is widely acknowledged that cancer cells rely on heightened rates of ribosome synthesis to facilitate the increased demands for cell growth and proliferation. As a result, ribosome biogenesis is often dysregulated in cancer which manifests as elevated rates of rRNA synthesis and greater sensitivity to disruptions in rRNA transcription (Hwang & Denicourt, 2024; Zisi et al., 2022). As the initial and rate-limiting step of ribosome biogenesis, transcription of rRNA by Pol I plays a pivotal role in setting the rate of ribosome biogenesis and has gained interest as a small-molecule target for selective inhibition (Hwang & Denicourt, 2024).

Several small molecules and clinically approved drugs have been identified to disrupt Pol I transcription. A majority of these compounds such as ActD, BMH-21, and CX-5461, function as DNA intercalators where they bind to rDNA and disrupt interaction with Pol I machinery (Bruno et al., 2020; Pitts & Laiho, 2022). However, DNA alkylating agents like cisplatin and oxaliplatin, as mentioned above, and antimetabolites such as methotrexate, have also been shown to inhibit rRNA synthesis (Zisi et al., 2022). While, several structural and chemical determinants for Pol I inhibition have been identified among small-molecule inhibitors, the precise mechanisms which dictate Pol I specificity are still poorly understood (Zisi et al., 2022). It is widely suggested that the high affinity of small-molecule inhibitors towards GC-rich regions of the genome, such as rDNA, drive selectivity towards Pol I inhibition (Peltonen et al., 2014; Penzo et al., 2019; Zisi et al.,

2022). This is not considered to be the only factor contributing to Pol I specificity. rDNA is intrinsically unstable as a consequence of the high repetitiveness and transcriptional rates, and thus is more susceptible to DNA damage, such as DSBs, which are often enriched in the rDNA regions of the genome (González-Arzola, 2024; Hwang & Denicourt, 2024). Recognition and processing of rDNA damage is handled through a distinct nucleolar DDR (n-DDR), which has emerged to describe the unique mechanisms that directly mediate Pol I inhibition in the presence of rDNA DSBs (González-Arzola, 2024). It's also been hypothesized that chemotherapeutics, such as oxaliplatin and CX-5461, may preferentially induce rDNA damage which then leads to specific Pol I inhibition via n-DDR (Xuan et al., 2021).

Conclusion

Within this dissertation, I will address three facets of nucleolar stress induced by Pt(II) compounds. Chapter II will address the chemical and structural properties of oxaliplatin which are necessary for nucleolar stress induction. Here we identify a subset of nucleolar stress inducing Pt(II) compounds which share several chemical and structural properties. Chapter II was originally published in the *Journal of the American Chemical Society* by Emily C. Sutton, Christine E. McDevitt, Jack Y. Prochnau, Matthew V. Yglesias, Austin M. Mroz, Min Chieh Yang, Rachael M. Cunningham, Christopher H. Hendon, and Victoria J. DeRose (Sutton, McDevitt, Prochnau, et al., 2019). Chapter III expands this inquiry to monofunctional Pt(II) compounds and describes how spatial orientation and steric bulk specifically factor into nucleolar stress induced by monofunctional Pt(II) compounds. Chapter III was published the *Journal of Biological Inorganic Chemistry* by Christine E. McDevitt, Matthew V. Yglesias, Austin M. Mroz, Emily C. Sutton, Min Chieh Yang, Christopher H. Hendon, and Victoria J. DeRose (McDevitt et al., 2019).

In chapter IV we address potential variability in the robustness and kinetics of nucleolar stress induced by Pt (II) analogs of oxaliplatin. This chapter demonstrates spatiotemporal differences in nucleolar stress between Pt(II) compounds, which were not explained by trends in cytotoxicity, DNA platination or intracellular Pt accumulation. Chapter IV was previously published in *ACS Chemical Biology* and co-authored by Hannah C. Pigg, Matthew V. Yglesias Emily C. Sutton, Christine E. McDevitt, Michael

Shaw, and Victoria J. DeRose (Pigg et al., 2022). Chapter V explores the biological and molecular interactions involved in Pol I inhibition by oxaliplatin and their connection to nucleolar stress. In this chapter we describe the recent progress in applying chromatin immunoprecipitation and DNA sequencing technique to map the rDNA occupancy of Pol I machinery. Chapter V contained unpublished work by Matthew V. Yglesias.

Lastly, Chapter VI will review the interactions of coordinate metal ions with DNA, RNA, and nucleic acid enzymes, with a focus on insights gained from more recently published NMR and x-ray crystallography structures. Chapter VI was co-written with Victoria J. DeRose and first published in *Comprehensive Coordination Chemistry III* (Victoria J. DeRose & Yglesias, 2021).

Bridge to Chapter II

This introductory chapter establishes the current and historical significance of Pt-based chemotherapeutics in the medical fields, and their influence in cancer biology and inorganic chemistry. A current knowledge of the mechanisms of action for Pt chemotherapeutics, and potential mechanisms underlying side-effect and resistance/sensitivity profiles, was discussed, emphasizing how novel insights into these interactions are translatable to the clinical setting and will be needed to overcome the limitations of current Pt chemotherapeutics.

This chapter also provides a summary on ribosome biogenesis and the nucleolus, in the context of nucleolar stress and its connection to Pt compounds, including the finding that some Pt chemotherapeutics induce cell death through a disruption in ribosome biogenesis. Ribosome biogenesis and Pol I are importantly highlighted as potential targets for novel chemotherapeutic agents, necessitating a greater understanding of these mechanisms.

Chapter II will describe an immunofluorescence assay for determining nucleolar stress which was developed and used to identify chemical and structural properties necessary for Pt(II) analogs of oxaliplatin to induce nucleolar stress.

CHAPTER II: NUCLEOLAR STRESS INDUCTION BY OXALIPLATIN AND DERIVATIVES

This chapter has been previously published as: Sutton, E. C.; McDevitt, C. E.; Prochnau, J. Y.; Yglesias, M. V.; Mroz, A. M.; Yang, M. C.; Cunningham, R. M.; Hendon, C. H.; DeRose, V. J. Nucleolar Stress Induction by Oxaliplatin and Derivatives. *J. Am. Chem. Soc.* **2019**, *141* (46), 18411–18415. <https://doi.org/10.1021/jacs.9b10319>.

E.C.S. and C.E.M. share co-first authorship. E.C.S., C.E.M. and V.J.D. wrote the original manuscript with input from all authors.

Nucleolar Stress Induction by Oxaliplatin and Derivatives

The chemotherapeutic agent cisplatin has inspired the synthesis and investigation of thousands of Pt(II) analogs (Kelland, 2007). Of these, only two other compounds—carboplatin and oxaliplatin—have met FDA standards for medical use. Until recently, it was believed that the cytotoxicity of these compounds could be attributed solely to their DNA crosslinking abilities and subsequent induction of the DNA damage response (DDR), a known trigger of apoptotic pathways (Wexselblatt et al., 2012). As the body of research on Pt(II) reagents has grown, a more complex picture has emerged of the mechanisms of action behind these ubiquitous drugs (Wexselblatt et al., 2012). A striking recent discovery is that oxaliplatin, but not cisplatin or carboplatin, cause cytotoxicity via disruptions in ribosome biogenesis rather than DDR (Bruno et al., 2017). Ribosome biogenesis occurs in the nucleolus, a conserved and highly structured membrane-less organelle in eukaryotes. Disruptions of the nucleolus or ribosome biogenesis trigger the nucleolar stress response, which leads to cell death or senescence via activation of the tumor suppressor p53. Because its molecular mechanisms are not fully understood, and due to its potential role as a chemotherapeutic target, this fascinating stress process is an area of intense interest in the fields of molecular biology and medicine (Boulon et al., 2010; Farley-Barnes et al., 2018; Tsai & Pederson, 2014; Woods et al., 2015).

The specificity of oxaliplatin as a nucleolar stress inducer is intriguing when considered alongside other data indicating a relationship between Pt(II) compounds and the nucleolus (Pickard & Bierbach, 2013). Post-treatment fluorescent labeling of clickable

Pt(II) drug analogs has shown localization of these compounds to the nucleolus, (Pickard & Bierbach, 2013; Wirth et al., 2015) and there is significant evidence that Pt(II) compounds associate with ribosomes and ribosomal RNA (Hostetter et al., 2012; Melnikov et al., 2016; Osborn et al., 2014; Plakos & DeRose, 2017; Rijal & Chow, 2008; Saunders & DeRose, 2016; Sutton, McDevitt, Yglesias, et al., 2019). The structural determinants and molecular mechanisms by which only specific Pt(II) compounds may cause a nucleolar stress response are not understood. Here, we explore properties of oxaliplatin and other Pt(II) compounds and find that a narrow window of derivatives are able to induce nucleolar stress. The results define a set of constraints for Pt(II) compounds to induce this unique cell death pathway.

We selected Pt(II) compounds to test a variety of properties including steric bulk, hydrophobicity, cross-linking ability, and ligand orientation (**Figure 2.1**). The extent of nucleolar stress was measured by nucleophosmin (NPM1) imaging (**Figure 2.2** and **A.1**). Translocation of NPM1 from the granular component (GC) of the nucleolus to the nucleoplasm is a hallmark of the nucleolar stress response (Rubbi & Milner, 2003; Yang et al., 2016). NPM1 translocation has been shown to be a necessary, but not sufficient, feature of p53-mediated cell death upon nucleolar stress (Yang et al., 2016) and thus is a robust and appropriate marker. A549 cells were selected for this study as they are well-established to have a characteristic nucleolar stress response resulting in p53-mediated apoptosis (Bursac et al., 2014; Nicolas et al., 2016).

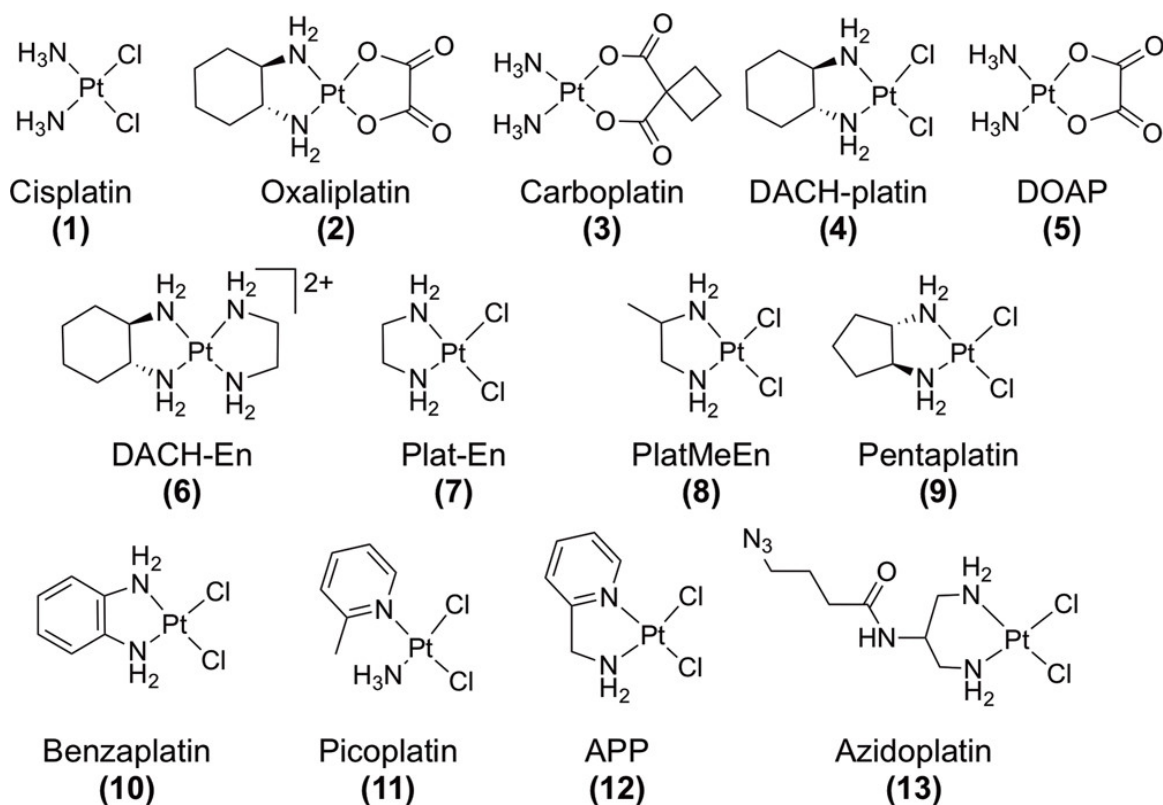


Figure 2.1. Compounds tested for inducing nucleolar stress via NPM1 relocalization in mammalian cells.

Cells were treated for 24 h with a given compound prior to fixation and secondary immunofluorescence to detect NPM1 (**Figure 2.2** and **A.1**). The extent of NPM1 redistribution was quantified using an image analysis pipeline (**Figure A.1**) to calculate the coefficient of variation (CV) of NPM1 intensity in each cell (**Figure 2.3**). The uniform distribution of NPM1 in cells undergoing nucleolar stress yields a low CV, as seen in positive control samples treated with known stress inducer, actinomycin D (ActD) (**Figure 2.3**). In addition to the observation of NPM1 redistribution, we noted a change in the shape of nucleoli from eccentrically shaped aggregates to round, sphere-like structures upon stress induction (**Figure 2.2**).

As predicted, (Bruno et al., 2017; McDevitt et al., 2019) oxaliplatin (2) induces robust redistribution of NPM1, similar to the positive control (ActD), while NPM1 distribution in cisplatin (1) and carboplatin (3) treated cells more closely resembles that of the no-treatment control (**Figure 2.2** and **2.3**).

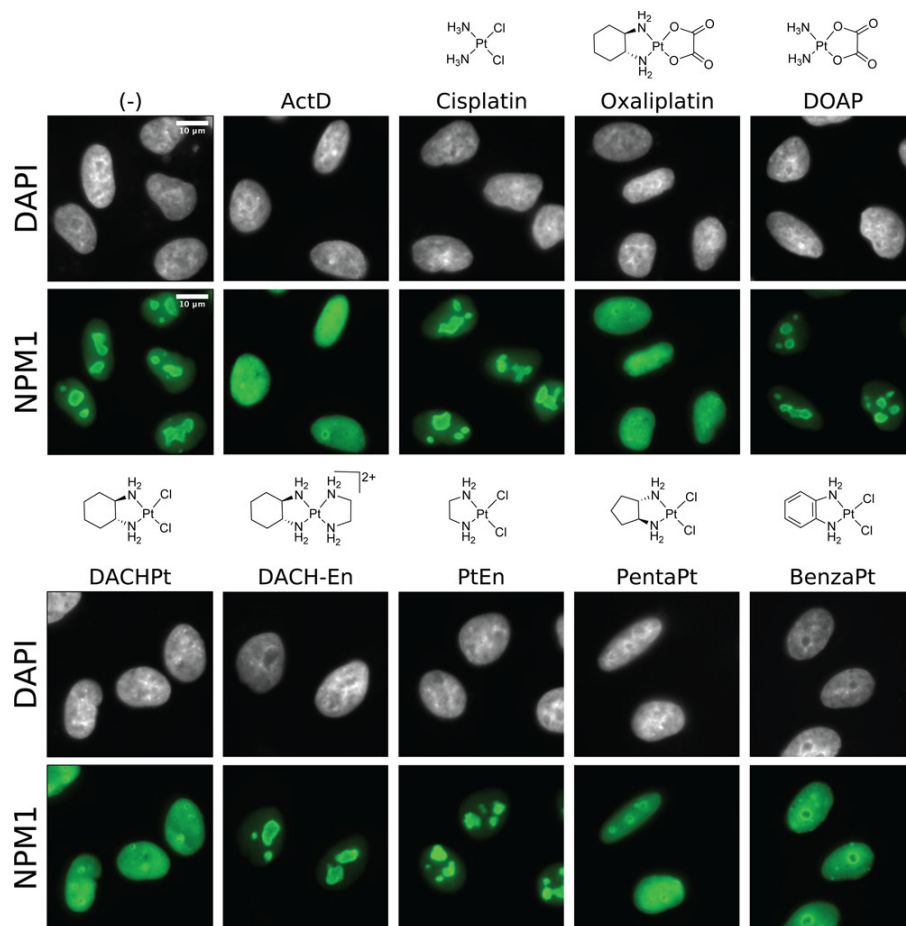


Figure 2.2. Nucleolar stress induced by Pt(II) compounds. NPM1 (green) relocation following 24 h treatment in A549 cells. Treatment concentrations are 10 μM except for ActD (5 nM). Scale bar = 10 μm.

We note that for cisplatin-treated cells, a small amount of NPM1 redistribution was observed at this treatment concentration. This is likely because the 24 h IC_{50} value for cisplatin (12.8 μM, **Table A.1**), is close to the treatment concentration, which may result in a subset of cisplatin-treated cells experiencing abnormal NPM1 distribution downstream of other cell death pathways, such as those mediated by the DDR.⁴ Oxaliplatin, by contrast, shows robust NPM1 relocation at treatment concentrations well below the 24 h IC_{50} value (81.5 μM, **Table A.1**), suggesting that nucleolar stress significantly precedes cell death pathways (Bruno et al., 2017). NPM1 relocation at concentrations below IC_{50}

⁴ This model is supported by previously published data demonstrating that cisplatin causes significantly more DNA damage than oxaliplatin (Chaney et al., 2005; Faivre et al., 2003; Woynarowski et al., 2000) and that DDR-mediated cell death occurs upon cisplatin treatment, but not oxaliplatin treatment. (Bruno et al., 2017) Additionally, data from our lab shows that DNA damage occurs at early time points in cisplatin-treated cells, prior to observed NPM1 distribution in oxaliplatin-treated cells (unpublished).

value was observed with other stress-inducing compounds, some of which did not exhibit significant cell death until 48 h of treatment (**Tables A.1** and **A.2**). Thus, observation of nucleolar stress at 24 h does not necessarily predict measured toxicity.

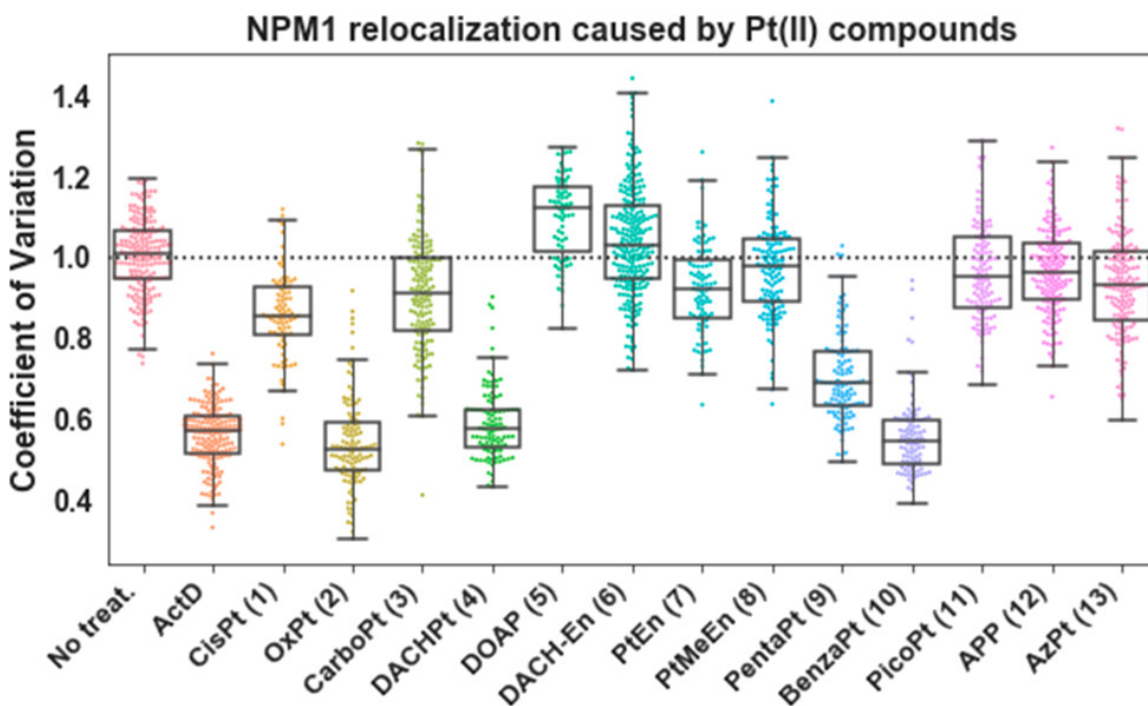


Figure 2.3. Quantification of NPM1 relocalization induced by Pt(II) compounds. Treatment conditions as in **Figure 2.2**; replicates, CV calculations, and boxplot presentation as described in Appendix A. For each treatment data set, boxes represent median, first, and third quartiles, and vertical lines are the range of data with outliers defined in the Appendix A.

Oxaliplatin is distinct from cisplatin and carboplatin in both labile and nonlabile Pt(II) ligands. The labile, chelating oxalate ligand of oxaliplatin delays aquation and therefore biomolecule cross-linking (Jerremalm et al., 2002) in comparison with cisplatin. We exchanged the labile and nonlabile ligands of oxaliplatin and cisplatin with DACHPt (4), and DOAP (5). We found that 4, which has the nonlabile DACH ligand of oxaliplatin and labile chloride groups of cisplatin, induces robust nucleolar stress. By comparison, 5, which possesses the nonlabile ammine ligands of cisplatin and the labile oxalic acid ligand of oxaliplatin, does not induce stress (**Figure 2.2** and **2.3**). The oxalic acid ligand alone also had no influence on NPM1 redistribution, nor did the DACH ligand by itself (**Figure A.2** and **A.3**). From this, we concluded that the nonlabile DACH ligand of oxaliplatin is responsible for the nucleolar stress response.

We next considered whether cross-linking of biomolecules by the Pt(II) compound is necessary for the induction of nucleolar stress. An alternate hypothesis is that the charged Pt(II) acts as a targeting agent to facilitate transport of the DACH moiety to the nucleolus where it disrupts nucleolar processes without forming a Pt(II)-DACH lesion on a biomolecule. DACH-En (**6**) retains the DACH ligand but is unable to form cross-links with biomolecules due to replacement of the oxalic acid with an ethylene diamine ligand (**Figure 2.1 6**). This positively charged compound did not induce stress (**Figure 2.2 and 2.3**), suggesting that cross-linking of Pt(II) to cellular targets is necessary to induce a nucleolar stress response.

To refine requirements of the Pt(II) ligands that cause nucleolar stress, we examined the effects of steric bulk by testing PtEn (**7**), PtMeEn (**8**), and pentaplatin (**9**). Compound **7** possesses a nonlabile ethylenediamine ligand. This small molecule did not induce stress in A549 cells (**Figure 2.2 and 2.3**), indicating that a chelating diamine ligand, a common feature between **7**, **4**, and oxaliplatin, is not sufficient to induce stress. The addition of a methyl group to generate the bulkier **8** was also not sufficient to induce stress (**Figure 2.3, A.2, and A.3**). Compound **9** possesses a five-membered ring that places its volume between the non-stress-inducing **8** and the stress-inducing six-membered **4** (**Figure 2.4.A**). Compound **9** was found to induce nucleolar stress (**Figure 2.2**), although with a slightly higher resultant CV than positive controls or oxaliplatin (**Figure 3**). These results suggest that bulk may be an important metric lending towards the ability of Pt(II) compounds to induce nucleolar stress. Using computed values for volume, we conclude that as a general trend Pt(II) compounds with more steric bulk are more likely to induce nucleolar stress (**Figure 2.4.A, y-axis**). Compound length, or steric reach, also generally appears to correlate with stress induction (**Figure 2.4.A, x-axis**). Some exceptions to this trend are discussed below.

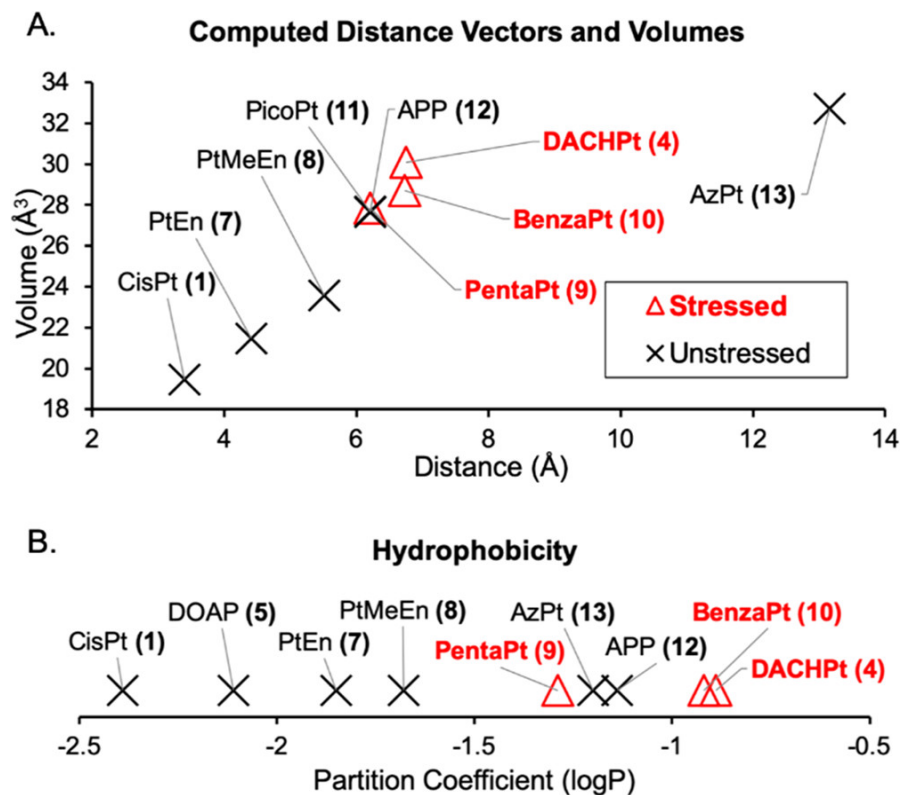


Figure 2.4. Size and hydrophobicity correlate with stress induction, with some exceptions. **A** | Ligand reach, or farthest distance from the Pt center, compared to computed volume measurements. **B** | Hydrophobicity of Pt compounds determined by the water/octanol partition coefficient. Compounds with a higher partition coefficient ($\log P$) are more hydrophobic than those with a lower $\log P$. $\log P$ measurements and calculations of compound volume and Pt-edge distance are described in the Appendix A.

The chair confirmation of the DACH ligand is not essential for stress induction. BenzaPt (**10**), in which the DACH cyclohexane is replaced with a planar aromatic ring (Figure 2.1, **10**), also induces robust NPM1 redistribution (Figure 2.2 and 2.3). Like compound **4**, **10** is more hydrophobic than the simpler diam(m)ine compounds. To estimate the relative hydrophobicity of our compounds of interest, we measured their water/octanol partition coefficients (Table A.3). All of the stress-inducing compounds were found to be relatively hydrophobic (Figure 2.4.B), leading to the conclusion that hydrophobicity, like steric bulk, positively correlates with stress induction. Similarly to steric bulk, however, exceptions to this trend were observed.

Picoplantin (**11**), APP (**12**), and azidoplatin (**13**) do not cause NPM1 relocalization despite being similar or higher in terms of size and hydrophobicity to compounds that do not cause nucleolar stress (Figure 2.4). These exceptions may provide insight into the elements responsible for causing stress.

One particularly interesting comparison is the ligand orientation between **12** and **10** (**Figure 2.5.A**). These two Pt(II) compounds both have an aromatic ring but differ in the orientation of the ring relative to the Pt(II) and, by extension, ring orientation relative to a biomolecule to which the compound is bound. While benzaPt causes nucleolar stress, AP does not. Similarly, **11** does not cause nucleolar stress despite having volume and reach similar to other compounds (**Figure 2.4.A and 2.5**). These results demonstrate a critical role for ring orientation in the ability of Pt(II) compounds to induce nucleolar stress.

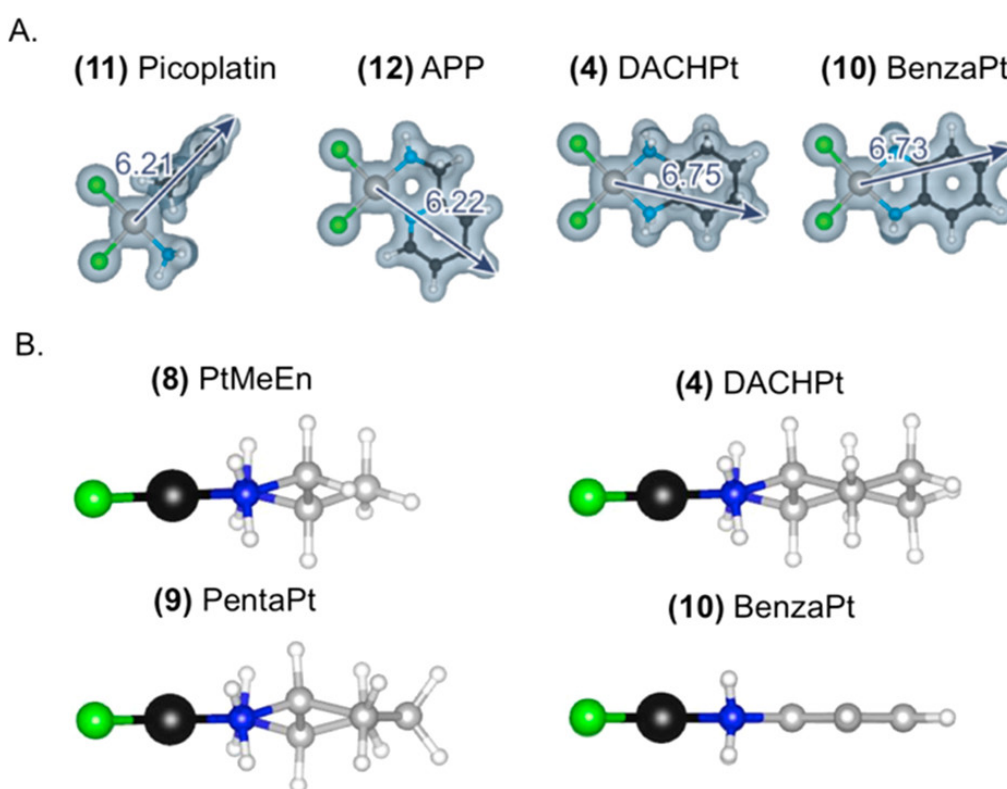


Figure 2.5. **A** | Computed distance measurements and volume representations for nonstress-inducing compounds **11** and **12** alongside stress-inducing compounds **4** and **10**. **B** | Ball and stick drawings of nonstress-inducing compound **8** alongside stress-inducing **4**, **9**, and **10**.

The observation that **13** does not cause stress is of interest as this compound has extended volume and has previously been shown to localize to the nucleolus (Wirth et al., 2015). Thus, nucleolar localization, even when combined with relatively high hydrophobicity and larger bulk and length, is not sufficient to induce nucleolar stress.

Taken together, the results described provide significant insight into the structural determinants of nucleolar stress induction among Pt(II) compounds. We conclude that there is an important role for ligand orientation and a general correlation between steric bulk and stress induction (**Figure 2.5**).

The differential responses induced by these compounds have clinical implications as the three currently FDA-approved Pt(II) chemotherapeutics are known to have different treatment and side effect profiles. Other important differences between these compounds have been observed in the literature. For example, oxaliplatin is noted to cause immunogenic cell death (ICD), while cisplatin does not (Englinger et al., 2019; Siew et al., 2015; Terenzi et al., 2016). Although this contrast is also observed in nucleolar stress, connections between ICD and nucleolar stress are not well-studied. Oxaliplatin has also been shown to cause changes in the size of neuronal nucleoli correlating with peripheral neuropathy, (McKeage et al., 2001) a common side effect associated with oxaliplatin chemotherapy regimens. The relationship between nucleolar stress and platinum-induced neurotoxicity has not been explored. Additionally, there is some evidence that p53 mutations in colon cancer cell lines result in resistance to oxaliplatin-mediated cell death (Toscano et al., 2007). This may be of interest given oxaliplatin's use in colon cancer treatments and p53's role in nucleolar stress-induced cell death.

Further study is warranted to provide clarification on the molecular mechanisms by which these compounds induce such different responses in the cell. For example, the stress-inducers may be interfering with progression of ribosome biogenesis, (Bursac et al., 2014; Rubbi & Milner, 2003) disrupting an intermolecular interaction of NPM1 that sequesters it in the nucleolus, (Yang et al., 2016) altering biophysical properties of nucleic acids, (Keck & Lippard, 1992; Malina et al., 2007) or globally perturbing the biomolecular interactions that maintain nucleolar integrity. More work is needed to understand this fascinating biological stress process and to define the specific properties of Pt(II) compounds that cause it.

Bridge to chapter III

In this chapter we sought to identify structural and chemical components of Pt(II) compounds necessary for the induction of nucleolar stress, hypothesizing that inherent

differences in the chemical nature of oxaliplatin and cisplatin are responsible for disparate cell death pathways induced by these two chemotherapeutics.

By designing a quantitative immunofluorescence-based assay to measure relocalization of NPM1—an analog for nucleolar stress and disruption of ribosome biogenesis—we performed a structure function study utilizing a strategic library of Pt(II) compounds. Chapter III expands this framework to a set of non-canonical monofunctional Pt(II) compounds based on phenanthriplatin, which has also been shown to induce cell death through disruption of ribosome biogenesis.

CHAPTER III: MONOFUNCTIONAL PLATINUM(II) COMPOUNDS AND NUCLEOLAR STRESS: IS PHENANTHRIPLATIN UNIQUE?

This chapter was originally published as: McDevitt, C. E.; Yglesias, M. V.; Mroz, A. M.; Sutton, E. C.; Yang, M. C.; Hendon, C. H.; DeRose, V. J. Monofunctional Platinum(II) Compounds and Nucleolar Stress: Is Phenanthriplatin Unique? *J Biol Inorg Chem* **2019**, *24* (6), 899–908. <https://doi.org/10.1007/s00775-019-01707-9>.

C.E.M. and V.J.D. wrote the original manuscript with input from all authors.

Introduction

Platinum-based drugs are an important class of chemotherapeutics. After the initial discovery of the anti-proliferative capabilities of cisplatin, the drug was FDA approved in 1978 and continues to be in significant use over 40 years later (Kelland, 2007; Rosenberg et al., 1965). Two additional Pt(II) compounds were subsequently approved by the FDA, carboplatin in 1989 and oxaliplatin in 1996. Improvements upon these three drugs have been attempted and some new compounds even entered into clinical trials, but none have been approved by the FDA (Kelland, 2007).

The three FDA-approved drugs are all considered classical platinum compounds. The characteristics of classical compounds are a result of early structure-activity relationship (SAR) studies that determined the necessary properties for platinum compounds to exhibit anti-proliferation activity (Johnstone et al., 2014). These required components are that the platinum compound be square planar, have a neutral overall charge, and contain two non-labile cis-am(m)ines and two labile cis anionic ligands (Johnstone et al., 2014). Although these rules led to the drugs that are used today, research into compounds that would not be within a traditional SAR study have produced non-classical platinum drugs with anti-proliferative activity. These non-classical compounds include Pt(IV) prodrugs, monofunctional platinum compounds, trans-platinum, polyplatinum, and tethered platinum, complexes (Johnstone et al., 2014; Sutton, McDevitt, Yglesias, et al., 2019). One of the most effective and well-studied non-classical compound is the monofunctional Pt(II) compound, phenanthriplatin (**Figure 3.1**) (Johnstone et al., 2014; Park et al., 2012). In addition to having only a single exchangeable

anionic ligand, the *N*-heterocyclic ligand of phenanthriplatin and others of this class, such as picoplatin (**Figure 3.1**), is perpendicular to the square-planar Pt ligand plane.

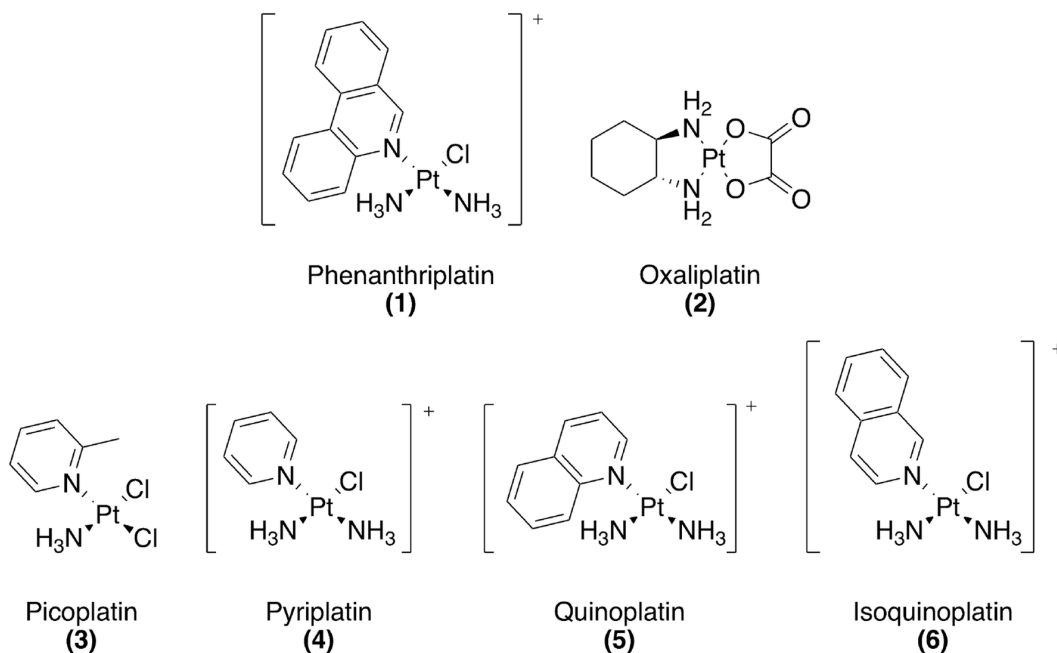


Figure 3.1. Platinum compounds used in this study

Phenanthriplatin has exhibited 7–40× higher activity in the NCI-60 human tumor cell line screen when compared to other platinum chemotherapeutics (Johnstone et al., 2014; Park et al., 2012). Phenanthriplatin has higher cellular uptake than cisplatin or pyriplatin (Park et al., 2012). In addition, the phenanthridine ligand of phenanthriplatin may facilitate rapid DNA binding through reversible intercalation between nucleobases before Pt-DNA binding occurs (Almaqwashy et al., 2019). Studies have also revealed some of the biological targets of phenanthriplatin. It has been shown to act as a topoisomerase II poison (Riddell et al., 2016). Phenanthriplatin lesions were also demonstrated to inhibit RNA Polymerase II activity, (Kellinger et al., 2013) but allows DNA polymerase η bypass (Gregory et al., 2014). Overall, these studies have shown that phenanthriplatin can affect biological processes in a variety of ways, and this has led researchers to suggest that the effectiveness of the compounds is through multiple cellular pathways (Facchetti & Rimoldi, 2019).

In a recent study, the classical platinum compound oxaliplatin and non-classical platinum compound, phenanthriplatin were both shown to induce ribosome biogenesis

stress as the primary pathway to induce cell death (Bruno et al., 2017). This surprising observation is in contrast with cisplatin and carboplatin, which were shown to cause cell death through DNA damage as expected for classical compounds. The ability to induce nucleolar stress shared between oxaliplatin and phenanthriplatin is perplexing considering the major structural differences between the two compounds. We endeavored to determine whether there were structural similarities between these two molecules which would explain this similar activity and determine whether the ability to induce nucleolar stress was inherent to the family of non-classical monofunctional platinum(II) compounds⁵. To do this, we synthesized a suite of monofunctional and related platinum compounds (**Figure 3.1**) and analyzed their ability to cause nucleolar stress by measuring nucleophosmin (NPM1) relocalization. We further compared structural and electronic properties of these compounds based on DFT calculations. We find that phenanthriplatin, but not related quinoplatin or isoquinoplatin, induce nucleolar stress as measured by NPM1 relocalization in human lung carcinoma A549 cells. Although phenanthriplatin has the largest total volume and hydrophobicity of the compounds tested, quinoplatin and isoquinoplatin may have similar potential to disrupt intermolecular interactions based on Pt-ligand distances. We conclude that the unique ability of phenanthriplatin to induce nucleolar stress is conferred by the acridine ring. The ligand disposition of these monofunctional *N*-heterocyclic Pt(II) compounds is sufficiently different from oxaliplatin to suggest that separate properties of oxaliplatin and phenanthriplatin lead to their abilities to both cause nucleolar stress.

Results and discussion

Oxaliplatin and phenanthriplatin cause NPM1 relocalization

A previous study examining cell death mechanisms of phenanthriplatin (**1**) and oxaliplatin (**2**) has shown that both compounds cause cell death through ribosome biogenesis stress (Bruno et al., 2017). In this study, we monitored NPM1 relocalization from the nucleolus to the nucleoplasm, which is a hallmark of nucleolar stress (Yang et al., 2016). Under non-stress conditions NPM1 is localized to the nucleolus; however, NPM1 is distributed throughout the nucleoplasm during nucleolar stress. We set out to

⁵ Monofunctional Pt(II) compounds following the structure *cis*-[Pt(NH₃(Am)Cl)]⁺ (Am = aromatic *N*-heterocyclic amine).

measure the extent of NPM1 relocalization when cells were treated with platinum compounds with cyclic ligands and either monofunctional or bifunctional substitution properties.

We first examined NPM1 relocalization following treatment with oxaliplatin and phenanthriplatin. Actinomycin D (ActD), a known ribosome biogenesis stress inducer, caused NPM1 relocalization to the nucleoplasm while the negative no-treatment control showed NPM1 localization in the nucleoli (**Figure 3.2.A**). Both **1** and **2** caused relocalization of NPM1 throughout the nucleus, confirming their ability to cause nucleolar stress as previously reported (Bruno et al., 2017).

To determine the extent of nucleolar stress, we quantified the heterogeneity of nuclear NPM1 intensity distribution by its coefficient of variation (CV). The CV is calculated as the standard deviation in pixel intensity corresponding to NPM1-based immunofluorescence within the nucleus, normalized by the mean intensity. In cells that are undergoing nucleolar stress, NPM1 is relatively evenly diffused throughout the nucleus, leading to homogeneous intensities and a small CV value. Histograms of representative NPM1 immunofluorescences in cell images show an even population of pixel intensities within the nucleus for compounds that cause NPM1 relocalization (**Figure 3.2.B**). For cells that are not undergoing stress, NPM1 is concentrated in the nucleolus while being absent in the nucleoplasm, resulting in a heterogeneous population of pixel intensities and a high CV value. Histograms of NPM1 immunofluorescences from compounds that do not cause NPM1 relocalization show a bimodal distribution in pixel intensities which would result in a large CV (**Figure 3.2.B**). The CV was calculated for individual cells and averaged for each treatment condition. Corresponding to our representative NPM1 images (**Figure 3.2.A**), compounds that caused no NPM1 redistribution had a median CV around 1 (when normalized to the no-treatment control) while compounds that caused NPM1 relocalization had a median CV at or lower than, 0.6 (normalized to the no-treatment control).⁶ NPM1 relocalization was observed upon treatment with **1**, **2**, and ActD (**Figure 3.2.C**). Additionally, treatment with phenanthridine ligand alone is not sufficient to induce nucleolar stress (**Figure 3.2.C**).

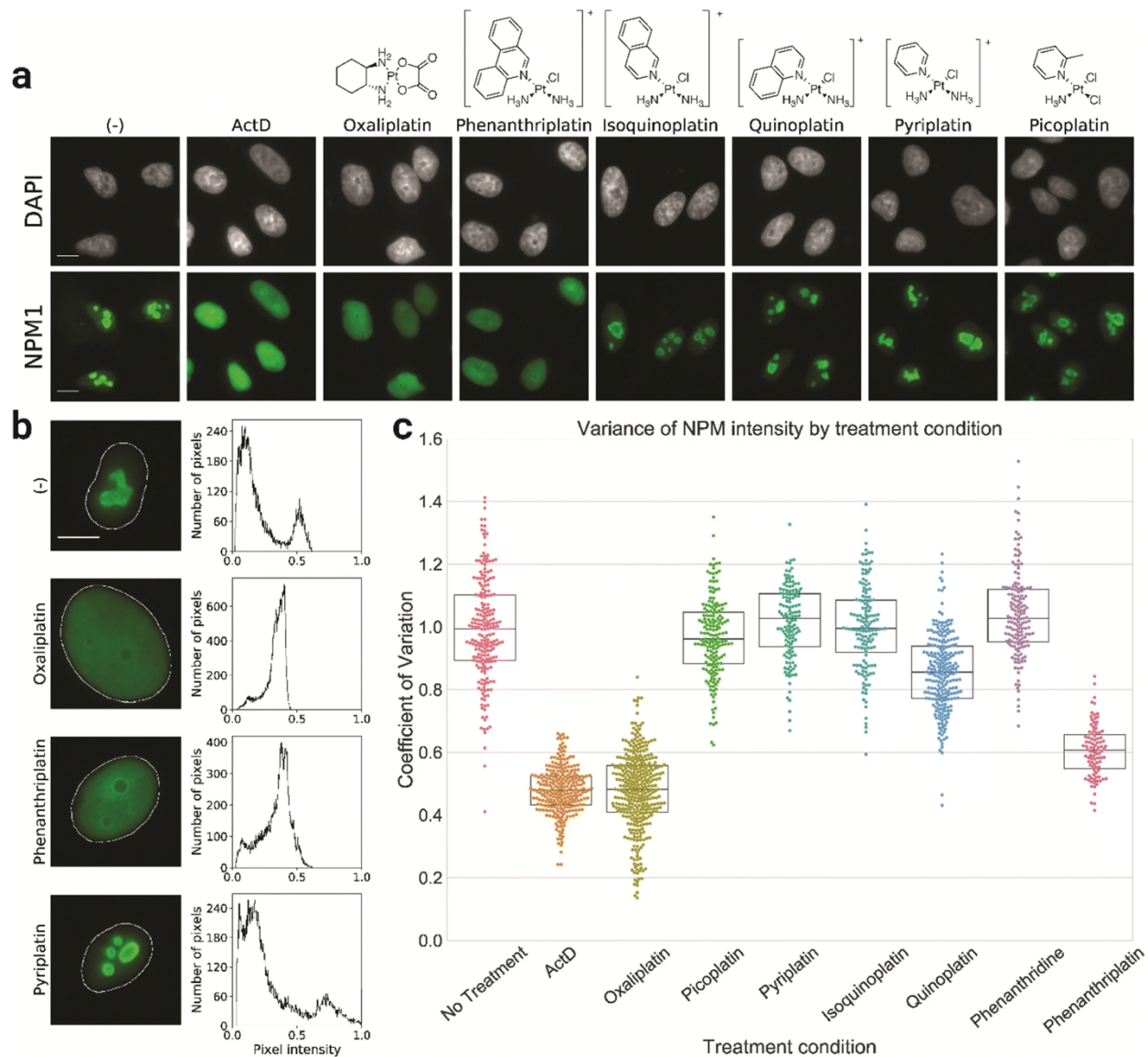
⁶ In this study we observed that cells undergoing nucleolar stress—when determined by relocalization of NPM1—had an average CV ≤ 0.6 when normalized to the untreated cells.

Picoplatin does not cause NPM1 relocation

There are large structural differences between oxaliplatin and phenanthriplatin; however, these disparate compounds are both able to activate nucleolar stress pathways whereas cisplatin does not. Both the DACH ligand of oxaliplatin and the phenanthridine ligand of phenanthriplatin add significant steric bulk in comparison to cisplatin. However, phenanthriplatin is a monofunctional compound. In addition, unlike the case of oxaliplatin, in phenanthriplatin, the phenanthridine ring is oriented perpendicular to the square-planar Pt ligand plane (Park et al., 2012). Picoplatin (**3**) is one compound that bridges these differences in that the 2-picoline ligand is oriented perpendicular to the square-planar Pt ligand plane (Chen et al., 1998). **3** is also a classical bifunctional platinum compound and enabled us to determine whether the added ligand bulk regardless of orientation was sufficient to induce NPM1 relocation. In A549 cells treated with **3**, NPM1 did not relocate to the nucleoplasm (**Figure 3.2.A**) as quantified by a median normalized CV of approx. 1 (**Figure 3.2.C**), indicating that **3** does not cause nucleolar stress.

NPM1 relocation is not a general property of monofunctional platinum compounds.

After determining that the bifunctional compound, **3**, did not cause NPM1 relocation despite having some similarities to oxaliplatin in terms of added ring and steric bulk, we next examined the properties of non-classical monofunctional platinum compounds. We synthesized three additional monofunctional compounds that have a pyridine or quinoline ligand to test whether nucleolar stress was inherent to ring-containing monofunctional platinum(II) compounds as a whole or whether it was a phenomenon only exhibited by phenanthriplatin.



We had tested **3** and determined that the perpendicular orientation of the picoline ligand is not sufficient to cause NPM1 relocalization. To further explore the influence of ligand orientation and the binding mode of monofunctional Pt compounds, we next tested pyriplatin (**4**). Similar to **3**, **4** contains a single aromatic ring. However, unlike **3**, **4** has more possible orientations of the aromatic ring due to the lack of steric interference involving the methyl group of the 2-picoline ligand (Johnstone & Lippard, 2014). In addition, **4** is more similar to **1** in being a monofunctional compound with an overall positive charge. Following a 24 h treatment at 10 μ M, **4** did not cause NPM1 relocalization and samples had a median normalized CV of approx. 1 (**Figure 3.2**). From this we concluded that the ability to cause NPM1 relocalization was not inherent to the class of monofunctional Platinum(II) compounds containing *N*-heterocyclic ligands.

We next considered whether steric bulk was a factor in NPM1 relocalization by examining the influence of the addition of a second ring. We synthesized the structural isomers quinoplatin (**5**) and isoquinoplatin (**6**) (**Figure 3.3**), to test whether a second aromatic ring would be sufficient to cause NPM1 relocalization. We tested these compounds and determined that neither **5** nor **6** caused increased NPM1 relocalization⁷, with NPM1 intensities from cells treated with both compounds having a median normalized CV of approx. 1 (**Figure 3.2**). From this we concluded that for monofunctional Pt(II) compounds, the steric bulk from a second ring alone does not induce NPM1 relocalization regardless of ring orientation. This added further evidence that NPM1 relocalization was not an inherent property of this non-classical class of platinum compounds and was unique to **1** under these conditions.

Steric bulk is not sufficient to predict NPM1 relocalization

From our data, we have determined that phenanthriplatin and oxaliplatin are unique to our suite of compounds. We next examined whether there are any trends present in steric bulk that could explain whether compounds caused NPM1 relocalization. The molecular structure for all platinum(II) compounds investigated in

⁷ Our conclusions here were ultimately based on the visual lack of well-defined NPM1 relocalization in cell images when compared to **1**, **2**, and ActD (**Figure 3.2.A**). We did however notice, CV measurements in cells treatments with **5** were slightly lower on average compared to untreated cells (norm. CV = 0.85, **Figure 3.2.B**). This prompted a subsequent concentration dependence experiment (**Figure B.1**) where we found that **5** did not induce significant levels of NPM1 redistribution even at high concentrations (20 μ M).

this study were optimized using DFT (**Figure 3.4**) and two variables were calculated to assess steric bulk. First, the volume of the optimized, non-hydrolyzed structure is obtained by sampling the respective electrostatic potential (**Table 3.1**). **2** and **1** were the compounds with the largest volume; however, this included the aquation-labile ligands which accounts for a large portion of oxaliplatin's volume.

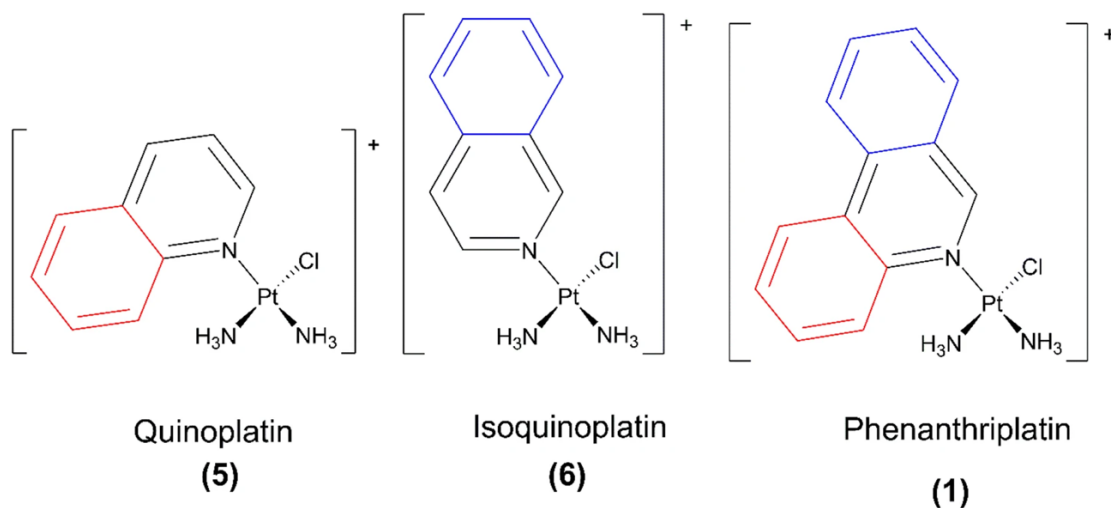


Figure 3.3. Two-ring structural isomers related to phenanthriplatin

Second, the magnitude of the maximum vector between the platinum center and the surface of the compound, where the surface of the compound is defined as the extent to which electrostatic potential permeates in space was calculated (**Table 3.1**). No trend was found with these distance measurements. Oxaliplatin, which causes NPM1 relocalization had similar distance to that of isoquinoplatin which did not cause NPM1 relocalization (**Table 3.1**). Thus, while phenanthriplatin exhibits the largest steric bulk, it does not have the maximum steric reach from platinum to the surface of the compound.

Table 3.1. Steric bulk measurements for platinum compounds in order of increasing volume.

Compound	Volume (\AA^3)	Maximum Pt-to-surface distance (\AA)
Pyriplatin (4)	24.91	6.27
Picoplatin (3)	27.69	6.21
Isoquinoplatin (6)	31.21	8.37
Quinoplatin (5)	33.89	7.15
Oxaliplatin (2)	34.13	6.78
Phenanthriplatin (1)	37.25	7.72

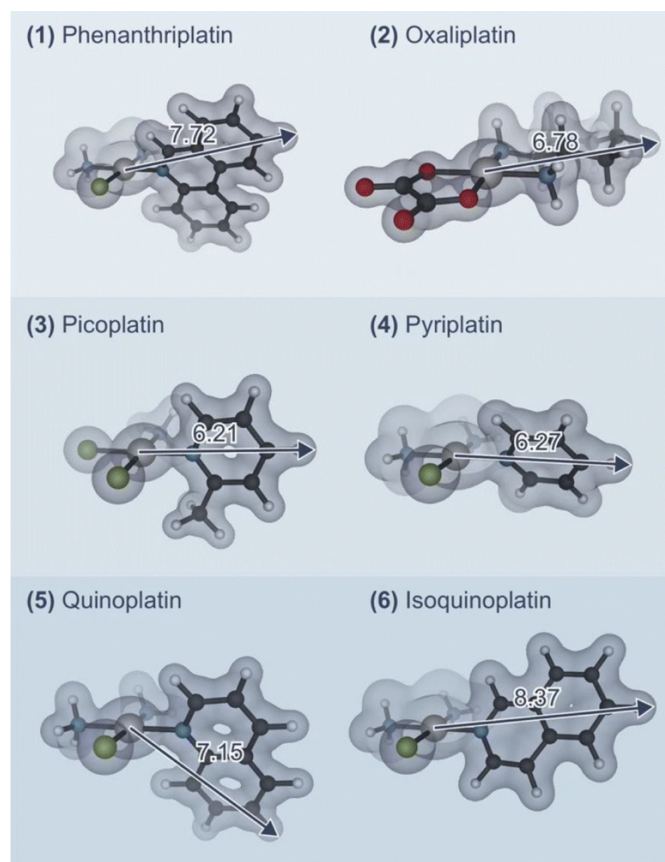


Figure 3.4. Optimized structures of the platinum(II) compounds are displayed at an isosurface level of $0.25 \text{ e}/\text{\AA}^{-3}$ for each compound, as implemented in VESTA. This illustrates the volume of the molecule that is reported. The distances between the platinum atom and the surface of each compound are shown with the corresponding vector. All measurements are reported in angstrom (\AA).

Hydrophobicity is not sufficient for predicting NPM1 relocalization

Hydrophobicity of the non-labile ligand may be an important factor for interrupting biomolecular interactions, or in partitioning into cellular compartments or subregions of the nucleolus. We examined if there was a trend in hydrophobicity that would explain why **2** and **1** cause NPM1 relocalization while all other compounds in our library did not. We used our optimized structures to calculate $\Delta G_{\text{water-octanol}}$ (**Table 3.2**). As expected, compounds with more aromatic rings were more hydrophobic and had a more positive $\Delta G_{\text{water-octanol}}$ while compounds with less rings showed the opposite trend. **1** is more hydrophobic than all other tested compounds except **3**, which does not cause NPM1 relocalization and is the most hydrophobic compound tested with a Gibbs solvation energy of 2.54 kcal/mol. Overall, this measure of hydrophobicity was not able to produce a trend that provides a satisfactory explanation for why oxaliplatin and

phenanthriplatin cause NPM1 relocalization while other platinum(II) compounds did not. Therefore, we can conclude that hydrophobicity alone is not sufficient for causing NPM1 relocalization.

Table 3.2. Gibbs free energy of transfer between octanol and water

Compound	$\Delta G_{\text{water-octanol}}$ (Kcal/mol)
Oxaliplatin (2)	-4.92
Pyriplatin (4)	-1.92
Isoquinoplatin (6)	-0.607
Quinoplatin (5)	-0.34
Phenanthriplatin (1)	0.94
Picoplatin (3)	2.54

Conclusions

This work aimed to find a structural relationship between oxaliplatin and phenanthriplatin which would provide information on necessary and sufficient structural components required for these platinum compounds to induce cell death via nucleolar stress. In comparison with cisplatin, which does not cause nucleolar stress, oxaliplatin and phenanthriplatin both have significantly larger ring-containing ligands. Phenanthriplatin is also a monofunctional Pt(II) compound. To explore this question, we synthesized a library of ring-containing platinum compounds, most being monofunctional Pt(II) compounds. This library was tested for the ability to induce nucleolar stress by monitoring NPM1 relocalization and quantifying the resulting images. First, we tested oxaliplatin and phenanthriplatin to confirm that they caused NPM1 relocalization in agreement with previous literature proposing that they cause nucleolar stress (Bruno et al., 2017). We then tested whether a heterocyclic ligand plane would be sufficient by testing picoplatin and found that picoplatin did not cause nucleolar stress as measured by NPM1 relocalization. Thus, for bifunctional platinum compounds, a ligand ring is insufficient to cause nucleolar stress.

We investigated the importance of ligand ring number and distribution in other compounds of the monofunctional platinum(II) class by testing pyriplatin, quinoplatin, and isoquinoplatin. None of these compounds caused NPM1 relocalization, indicating that phenanthriplatin was unique in this class of monofunctional Pt(II) compounds. We note that this limited study has been performed at a single concentration and treatment

time for all compounds. It is possible that longer treatment time or higher concentrations might lead to different effects, and this is being explored in further studies. None of the non-phenanthriplatin compounds cause significant levels of nucleolar stress at relatively high (10 μM) treatment concentrations compared to phenanthriplatin (0.5 μM), indicating that they are in a different class than phenanthriplatin in terms of activities.

We performed DFT calculations to optimize structures and calculate the solvent-dependent difference in Gibbs free energy between water and *n*-octanol, a measure of hydrophobicity. To further investigate structural characteristics, we calculated the maximum distance from the platinum atom to the surface of each structure and volume from DFT-optimized structures. We found no correlation between this distance and the ability to cause NPM1 relocalization. Further, there was no strong correlation between the solvent-dependent difference in Gibbs free energy between water and octanol for compounds that were able to induce NPM1 relocalization.

In view of these results, we suggest that phenanthriplatin is a unique compound in the monofunctional platinum(II) compound class in its ability to cause NPM1 relocalization. We suggest that the addition of a third aromatic ring in phenanthriplatin may play a large role in differentiating phenanthriplatin from other monofunctional platinum(II) compounds we tested for inducing nucleolar stress. The presence of a third aromatic ring increases steric bulk both above and below the square-planar platinum ligand plane. Additionally, a third ring increases hydrophobicity and provides intercalation potential to phenanthriplatin (Almaqwashy et al., 2019) in comparison to quinoplatin and isoquinoplatin. Phenanthriplatin exhibited the largest volume and was the most hydrophobic compound of the monofunctional platinum(II) compounds but did not exhibit the longest distance from the platinum atom to the edge of the non-labile ligand. Consequently, spatial orientation and/or hydrophobicity caused by the presence of a third aromatic ring may be significant factors in differentiating phenanthriplatin from the rest of its family. Derivatization of phenanthriplatin could further elucidate the structural components of this third aromatic ring that are responsible for causing NPM1 relocalization. We also note that the fast kinetics of DNA binding exhibited by phenanthriplatin may play a role in why phenanthriplatin is unique in the class of monofunctional platinum(II) compounds (Almaqwashy et al., 2019).

While oxaliplatin and phenanthriplatin both contain extended ligand structures around platinum(II), we find that steric properties alone are insufficient to explain the shared ability of these compounds to cause nucleolar stress. It is possible that monofunctional and bifunctional platinum(II) compounds may induce NPM1 relocalization through different binding effects or mechanisms.

Bridge to chapter IV

Chapter III applies an immunofluorescence-based assay to quantitate relocalization of NPM1 induced by monofunctional Pt(II) compounds in order to elucidate structure and chemical characteristics of phenanthriplatin which are necessary for induction of nucleolar stress.

In chapter IV we address differences in nucleolar stress induced by Pt(II) compounds identified in previous studies through time-dependent study of NPM1 relocalization and investigate the biological impacts these difference may impart.

CHAPTER IV: TIME-DEPENDENT STUDIES OF OXALIPLATIN AND OTHER NUCLEOLAR STRESS-INDUCING Pt(II) DERIVATIVES

This chapter was originally published as: Pigg, H. C.; Yglesias, M. V.; Sutton, E. C.; McDevitt, C. E.; Shaw, M.; DeRose, V. J. Time-Dependent Studies of Oxaliplatin and Other Nucleolar Stress-Inducing Pt(II) Derivatives. *ACS Chem. Biol.* **2022**, *17* (8), 2262–2271. <https://doi.org/10.1021/acscchembio.2c00399>.

H.C.P. and V.J.D. wrote the original manuscript with input from all authors.

Introduction

The success of cisplatin as a chemotherapy drug over the last 40 years has led to the investigation of thousands of Pt(II) compounds, only two of which, oxaliplatin and carboplatin, have been approved for clinical use by the FDA (Kelland, 2007). The mechanism of action for Pt(II) compounds has long been attributed to the DNA damage response (DDR) (Wexselblatt et al., 2012). Oxaliplatin, however exhibits different effects that have been attributed to both the larger diaminocyclohexane (DACH) carrier ligand and the chelating oxalate leaving group (**Figure 4.1 2**) (Schoch et al., 2020). Recently, it was reported that the cytotoxic effects of oxaliplatin are caused by the ribosome biogenesis stress response instead the DDR (Bruno et al., 2017). Ribosome biogenesis stress, occurs in the nucleolus and can lead to apoptotic cell death when ribosome biogenesis is disrupted, such as through disruption of the nucleolar structure or through disruption of rRNA synthesis, rRNA processing, or ribosome assembly (Tsai & Pederson, 2014). Only a few small organic molecules, such as actinomycin D (ActD), CX-5461, and BMH-21, are known to cause nucleolar stress through RNA polymerase I inhibition (Jacobs, Huffines, et al., 2022; Jean-Clément Mars et al., 2020; Yung et al., 1985). The inclusion of specific mononuclear platinum compounds on this list (Bruno et al., 2017; McDevitt et al., 2019, 2022; Sutton, McDevitt, Prochnau, et al., 2019; Sutton & DeRose, 2021) would be unique for metallodrugs and also opens new opportunities for mechanistic studies of nucleolar processes.

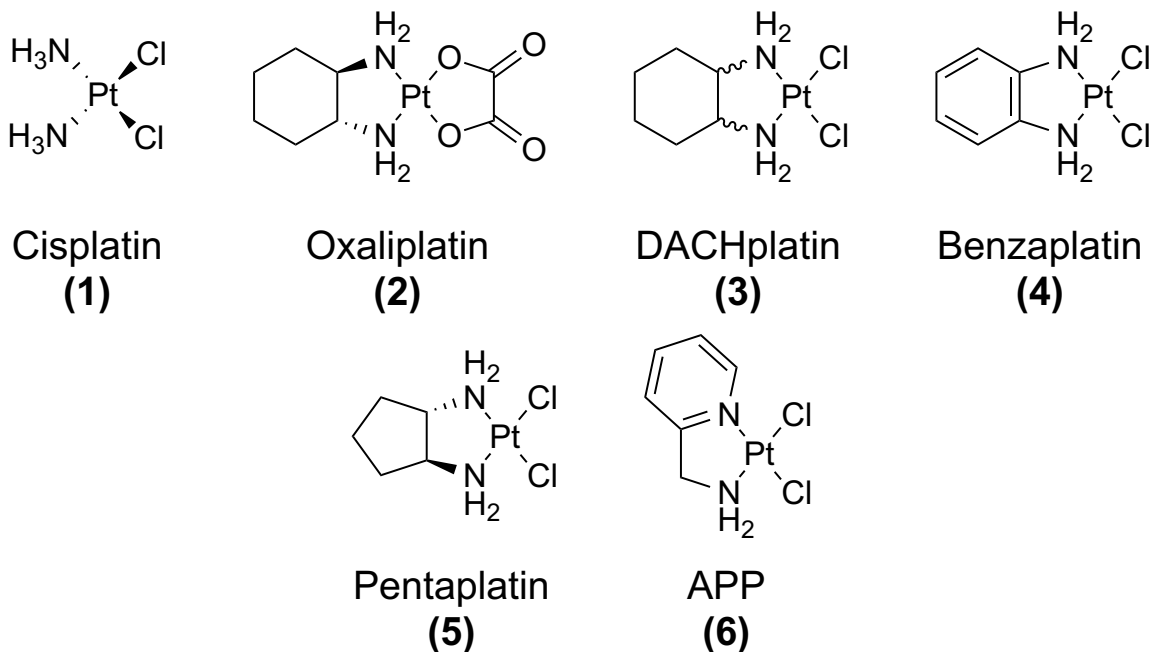


Figure 4.1. Pt(II) compounds used in this study. DACHplatin is a 1:1 mixture of the *1R,2R* and *1S,2S* isomers. Compounds 2–5 induce nucleolar stress.

In previous work, we investigated the structural requirements of platinum compounds necessary to cause nucleolar stress and found at least three derivatives in addition to oxaliplatin (**Figure 4.1 3–5**) that induce robust nucleolar stress responses. We found that Pt(II) coordination to the DACH ring, but not the oxalate leaving group, was sufficient to cause the nucleolar stress response as measured by the relocalization of nucleophosmin (NPM1) in mammalian cell culture (Sutton, McDevitt, Prochnau, et al., 2019). Further structure-function analysis found a narrow window of Pt(II) compounds, all containing a cyclic diamino bidentate ligand, that cause nucleolar stress (McDevitt et al., 2022). By contrast, Pt(II) compounds containing alkyl-diamine bidentate ligands do not cause nucleolar stress, even with large substituents (Sutton, McDevitt, Prochnau, et al., 2019). In addition, different orientations of ring substituents such as in picoplatin and [dichloro(2-picolylamine)platinum(II)] (APP) (**Figure 4.1 6**) apparently precludes induction of the nucleolar stress response (Sutton, McDevitt, Prochnau, et al., 2019). Phenanthriplatin, a monofunctional Pt(II) compound, also induces robust nucleolar stress but possibly through an alternative mechanism (Bruno et al., 2017; McDevitt et al., 2019). A trinuclear Pt(II) compound has also been shown to affect nucleolar processes (Peterson et al., 2015). For the oxaliplatin-related Pt(II) compounds investigated here (**Figure 4.1**),

the sensitivity of the stress response to small ligand changes suggests a model in which the ligand structure of the Pt(II) compound influences a molecular interaction in the nucleolus that induces the nucleolar stress response.

To further probe the mechanism of action for Pt(II) compounds in the nucleolus, we carefully compared effects of cisplatin and oxaliplatin on rRNA transcription and other nucleolar markers. At doses required to induce nucleolar stress, oxaliplatin (but not cisplatin) treatment inhibits rRNA transcription (Sutton & DeRose, 2021). Further, the onset of rRNA transcription inhibition appears to coincide with or precede NPM1 relocalization as well as changes in other nucleolar markers (Sutton & DeRose, 2021). Finally, at these conditions, oxaliplatin does not induce DDR markers to the extent that cisplatin does. These results support a model in which cisplatin primarily induces a DDR response, with downstream nucleolar effects, but oxaliplatin induces a primary nucleolar response. Inhibition of rRNA transcription and NPM1 relocalization are likely key factors in the onset of nucleolar stress induction by oxaliplatin.

In our previous work with oxaliplatin-like derivatives, nucleolar stress induction by all compounds was measured at 24 h after treatment (Sutton, McDevitt, Prochnau, et al., 2019). At that treatment time, both oxaliplatin and related ring-containing compounds lacking the oxalate leaving group (**Figure 4.1 3–5**) caused robust nucleolar stress. The relative rates at which these different compounds cause nucleolar stress and their ability to inhibit rRNA transcription are not known. Additionally, the relationship between nucleolar stress induction, cellular platinum accumulation and DNA binding are not well-established for any platinum compound. In this study we explore the time-dependence of nucleolar stress induction by Pt(II) compounds as measured by NPM1 redistribution. We also measure the extent of rRNA transcription inhibition by these stress-inducing compounds. Additionally, we determine whether cellular platinum accumulation is related to nucleolar stress induction, measured by using inductively coupled plasma mass spectrometry (ICP-MS) analysis on whole cell as well as nuclear fractions. We also determine whether *in vitro* and in-cell binding of platinum compounds to DNA correlate with the onset of NPM1 redistribution.

We find that not all stress-inducing Pt(II) compounds induce stress at the same time or even to the same degree. Additionally, we find correlation between rRNA transcription inhibition and NPM1 redistribution (Sutton & DeRose, 2021). We also

observe that differences in NPM1 redistribution could not be accounted for by whole cell or nuclear platinum accumulation, or Pt(II)-DNA binding kinetics *in vitro* or in-cell. This indicates that it is not likely the amount of Pt(II) compound entering cells or the amount binding to DNA that is determining whether a compound will cause nucleolar stress. Finally, we find that the 1*R*,2*R*-isomers of pentaplatin and DACHplatin induce a more robust nucleolar stress response when compared to their 1*S*,2*S*-isomers. Taken together, these results reinforce the proposal that Pt(II) compounds induce nucleolar stress through a specific molecular interaction and further characterizes new Pt(II) compounds that robustly cause inhibition of rRNA transcription.

Results and Discussion

Differences in Kinetics of Nucleolar Stress Induction by Pt(II) Compounds.

Compounds **2**, **3**, **4**, and **5** (**Figure 4.1**) have all been observed to cause nucleolar stress after 24 h of drug treatment time in A549 cells (Sutton, McDevitt, Prochnau, et al., 2019). It has previously been observed that oxaliplatin induces slight⁸ nucleolar stress as early as 90 min after treatment (Sutton & DeRose, 2021). Structural differences in these stress-inducing Pt(II) derivatives as in DACHplatin (**3**), with chloride ligands substituting for the chelating oxalate leaving group, an aromatic ring in benzaplatin (**4**), and a smaller ring size of pentaplatin (**5**) might influence the rate of inducing nucleolar stress. We used an NPM1 imaging assay, (McDevitt et al., 2019; Sutton, McDevitt, Prochnau, et al., 2019) to determine whether some of these compounds might have a more rapid influence on nucleolar processes than does oxaliplatin. In cells undergoing nucleolar stress, NPM1 is translocated from the granular component (GC) of the nucleolus to the nucleoplasm, (Rubbi & Milner, 2003; Yang et al., 2016) providing a convenient assay for stress induction. Timepoints ranging from 30 min to 24 h of drug treatment were tested in A549 cells. A549 cells were chosen because they have wild-type tumor suppressor protein p53, and Pt(II)-induced nucleolar stress has been characterized in this cell line (Sutton, McDevitt, Prochnau, et al., 2019; Sutton & DeRose, 2021). Each experiment was accompanied by an untreated negative control and positive control of low dose (5 nM) ActD, a known inducer of nucleolar stress via specific inhibition of RNA polymerase I

⁸ Reference to the “degree” or “amount” of nucleolar stress within this study refer specifically to CV measurements of NPM1 relocalization within the nucleolus.

(Pol I), which transcribes rRNA (Yung et al., 1985). Cells were imaged by NPM1 immunofluorescence and the extent of nucleolar stress, based on NPM1 redistribution, was quantified using the calculated coefficient of variation (CV) of NPM1 intensity in each cell (Sutton, McDevitt, Prochnau, et al., 2019). Data was normalized to no-treatment controls. Cells with extensive NPM1 relocalization, indicating nucleolar stress, produce CV values close to that of ActD of approx. 0.5–0.7 (McDevitt et al., 2019; Sutton, McDevitt, Prochnau, et al., 2019).

Timepoints of 90 min, 3 h, and 5 h, were found to be significant in discriminating the onset of nucleolar stress for the four Pt(II) compounds of interest. Specifically, we saw significant nucleolar stress occurring for **3** by 90 min, oxaliplatin and **4** by 3 h, and **5** by 5 h (**Figure 4.2**). ActD as well as cells containing no drug treatment were used as positive and negative controls, respectively.

A comparison of compound structures to the onset of nucleolar stress reveals interesting relationships. Oxaliplatin takes roughly double the time of **3** to induce stress. This is likely due to the slower exchange kinetics of the oxalate leaving group in comparison with the chloride ligands on **3** (Ahmad, 2017). However, **4** also takes double the time of **3** to induce stress, indicating that changing the aromaticity of the nonlabile ligand influences the time for nucleolar stress induction. As described below, this is not due to slower cellular accumulation of **4**, and therefore may be related to the behavior of the aromatic ring in cells. Finally, the 5-membered ring **5** not only takes longer than the other three compounds to induce detectable NPM1 relocalization, but also shows a lower overall degree of stress, indicated by the higher end point CV of ~0.7. A lower degree of stress induction by **5** was also observed at 24 h in our earlier work (Sutton, McDevitt, Prochnau, et al., 2019). **3** and **5** only vary in the size of the nonlabile ligand ring, indicating that there is likely a specific size that must be met for a compound to induce stress and slightly changing that not only changes the degree of stress that will occur, but also how quickly that compound will induce stress.

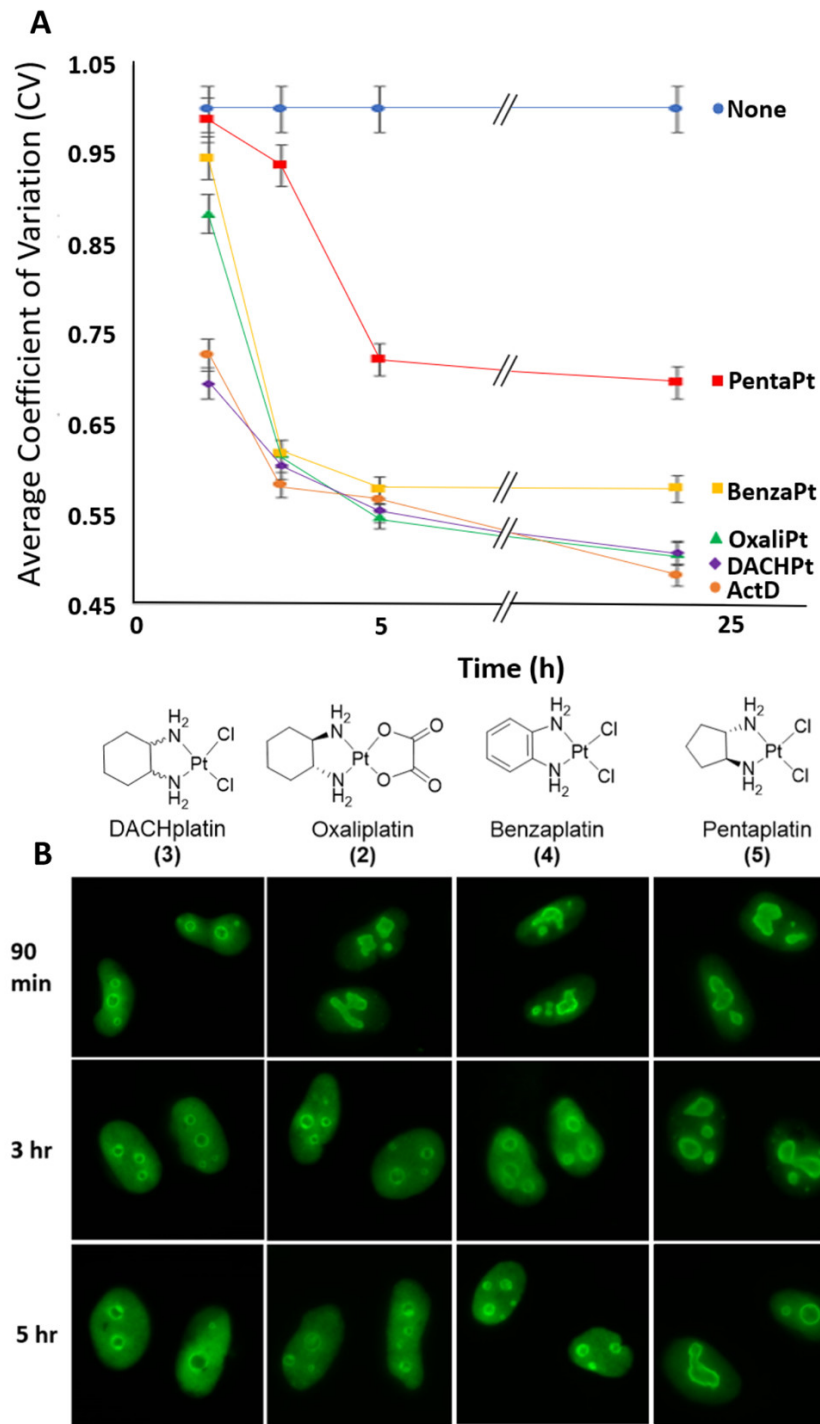


Figure 4.2. Quantification of NPM1 relocalization induced by Pt(II) compounds at various time points. A549 cells were treated with 10 μ M of Pt(II) compound or 5 nM ActD and NPM1 distribution was quantified by immunofluorescence (Methods). **A** | Each point is the average CV value and standard deviation for 3 biological replicates performed on 3 separate days. **B** | Representative cell images of A549 cells treated with each compound at given treatment times.

Pentaplatin Induces Lower Inhibition of rRNA Transcription.

Previous work has shown that oxaliplatin induces nucleolar stress accompanied by early inhibition of rRNA synthesis by Pol I (Sutton & DeRose, 2021). It was of interest to determine the relationship between rRNA synthesis inhibition and the range of NPM1 redistribution kinetics observed for compounds 2–5. To measure rRNA transcription, we conducted metabolic radiolabeling experiments using methods previously described (Burger et al., 2010; Sutton & DeRose, 2021). A549 cells were treated with compounds 2–5 for 3 h, and then cells were incubated in drug-free media containing ³²P-labeled phosphate which would be incorporated into any newly synthesized RNA in a pulse step. Media were replaced with cold, drug-containing media for 3 h to track the fate of any radiolabeled RNA. Low dose (5 nM) ActD was used as a positive control for inhibition of rRNA synthesis.

All of the Pt(II) derivatives previously found to induce NPM1 redistribution, compounds 2–5, inhibited synthesis of rRNA to an extent similar to the extent of NPM1 redistribution at 3 h (**Figure 4.3**). In agreement with previous data, (Sutton & DeRose, 2021) a 3 h treatment with oxaliplatin reduced 47S pre-rRNA transcript levels to below 10% of the untreated control, while the fully processed 28S transcript was reduced to roughly 20% of control levels. **3** inhibited rRNA synthesis even more robustly, with both 47S and 28S transcript levels being reduced to under 5% of the untreated control by 3 h. This enhanced inhibition relative to oxaliplatin may be due to more rapid aquation of the labile ligands, greater cellular platinum accumulation, or more extensive disruption of the Pol I transcription machinery. **4** showed a reduction of both 47S and 28S transcripts comparable to oxaliplatin and consistent with similar levels of NPM1 redistribution at 24 h. While reduction of both rRNA transcripts was observed after **5** treatment, this reduction was modest in comparison to the other platinum compounds and the positive control of ActD. With **5** treatment, 47S transcripts were reduced to about 40% of the negative control, while 28S transcripts were about 50%. This result is consistent with the lower amount of NPM1 redistribution caused by **5** at the 3 h timepoint (**Figure 4.2.A**).

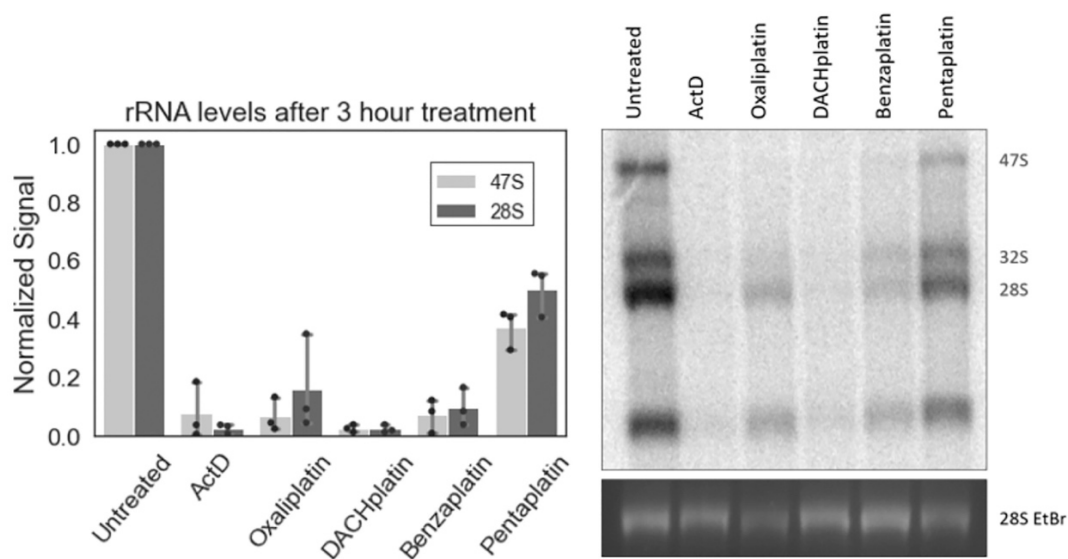


Figure 4.3. Metabolic labeling to measure rRNA synthesis and processing at 3 h of treatment. Cells were treated with 10 μ M platinum compounds or 5 nM of ActD for 3 h prior to a 1 h pulse step, followed by a 3 h chase step. Bottom frame in the gel image shows total RNA (EtBr stain of 28S rRNA) while the top image shows ³²P-labeled rRNA. Transcript sizes are shown on the right. Error bars represent the standard deviation of three replicates of A549 cells across three separate days.

Next, we wondered if **5** might inhibit rRNA synthesis more robustly after 5 h of drug treatment prior to the pulse step. We also considered whether APP (**6**), previously shown to not induce nucleolar stress despite structural similarities to the stress-inducing compound benzaplatin, (Sutton, McDevitt, Prochnau, et al., 2019) could inhibit rRNA synthesis despite its inability to cause NPM1 redistribution. We found that **5** did inhibit synthesis slightly more at 5 h of treatment than at 3 h of treatment, with 47S levels reaching roughly 30% of the negative control, and 28S levels being reduced to 40% (**Figure 4.4**). By contrast, **6** caused a slight inhibition of rRNA synthesis, although his inhibition was inconsistent with a high standard deviation over three trials with separate biological replicates. With APP treatment, 47S and 28S levels were reduced to around 85% and 50% of the untreated control levels respectively (**Figure 4.4**).

Similar levels of rRNA synthesis inhibition are incurred by cisplatin treatment at 3 h, which we previously attributed to effects downstream of the DDR (Sutton & DeRose, 2021). In conclusion, all Pt(II) derivatives that induce NPM1 relocation by 24 h also induce significant inhibition of rRNA synthesis by 3 h of treatment, with **3** causing the most robust inhibition and **5** inducing only modest inhibition. **5** inhibition of rRNA synthesis intensifies by 5 h of treatment, consistent with the further extent of NPM1 redistribution.

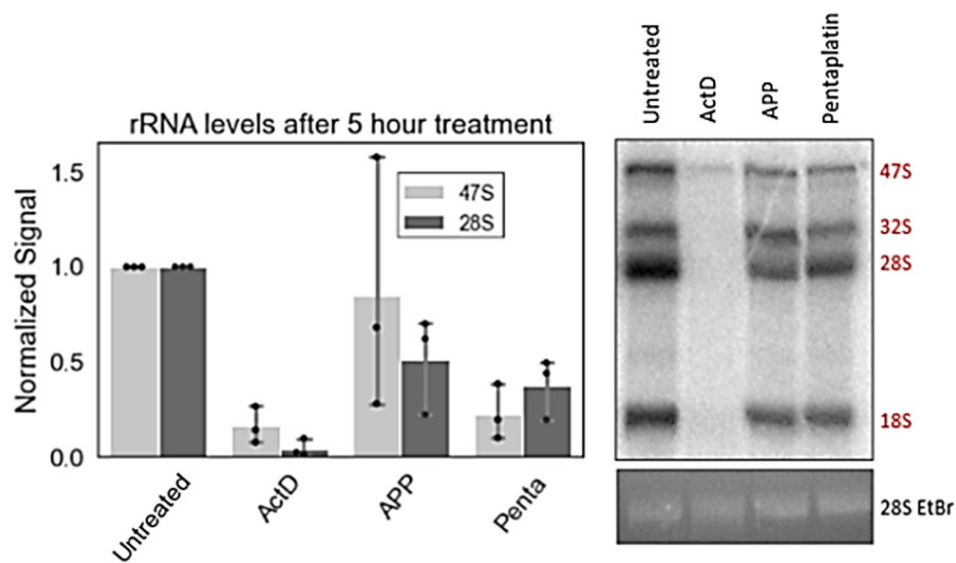


Figure 4.4. Metabolic labeling to measure rRNA synthesis and processing at 5 h of treatment. Cells were treated with 10 μ M platinum compounds or 5 nM of ActD for 5 h prior to the pulse step. Bottom frame in gel image shows total RNA (EtBr stain of 28S rRNA) while top image shows 32 P-labeled rRNA. Transcript sizes are shown on the right. Error bars represent the standard deviation of three replicates of A549 cells across three separate days.

Whole Cell and Nuclear Platinum Accumulation Do Not Correlate with Nucleolar Stress Induction by Pt(II) Compounds.

Pt(II) compounds can enter the cell either through passive diffusion or active transport and their uptake is highly dependent on the size, charge, and lipophilicity of the complex (Hall et al., 2008; Levina et al., 2017). While it is generally believed that passive diffusion is the primary way by which Pt(II) compounds enter the cell, certain transport proteins, such as the organic cation transporters and copper transporter 1 (CTR1), are also known to facilitate Pt(II) uptake (Hall et al., 2008). We questioned whether cellular uptake and accumulation influenced the rates of nucleolar stress induction observed for different Pt(II) compounds. To quantify the cellular accumulation of compounds 1–5, we utilized ICP-MS to determine the platinum content in whole cell lysate, nuclear fractions, and DNA extracted from treated A549 cells (Ghezzi et al., 2004; Hermann et al., 2013; Yamada et al., 2005).

Average cellular platinum accumulation at 90 min, 3 h, and 24 h after treatment with 10 μ M of Pt(II) compound are summarized in **Figure 4.5.A**. Cellular accumulation for each Pt(II) compound was quantified by the amount of platinum measured by ICP-MS relative to the total protein mass in each sample (ng Pt/mg protein). The measured

cellular platinum accumulation overtime for each of the stress-inducing Pt(II) compounds (**Figure 4.5.A**) follows a general trend that does not correlate to the timepoints where nucleolar stress is observed. Cellular accumulation of cisplatin was observed to be significantly higher than oxaliplatin and **3**, which agrees with previous studies (Ghezzi et al., 2004). Cellular accumulation for oxaliplatin was observed to be lower than the non-oxalate derivative, **3**, which is likely due to the slower aquation rate of oxaliplatin compared to **3**. Surprisingly, we found that the measured platinum accumulation in cells treated with 10 μ M of **4** was significantly higher than the other Pt(II) compounds tested, at all timepoints. The higher cellular accumulation of **4** may be due to hydrophobicity, or to the observation that Pt(II) complexes with aromatic diamine ligands, such as **3**, have been shown to undergo rapid exchange of labile chloride ligands (Bednarski & Trümbach, 1994).

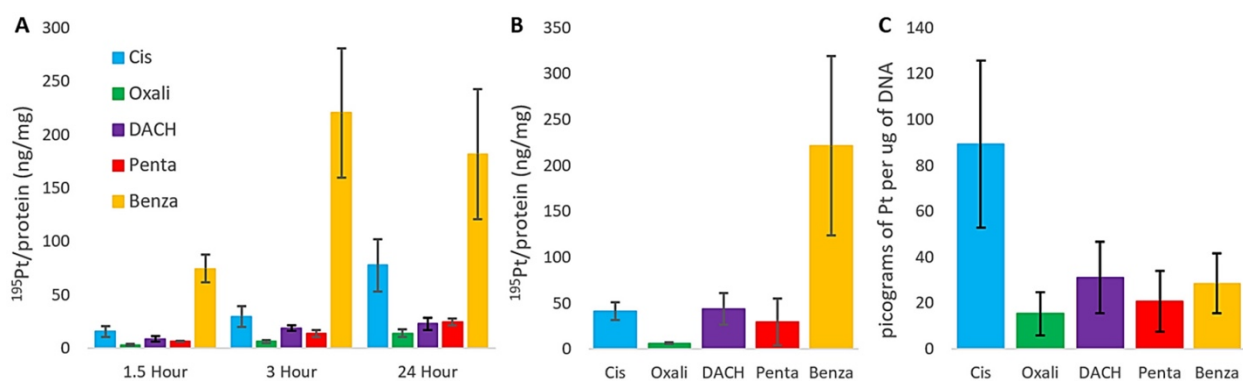


Figure 4.5. Platinum content in whole cell, nuclear, and DNA samples measured by ICP-MS. **A** | Cellular platinum content at varying drug treatment times. **B** | Platinum in nuclear fractions at 24 h drug treatment time. **C** | Platinum content in DNA extracted from cells at 24 h drug treatment time. **A** and **B** are averages of 3 biological replicates. Measurements in **C** reflect 5 biological replicates. All measurements are from A549 cells treated with 10 μ M platinum compound.

In addition to whole cell platinum accumulation studies, we also measured platinum levels in nuclear extracts of cells treated with compounds **1–5** for 24 h (**Figure 4.5.B**). The results from these studies closely mimicked those seen for whole cell platinum accumulation. **4** again showed the highest levels of nuclear accumulation. Additionally, there does not appear to be any correlation between the onset of nucleolar stress and nuclear platinum accumulation. This suggests that nuclear platinum accumulation is also less sensitive to the minor structural changes that modulate the nucleolar stress response.

Pt(II)-DNA Binding In Vitro and in Cell Does Not Correlate with Nucleolar Stress Induction

It is widely accepted that the cytotoxicity of platinum compounds is at least in part due to the formation of DNA-Pt adducts, (Hah et al., 2007) which are primarily 1,2-intrastrand cross-links on adjacent guanines (Chaney et al., 2005; Jamieson & Lippard, 1999). Because of this, the understanding of binding kinetics and adduct formation of oxaliplatin and cisplatin to DNA has been a topic of interest for many decades (Alian et al., 2012; Johnson et al., 2018; Woynarowski et al., 2000). Pt(II)-DNA adducts form more rapidly following cisplatin treatment than oxaliplatin treatment, and to a higher extent following cisplatin treatment both *in vitro* with varying DNA types and in multiple cell line (Raymond et al., 2002). Although the DNA binding characteristics of cisplatin and oxaliplatin have been extensively covered in the literature, little is known about the relationship between DNA platination and nucleolar stress induction.

To further investigate the relationship between DNA platination and nucleolar stress induction, we measured relative DNA-platinum adduct amounts for compounds **1–5** in a model oligonucleotide and in DNA extracted from treated A549 cells. Model oligonucleotide studies measured platinum binding to a short DNA hairpin sequence containing adjacent guanines 5'-(TATGGTATTTTATACCATA)-3' analyzed by dPAGE following incubation times from 90 min to 24 h (**Figure C.1**). By 24 h, all compounds except oxaliplatin and **4** appear to bind in similar amounts showing ~100% relative intensity of platinated to non-platinated DNA. Based on previous work, in these model studies oxaliplatin was expected to show slower overall binding and less adduct formation than cisplatin but it is notable that at 3 h treatment, oxaliplatin treatment induces significant nucleolar stress in cells. Another interesting result obtained from this study was that **4** appeared to show no binding to the hairpin DNA at 24 h incubation, even though it shows stress induction in cells (**Figure C.1**). The reason for this observation is not known, but it is possible that due to the aromatic ring, **4** may be forming a species in solution that is preventing interaction with the hairpin DNA.

To further investigate the relationship between Pt(II)-DNA adduct formation and nucleolar stress induction, we quantified the amount of Pt(II)-DNA adduct in A549 cells that formed after 24 h of incubation with compounds **2–5** (**Figure 4.5.C**) using ICP-MS. The results from the in-cell Pt(II)-DNA binding assays showed some notable differences compared to the *in vitro* studies. As expected, cisplatin showed significantly more

binding to cellular DNA at 24 h than oxaliplatin (Saris et al., 1996). Unlike in the model studies, where cisplatin seemed to bind at similar rates as both **3** and **5**, the in-cell binding assays indicated that cisplatin binds to DNA in a higher amount than any of the stress-causing compounds. Importantly, **5**, which shows less overall nucleolar stress at 24 h compared to the other oxaliplatin-like compounds of interest, shows relatively the same amount of in-cell DNA binding as **3** and **4**, indicating that it is not likely the ability of **5** to bind to DNA that is causing it to show less nucleolar stress. Finally, **4**, which did not exhibit any DNA binding in the *in vitro* studies, has in-cell Pt(II)-DNA levels that are similar to those of the other nucleolar stress-causing compounds. This indicates that there may be some cellular interactions occurring with **4** that is allowing it to bind to DNA that is not occurring in buffered solutions. Understanding this reaction may help to better understand the nucleolar stress pathway and how it differs from DDR induced by cisplatin and carboplatin. Based on these results, it can be concluded that whether a compound will cause nucleolar stress is not likely directly related to the rate of DNA platination or the overall level of Pt(II)-DNA adduct formation.

Chirality of Pt(II) Compounds Influences the Degree of Nucleolar Stress

It has previously been reported that the 1*R*,2*R*- and 1*S*,2*S*-isomers of **3** and **5** have different DNA-binding properties, with the 1*S*,2*S*-isomer of both compounds showing more interstrand DNA crosslinking compared to the 1*R*,2*R*-isomer (Johnson et al., 2018; H.-Y. Zhang et al., 2013). Growth inhibition studies in the NCI-60 human tumor cell line panel show that the 1*R*,2*R*-isomer of **3** is nearly 5 times more potent when compared to the 1*S*,2*S*-isomers (Schoch et al., 2020). In a study of acridine-linked monofunctional Pt(II) compounds, 1*R*,2*R*-isomer of **3** was also slightly more toxic when measured in A549 cells (Rose et al., 2019). The previous experiments in our study used a racemic mixture for **3**, but only the 1*S*,2*S*-isomer for **5** (Sutton, McDevitt, Prochnau, et al., 2019). We questioned whether the 1*S*,2*S*-isomer of **5** was the source of lower levels of nucleolar stress induction observed for this compound. To test this, we performed NPM1 relocalization studies with pure 1*S*,2*S*- and 1*R*,2*R*-isomers for both **5** and **3** (**Figure 4.6, 7–10**).

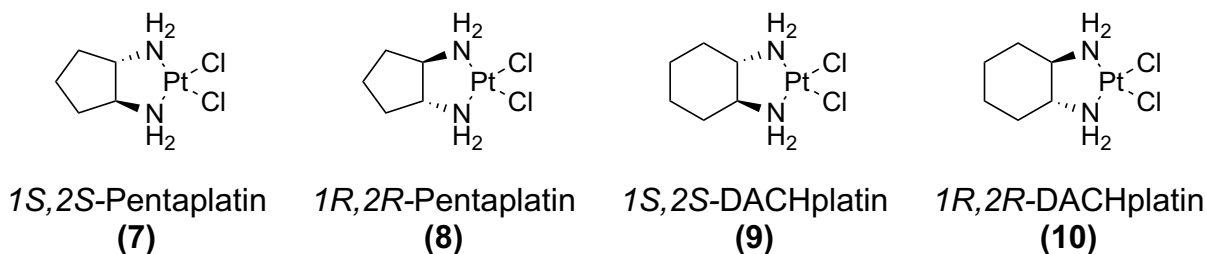


Figure 4.6. Pt(II) compounds used in isomer-specific NPM1 relocation studies.

We find that there is indeed a relationship between a Pt(II) compound's isomeric form and its ability to induce nucleolar stress (Figure 4.7). **8** induces nucleolar stress at an earlier timepoint and to an overall higher degree than **7**. Specifically, at the 3 h time point **8** is causing robust nucleolar stress (CV = 0.65), while **7** is not (CV = 0.88). While both compounds are inducing nucleolar stress at longer treatment times, **8** is causing a higher degree of stress than **7** at both 5 and 24 h timepoints.

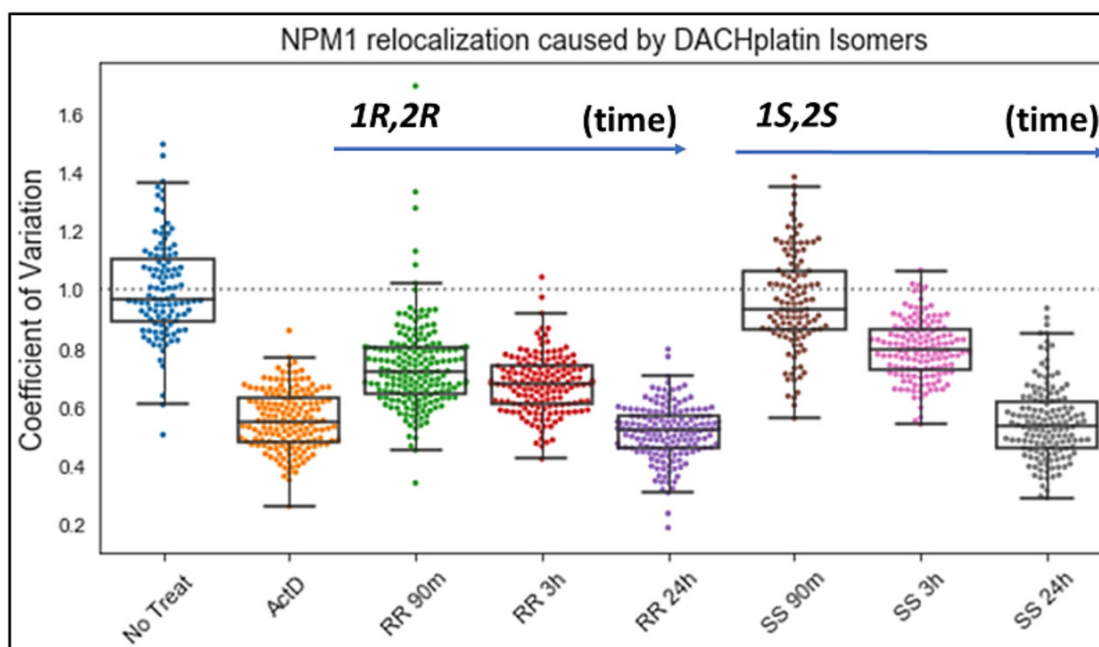


Figure 4.7. Quantification of NPM1 relocation induced by pentaplatin isomers. Treatment conditions are the same as in Figure 4.2. For each treatment individual dots represent single cells, data set boxes represent median, first, and third quartiles, and vertical lines are the range of data.

We next measured NPM1 relocation following treatment with **9** and **10**. We find the same trends as observed for **7** and **8**, however not to the same degree (Figure 4.8). At the 90 min timepoint, **10** induces significant nucleolar stress (CV = 0.73) while **9** (CV =

0.96) does not exhibit much of an effect on NPM1 relocalization. Additionally, at the 3 h timepoint, **10** shows a higher degree of stress (CV = 0.67) than **9** (CV = 0.80). By 24 h, however, both isomers of **3** show relatively the same degree of nucleolar stress; this differs from the case of **5**, where **7** (CV = 0.68) does not reach the same degree of nucleolar stress as **8** (CV = 0.53) by 24 h. These comparisons indicate that although the stereochemistry plays a role in the degree of nucleolar stress induced by these compounds, the size of the ring is still involved and the 6-membered DACH ring is more effective at inducing nucleolar stress than is the 5-membered ring of **5**.

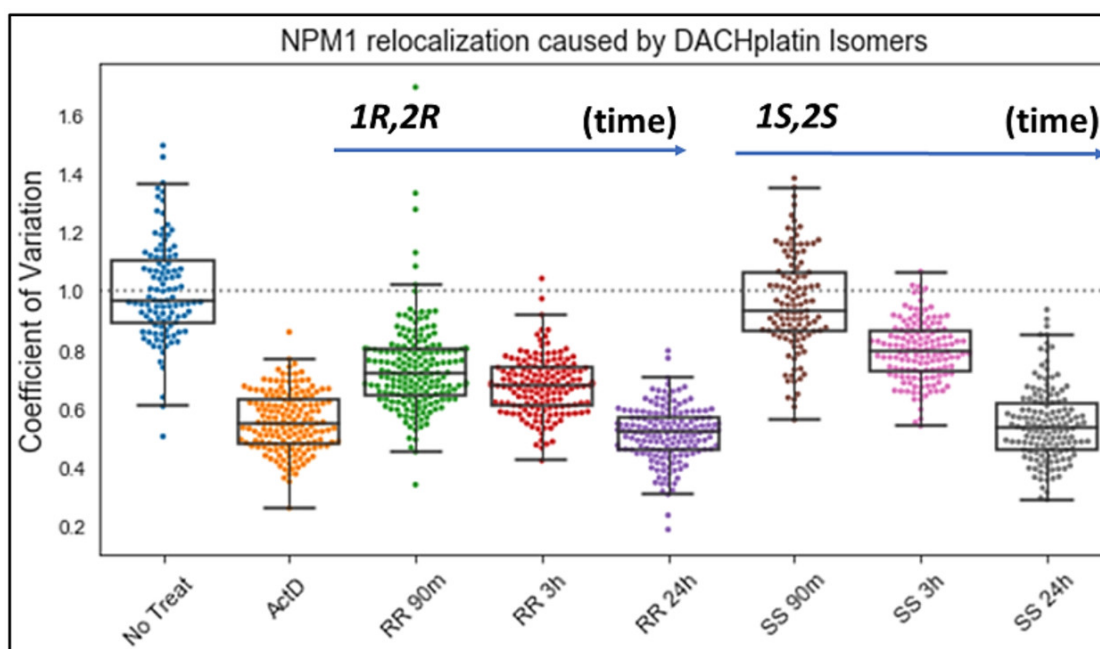


Figure 4.8. Quantification of NPM1 relocalization induced by DACHplatin isomers. Treatment conditions are the same as in **Figure 4.2**. For each treatment individual dots represent single cells, data set boxes represent median, first, and third quartiles, and vertical lines are the range of data.

Based on these data it appears that some property of the 1S,2S-isomers, and specifically **7**, makes it less ideal for NPM1 relocalization and nucleolar stress induction. It has previously been suggested that the bend and unwinding angles of the DNA double helix caused by platinum cross-linking are slightly different for the two isomers and that the amino protons of the 1S,2S-isomer have different hydrogen bonding interactions than in the 1R,2R-isomer when bound to DNA (Suchánková et al., 2012). Energy-minimized structures of **7** and **8** are shown in **Figure 4.9**. When bound to DNA or RNA the **7** and **8**

would present slightly different faces in the 3'- and 5'-directions that could influence nucleic acid structure or interactions with binding partners or polymerases. To visualize these potential differences, the structures are oriented "end-on" to show relative orientations of -NH_2 groups as well as orientation of steric bulk. Stereospecific interactions are also possible when bound to nucleolar proteins.

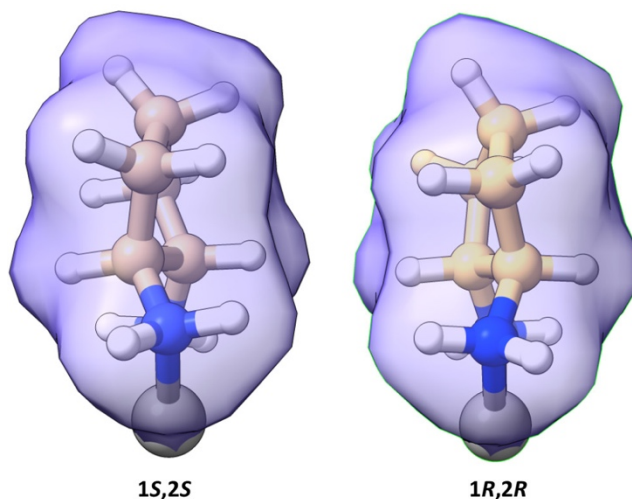


Figure 4.9. Lowest-energy conformations of pentaplatin in the 1*S*,2*S*- and 1*R*,2*R*-configurations (see Appendix C). Chloride ligands have been removed.

Conclusions

It has long been known that oxaliplatin and cisplatin induce different cellular effects and vary in the cancers that the compounds are most effective in treating. Some variations between these compounds include differences in their ability to form cellular Pt(II)-DNA adducts, variations in their cytotoxicity across various cell lines, and differences in the chemotherapeutic side effects induced by these compounds in cancer patients (Desoize & Madoulet, 2002; Raymond et al., 2002; Vekris et al., 2004). Although there is much research surrounding both cisplatin and oxaliplatin, the cellular mechanisms that induce the variations between these two compounds are not well understood. It has been reported that unlike cisplatin, oxaliplatin does not induce cell death via DDR, but rather through ribosome biogenesis stress (Bruno et al., 2017). Our lab has previously tested a limited library of Pt(II) compounds and found a subset that cause nucleolar stress induction (McDevitt et al., 2019, 2022; Sutton, McDevitt, Prochnau, et al., 2019). Here we performed more thorough investigations with four-stress inducing Pt(II)

compounds we had previously identified: oxaliplatin, benzaplatin, DACHplatin, and pentaplatin (2–5).

We were first interested in determining relative rates of nucleolar stress induction based on NPM1 relocation from the nucleolus to the nucleoplasm. We found that not all stress inducing Pt(II) compounds induce nucleolar stress at the same time or even to the same degree (**Figure 4.2**). Further, there are measurable differences in the levels of nucleolar stress induced by 1*R*,2*R*- and 1*S*,2*S*-isomers (**Figure 4.7** and **4.8**). Specifically, we see that **10** causes nucleolar stress earlier than other stress inducing compounds, initially observed at 90 mins. By contrast **7** does not induce stress until a longer timepoint of 5 h and to a lesser overall degree. This indicates that there are likely some intermolecular interactions occurring with the Pt(II) stress-inducing compounds that allow certain enantiomers to be favored over others in terms of inducing stress.

Next, we sought to confirm that stress causing compounds cause an inhibition of rRNA transcription as previously observed for oxaliplatin (Bruno et al., 2017; Sutton & DeRose, 2021). From these studies (**Figure 4.3** and **4.4**) there appears to be a direct correlation between rRNA transcription inhibition and observation of nucleolar stress by NPM1 redistribution. This correlation is particularly apparent when observing **7**, which showed less NPM1 redistribution than the other stress causing compounds and also showed less rRNA transcription inhibition. **7** still exhibits rRNA transcription inhibition in comparison with untreated cells, but not to the same degree as oxaliplatin, **3**, and **4**, suggesting that ring size has a significant influence on the ability to cause nucleolar stress in this class of Pt(II) compounds.

We were then interested in determining if cellular accumulation of Pt(II) compounds or DNA binding could account for the differences in nucleolar stress induction (**Figure 4.5**). From ICP-MS cellular platinum accumulation studies, we found that there does not appear to be a correlation between a compound's ability to enter and remain in cells and its ability to cause nucleolar stress. **7** showed similar whole cell and nuclear platinum accumulation to that of oxaliplatin and **3** even though it was causing less overall nucleolar stress than these compounds. Interestingly, **4** exhibits much higher cellular accumulation than all other Pt(II) compounds tested. The specific reason for this is still not well understood but is potentially related to the aromaticity of the benzene ring

and its ability to form reactive species that may allow it to be taken up by the cells more easily.

Finally, we looked at the rate and overall amount of Pt(II)-DNA adducts being formed both *in vitro* and in-cell for both stress inducing and nonstress inducing Pt(II) compounds. While cisplatin bound to a DNA hairpin at a similar rate *in vitro* as the other stress-inducing compounds, it is bound at a much higher relative level in DNA extracted from cells treated for 24 h. This indicates that induction of nucleolar stress does not require higher levels of binding to cellular DNA than for compounds that cause cell death via DDR. Additionally, there appeared to be low correlation between the degree of stress a compound caused, and the level of DNA adduct formed. This can be observed when comparing oxaliplatin, which showed a lower amount of DNA adduct formation with a higher degree of nucleolar stress, to **7**, which showed a higher amount of adduct formation and a lower degree of nucleolar stress. Although **3** and **5** were found to differ significantly in their onset and degree of nucleolar stress (**Figure 4.2**), the platinum content in cells, nuclear extracts, and extracted DNA from treated cells are remarkably similar (**Figure 4.5**). These results indicate that cellular platinum accumulation is less sensitive to the minor structural changes that modulate the nucleolar stress response.

Overall, the sensitivity of nucleolar stress induction to size and stereochemistry of cyclic diamine Pt(II) ligands points towards a model by which oxaliplatin-related Pt(II) compounds induce nucleolar stress via a mode that is highly specific and likely involves one or a few key intermolecular interactions. These interactions result in early inhibition of rRNA transcription and disruption of nucleolar structure. Future studies will focus on continuing to understand the Pt(II)-induced nucleolar stress pathway and identifying key molecular interactions that occur or are inhibited in order to cause Pt(II)-induced nucleolar stress.

Bridge to Chapter V

Chapter IV identifies differences in the both the degree and kinetics of NPM1 relocalization induced by Pt(II) compounds, demonstrating that isomer effects of Pt(II) chemotherapeutics influence induction of nucleolar stress for DACHplatin and pentaplatin. We investigated potential biological characteristics which may explain these

differences and found that cellular accumulation and DNA binding did not correspond to difference in nucleolar stress while a reduction rRNA synthesis did.

In Chapter V we test the hypothesis that oxaliplatin disrupts ribosome biogenesis by inhibiting rRNA synthesis by RNA Polymerase I, based on findings that oxaliplatin induced nucleolar stress is concomitant with an inhibition of pre-rRNA synthesis (Sutton & DeRose, 2021), and draw further connections to the nucleolar structure.

CHAPTER V: INFLUENCE OF NUCLEOLAR STRESS INDUCING COMPOUNDS ON THE INTERACTION OF POLYMERASE I TRANSCRIPTION MACHINERY WITH RIBOSOMAL DNA

Introduction

Ribosome biogenesis is a highly coordinated essential process which involves the synthesis, processing and assembly of numerous ribosomal RNAs (rRNA) and proteins into functional ribosomes. The majority of rRNA is transcribed by RNA polymerase I (Pol I), which accounts for nearly 50% of all RNA transcription in the cell (Russell & Zomerdijk, 2005). As the initial and rate-limiting step of ribosome biogenesis, the rate of rRNA transcription is a key mediator in ribosome production, and is proportional to cell growth and proliferation (Lafontaine et al., 2021; Pitts & Laiho, 2022).

In humans Pol I solely transcribes the 47S pre-rRNA from ribosomal DNA genes (rDNA), which are organized in clusters of tandem repeats situated on the short arm of acrocentric chromosomes (Xuan et al., 2021). The 47S pre-rRNA undergoes several co- and post-translational processing steps to generate the mature 18S, 5.8S, and 28S rRNAs; the 5S is transcribed separately by RNA polymerase III (Penzo et al., 2019). Pol I transcription takes place in the nucleolus, a membrane-less organelle within the nucleus, which serves as the primary site of ribosome biogenesis. The nucleolus is organized into three nested layers maintained in part via liquid-liquid phase separation (LLPS): the fibrillar center (FC), dense fibrillar component (DFC) and the granular component (GC) (Lafontaine et al., 2021). The organization of nucleolar subcomponents reflects the individual steps in ribosome biogenesis. Initial Pol I transcription of pre-rRNA takes place in the FC, near the border of the DFC, to allow for nascent pre-rRNA to be co-transcriptionally processed in the DFC (Pitts & Laiho, 2022). Mature rRNAs migrate into the GC where they, along with the 5S rRNA, are assembled with ribonucleoproteins to generate the small 40S and large 60S pre-ribosomal subunits. The pre-40S and pre-60S subunits then enter the nucleoplasm, where they undergo late-stage maturation before final export into the cytoplasm where they combine to form fully functional ribosomes (Penzo et al., 2019).

To facilitate the increased translational and metabolic demands of tumorigenesis, cancer cells often display dysregulations in ribosome biogenesis, and heightened rates of rRNA synthesis, which also functions as an important clinical biomarker (Penzo et al., 2019). The inherent instability of rDNA, coupled with the hyperactivation of ribosome biogenesis, make cancer cells particularly susceptible to disruptions in ribosome biogenesis and Pol I activity, which has found growing interest as a potential chemotherapeutic target (Hwang & Denicourt, 2024; Xuan et al., 2021).

Several small molecule and clinically relevant drugs have been reported to target Pol I and rRNA synthesis. Actinomycin D (ActD), widely used as an RNA transcription inhibitor, blocks polymerase transcription elongation by intercalating into DNA. RNA Pol I is ~10× more sensitive to ActD compared to RNA Pol II and III, which effectively allows for selective inhibition of Pol I when treating at low concentrations of ActD (Burger et al., 2010; Bensaude, 2011).

BMH-21, a quinazolinone derived DNA intercalator, has been shown to inhibit rRNA transcription by disrupting Pol I activity, leading to loss of rDNA occupancy and subsequent degradation of the RNA Pol I subunit, RPA194 (Jacobs, Huffines, et al., 2022; Peltonen et al., 2014; Wei et al., 2018). *In vitro* studies further demonstrated that BMH-21 selectively inhibits Pol I transcription initiation, promoter escape, and elongation (Jacobs, Fuller, et al., 2022; Jacobs, Huffines, et al., 2022).

The small molecule intercalator CX-5461 was identified in a screen for inhibitors of rRNA transcription and was initially characterized as a selective Pol I inhibitor. CX-5461 stabilizes G-quadruplexes found in rDNA, and disrupts the Pol I initiation complex (PIC) by preventing promoter binding and release (Drygin et al., 2009, 2011; Jean-Clément Mars et al., 2020). In additional studies, the cytotoxic effects of CX-5461 have been attributed to topoisomerase II (TOP2) poisoning (Bruno et al., 2020), and implicated in the inhibition of TOP2 α associated with Pol I in the mechanism of action (D. P. Cameron et al., 2024).

Pt(II)-based chemotherapeutics have long been known to cause disruptions in ribosome biogenesis and rRNA synthesis, at elevated concentrations (Burger et al., 2010; Jordan & Carmo-Fonseca, 1998; Peterson et al., 2015). However, this was not considered a primary mechanism for cytotoxicity until later work identified oxaliplatin as inducing cell death specifically through a disruption in ribosome biogenesis, in contrast to cisplatin and other Pt(II) chemotherapeutics, which act by triggering the DNA damage response

(DDR) (Bruno et al., 2017). Later work reinforced these findings, demonstrating that oxaliplatin induces nucleolar stress—a hallmark for disruption of ribosome biogenesis—that proceeds from the rapid inhibition of nascent rRNA synthesis (Sutton, McDevitt, Prochnau, et al., 2019; Sutton & DeRose, 2021).

ActD, CX-5461, and BMH-21, show high affinity for GC-rich regions of the genome, such as in rDNA, which is purported to drive their selectivity and sensitivity for Pol I transcription (Bensaude, 2011; Goodisman et al., 1992; Peltonen et al., 2014). Pt(II) complexes also show selectivity for GC-rich regions of the genome but differ from DNA intercalators in their ability to form multiple covalent adducts with DNA through formation of 1,2-intrastrand crosslinks between adjacent purine nucleobases (Riddell & Lippard, 2018; Shu et al., 2016; Woynarowski et al., 1998).

The overall cellular mechanisms which dictate the various stress pathways induced by oxaliplatin, cisplatin, or other Pt compounds are not well understood, and a sufficient molecular understanding of rRNA transcription inhibition induced by oxaliplatin is currently lacking. Therefore, to better understand on how oxaliplatin and BMH-21 perturb Pol I activity, we utilized chromatin immunoprecipitation sequencing (ChIP-seq) techniques to directly map the engagement or “occupancy” of rDNA transcription machinery along rDNA (Jean-Clement Mars et al., 2018; Sullivan & Santos, 2020). In addition to mapping rDNA occupancy of the Pol I machinery, we utilized immunofluorescence imaging to characterize the connection between nucleolar function and morphology under treatment with Pol I inhibitors oxaliplatin and BMH-21.

High-throughput sequencing techniques such as native elongating transcript sequencing (NET-seq) have been adapted in *S. cerevisiae* for mapping Pol I occupancy on rDNA (Clarke et al., 2018), and have been previously used to elucidate the mechanism of Pol I transcription factor, Spt4 (Huffines et al., 2021) and track the transcription rates of Pol I mutants (Huffines et al., 2022). NET-seq experiments performed on *S. cerevisiae* treated with BMH-21, revealed an acute reduction in Pol I occupancy as well as sequence-specific stalling of the Pol I elongation complex upstream of G-rich rDNA sequences (Jacobs, Huffines, et al., 2022). While NET-seq allows for precise probing of Pol I occupancy at a single-nucleotide resolution, high-levels of mature rRNAs have limited *in vivo* applications to yeast models expressing tagged-Pol I complex. Additionally, NET-seq

may not capture changes in Pol I occupancy caused by Pol I inhibitors prior to transcription initiation, necessitating complementary sequencing techniques.

ChIP analysis was performed using antibodies targeting proteins essential to rDNA transcription, Pol I subunit A (RPA194) and upstream binding factor (UBF). RPA194 is the largest catalytic subunit of the Pol I complex and is not found in RNA polymerases II or III (Pitts & Laiho, 2022). UBF is a member of the HMG-box DNA-binding protein family and is essential for mediating recruitment of the Pol I initiation complex to the rDNA promoter (Hamdane et al., 2014). UBF binds along the full rRNA gene, which maintains rDNA clusters in an open chromatin state to promote Pol I transcription, (Pitts & Laiho, 2022) and is purported to mark actively transcribing rDNA genes (Sanij et al., 2008).

Despite the fundamental importance of rRNA transcription and accessibility of sequencing techniques, relatively few ChIP-seq analyses of Pol I transcription have been reported in the literature. ChIP-seq occupancy assays have been applied to mechanistic studies of CX-5461, and demonstrated that CX-5461 disrupts the Pol I transcription initiation complex by irreversibly blocking release of the promoter RNA polymerase I transcription factor (RRN3) (Jean-Clément Mars et al., 2020). ChIP-based occupancy assays of Pol I and related transcription machinery were also used to identify the transcription factor C/EAP alpha (CEBPA) as a factor in Pol I-RRN3 recruitment to rDNA (Antony et al., 2022).

Our findings suggest that BMH-21 and oxaliplatin disrupt rRNA synthesis through distinct mechanisms, which lead to the rapid disengagement of RNA Pol I, but not UBF. These effects were specific to ribosome biogenesis inhibitors and not observed in cisplatin treatments. This information may reveal a possible mechanistic target or pathway that may be beneficial to the development of new chemotherapeutics or improve the efficacy of oxaliplatin.

Results

BMH-21 and oxaliplatin induce reorganization of FC components

Disruptions in ribosome biogenesis induce nucleolar stress and causes a redistribution of nucleolar subcomponents. A well-known hallmark for nucleolar stress is the relocalization of the nucleolar protein nucleophosmin (NPM1) from the GC to the

nucleoplasm (Yang et al., 2018). In prior work we utilized the relocalization of NPM1 as a measure for quantifying nucleolar stress, and found that oxaliplatin treatments induced significant NPM1 relocalization by 3 h, which also corresponds with an inhibition in rRNA synthesis under these treatment conditions (Sutton & DeRose, 2021). To determine if relocalization of FC components follows a similar trend, we utilized immunofluorescence imaging to track the nucleolar localization of UBF and RPA194 (Figures 5.1 and 5.2).

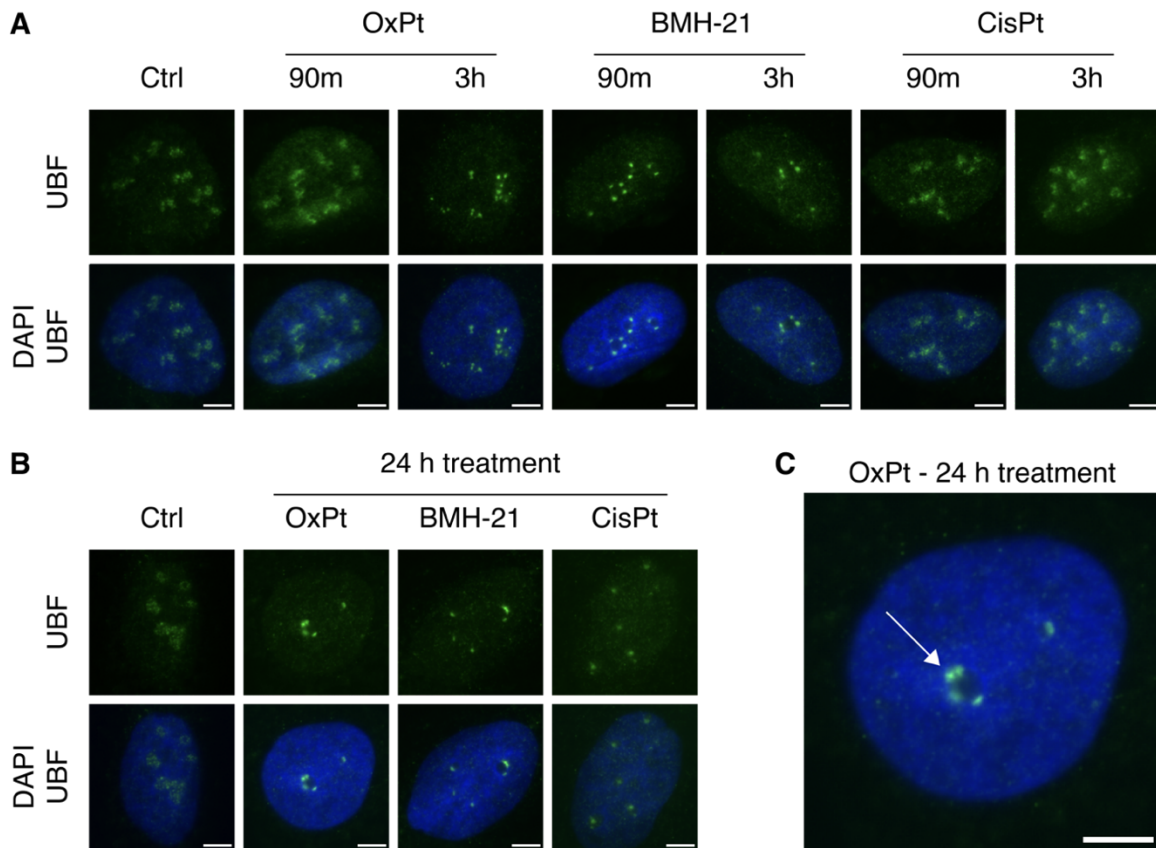


Figure 5.1. Oxaliplatin and BMH-21 induce nucleolar caps containing UBF. Representative images of UBF localization in U2OS cell treated with cisplatin (CisPt, 10 μ M), oxaliplatin (OxPt, 10 μ M), or BMH-21 (1 μ M). A | UBF localization following 90 m and 3 h treatment; B | following 24 h treatment. C | Expanded image following 24 h treatment with oxaliplatin. White arrow indicates nucleolar cap. Cells were immunostained for UBF (green) and DNA (DAPI, blue). Scale bars = 5 μ m.

U2OS cells were treated with 10 μ M of cisplatin or oxaliplatin, or 1 μ M of BMH-21 and immunostained for UBF (Figure 5.1). Treatment with BMH-21 or oxaliplatin induced a coalescence of UBF into round puncta which localized at the periphery of the nucleolus; commonly referred to as "nucleolar caps", these structures are reported to form following

inhibition of rRNA transcription or sustained rDNA damage (Boukoura & Larsen, 2024; Hwang & Denicourt, 2024; Lafontaine et al., 2021). We observed initial formation of nucleolar caps in UBF labeled images following 90 min treatment with BMH-21 and 3 h treatments with oxaliplatin (**Figure 5.1.A**). Characteristic nucleolar caps were not observed in cisplatin treatments, which displayed a moderate condensation of UBF following 24 h treatment (**Figure 5.1.B and C**).

The onset of nucleolar redistribution and cap formation was mirrored in RPA194 immunofluorescence cell images (**Figure 5.2**). RPA194-containing nucleolar caps were observed following 90 m and 3 h treatments with BMH-21 and oxaliplatin, respectively (**Figure 5.2.A and C**). In contrast, nucleolar caps containing RPA194 were only observed in cisplatin treatments after 24 h (**Figure 5.2 B**), consistence with our previous observations of nucleolar rearrangement occurring via downstream responses to DNA damage (Sutton, McDevitt, Prochnau, et al., 2019; Sutton & DeRose, 2021).

In agreement with previous literature reports, formation of nucleolar caps with BMH-21 treatments coincided with a depletion of RPA194 (Colis et al., 2014; Wei et al., 2018). Depletion was observed by a loss in immunofluorescence signal intensity, which occur at 90 min and increased at later timepoints (**Figure 5.2.A and B**). More robust RPA194-containing nucleolar caps were observed at later timepoints in oxaliplatin treatments as initial cap-like structures appeared to coalesce. This kinetic component of nucleolar reorganization in the nucleolar stress response has been previously observed, in a library of stress-inducing Pt(II) compounds (McDevitt et al., 2019; Pigg et al., 2022).

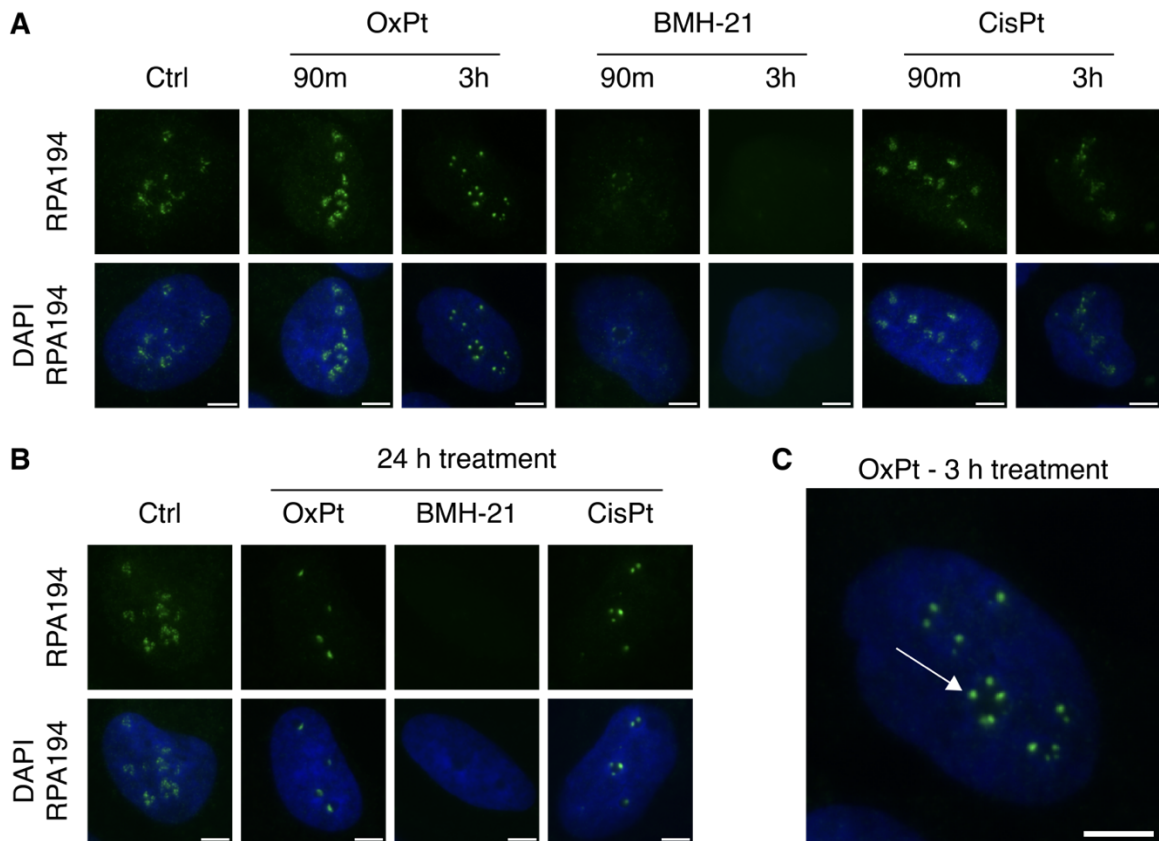


Figure 5.2. Oxaliplatin and BMH-21 induce condensation of Pol I. Representative images of Pol I (RPA194) localization in U2OS cells treated with cisplatin (CisPt, 10 μ M), oxaliplatin (OxPt, 10 μ M), or BMH-21 (1 μ M). **A** | RPA194 localization following 90 m and 3 h treatment; **B** | following 24 h treatment. **C** | Expanded image following 3 h treatment with oxaliplatin. White arrow indicates nucleolar cap-like structure. Cells were immunostained for RPA194 (Pol I, green) and DNA (DAPI, blue). Scale bars = 5 μ m.

ChIP-based occupancy assay of Pol I transcription of rDNA.

To directly investigate how rRNA transcription is inhibited by oxaliplatin we performed a ChIP-seq analysis on A549 and U2OS cells to map the rDNA occupancy of the Pol I machinery during early induction of nucleolar stress (Jean-Clement Mars et al., 2018).

ChIP-seq analysis of Pol I (RPA194) in untreated A549 cells revealed broad enrichment of Pol I throughout the promoter and transcribed regions of rDNA, which sharply decreased in the intergenic spacer (IGS) (**Figure 5.3**). Both oxaliplatin and BMH-21 induced Pol I disengagement from rDNA in A549 cells, with a relative depletion in Pol I occupancy of ~51% for oxaliplatin, and ~73% for BMH-21 (**Figure 5.4.A**). The dramatic reduction in Pol I occupancy by BMH-21 is likely accompanied by BMH-21 induced

degradation of RPA194 (Jacobs, Huffines, et al., 2022). Cisplatin induced a moderate ~20% reduction in total relative Pol I occupancy.

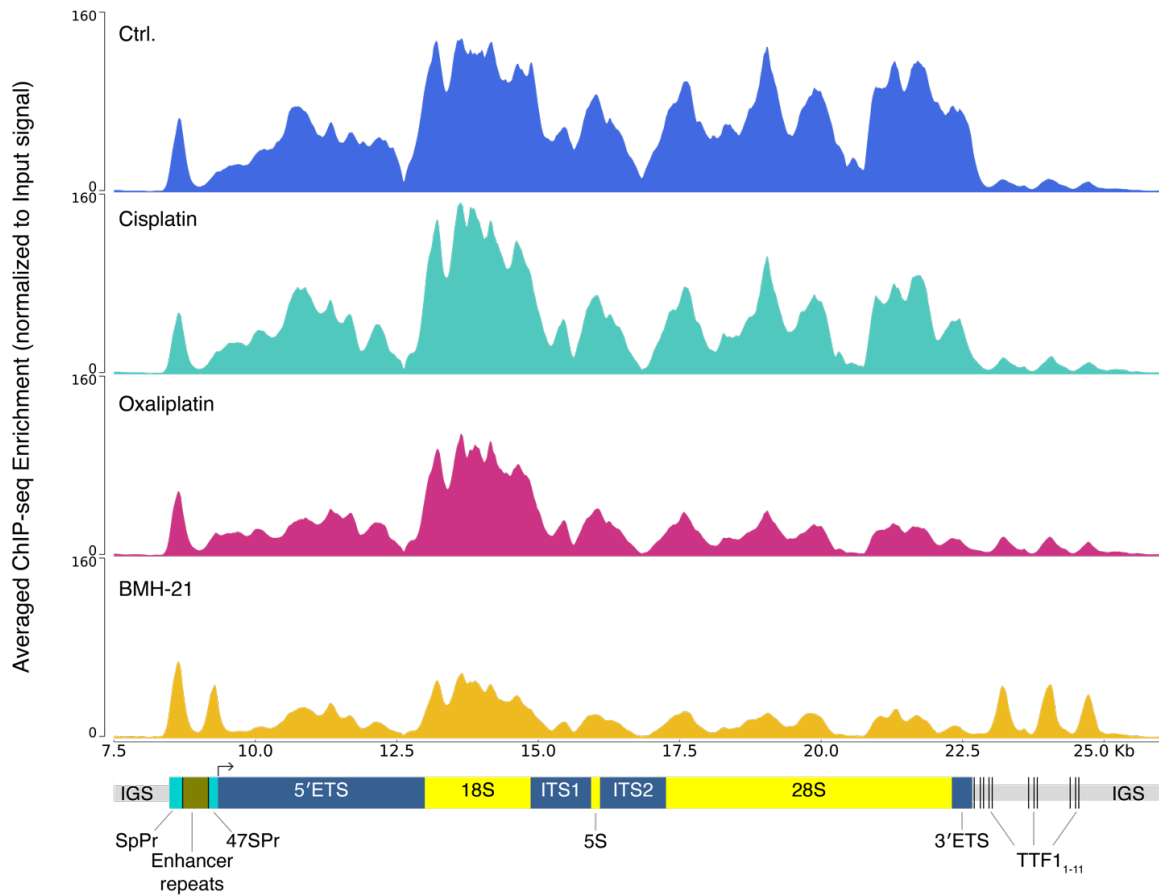


Figure 5.3. Influence of platinum and BMH-21 treatment on rDNA occupancy of Pol I. ChIP-seq mapping of Pol I (RPA194) occupancy along the rDNA gene in A549 cells, following 3 h treatment with 10 μ M cisplatin or oxaliplatin, or 1 μ M BMH-21. Average sequence coverage is normalized to the read count per million reads (CPM) and shown as enrichment over the input for the associated treatment. $n = 2$. Diagram of rDNA gene aligned below: intergenic spacer region (IGS), spacer and 47S promoter (SpPr, 47SPr), internal transcribed spacer (ITS1, ITS2), transcription termination factor binding sites (TTF1₁₋₁₁), external transcribed spacers (5'ETS and 3'ETS), arrow indicates transcription start site.

Pol I occupancy maps in U2OS cells, showed similar decrease in occupancy following oxaliplatin and BMH-21 treatments when compared to A549 cells (**Figure D.1**). BMH-21 treatment in U2OS cells induced depletion in Pol I, leading to a ~60% reduction in relative Pol I occupancy (**Figure 5.4.B**). However, treatment with oxaliplatin did not cause any significant change in Pol I occupancy, and cisplatin treatments lead to a nearly 2-fold enrichment in Pol I occupancy in comparison with untreated cells (**Figure 5.4.B**).

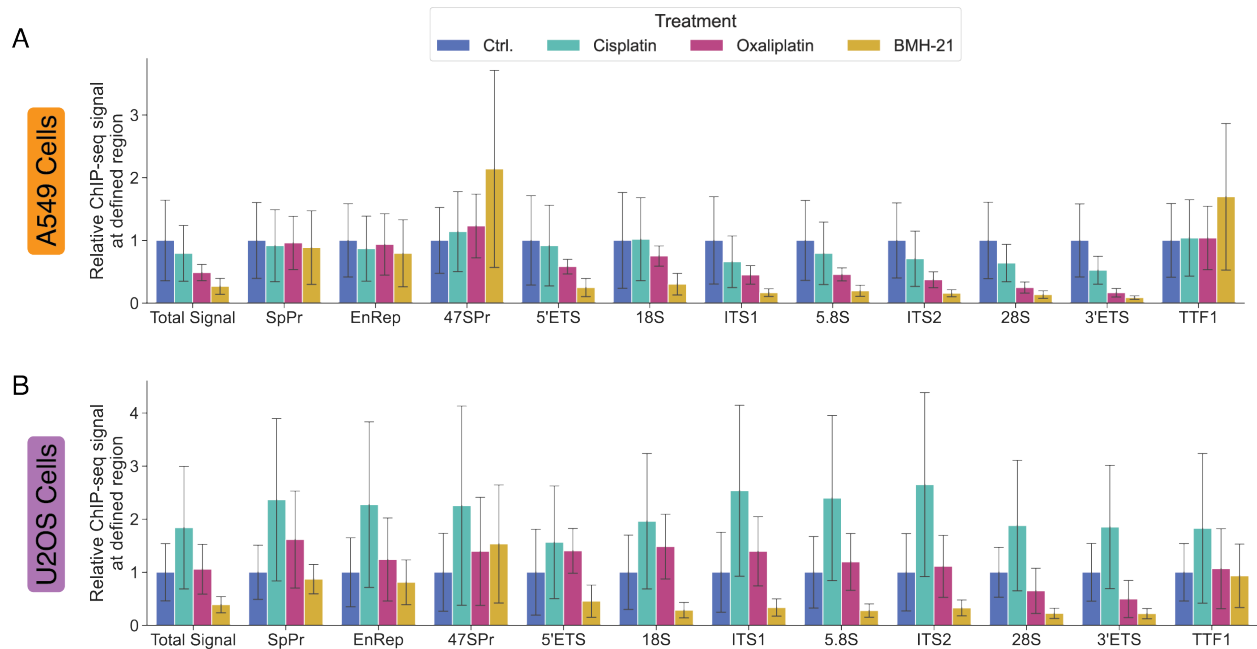


Figure 5.4. Relative Pol I ChIP-seq signal mapped at defined regions of rDNA in **A** | A549 cells and **B** | U2OS cells. Total read density within each defined rDNA region is normalized to the ChIP-seq signal in untreated cells. Plotted as mean \pm SD, $n = 2$.

ChIP-seq analysis of UBF in untreated A549 and U2OS cells showed expected rDNA enrichment patterns throughout the promoter and transcribed regions of rDNA, which sharply decreased in the IGS (**Figure 5.5** and **D.2**). UBF occupancy patterns in A549 and U2OS cells did not appear to be significantly affected by treatment with any compound. Relative UBF occupancy in A549 cells increased substantially in oxaliplatin treatments, showing $\sim 1.5\times$ overall enrichment compared to untreated cells (**Figure 5.6.A**). BMH-21 and cisplatin induced a slight 30% depletion in UBF occupancy. In contrast, cisplatin and oxaliplatin treatments in U2OS cells revealed a substantial increase in overall rDNA enrichment, $\sim 2\times$ and $1.8\times$ respectively, when compared to untreated cells, whereas BMH-21 treatments induced a moderate 20% reduction in relative UBF occupancy (**Figure 5.6.B**).

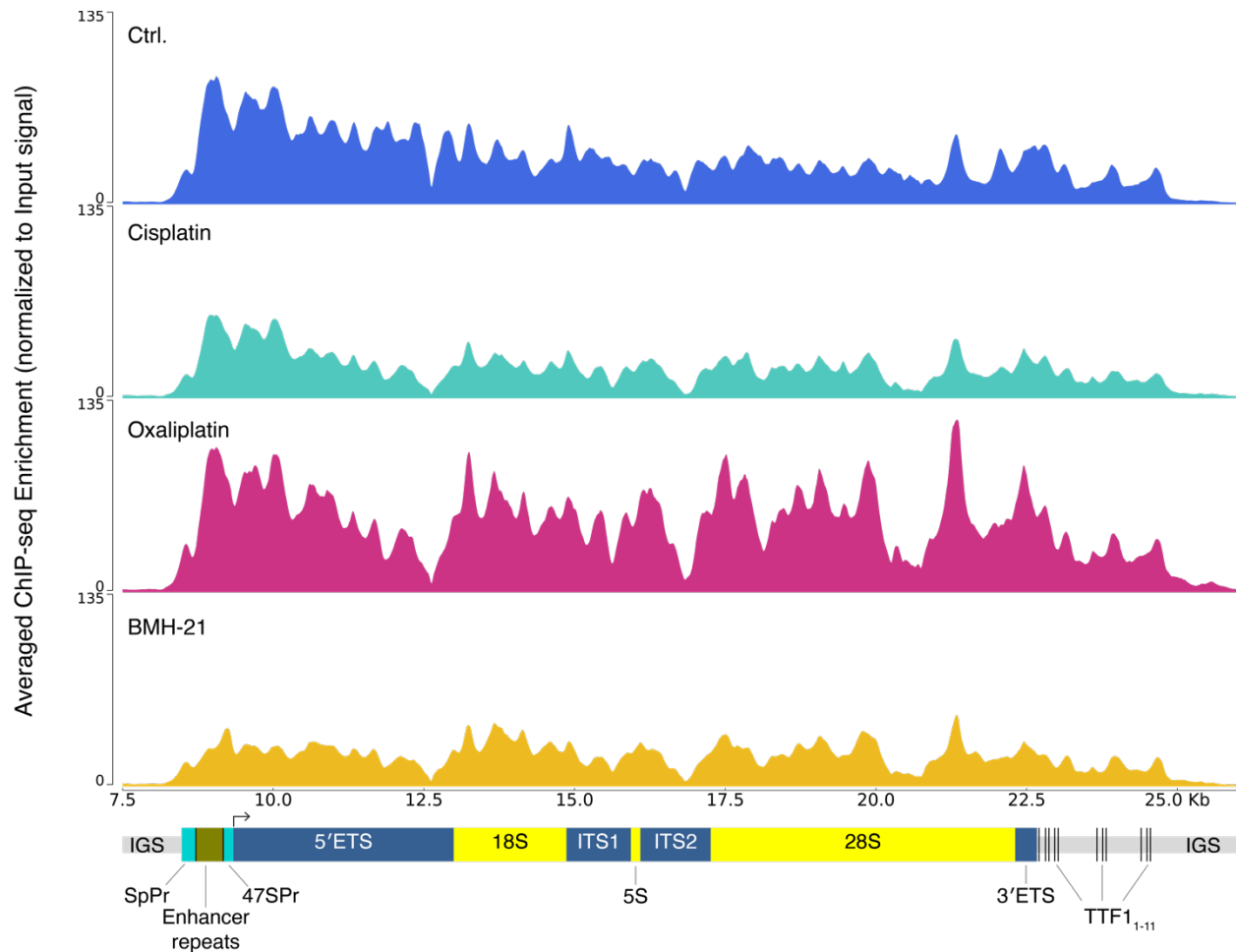


Figure 5.5. Influence of platinum and BMH-21 treatment on UBF-rDNA occupancy. ChIP-seq mapping of UBF occupancy along the rDNA gene in A549 cells, following 3 h treatment with 10 μ M cisplatin or oxaliplatin, or 1 μ M BMH-21. Average sequence coverage is normalized to the read count per million reads (CPM) and shown as enrichment over the input sequence for the associated treatment. $n = 2$. Diagram of rDNA gene aligned below: intergenic spacer region (IGS), spacer and 47S promoter (SpPr, 47SPr), internal transcribed spacers (ITS1, ITS2), transcription termination factor binding sites (TTF1₁₋₁₁), external transcribed spacers (5'ETS and 3'ETS), arrow indicates transcription start site.

BMH-21 induces Pol I stalling along rDNA

Overall Pol I occupancy decreased under treatment with BMH-21 (**Figure 5.3**), however a relative enrichment in Pol I occupancy BMH-21 treatment also led to an enrichment in Pol I occupancy at the 47S promoter region and downstream of the transcription termination factor (TTF1) binding clusters (**Figure 5.4.A**). The relative occupancy of Pol I within the 47S promoter region increased approximately 2-fold following BMH-21 treatment in A549 cells (**Figure 5.4.A**), which peaked approximately 50 bp upstream of the transcription start site or 125 bp downstream of the TTF1 binding site, T_0 (**Figure 5.7**).

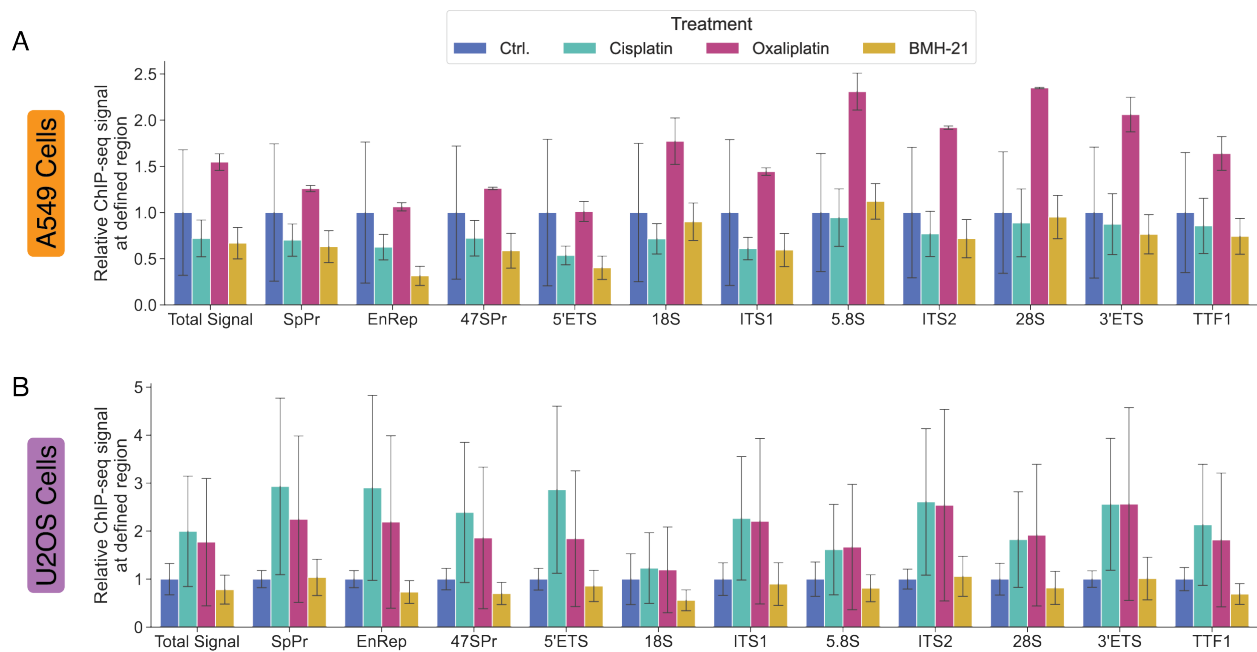


Figure 5.6. Relative UBF ChIP-seq signal mapped at defined regions of rDNA in **A** | A549 cells and **B** | U2OS cells. Plotted as mean \pm SD, $n = 2$.

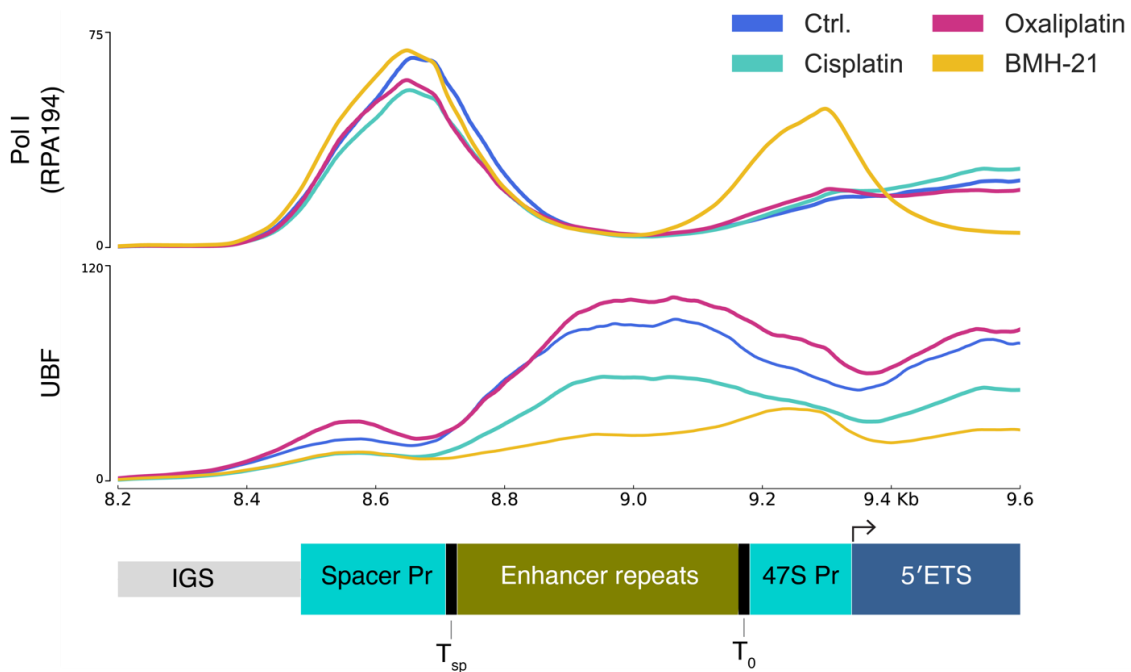


Figure 5.7. BMH-21 induces Pol I stalling at the 47S promoter (47S Pr). Zoom-in of rDNA promoter region of Pol I (RPA194) and UBF occupancy in A549 cells shown in **Figure 5.3** and **5.5**. TTF1 space promoter and initial binding sites are labeled below (T_{sp} and T_0).

Relative enrichment in Pol I occupancy at TTF1 binding sites, TTF1₁₋₁₁ was also observed in BMH-21 treated A549 cells (**Figure 5.8**). TTF1 is an rDNA specific transcription termination factor which binds to Sal Box terminator elements downstream of the 3' end of the pre-rRNA. TTF1 binding induces pausing of the Pol I complex, which mediates RNA Pol I transcription termination by promoting polymerase release (Németh et al., 2008). Peaks in RPA194 occupancy in the TTF1 region were observed approx. 60–80 bp downstream of TTF1 binding clusters, which suggests that subsequent polymerase release may also be disrupted by BMH-21.

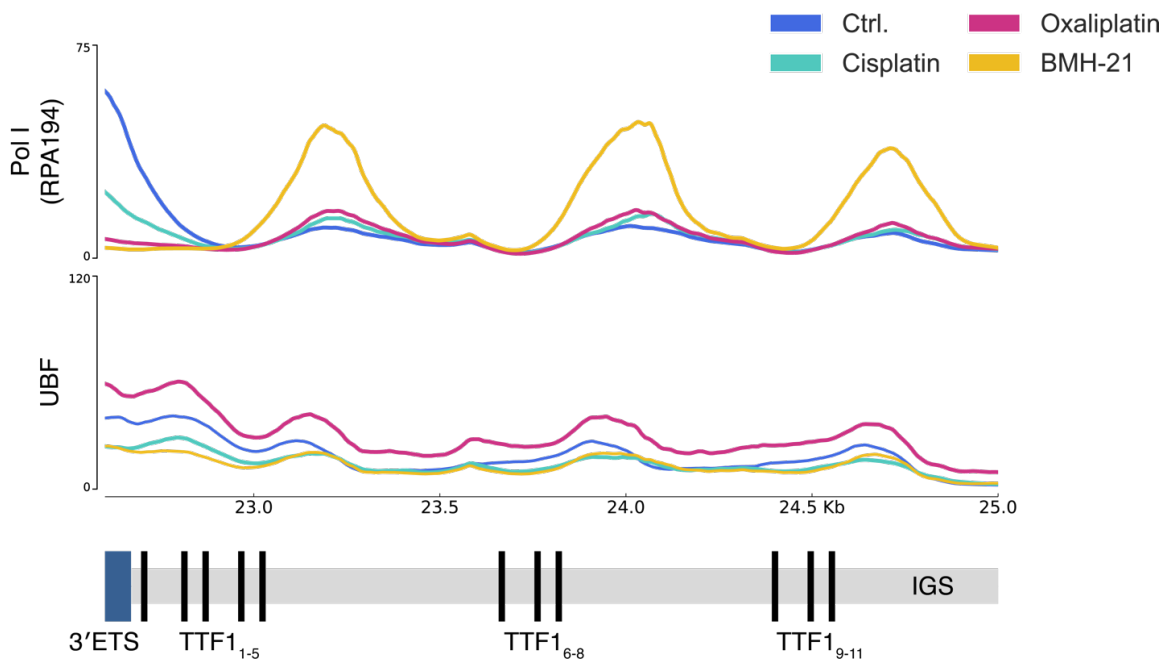


Figure 5.8. BMH-21 induces Pol I stalling downstream of TTF1 binding sites. Zoom-in of rDNA terminator region of Pol I (RPA194) and UBF occupancy in A549 cells shown in **Figures 5.3** and **5.5**. TTF1 space promoter and initial binding sites are labeled below (T_{sp} and T_0).

Pol I and UBF occupancy does not correlate to relative rDNA GC-content.

BMH-21 preferentially interacts with GC-rich regions of the genome, such as those found in the coding regions of rDNA (Peltonen et al., 2014). In *S. cerevisiae*, BMH-21 was shown to induce a sequence-specific Pol I stalling upstream of G-rich sequences in transcribed spacer regions of rDNA (Jacobs, Huffines, et al., 2022).

Comparing occupancy measurements of RPA194 or UBF in A549 cells with the relative GC-content within the rDNA did not show a strong correlation with relative GC-

content in A549 cells for any treatment condition (**Figure 5.9**). However, the long read lengths required for occupancy mapping, and the inherent biases in sequencing GC-rich fragments make it difficult to conclude from these experiments whether GC-content plays a meaningful role in directing Pol I specificity.

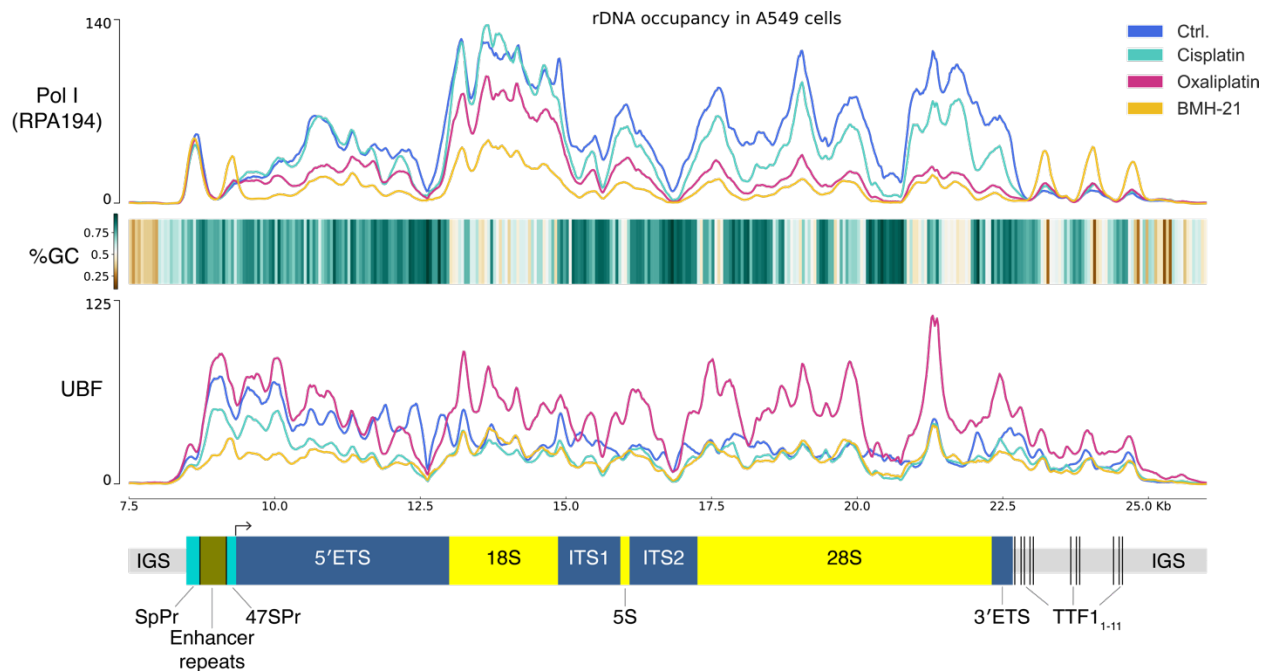


Figure 5.9. Pol I and UBF occupancy does not correlate with relative rDNA GC-content. Superimposed ChIP-seq maps of Pol I (RPA194) and UBF rDNA occupancy in A549 cells following 3 h treatment with cisplatin (10 μ M), oxaliplatin (10 μ M), or BMH-21 (1 μ M). Percent GC-content (%GC) is calculated from a 50 bp sliding window at each bp across the length of the rDNA gene. Plotted as mean, n = 2.

Discussion

The data presented here indicate that Pol I inhibition—and ensuing nucleolar stress—induced by BMH-21 and oxaliplatin occur through distinct mechanisms, which share similarities in their downstream cellular response.

Following a 3 h treatment with oxaliplatin, A549 cells showed a broad depletion in Pol I occupancy (**Figures 5.3 and 5.4.A**) which strongly suggests the loss of 47S pre-rRNA transcript previously measured by metabolic labeling (Pigg et al., 2022) is the result of Pol I inhibition. ChIP-seq occupancy mapping of oxaliplatin treated cells did not reveal a distinct pause site or enrichment motif, suggesting that Pol I inhibition does not result from a specific molecular disruption of the Pol I complex-rDNA interaction. However, similar to BMH-21, oxaliplatin treatment induced a slight decreasing gradient in relative

Pol I occupancy in the 5' to 3' direction (**Figure 5.4**) which appears similar to reported Pol I occupancy maps of ActD treated cells (Jean-Clément Mars et al., 2020).

Despite the strong connection between UBF occupancy and the rate of rRNA synthesis (Sanij et al., 2008; Theophanous et al., 2023) we did not observe a significant decrease in UBF occupancy or specific enrichment sites, following treatment with any compound when measured in A549 and U2OS cells. Recent studies have shown UBF binding to rDNA promoter to be unaffected by cisplatin or oxaliplatin treatments *in vitro* (Nechay et al., 2023). We found treatment with oxaliplatin and cisplatin, induce a relative enrichment in UBF bound to rDNA (**Figure 5.6**) which aligns with previous studies which show that UBF has unusually high affinity for cisplatin-DNA adducts (Hamdane et al., 2015; Zhai et al., 1998). However, the lack of specific UBF enrichment sites along the rDNA gene suggests the overall increase in UBF occupancy observed in cisplatin and oxaliplatin treatment may be due to more global impacts on rRNA transcription and not specific recognition of rDNA-adducts.

Based on previous work (Pigg et al., 2022; Sutton & DeRose, 2021) and immunofluorescence experiments, we chose a 3 h treatment time point for our ChIP-seq experiments as this represented an early timepoint where nucleolar stress and inhibition of rRNA synthesis were observed in oxaliplatin treatments. This however does not preclude the possibility that oxaliplatin has a more specifically perturbation of Pol I function prior in the earlier stages of nucleolar stress, which lead to the downstream inhibition of rRNA transcription and general loss of Pol I occupancy across the rDNA gene as observed here.

Some studies have proposed that oxaliplatin-induced Pol I inhibition and nucleolar stress may result from a biophysical disruption in nucleolar structure or function rather than a specific small molecule interaction. Oxaliplatin has been reported to alter phase separation and dynamics of DFC and GC components leading to a disintegration of nucleolar subcomponents, which in turn are proposed to disrupt Pol I activity, eventually signaling for cell cycle arrest and apoptosis (H. B. Schmidt et al., 2022).

Oxaliplatin inhibition of Pol I has also been proposed to involve the DDR kinase ATM/ATR signaling despite an in the absence of nucleolar specific DNA damage (Nechay et al., 2023). Interestingly Pol I inhibition involving ATM/ATR signaling has

also been demonstrated with CX-5461 (Negi & Brown, 2015; Quin et al., 2016). However, others have demonstrated that rRNA transcription inhibition and nucleolar stress induction by oxaliplatin is not dependent on ATM/ATR activity (Pigg et al., 2024). The lack of a specific enrichment pattern in Pol I-rDNA occupancy induced by oxaliplatin, despite changes in nucleolar morphology and inhibition of Pol I activity, suggest Pol I inhibition may not be primarily caused by a molecular disruption of Pol I interaction with rDNA, but may reflect broader down regulation of rRNA synthesis following induction of nucleolar stress.

By contrast, Pol I occupancy mapping of BMH-21 treated cells revealed a distinct peak in the 47S promoter region, consistent with polymerase stalling. This observation aligns with early findings in *S. cerevisiae* that BMH-21 primarily disrupts transcription initiation and early elongation phase, and may demonstrate a specific mode for Pol I inhibition induced by BMH-21 at pre-initiation or very early elongation steps (Jacobs, Fuller, et al., 2022; Jacobs, Huffines, et al., 2022). Additional occupancy mapping of Pol I transcription factors involved in polymerase initiation, such as the Pol I-specific transcription initiation factor, RRN3 or selective factor 1 (SL-1) may elucidate the specific step of inhibition.

BMH-21 treatment also led to an enrichment in Pol I occupancy downstream of the TTF-1 binding clusters, which suggests that Pol I termination and polymerase release, or both may also be disrupted by BMH-21. To our knowledge, BMH-21 induced disruptions in Pol I transcription termination or polymerase release have not been otherwise reported, and may represent an additional mode of late stage disruption of Pol I.

BMH-21 and other specific Pol I inhibitors are thought to gain specificity through their preferential interaction with GC-rich regions of the genome (Pitts & Laiho, 2022). BMH-21 has previously been demonstrated through NET-seq in *S. cerevisiae* to induce Pol I stalling upstream of G-rich regions of rDNA, (Jacobs, Huffines, et al., 2022) consistent with the hypothesis that GC-rich sequences direct Pol I specificity in that small molecule inhibitors. In our ChIP-seq mapping data, we were unable to find significant enrichment in Pol I or UBF occupancy upstream of GC-rich regions in rDNA. It is also possible that the resolution of broad ChIP-seq signals is insufficient to detect these small nucleotide sequence motifs in our occupancy measurements, in comparison to higher resolution NET-seq experiments.

In conclusion, we performed ChIP-seq occupancy measurements for Pol I and UBF in oxaliplatin, cisplatin and BMH-21 treated cells in addition to immunofluorescence imaging of the same Pol I transcription factors. Immunofluorescence analysis of nucleolar relocalization of Pol I transcription factor revealed a clear disruption in FC separation, followed by the formation of characteristic nucleolar caps upon treatment with inhibitors of rRNA synthesis, which was absent in cisplatin treatments. Our short immunofluorescence time-course experiments recapitulated previous work measuring the relocalization NPM1, which identified that early induction of nucleolar stress took place following 3 h treatment with oxaliplatin, but not cisplatin (Sutton & DeRose, 2021). We found in addition to inducing relocalization of GC component, NPM1, oxaliplatin also induced initial formation of nucleolar caps containing FC components UBF and RPA194, at comparable timepoints.

ChIP-seq maps of Pol I-rDNA occupancy with oxaliplatin treatments showed a general loss of occupancy in A549 cells, consistent with previously observed loss of rRNA synthesis. However, at the resolution of these experiments there was no evidence for a sequence-specific buildup of occupancies that would suggest specific disruptions in Pol I engagement which could result in perturbed rRNA transcription. In contrast, rDNA occupancy maps of RPA194 in BMH-21 treatment revealed potential pause sites at 47S promoter region, and TTF1 binding sites, which warrant further study.

In a broader context, our ChIP-seq experiments also underscore the high degree of sequence specificity of Pol I transcription factors for the transcribed regions of rDNA, which is maintaining despite of the dramatic relocalization events which take place during nucleolar stress. These protein–nucleic acid interactions may be an important factor in further understanding the complex interactions between biomolecules which maintain nucleolar homeostasis and direct response to cellular stress.

Bridge to Chapter VI

Chapter V investigates the direct influence of oxaliplatin on RNA Polymerase I function by applying ChIP-seq analysis of Pol I machinery to probe their occupancy along rDNA.

In Chapter VI, the interactions of metal coordination complexes with RNA and DNA are reviewed based on relatively recent NMR and x-ray crystal structures from the literature to provide a comprehensive look at metal interactions with nucleic acids.

CHAPTER VI: METAL ION INTERACTIONS WITH DNA, RNA, AND NUCLEIC ACID ENZYMES

This chapter was originally published as: DeRose, V. J.; Yglesias, M. V. Metal Ion Interactions With DNA, RNA, and Nucleic Acid Enzymes. In *Comprehensive Coordination Chemistry III*; Elsevier, 2021; pp 968–993. <https://doi.org/10.1016/B978-0-08-102688-5.00112-4>.

Introduction

Background: Roles of Metals in DNA and RNA Structure and Function

Nucleic acids play crucial roles in biology, as well as bio-inspired functional materials and therapeutics. In nature, deoxyribonucleic acid (DNA) is found in highly condensed chromosomes, plasmids, helical and non-helical structures, and, in eukaryotic organisms, mainly confined to the nucleus. Ribonucleic acid (RNA), transcribed from DNA, has more diverse functions encompassing both protein coding and non-coding activities (Novikova et al., 2013; Schmitz et al., 2016). Cellular RNAs occur in a variety of sizes and shapes, from short 21-nucleotide (nt) siRNAs to thousands of nucleobases in the protein-RNA machine of the ribosome (Milo et al., 2016). Both RNA and DNA undergo programmed chemical modifications in cells as well as modifications from genotoxic agents (Rausch et al., 2020; Roundtree & He, 2016). Examples of bio-inspired materials include DNA origami (Kuzuya & Ohya, 2014; Ramezani & Dietz, 2020), DNA and RNA-based enzymes (Ward et al., 2014), and DNA-based sensors (Lake et al., 2019). Gene silencing by introduced nucleic acids is a powerful laboratory and therapeutic tool (Jiang & Doudna, 2017; R. C. Wilson & Doudna, 2013). Novel RNA-based vaccines are currently being widely deployed (Dolgin, 2021).

The coordination chemistry of nucleic acids is a rich topic. Nucleic acids are negatively charged biopolymers with phosphodiester linkages, nitrogen and oxygen ligands in heterocyclic nucleobases, and oxygen ligands in ribose rings. From counterion condensation driving large structure changes to specific metal sites driving chemistry, cations play critical roles in nucleic acid structure and function (Bowman et al., 2012; Hoogstraten et al., 2002). Both monovalent and divalent cations play roles, with K^+ , Na^+ ,

and Mg^{2+} having highest cellular concentrations of approximately ~150, ~5, and ~1 mM respectively and with variation in cell types and compartments (I. L. Cameron et al., 1980; van Eunen et al., 2010; Palmer, 2015; Pechlaner & Sigel, 2012; Romani, 2011). The diversity of nucleic acid ligands and structures supports selectivity in metal interactions, leading to biological transition metal-dependent “riboswitches” (Saunders & DeRose, 2016; Wedekind et al., 2017) and *in vitro* DNA sensors for specific metals (Lake et al., 2019). Nucleic acids are targets of metal-based therapeutic agents such as the widely-used Pt(II) compounds, Au compounds, and others in development (Pizarro & Sadler, 2009).

Metal-nucleic acid interactions can be detected or inferred based on a variety of methods (V.J. DeRose, 2008; Erat & Sigel, 2011; Hunsicker-Wang et al., 2009). Metal-dependent activity studies report on and confirm the relevance of the influences of different cations on nucleic acid function. Atomic-level information from X-ray crystallography and magnetic resonance spectroscopies, along with optical spectroscopies, thermodynamic and activity-based measurements, and scattering methods all provide important information to either directly detect or develop models for molecular-level interactions. Theory can help rationalize or predict how metals bind to nucleic acids.

It is interesting to consider the different levels of complexity in nucleic acid structures that have been revealed over the decades. From early time, principles of metal coordination in nucleic acids have been illustrated using small molecule models of metals with nucleobases. Early studies of more complex nucleic acid structures focused on DNA duplexes and on transfer RNA (tRNA), the latter containing at least one conserved metal site detected in earlier structures and revisited in 2000 (Shi & Moore, 2000). RNA-based enzymes, ribozymes, provided sources of complex structures beginning in the 1980s. X-ray crystallography of the ribosome, >3000 nt of RNA, several proteins, and source of the 2009 Nobel prize, provides evidence for hundreds of sites with Mg^{2+} or other cations (Bashan & Yonath, 2008; Klein et al., 2004). Most recently, as described below, crystallography of metal-dependent riboswitches and DNAzymes have revealed principles of metal ion selectivity conferred by nucleic acid ligand structures.

This chapter updates and expands a previous thorough review of metal ion interactions with nucleic acids (V.J. DeRose et al., 2003) and expands content regarding both RNA and DNA. We will briefly summarize the metal ion coordination properties of

nucleic acids, which are a composite of traditional metal-ligand principles in context of the polyanionic and supramolecular structures of RNA and DNA biopolymers. Information about structures obtained since 2003 is included in this review, with the majority summarized from X-ray crystallography. An interesting increase in metal-nucleic acid structures has been from new structures of RNA riboswitches and ribozymes, showing a plethora of metal-binding environments in context of complex structured RNAs. In addition to the primary sources cited in this chapter, readers are referred to additional reviews, (Auffinger et al., 2011; Hadjiliadis & Sletten, 2009; Hannon & Reedijk, 2015; Hud, 2008; Pages et al., 2015) including spectroscopic approaches to metal-nucleic interaction (V.J. DeRose, 2008; Pechlaner & Sigel, 2012) and functional interactions between transitional metals and RNA, (Saunders & DeRose, 2016) as well as sections from reviews on RNA- and DNA-enzymes, (V.J. DeRose, 2003; Frederiksen & Piccirilli, 2009; Kolev et al., 2018; Ward et al., 2014) nucleic acid-metal interactions in sensors, (Kanellis & Dos Remedios, 2018; Zhou et al., 2017) and materials applications (W. Xu et al., 2019).

Nucleic Acids as Ligands

Overview of DNA/RNA Structure

Nucleic acids are biopolymers consisting of sugar-nucleobase units linked by phosphodiester groups. **Figure 6.1** provides the unit chemical structures and a reminder of nomenclature. It is important to note that the estimated pK_a 's of potential metal ligands (Schnabl & Sigel, 2010) depend on structure context, and are shown in **Figure 6.1** for the isolated unit. The estimates in **Figure 6.1** indicate that none of the nucleobases are protonated at neutral pH, meaning that unless there is environmental pK_a perturbation, (Lippert, 2008; Thaplyal & Bevilacqua, 2014) oligonucleotides carry only negative charges from phosphodiester linkages. In longer oligonucleotides this property supports a negatively-charged electrostatic environment that in solution conditions creates "counterion condensation" or a locally higher concentration of cations around the biopolymer (Draper et al., 2005). The polyelectrolyte properties of nucleic acids influence metal ion coordination, as described further below.

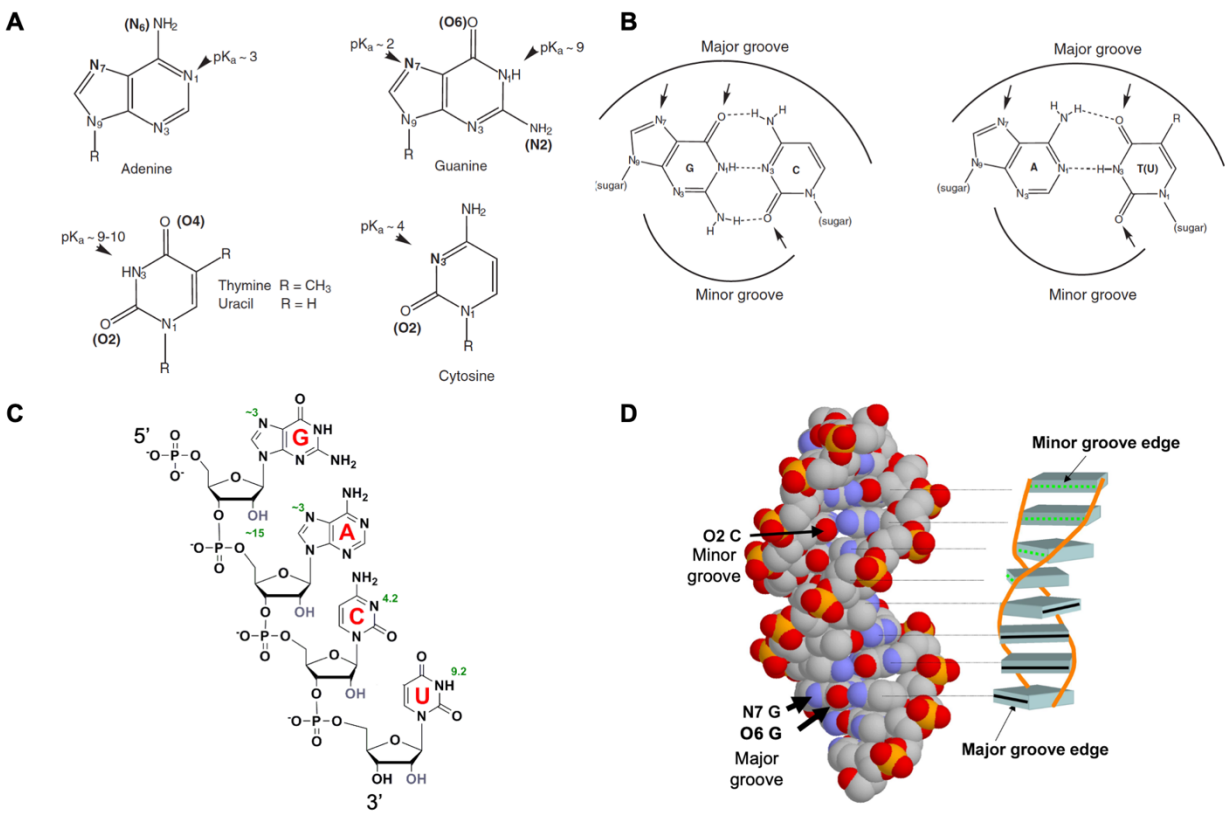


Figure 6.1. Metal binding sites of nucleic acids. **A** | Nucleobases with canonical numbering and approximate pK_a values for some common metal ligand sites. Note that pK_a values depend on local environment. Metal coordination is possible at all N/O ligands and also depends on local environment. R = H, nucleobase; R = ribose, deoxyribose (sugar), nucleoside; R = sugar-phosphate, nucleotide. **B** | Oligonucleotide, ribonucleic acid shown with approximate pK_a values for 2'-OH and non-bridging phosphodiester oxygens. **C** | Canonical base pairing with major and minor groove edges; arrows indicate most common metal interactions in duplex regions. **D** | Space-filling model of DNA duplex showing exposure of common metal ligands in major and minor groove; cartoon at right. From (V.J. DeRose et al., 2003). Ranges for nucleobase pK_a values also from (Schnabl & Sigel, 2010) and references therein.

The supramolecular structures of RNA and DNA are complex. Canonical base-paired double-helical structures are supported by hydrophobic, electrostatic, and hydrogen bonding interactions. Hydrogen-bonding faces of the nucleobases are protected within the helix, and the accessible “major” and “minor” grooves and phosphodiester bond backbone have exposure to solvent and thus are more likely to be metal binding sites for helical regions (**Figure 6.1**). Substitutions at the furanose 2-position affect the ribose conformation. For DNA, the deoxyribose conformation is predominantly C3-exo, whereas for RNA, the ribose conformation has a larger population of C3-endo. These conformations propagate to create different dimensions in the double-helix supramolecular structure (**Figure 6.2**). Standard B-form DNA has a wider major groove,

exposing the purine N7 positions, whereas A-form RNA has a narrower major groove and closer phosphodiester bond spacing, supporting a slightly more electronegative environment (Gebala & Herschlag, 2019). The third most discussed structure, the rare Z-form helix, has unusual nucleobase exposure (Ho & Mooers, 1997) and has been linked to biological processes (de Rosa et al., 2010). For helical structures, most metal interactions occur at the major and minor grooves, with some exceptions in which metal coordination within the helix is engineered (Jayarathna et al., 2018). Not only do the types of helices affect metal interactions, but conversely, metal coordination can alter the properties of helical regions. For example, the $[(\text{NH}_3)_3\text{Pt}]^{2+}$ unit of cisplatin bound to B-form DNA locally widens the dimensions of the major groove and influences protein recognition (Brabec et al., 2017). Addition of transition metals and complexes can drive Z-form DNA conformation (Medina-Molner & Spingler, 2012).

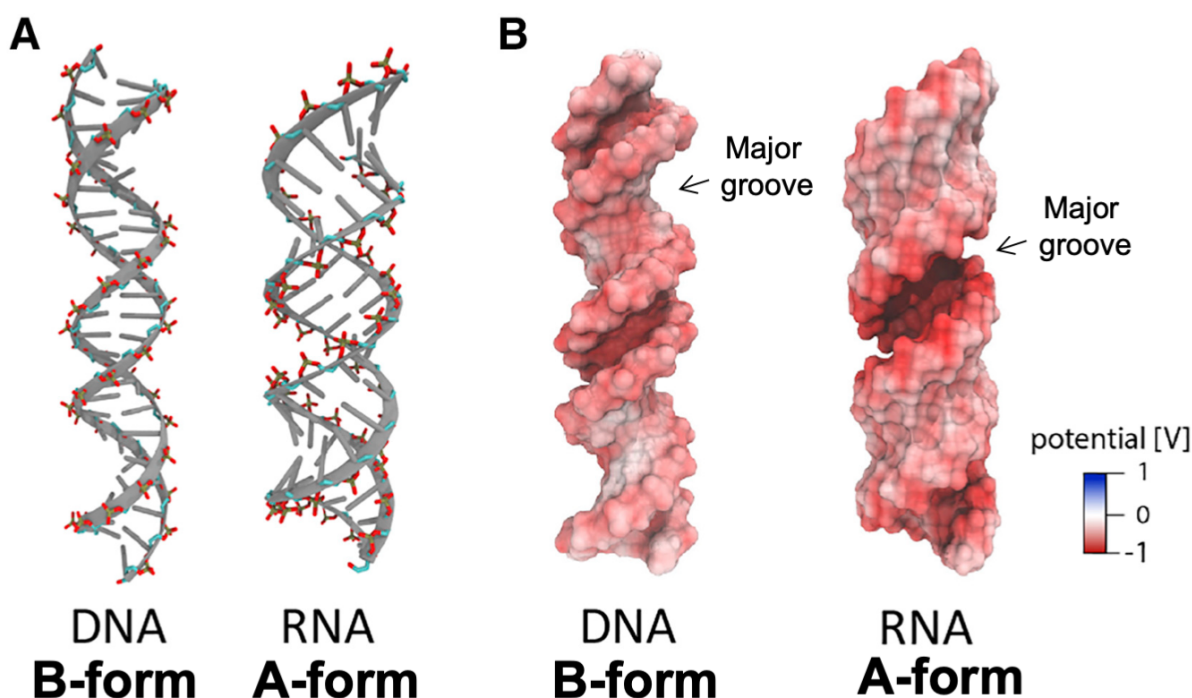


Figure 6.2. Canonical A- and B-form helices adopted by double-stranded RNA and DNA, respectively. **A** | Ladder and backbone model of double-stranded RNA and DNA. **B** | Poisson-Boltzmann (PB) calculations of electrostatic surface potential of the DNA and RNA duplexes from **A**. The influence of different ribose 2' substituents affects overall helical geometries and density and orientations of negatively charged phosphodiester groups, leading to higher negative electrostatic potential in the RNA major groove. Adapted with permission from (Gebala & Herschlag, 2019)

While the most common biological presentation of DNA is base-paired helices, both RNA and DNA form additional types of structures. Biological RNA is transcribed as a single strand that folds into structures that include base-paired regions with capping loops (hairpins) as well as many types of additional secondary and tertiary interactions (Butcher & Pyle, 2011; Leontis & Westhof, 2003). The RNA ribose 2'-OH affords additional hydrogen bond interactions that are involved in structural motifs such as “ribose zippers”. In biology, DNA and RNA also form G-quadruplex structures (Rhodes & Lipps, 2015). Very large supramolecular structures can be programmed as “DNA origami” (Jia et al., 2019). **Figures 6.3** and **6.4** show examples that preview how metal interactions, described in more detail below, can intersect with larger nucleic acid structural properties.

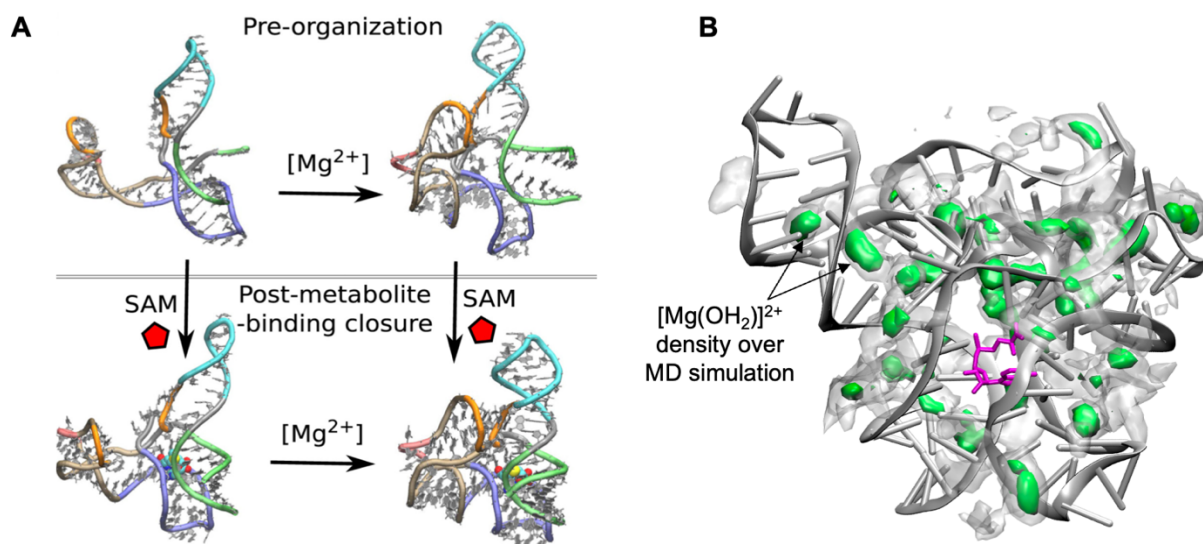


Figure 6.3. Predicted influence and distribution of Mg^{2+} ions on folding of the SAM-1 riboswitch. **A** | Both Mg^{2+} and SAM ligand are required for active riboswitch conformation; Mg^{2+} supports tertiary structure (upper) that templates SAM ligand binding. From (Roy et al., 2017). **B** | Spatial distribution functions of Mg^{2+} for SAM-I calculated from 2 μs molecular dynamics trajectories in bulk 10 mM Mg^{2+} and shown as effective concentrations; Mg^{2+} density surfaces of 1.4 and 7 M are shown in transparent white and solid green respectively. From (Hayes et al., 2012).

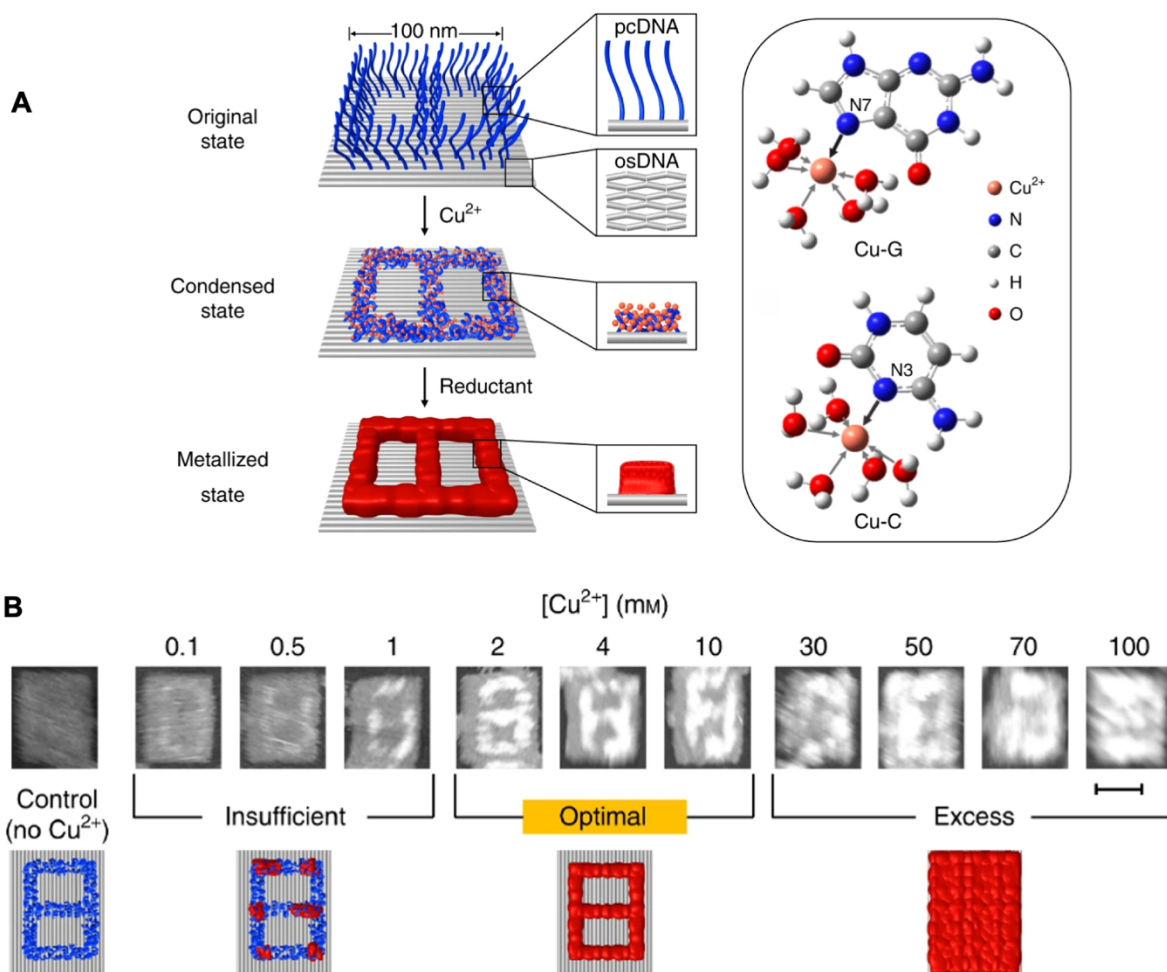


Figure 6.4. Metal nanostructure templated by DNA origami substrate (osDNA) with programmed “protruding cluster” triplexes (pcDNA) that bind Cu(II) for reduction and metalation. **A** | Left, 100 nm 2 nm thick osDNA template made of M13 viral DNA (7249 bases) programmed with single-strand 30-nt pcDNA strands. Addition of Cu(II) and ascorbate reductant induces metalation from pcDNA-enriched Cu, with QM-calculated Cu(II)-nucleobase interactions at right. **B** | AFM images of metallized patterns constructed with different CuCl_2 concentrations. Scale bar: 50 nm. Adapted with permission from (Jia et al., 2019)

Ligand Properties of Bases, Nucleosides, and Nucleotides

The nucleobases, sugar, and phosphate units of oligonucleotides contain multiple potential N/O metal ligands. Metal-coordinating properties of these sites have been studied in small model compounds and observed in larger polymers. Based on their relatively low pK_a values in unmodified nucleobases, the guanine N7, adenine N1, and cytosine N3 positions are expected and observed to readily form coordination complexes with transition metals at neutral pH. At higher pH values, metal coordination to deprotonated N1 of guanine and N3 of thymine/uracil is also observed. Metal

coordination or protonation at one position alters the pK_a of others (Lippert, 2008). Since the adenine N1 has a lower pK_a than N7, it is protonated first in solution and the N7 pK_a is difficult to access experimentally (Kapinos et al., 2011). However, in helical structures the N1 position is hydrogen-bonded, and metal coordination to adenine N7 is readily observed. Coordination to the exocyclic amino nitrogens (adenine N6, guanine N2, cytosine N4) is less favorable in these heterocycles because of delocalization of the nitrogen lone pairs into the ring (Fonseca Guerra et al., 2014).

Potential oxygen ligands include the nucleobase carbonyl groups, furanose 2'- and 3'-OH, and non-bonding phosphodiester oxygens. A comprehensive PDB survey found most prevalent inner-sphere coordination of monovalent cations to carbonyl groups (Leonarski et al., 2019). Hydroxyl groups have high pK_a values that inhibit coordination at neutral pH, but at high pH or with very oxophilic metals, 2'-3' metal chelates can be observed in ribonucleosides (Petrou, 2002). In ribozyme active sites, metal coordination to the 2'-OH has been invoked to lower its pK_a , promoting nucleophilic attack on neighboring phosphodiester bonds (Ward et al., 2014).

Coordination of metals to phosphodiester non-bonding oxygen ligands is common. As expected for mainly ionic interactions, affinities for oligonucleotide phosphodiester trends with the Irving-Williams series of first-row transition metal ions but there is an interesting exception for Mn(II), which has an anomalously higher affinity for phosphodiester ligands (Schnabl & Sigel, 2010; Sigel & Sigel, 2010).

In aqueous solution, metal ions are coordinated by water ligands and/or anions if the latter are in very high concentration. The coordination reaction to nucleic acids thus requires substitution of aqua ligands for the nucleic acid ligand. As will be described below, it is very common that metals that are bound to nucleic acids by at least one coordinate bond also retain multiple aqua ligands, and those aqua ligands provide second-shell interactions to surrounding sites. An interesting example is found in guanosine 5'-monophosphate (GMP), which presents both guanine N7 and phosphate ligands in proximity. For Mn(II), inner-sphere coordination to the guanine N7 is favored, and interaction with the phosphate is through hydrogen-bonded aqua ligands (De Meester et al., 1974). By contrast, the Mg(II)-GMP complex shows direct Mg-phosphate coordination, with outer-sphere interactions to the guanine N7. When two phosphate

ligands are available in guanine triphosphate, however, both Mn(II) and Mg(II) form all-phosphate complexes (Hoogstraten et al., 2002).

Metal Interactions with RNA and DNA Biopolymers

Properties of Metal Interactions with Oligonucleotides

The introduction so far has described metal-ligand properties for the isolated units of nucleic acids. When considering metal coordination to sites within larger nucleic acid structures, these metal-ligand properties occur in context of the very interesting effects of electrostatics in polyanions. The negatively charged phosphodiester backbone creates one negative charge per unit, which can amount to several hundred negative charges in a compact folded structure. In solution, a counterion atmosphere consisting of mobile, hydrated cations concentrates around and “shields” the nucleic acid. The complex folded structures of nucleic acids also induce proximities between diverse metal ligands, creating binding pockets of two or more ligands that are otherwise separated in primary sequence.

In this context of oligonucleotide structures, metal interactions have been sorted into three general types (Draper et al., 2005; Lake et al., 2019; Lipfert et al., 2014) (**Figure 6.5**): (a) The “ion atmosphere” consisting of a mobile charged layer of mainly hydrated cations that surround the nucleic acid polyanion. (b) Hydrated “site-binding” the association of hydrated cations with pockets of negative electrostatic potential created by the nucleic acid structure. There is little discrimination in types of cations that can be bound at a particular site, and this is also called “nonspecific site-binding”. (c) Coordinated “site-binding” in which at least one cation aqua ligand is replaced by a ligand from the nucleic acid. Because different metals may have distinguishing metal-ligand properties, this is also called “specific site-binding”.

These metal interaction categories are supported by evidence from many types of experiments as well as computational studies. Experimental information about the “ion atmosphere” around helices has been most recently based on analytical methods to quantify ions associated with the nucleic acid (Gebala & Herschlag, 2019; Greenfeld & Herschlag, 2009). The breadth and density of ion distribution around helices has been measured by X-ray scattering methods (Lipfert et al., 2014; Meisburger et al., 2015). Most ions in the mobile ion atmosphere are unresolved in X-ray crystallographic structures. X-

ray crystallography and other structural studies can, however, resolve site-bound hydrated cations as well as coordinated site-bound metals that have at least one direct metal-nucleic acid coordinate bond. As noted below, interpretation of X-ray crystallographic studies must be considered carefully with respect to resolution and occupancy of the ion. Spectroscopic methods have also been applied to metal-nucleic acid interactions (V.J. DeRose, 2008; Pechlaner & Sigel, 2012). If the bound metal ion influences folding or reactivity, evidence for site-bound cations can also be inferred from functional assays in different types of metals (Frederiksen & Piccirilli, 2009). For example, if the ion $[\text{Co}(\text{NH}_3)_6]^{3+}$, which is ligand exchange-inert, supports function this is presumably solely through outer-sphere interactions. Coordinated site-binding is also inferred from metal specificity switch studies, the most common of which is the thio-substitution of a nucleic acid oxygen that interrupts function in the presence of an oxophilic metal (i.e., Mg^{2+}), but finds it restored with a more thiophilic metal, Cd(II) (Frederiksen & Piccirilli, 2009; Ward et al., 2014). Over time and with increasingly sophisticated models, the relationships between the above categories have been explored. For example, a fourth category of metal-nucleic acid interactions that are regionally constrained while not specifically bound has been termed “glassy” (Bowman et al., 2012) and examples are reflected in increasingly sophisticated molecular dynamics simulations that provide information about the dynamic nature of “nonspecific” interactions (**Figure 6.3**) (Hayes et al., 2012).

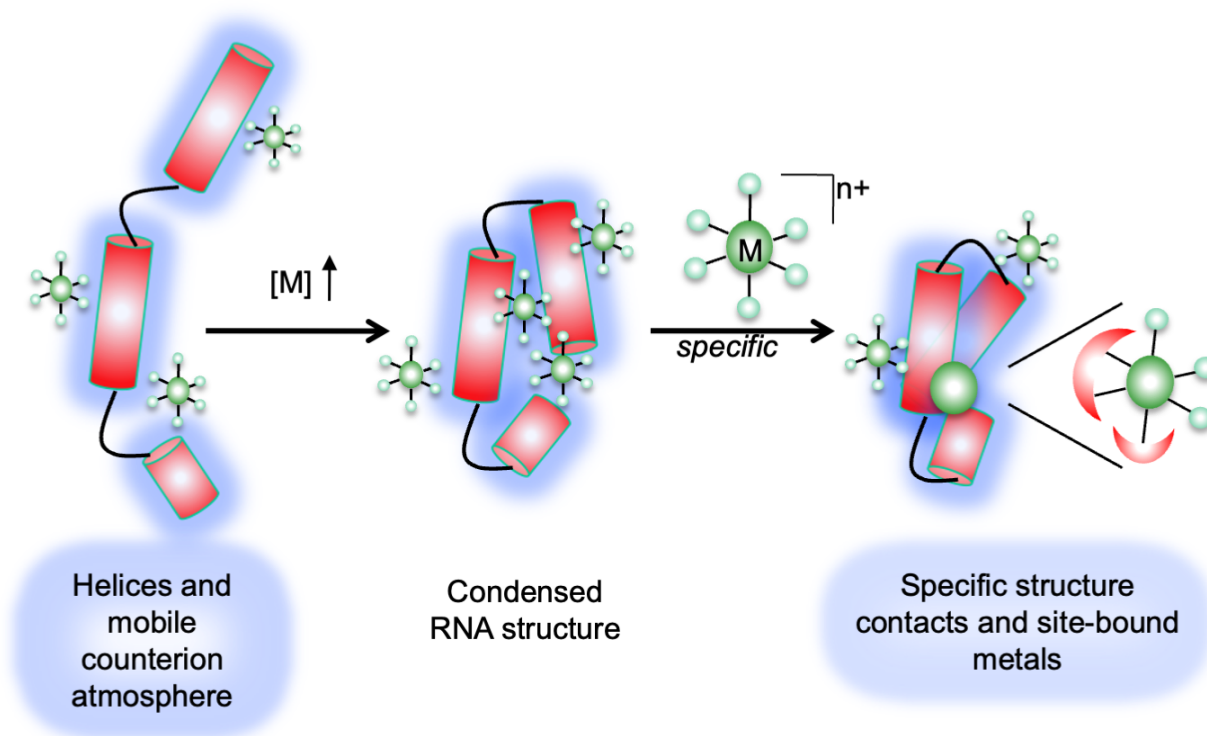


Figure 6.5. Classes of cation interactions and influence on nucleic acid structure. (left) Counterion atmosphere of mobile, hydrated cations surrounds single-stranded and helical regions. (center) Some higher-order structures condense with higher cation concentrations that shield high negative charge density of folded oligonucleotides. (right) Stabilities of some structures may be influenced by metal ions that occupy specific sites, coordinating directly to one or more nucleic acid ligands. Cations in these specific sites are rarely fully dehydrated. As noted in the text and depicted in **Figure 6.3**, regions may occur in structured nucleic acids in which mobile cations sample categories (b) and (c). Adapted from (V.J. DeRose et al., 2003).

Scope of Review

This Review will focus entirely on “coordinated” site-bound metals that have at least one direct metal-ligand bond with nucleic acids. The major evidence for such interactions that will be reviewed is from X-ray crystallography in structures entered into the Protein Data Base (PDB) (Berman et al., 2000). Each section highlights examples of particular interest, including novel findings. The sections also include Tables of structures from the PDB for each discussed metal ion. While an effort has been made to be comprehensive, there are limitations in reviewing this vast topic. Because the focus is mainly on canonical nucleobase and phosphodiester backbone structures, the powerful topic of using hybrid nucleic acids with incorporated metal ligands to template metal binding sites will not be included (Jayarathna et al., 2018; Kaul et al., 2011; Müller, 2019; Takezawa & Shionoya, 2012). It is important to note that identities of metals entered into

the PDB are inferred based on electron density, metal-ligand distances, and other factors. For large and complex nucleic acid structures that have been crystallized from a mixture of solution species, metal ion identification can be challenging. As has been noted in many places, both Mg^{2+} and H_2O have 18 e^- and therefore similar electron densities (vide infra). As discussed in below sections, misidentification of Mg^{2+} , K^+ , and Na^+ has been possible. The higher electron density on transition metals, however, enables more confident assignments. In order to bring the topic to a manageable level, the majority of the structures listed are nucleic acid-only, although some polymerase and other protein complex structures with metal-bound nucleic acids are included, in particular for the section on Pt(II). The structures selected have average resolutions of $<2.5 \text{ \AA}$, span a range of biological and abiological structures, and have been published since our prior review (V.J. DeRose et al., 2003).

Monovalent Cations: Group I and Thallium(I)

Monovalent cations such as Na^+ and K^+ are most often associated with the hydrated, mobile counterion atmosphere around nucleic acids. However, as has been separately reviewed, there are instances of apparent direct binding to various nucleic acid sites (Auffinger et al., 2016; Kolev et al., 2018; Leonarski et al., 2019) As described in those reviews, for “hard” oxophilic Na^+ and K^+ the most common interaction sites are with O6 of guanine and O2 of thymine/uracil, as well as phosphodiester nonbridging oxygens. Rb and Cs can take on additional structures. Tl^+ is used as a monovalent cation substitute for structure and function studies and is included here. Of note, recent reports suggest that in some X-ray crystallographic studies, particularly of larger nucleic acids, sites originally identified as Mg^{2+} may be misinterpreted and should be reassessed as Na^+ or K^+ based on ligand environment and stereochemistry (Leonarski et al., 2019; Rozov et al., 2019). **Table 6.1** includes nucleic acid structures with thallium, rubidium and cesium.

Table 6.1. Nucleic acid structures with thallium, rubidium and cesium.

	PDB Description ^a	Type	PDB	R(Å)	Ref.	
Thallium	G-quadruplex stabilized by Tl ⁺	DNA	1S45	2.20	(Caceres, 2004)	
	G-quadruplex stabilized by Tl ⁺	DNA	1S47	2.50	(Caceres, 2004)	
	Tl ⁺ soaked Dickerson-Drew dodecamer	DNA	1Z5T	1.60	(Moulaei et al., 2005)	
	Tl ⁺ form of G-quadruplex	DNA	2HBN	1.55	(Gill et al., 2006)	
	Ribozyme precursor, C75U mut bound to Tl ⁺ and Co(II) complex	Protein/RNA	2OJ3	2.90	(Ke et al., 2007)	
	Same but bound to monovalent Tl ⁺	Protein/RNA	2OIH	2.40	(Ke et al., 2007)	
	Riboswitch bound to lysine Tl-acetate soaked	RNA	3DJ2	2.50	(Serganov et al., 2008)	
	Protein-DNA complex in the presence of Tl ⁺	Protein/DNA	3JXC	1.90	(Watkins et al., 2010)	
	Tl-acetate soaked glycine riboswitch	RNA	3OXM	2.95	(L. Huang et al., 2010)	
	Tl-acetate soaked fluoride riboswitch	RNA	4EN5	2.96	(Ren et al., 2012)	
	Group II intron in the presence of Tl and Mg ²⁺	RNA	4E8Q	2.84	(Marcia & Pyle, 2012)	
	Riboswitch bound to ppGpp ligand; Tl-acetate soaked	RNA	6DME	2.70	(Peselis & Serganov, 2018)	
	Same but bound to PPRPP precursor ligand	RNA	6DLS	2.88	(Peselis & Serganov, 2018)	
	Rubidium	Protein-DNA complex in the presence of Rb ⁺	Protein/DNA	3JXD	2.10	(Watkins et al., 2010)
		Nucleosome Core with Rb ⁺ ion binding	Protein/DNA	3MGR	2.30	(Mohideen et al., 2010)
Group II intron in the presence of Rb and Mg ²⁺		RNA	4E8P	3.28	(Marcia & Pyle, 2012)	
Ribonuclease in complex with RNA/DNA hybrid in Mg ²⁺ and Rb ⁺		Protein/ DNA-RNA	6DOT	1.42	(Samara & Yang, 2018)	
Cesium	SAM-II riboswitch bound to SAM	RNA	2QWY	2.80	(Gilbert et al., 2008)	
	Riboswitch bound to lysine, Cs ⁺ soaked	RNA	3DIM	2.90	(Serganov et al., 2008)	
	FMN riboswitch bound to FMN, Cs ⁺ soaked	RNA	3F2X	3.11	(Serganov et al., 2009)	
	Nucleosome Core with Cs ⁺ ion binding	RNA	3MGS	3.15	(Mohideen et al., 2010)	
	Cs ⁺ soaked, riboswitch bound to ligand	RNA	3SKW	2.95	(Pikovskaya et al., 2011)	
	Cs ⁺ soaked, fluoride riboswitch	RNA	4ENA	2.85	(Ren et al., 2012)	
	Group II intron in the presence of Cs and Mg ²⁺	RNA	4E8R	3.36	(Marcia & Pyle, 2012)	
	preQ1 riboswitch Cs ⁺ soaked	RNA	4JF2	2.28	(Lieberman et al., 2013)	
	Cs bound G-quadruplex RNA	Protein/RNA	5DEA	2.80	(Vasilyev et al., 2015)	
	Cs ⁺ soaked, glutamine riboswitch bound with <i>l</i> -glutamine	Protein/RNA	5DDR	2.60	(Ren et al., 2015)	
	DNA junction-resolving enzyme GEN-1 binding w/Cs	Protein/DNA	6GRD	2.66	(Y. Liu et al., 2018)	
Cs ⁺ soaked SAM-VI riboswitch bound to SAH	RNA	6LAU	3.11	(Sun et al., 2019)		

^a Structures from Protein Data Bank (Berman et al., 2000) deposited since 2003. Selected structures include direct metal-nucleic acid coordination. Some lower- resolution or redundant structures excluded.

Sodium

Most of the structures reported in **Table 6.1**, including duplexes, G-quadruplexes, and a DNA 4-way junction, support the theme that site-bound Na^+ is mainly bound to oxygen ligands at distances around 2.5–2.7 Å. A very high-resolution 1.55 Å crystal structure of the hammerhead ribozyme reveals an unusual coordination of Na^+ to N7 of guanine (2.6 Å) (**Figure 6.6**) (Anderson et al., 2013) in a known metal binding site previously observed occupied by Mn(II) (Mn-N bond distance 2.04 Å) (Martick et al., 2008) and also confirmed occupied in solution by advanced EPR spectroscopy (Vogt et al., 2006). Metals in this site are also bound to the A9 phosphodiester non-bridging O in a functionally important interaction revealed by phosphorothioate substitution/metal rescue studies (Ward et al., 2014). Another unusual purine N7-bound Na^+ ion is predicted in the high-resolution 1.5 Å U-helix structure (PDB 3ND3) (**Figure 6.7**) (Mooers & Singh, 2011).

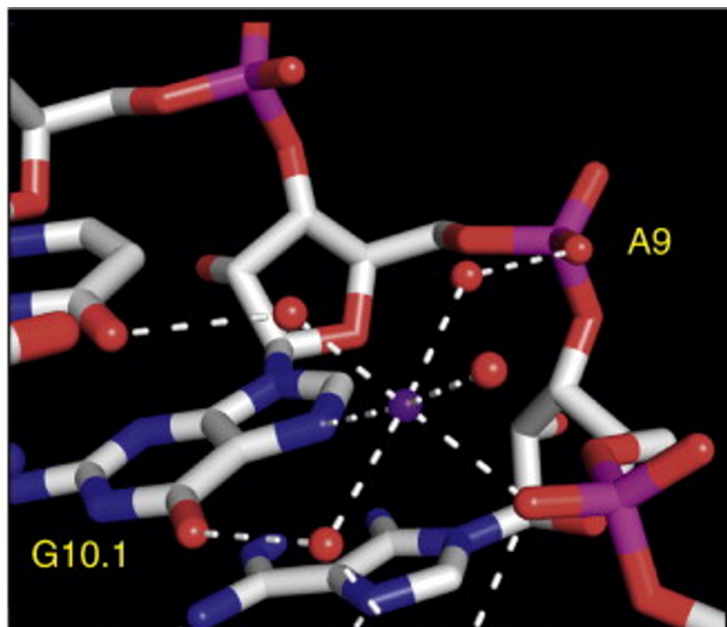


Figure 6.6. Na^+ ion in Hammerhead ribozyme canonical “A9” metal site bound directly to N7 G and through water to A9 non-bridging phosphodiester oxygen ligand (1.55 Å resolution structure, crystals grown in 4 M Na^+ , PDB 37P8). Mn(II) in this site binds directly to both ligands. Adapted with permission from (Anderson et al., 2013).

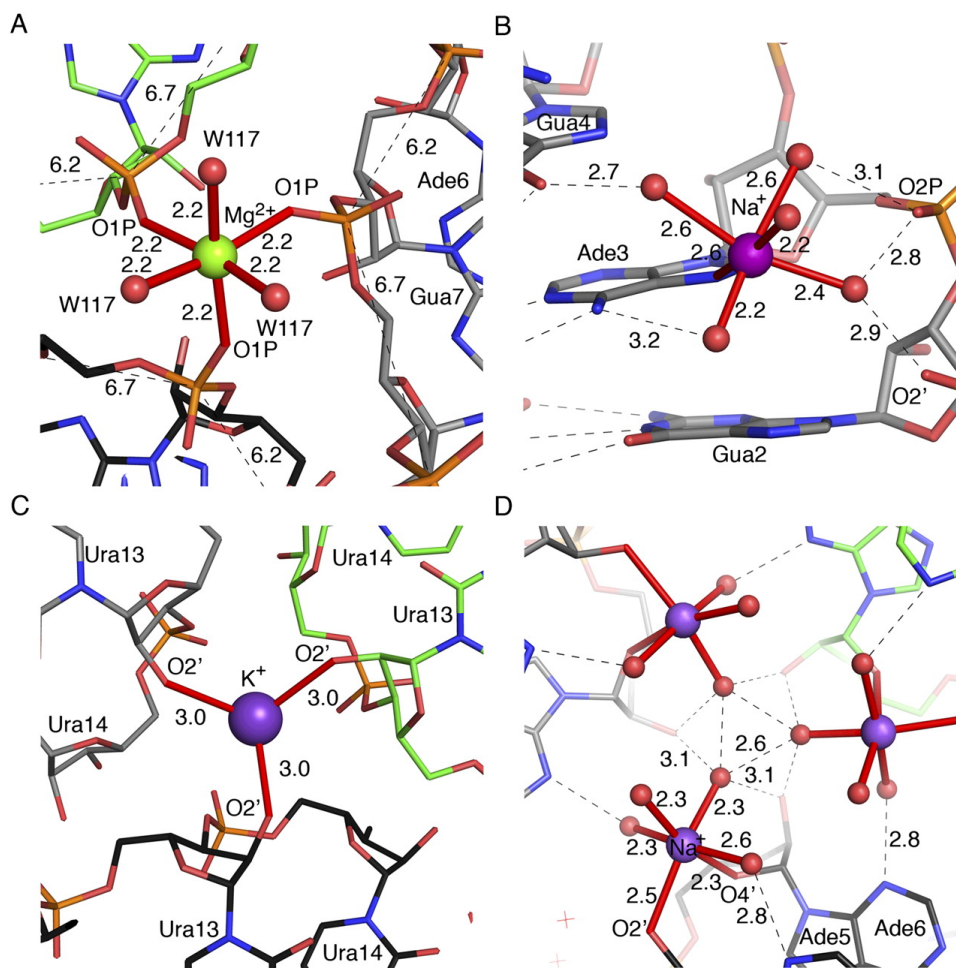


Figure 6.7. Metal sites modeled in crystal structures of a 16-nt RNA duplex (**A,B**, PDB 3ND4) and RNA helix containing 6 U:G mismatches (**C,D**, PDB 3ND3). Bond distances in Å ; structure resolutions ~ 1.4 Å. **A** | $[\text{Mg}(\text{H}_2\text{O})_3]^{2+}$ on a threefold crystallographic axis. **B** | A sodium cation modeled in the major groove with inner sphere coordination to the N7 nitrogen atom of A3. **C** | A potassium cation sits on a crystallographic threefold axis and bridges three symmetry-related O1P oxygen atoms. **D** | $[\text{Na}(\text{H}_2\text{O})_4]^+$ modeled bound to a ribose O2 hydroxyl and O4 ring oxygen of A6 in the minor groove near a crystallographic threefold axis. Adapted with permission from (Mooers & Singh, 2011).

Potassium, Thallium

As with Na^+ , the majority of structures containing K^+ exhibit the expected O-ligand coordination (**Figure 6.7**). An interesting structure includes a fully dehydrated K^+ in an RNA G-quadruplex of the fluorogenic RNA “mango” aptamer (PDB 5V3F); here, K^+ is coordinated by 8 guanine carbonyl oxygen ligands at ~ 2.8 Å distance (Trachman et al., 2017) As noted above, interested readers should keep an eye out for the reinterpretation of existing Mg^{2+} sites as possible monovalent cations (Leonarski et al., 2019). A striking example of this is through a recent long-wavelength structure determination of the T.

thermophilus 70S ribosome elongation complex, which reassigned several prior Mg^{2+} assignments to K^+ or water species (Rozov et al., 2019).

Several new structures with Tl^+ have been determined (**Table 6.1**); the higher electron density of Tl^+ is valuable in anomalous diffraction-based phasing. This property was used to locate cations in the hepatitis delta virus ribozyme (PDB 2OJ3), (Auffinger et al., 2016; Ke et al., 2007) with structures obtained by soaking Sr^{2+} -derived crystals in Tl^+ . Several Tl^+ were modeled bound directly to guanine O6-N7 ligands. In the ribozyme active site, a previously identified divalent cation site was occupied by one highly-occupied Tl^+ coordinating two carbonyl O2 and O4 uracil ligands, and a second Tl^+ ions, while retaining a well-established minor-groove A:T step monovalent cation binding site consisting of four DNA-derived O-atom donors and two aqua ligands (Moulaei et al., 2005). These examples show potential Tl^+ coordination to both N and O ligands of the nucleic acids.

Rubidium, Cesium

Rb^+ and Cs^+ are valuable as heavy-atom replacements for monovalent cations that allow phasing for structure refinement. To this end, structures of the RNA Group II intron with both Rb^+ and Cs^+ were solved, (Marcia & Pyle, 2012) as well as large nucleosome particles with both cations (Mohideen et al., 2010). In the latter case, both Rb^+ and Cs^+ were modeled as binding to thymine oxygen ligands in the minor groove around AT steps, in a manner similar to that previously observed for the “Dickerson–Drew dodecamer” which has been the subject of several high-resolution X-ray crystallographic studies. AT steps have a narrower minor groove that brings four thymine oxygen ligands into proximity, supporting metal binding sites. The structure of the pre Q_1 -II riboswitch provides an interesting example of Cs^+ used in single-wavelength anomalous diffraction phasing. In this structure 13 Cs^+ ions were resolved, mainly bound to oxygen ligands (Lieberman et al., 2013). Additional structures are provided in **Table 6.1**.

Group IIA: Magnesium/Calcium/Strontium/Barium

Mg^{2+} is in relatively high (mM) concentration in cells, (Pechlaner & Sigel, 2012; Romani, 2011) and binds nucleic acids mainly through phosphodiester or nucleobase oxygen ligands, with rare loss of the full hydration shell. Many nucleic acid structures

demonstrate these Mg-binding properties. As described above, crystallographic identification of Mg²⁺ can be challenging, and reinterpretation as K⁺ has occurred in some cases, (Leonarski et al., 2019; Rozov et al., 2019) including with the aid of anomalous X-ray diffraction signals near the potassium K-edge (Rozov et al., 2019). Substitution with Mn(II) has been one method to help confirm divalent cation sites. One example is in a multi-metal cation binding region of the “M-box RNA” originally thought to be a putative Mg²⁺-sensing riboswitch, (Dann et al., 2007; V.J. DeRose, 2007) where both Mg and Mn occupy phosphodiester bound sites. As previously noted, while other metals with higher electron density might occupy the same metal pockets as Mg²⁺, the specific ligands might be altered from the mainly O-ligand-Mg²⁺ interactions to, for example, Mn(II)-imino N coordination.

One of the more remarkable Mg²⁺-containing structures since the last review is that of the fluoride riboswitch (Ren et al., 2012). This RNA binds F⁻ with an apparent $K_D \sim 100$ mM only in the presence of Mg²⁺. The structure of the fluoride riboswitch demonstrates how a binding site for a small, negatively charged anion can be formed in a polyanionic RNA; the F⁻ ion is bound between three closely spaced Mg²⁺, which are sequestered by five phosphodiester oxygen ligands, some of which act as bidentate ligands bridging two Mg²⁺ (**Figure 6.8**).

Ca²⁺ often coordinates to phosphate oxygen ligands and in an interesting metal-substitution RNA duplex study, was not easily displaced by other metals (Schaffer et al., 2016). The larger sizes of Sr²⁺ and Ba²⁺ accommodate expanded coordination spheres. As one example, a high-resolution RNA G-quadruplex crystallized with Sr²⁺ shows the centrally located Sr²⁺ ions coordinated by eight guanine O6 ligands at ~ 2.6 Å Sr-O distance, and 6.4 Å spacing between Sr²⁺ cations in the channels (Fyfe et al., 2015). The expanded coordination sphere and flexible “less hard” coordination properties of Sr²⁺ have been credited with and exploited to improving nucleic acid crystal properties and ensuing diffraction resolution. In one example, Sr²⁺ bridges two terminal 2'-3'-diols with six additional water ligands (Jinwei Zhang & Ferré-D'Amaré, 2014). In another example, Sr²⁺ and Ba²⁺ occupy the same position bridging two uracil O-ligands to create crystal contacts, completing the coordination sphere with 5–6 water ligands in both cases (Dodd et al., 2016) Another example of Ba²⁺ is found in the structure of the DNA hexamer duplex d(CGTACG)₂ crystallized in a solution containing both Ba²⁺ and Co(II) (Valls et al., 2005).

Ba²⁺ coordination to guanine O6 and to phosphodiester groups is observed, whereas Co(II) coordinates to guanine imino N7-donor ligands.

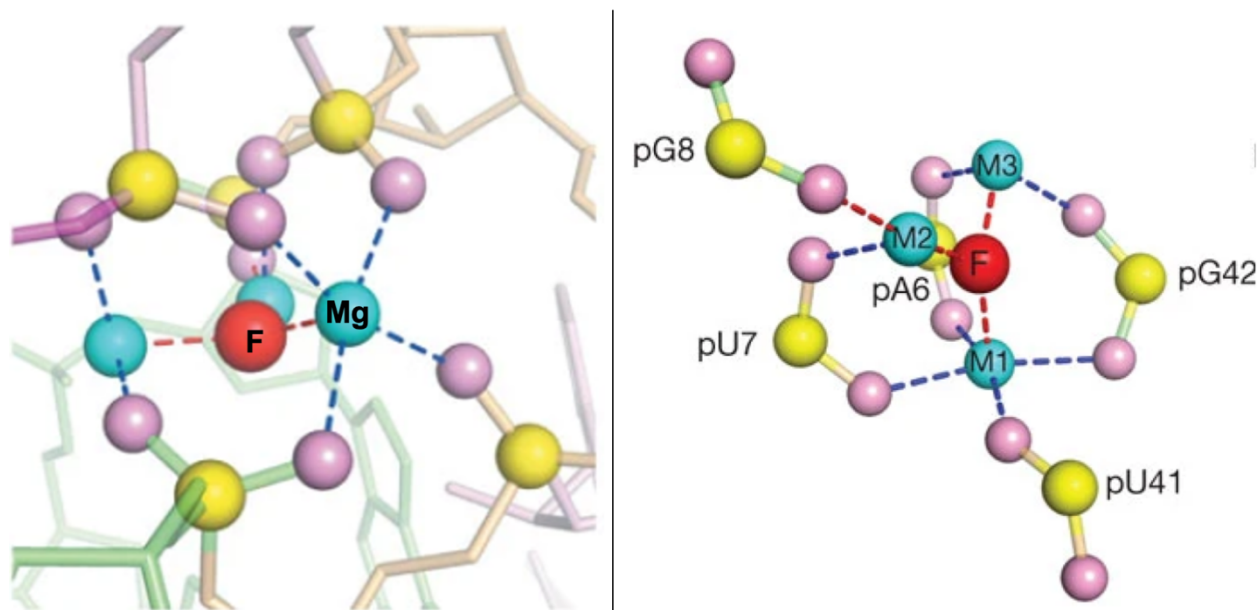


Figure 6.8. Mg-F cluster in a 52-nt fluoride-sensing riboswitch from *T. petrophila* crystal structure (2.3 Å resolution). Three Mg²⁺ sites supported by Mn(II) substitution. Mg-F bond distances are 1.9 Å. M1 bridges M2, M3 by two bidentate phosphodiester ligands; all remaining hexacoordinate M ligands are H₂O (not shown). Adapted with permission from (Ren et al., 2012)

Transition Metals

There is a long history of studying interactions between transition metals and nucleic acids (V.J. DeRose et al., 2003; Morris, 2014; Pages et al., 2015). In some cases, described below, transition metals are used as heavy-metal substitutes to help identify Mg²⁺ binding sites, or for phasing. The ability of some metals to catalyze phosphodiester bond hydrolysis has been the basis for DNA- and RNA-based enzymes, which can show selectivity between different metals (Lake et al., 2019; Ward et al., 2014). Recent research has also uncovered endogenous transition metal-binding RNAs that act as metal-sensing riboswitches (S. Bandyopadhyay et al., 2021; Saunders & DeRose, 2016; Wedekind et al., 2017; J. Xu & Cotruvo, 2020). Although the vast majority of transition metal-nucleic acid coordination involves bonds to purine N7 positions, the late and lower-row transition metals can show interesting alternatives such as binding to deprotonated pyrimidine N3 sites. A selection of recent nucleic acid structures with first-row transition metals is found in **Table 6.2**.

Table 6.2. Nucleic acid structures with first-row transition metals.

	PDB Description ^a	Type	PDB	R(Å)	Ref. ^b
Chromium	High-res Z-DNA complex with Cr ³⁺	DNA	4R15	0.97	(Drozdal et al., 2015)
Manganese	Manganese riboswitch	RNA	6N2V	2.85	(Suddala et al., 2019)
	Mn- soaked riboswitch	RNA	6DLQ	2.80	(Peselis & Serganov, 2018)
	four-way junction ribozyme	RNA	5Y87	2.13	(Zheng et al., 2017)
	riboswitch bound with L-glutamine soaked with Mn ²⁺	RNA	5DDQ	2.40	(Ren et al., 2015)
	hammerhead ribozyme in Mn ²⁺	RNA	5DI2	2.99	(Mir et al., 2015)
	<i>yypP-ykoY</i> riboswitch bound to Mn ²⁺	RNA	4Y1I	2.85	(Price et al., 2015)
	riboswitch in complex with hypoxanthine	RNA	4NYD	2.90	(Warner et al., 2014)
	Mn ²⁺ interaction with non-self-complementary Z-type DNA duplex	DNA	4DWY	1.61	(Mandal et al., 2012a)
	fluoride riboswitch, Mn ²⁺ soaked	RNA	3VRS	2.60	(Ren et al., 2012)
	tetra-decanucleotide A-DNA duplex	DNA	3V9D	2.50	(Mandal et al., 2012b)
	Mn ²⁺ bound M-box RNA	RNA	3PDR	1.85	(Ramesh et al., 2011)
	glycine riboswitch, Mn ²⁺ soaked	RNA	3OXE	2.90	(L. Huang et al., 2010)
	B-DNA in the presence of Mn ²⁺	RNA	3EIL	2.60	(Millonig et al., 2009)
	Full-length hammerhead ribozyme with Mn(II) bound	RNA	2OEU	2.00	(Martick et al., 2008)
	Ultrahigh-resolution crystal structure of Z-DNA in complex with Mn ²⁺ ion.	DNA	4HIG	0.75	(Drozdal et al., 2013)
	Structure of the native RNA tridecamer r(GCGUUUGAAACGC)	RNA	2R22	1.40	(—)
	Octameric RNA duplex soaked in manganese(II)chloride	RNA	4U3O	1.80	(Schaffer et al., 2016)
APO PreQ1 riboswitch aptamer grown in Mn ²⁺	RNA	6VUH	2.00	(G. M. Schroeder et al., 2020)	
Crystal structure of d(CACGCG).d(CGCGTG) cocrystallized with MnCl ₂	DNA	3G2R	2.15	(—)	
Cobalt(II)	[Co ²⁺ -(Chromomycin A3) ₂]-d(TTGGCGAA) ₂ complex	DNA	6J0I	2.50	(Satange et al., 2019)
	9DB1* deoxyribozyme (Cobalt hexammine soaked crystals)	DNA	5CKI	2.98	(Ponce-Salvatierra et al., 2016)
	NiCo transition-metal riboswitch bound to cobalt	RNA	4RUM	2.64	(Furukawa et al., 2015)
	Octameric RNA duplex co-crystallized with cobalt(II)chloride	RNA	4U3R	1.70	(Schaffer et al., 2016)
	complex between anticancer drug Variolin B and DNA	DNA	4MNB	1.40	(Canals et al., 2017)
	d(GTGGAATGGAAC)	DNA	5GUN	2.59	(T.-Y. Huang et al., 2017)
	cobalt-bound B-DNA duplex	DNA	4R4A	1.49	(Mandal et al., 2014)
Nickel	AT-rich DNA dodecamer with extra helical guanine-nickel coordination	DNA	5M68	2.64	(—)
	[Ni ²⁺ -(chromomycin A3) ₂]-CCG repeats complex	DNA	5XEW	1.75	(Tseng et al., 2017)
	Ni ²⁺ B-DNA GAATTCG	DNA	1S9B	2.81	(Valls et al., 2004)
	AntpHD with 15bp DNA duplex S-monothioated at Cytidine-8	Protein/ DNA	5JLX	2.75	(Nguyen et al., 2016)

Table 6.2. (continued).

	PDB Description ^a	Type	PDB	R(Å)	Ref. ^b
Copper	Ca(II) and Cu(II) bound to the Z-DNA, d(CGCGCG)	DNA	4XSN	1.45	(Rohner et al., 2016)
	Octameric RNA duplex soaked in copper(II)chloride	RNA	4U78	1.50	(Schaffer et al., 2016)
	Calcium(II) and copper(II) bound to the Z-DNA form of d(CGCGCG), complexed by L-lactate and succinate	DNA	5IHD	1.57	(Rohner et al., 2016)
	Calcium(II) and copper(II) bound to the Z-DNA form of d(CGCGCG), complexed by chloride and MES	DNA	4XOZ	2.15	(Rohner et al., 2016)
	Crystal structure of GNA with synthetic copper base pair	GNA	2JIA	1.30	(Schlegel et al., 2008)
Zinc	double-stranded DNA AGGGATCCCT in complex with Zn ²⁺	DNA	6DY5	1.26	(Hou & Tsodikov, 2019)
	tetradecamer sequence d(CCCGGGTACCCGGG) ₂	DNA	5IYE	1.69	(Karthik et al., 2017)
	mithramycin analogues bound to DNA	DNA	5JVW	2.00	(Hou et al., 2016)
	Pribnow box consensus promoter sequence	DNA	5J0E	2.81	(Mandal et al., 2016)
	Z-DNA in complex with Zn ²⁺ ions	DNA	4HIF	0.85	(Drozdal et al., 2013)
	HIV-1 DIS RNA subtype F-Zn soaked	RNA	1YXP	2.40	(Ennifar & Dumas, 2006)
	Crystal structure of zinc(II)-d(GGCGCC) ₂	DNA	1P26	2.92	(Labiuk et al., 2003)
	HIV-1 DIS(Mal) duplex Zn-soaked	RNA	1NLC	1.85	(Ennifar et al., 2003)
	Structural Basis for Bifunctional Zn(II) Macrocyclic Complex Recognition of Thymine Bulges in DNA	RNA	2LOA	NMR	(del Mundo et al., 2012)
	Crystal Structure of Chiral Gamma-PNA with Complementary DNA Strand: Insight Into the Stability and Specificity of Recognition an Conformational Preorganization	PNA	3PA0	1.60	(Yeh et al., 2010)

^a Structures from Protein Data Bank (Berman et al., 2000) deposited since 2003. Selected structures include direct metal-nucleic acid coordination. Some lower- resolution or redundant structures excluded.

^b (—), No primary publication associated with structure.

Chromium

Oxophilic Cr(III) is used to create exchange-inert nucleotide triphosphate complexes for mechanistic studies (Arndt et al., 2001; Dunaway-Mariano & Cleland, 1980). Cr(III) is expected to interact with oligonucleotides, (Wise & Wise, 2012) but few structure studies have been performed. In one report, a high-resolution Z-DNA structure included outer-sphere interactions with Cr(III) as hexahydrated species (Drozdal et al., 2015).

Manganese

Mn(II) is often found coordinated to purine N7 imino N-ligands as well as phosphodiester O-donor ligands (Erat & Sigel, 2011). A classic example of the former is a Z-DNA structure, showing Mn(II) coordinated to both guanine and adenine N7 ligands (Mandal et al., 2012a).

Because high-spin Mn(II) has a similar ionic radius to Mg^{2+} , Mn has been used as a heavy-atom replacement to confirm divalent cation sites in RNAs. In many cases, in particular for structured RNAs, Mn(II) occupies the same site as Mg^{2+} with similar O-atom, most often non-bridging phosphodiester, ligands. An example is the 'twister-sister' ribozyme, where 7 Mg^{2+} are recapitulated with a Mn^{2+} -soaked structure (Zheng et al., 2017). All of these sites are of partially hydrated cations, with 1–2 inner-sphere phosphodiester or purine carbonyl O-ligands from the RNA; in addition to these inner-sphere contacts, the metal aqua ligands are proposed to be critical in mediating hydrogen-bonding interactions supporting the active structure. However, Mn(II) has a preference for imino N7 purine ligands, and this ribozyme shows one additional Mn site coordinated to a guanine N7 that is not observed with Mg^{2+} . Another example is the M-box RNA noted above under Mg^{2+} , where the structure in the presence of Mn^{2+} recapitulates the main phosphodiester-bound ligands (Ramesh et al., 2011).

One might predict, therefore, that selecting between Mg^{2+} and Mn(II) in a cellular context might rely on the preference of Mn(II) coordination to nitrogen ligands. This is indeed observed in the structure of a Mn-sensing riboswitch (Price et al., 2015; Suddala et al., 2019) (**Figure 6.9**), which contains two sites that each bind metals with five phosphoryl oxygen ligands. Site M_B also contains, however, an adenine N7 ligand and is selectively populated with Mn(II), presumably conferring metal ion selectivity for this RNA. As described below in context of Cd(II), it has been proposed that the transition metal site in this riboswitch also uses heptacoordination as a metal-selective property (Bachas & Ferré-D'Amaré, 2018).

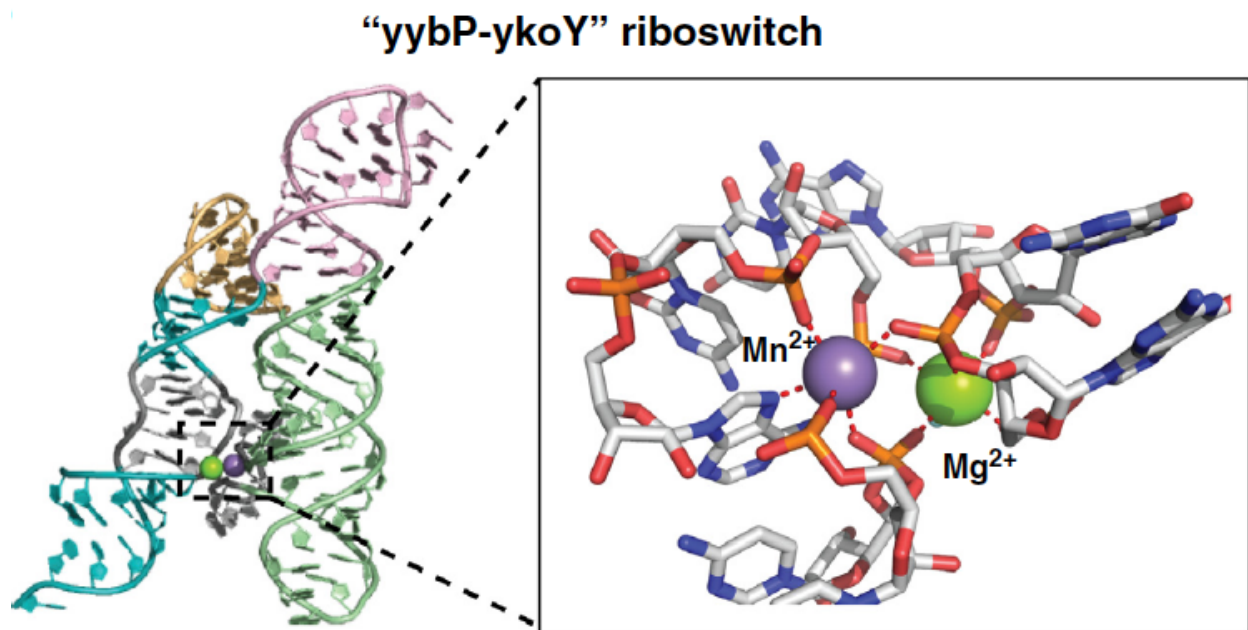


Figure 6.9. Crystal structure of *L. lactis* Mn-sensing riboswitch (PDB 4Y1I, 2.85 Å). Zoomed region shows coordination of the Mn(II) ion by N7 of a strictly conserved A41, differentiating the transition metal binding site. A second site (green) is less selective for transition metals. Adapted from (Saunders & DeRose, 2016)

Iron

As noted in 2003, there are no reported crystal structures of Fe-bound nucleic acids. However, Fe(II) substitution (under anaerobic conditions) supports RNA structure and function (Athavale et al., 2012; Popović et al., 2015) as well as DNAzyme activity (Moon & Liu, 2020). DFT simulations predict that Fe(II) will be as stable as Mg²⁺ in “phosphate clamp” bis-phosphodiester coordination environments (Athavale et al., 2012). Exciting recent discoveries of Fe-dependent riboswitches suggest promise for future structural work to elucidate principles of coordination and selectivity (S. Bandyopadhyay et al., 2021; J. Xu & Cotruvo, 2020).

Cobalt

Like Mn(II), Co(II) can occupy some general cation sites in nucleic acid structures. In general, Co(II) favors N-donor ligands, as has been observed for B-form DNA (Mandal et al., 2014). One unusual all O-coordination sphere is observed for all bound Co(II) as well as Cu(II) and Mn(II) in an octameric RNA helix structure that includes coordination to uracil O4 (Schaffer et al., 2016).

A fascinating Co(II)-bound RNA structure was reported for a transition metal-sensing Ni/Co riboswitch consisting of 4 Co(II) sites dominated by Co–N coordination (**Figure 6.10**) (Furukawa et al., 2015; Saunders & DeRose, 2016). Sites Co(I) and Co(II) coordinate imino N7 ligands from two guanines that are stacked, and Co(I) and Co(III) are bound to neighboring guanines, demonstrating an interaction network supported by the Co(II) ions.

Trivalent Co(III) is typically considered to be ligand-exchange inert under neutral pH and mild conditions. $[\text{Co}(\text{NH}_3)_6]^{3+}$ is therefore commonly used as a test for whether inner-sphere metal ion coordination is required to support RNA function. A rare and interesting exception wherein two Co(III)-ammine ligands exchanged with N7 and phosphate ligands in a DNA structure has been described (Ennifar & Dumas, 2006). Another unique application of this supposedly inert complex has been the observation that photoexcitation of RNA-bound $[\text{Co}(\text{NH}_3)_6]^{3+}$ can lead to ligand exchange and crosslinking, demonstrated in the hairpin ribozyme and with yield dependent on ligand proximity and pH (Kraemer-Chant et al., 2014). $[\text{Co}(\text{NH}_3)_6]^{3+}$ and $[\text{Ir}(\text{NH}_6)]^{3+}$ have been noted as particularly useful for phasing (Batey & Kieft, 2016).

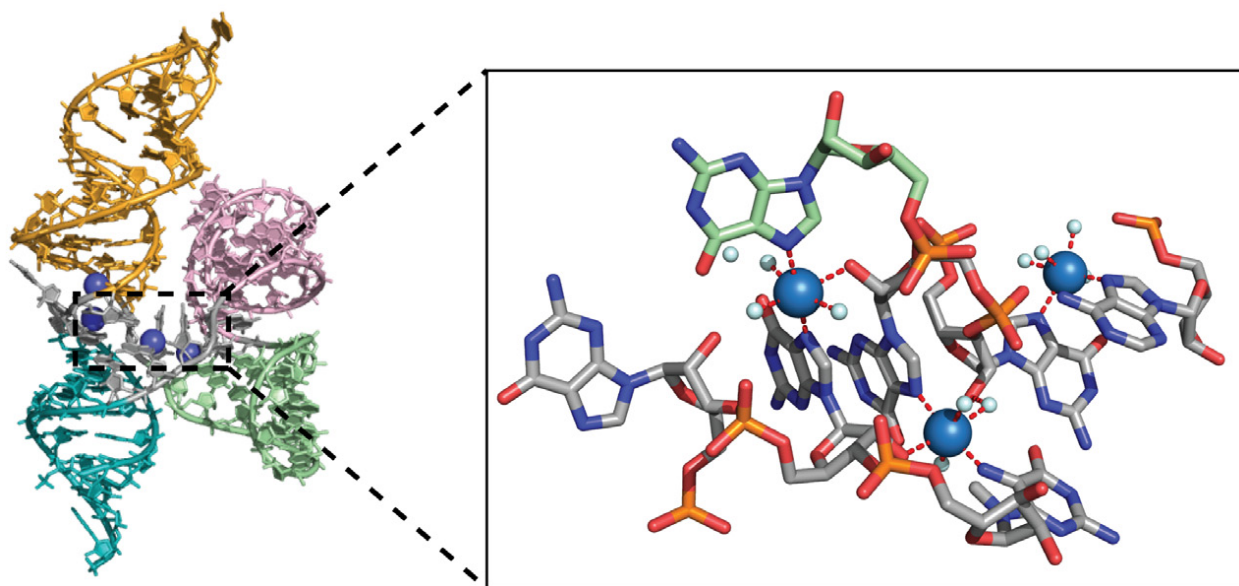


Figure 6.10. Crystal structure of NiCo riboswitch from *E. bacterium* bound to Co(II) (PDB 4RUM). Tinted regions indicate different stem loops. Zoomed region shows a network of interactions linking the Co(II) binding sites 1–3. Cyan spheres are water ligands. Adapted from (Saunders & DeRose, 2016)

Nickel

The few new Ni(II)-containing nucleic acid structures that have been reported (**Table 6.2**) demonstrate the expected Ni(II)-N7 coordination in context of an octahedral coordination sphere containing additional aqua ligands. Of note, the Ni/Co-responsive riboswitch described above (Furukawa et al., 2015) has been biochemically characterized with Ni(II) but Ni-bound structures are not yet reported.

Copper

An interesting structure of Z-form DNA containing several bound Cu(II) ions demonstrates a range of octahedral Cu(II) sites containing mixtures of 1–3 DNA-derived ligands and aqua ligands (Rohner et al., 2016). Both *cis*- and *trans*-nitrogen coordination to guanine N7 positions are reported, including an intermolecular Cu(II) interaction, along with additional coordination to guanine O6 and phosphodiester nonbridging O-donor ligands.

A different example is found in a structure of duplexed GNA, glycol nucleic acid, that includes a Cu-mediated artificial base pair interaction wherein square-planar Cu(II) bridges hydroxypyridones introduced into nucleobase positions (Schlegel et al., 2008). Finally, the ability to use DNA origami structures to pattern Cu-metal nanostructures through spatially designed Cu(II) binding and reduction to Cu(0) was noted above (**Figure 6.4**) (Jia et al., 2019).

Zinc, Cadmium

Zn²⁺ preferentially coordinates to the N7 of guanine, similar to other transition metals, and is often substituted for Mn(II) and Mg²⁺ in crystal structures due to similar chemical properties and biological importance (Zhou et al., 2017). Coordination of Zn²⁺ to N7-guanine had previously been used for phase determination in DNA duplexes by single-wave anomalous diffraction (SAD) (Hou & Tsodikov, 2019).

Ultrahigh-resolution crystal structures of a Z-DNA duplex d(CG)₃ in complex with Zn²⁺ have also found Zn²⁺ bis-coordinated to the N7 of two symmetry related guanine residues forming a tetrahedral complex, with additional Cl⁻ and water ligands (Drozdal et al., 2015). The Zn²⁺-N7 bond lengths are 1.990 Å and 2.032 Å. Additionally, the ligated water molecule is hydrogen-bonded to the O6 of the two guanine ligands (**Figure 6.11**).

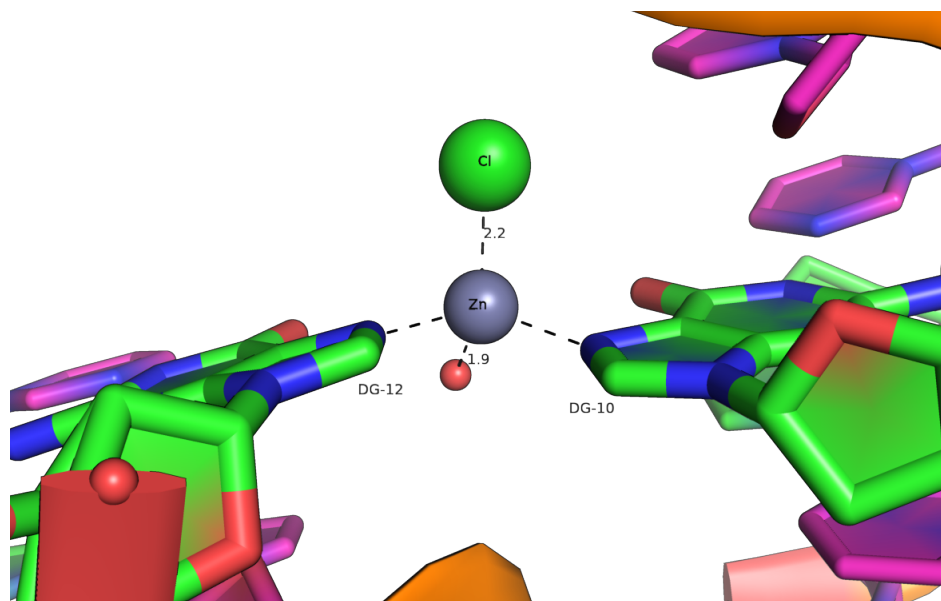


Figure 6.11. Ultrahigh-resolution structure (rendered from PDB 4HIF, 0.85Å) of Z-DNA in complex with Zn^{2+} . Zn is bis-coordinated to the N7 atoms of guanine from two symmetry-related molecules in a tetrahedral geometry that includes a Cl^{-} ion (green) and water molecule (red). Distance between the Zn and N7 atoms of DG-12 and DG-10 are 1.990 Å and 2.032 Å respectively.

In a metal site in an RNA duplex with noncanonical structure, the Zn^{2+} site also contained two phosphodiester O-ligands as well as the guanine N7 anchor (Ennifar et al., 2003). The Zn-bound structure reflected a conformational change over the same area when only Mg^{2+} was present, suggesting that Zn-ligand interactions could stabilize an alternative local structure in a flexible RNA region.

In contrast to the smaller ionic radius of Zn^{2+} , it is thought that the ability for larger Cd(II) and Mn(II) to be heptacoordinate explains ion selectivity in *yybP-ykoY* riboswitches, constructs of which show high in vitro affinity for several divalent transition metals (Bachas & Ferré-D'Amaré, 2018). Crystal structures revealed several multinuclear binding modes for Cd(II) that all predict the Cd^{2+} ion to be heptacoordinated to the N7 of adenosine A41 and six oxygen atoms from the phosphate backbone or water. The heptacoordinate binding site is preorganized through a second metal ion that is bound to six oxygen atoms from the phosphate backbone or water in another hexacoordinate binding site (**Figure 6.12**) (Bachas & Ferré-D'Amaré, 2018).

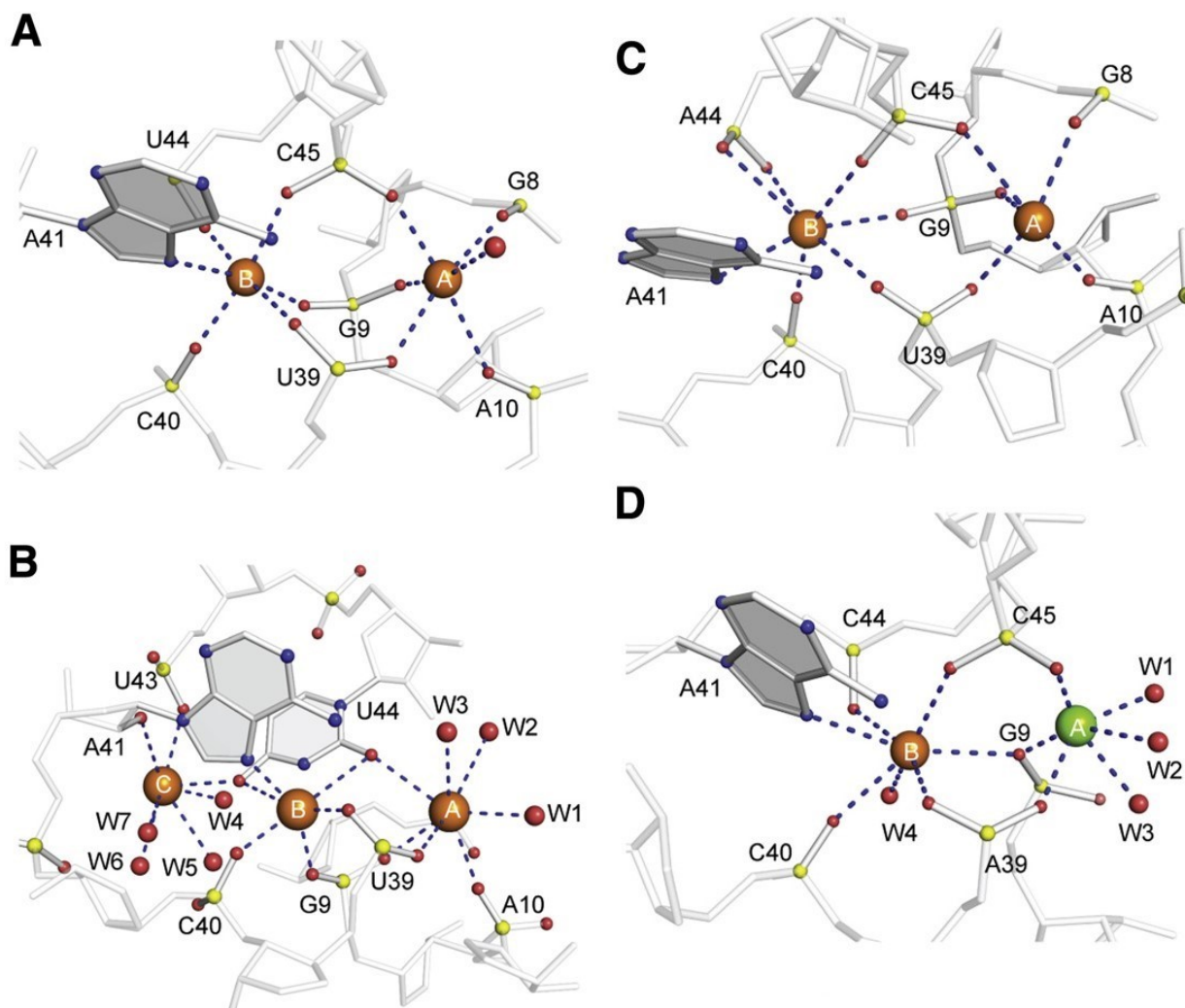


Figure 6.12. Observed binding modes of Cd(II) in *ykoY*-aptamer domain crystal structures demonstrating heptacoordination in transition metal-selective B site. Cd(II) ions are shown in orange, water molecules in red, and Mg²⁺ ion in green. **A** | Binuclear site in Chain A of *ykoY*-aptamer showing Cd(II) binding to the N7 of adenosine A41 in the B-site, bridge through coordination to the phosphate backbone to the A-site bound Cd(II). **B** | Trinuclear site in Chain B of *ykoY*-aptamer. Uracil (U44) bridges the three Cd ions through coordination to O7 and O8. **C** | Binuclear site in *ykoY^{nlx}* aptamer demonstrating heptacoordinate binding to Cd(II) in B-site. **D** | Binuclear site in *ykoY^{mntP}* aptamer showing solvent exposed Mg²⁺ ion bound to the A-site and heptacoordinate Cd(II) in the B-site. Adapted with permission from (Bachas & Ferré-D'Amaré, 2018)

Transition Metals: Second and Third Row

Selected structures of nucleic acids with second- and third-row transition metals are shown in **Table 6.3**. Because of the large number of new structures containing platinum-nucleic acid adducts, these are displayed separately in **Table 6.4**.

Table 6.3. Nucleic acid structures with second and third row transition metals, lead, and terbium.

	PDB Description ^a	Type	PDB	R(Å)	Ref.
Silver	Ag(I)-modified AT DNA oligonucleotide	DNA	2KE8	NMR	(Johannsen et al., 2010)
	refined structure silver(I)-modified DNA	DNA	2M54	NMR	(Kumbhar et al., 2013)
	RNA hybrid duplex w/ C-Ag(I)-C base pair	RNA	5AY2	1.30	(Kondo et al., 2015)
	DNA duplex w/ C-Ag(I)-C base pair	DNA	2RVP	NMR	(Dairaku et al., 2016)
	Ag(I) array in DNA oligonucleotide	DNA	5IX7	1.40	(Kondo, Tada, et al., 2017)
	DNA duplex w/ T-Ag(I)-T base pair	DNA	5XUV	1.90	(Kondo, Sugawara, et al., 2017)
	DNA containing Ag(I)-mediated G:G and C:C base pair	DNA	5XJZ	0.98	(H. Liu, Shen, et al., 2017)
	fluorescent 8 Ag Cluster in DNA	DNA	6NIZ	0.93	(Huard et al., 2019)
Ruthenium	DNA-stabilized 16 Ag cluster	DNA	6JR4	1.80	(Cerretani et al., 2019)
	Ru hexamine-soaked RNA duplex	RNA	1O3Z	2.65	(Ennifar et al., 2003)
Rhodium	Rhodium Complex Bound to an Adenosine-Adenosine DNA Mismatch	DNA	3GSI	1.80	(Zeglis et al., 2009)
	RH(BPY)2CHRYSI complexed to mismatched DNA	DNA	2OII	1.10	(Pierre et al., 2007)
Iridium	T-box riboswitch complex w/ tRNA-Gly	RNA	6PMO	2.66	(S. Li et al., 2019)
	RNA Aptamer-Ir(hexammine) soaked	RNA	6E80	2.90	(Sjekloća & Ferré-D'Amaré, 2019)
	RNA aptamer in complex with DFHO, iridium hexammine soak	RNA	5BJP	2.51	(Warner et al., 2017)
Osmium	TTP riboswitch w/ regulatory ligand	RNA	2CKY	2.90	(Thore, 2006)
	metal-binding sites in catalytic domain of RNase P	RNA	3DHS	3.60	(Kazantsev et al., 2009)
Gold	RNA subunit of Ribonuclease P	RNA	2A2E	3.85	(Torres-Larios et al., 2005)
	7SK RNA hairpin Au(I) derivative	RNA	5LYS	2.32	(Martinez-Zapien et al., 2017)
Mercury	AuCl ₃ soaked RNA duplex	RNA	2OIJ	2.31	(Ennifar et al., 2003)
	DNA-transcription factor	Protein/ DNA	4AUW	2.90	(Textor et al., 2007)
	metallo DNA duplex	DNA	2RT8	NMR	(Yamaguchi et al., 2014)
	metallo-DNA duplex w/ T-Hg(II)-T base pair	DNA	4L24	2.70	(Kondo et al., 2014)
	DNA duplex complex w/ Hg(II) and Sr(II)	DNA	5GSK	1.05	(H. Liu, Cai, et al., 2017)
	T-Hg(II)-T pair containing DNA duplex	DNA	5WSR	1.50	(H. Liu, Cai, et al., 2017)
	C-Hg(II)-T pair containing DNA duplex	DNA	5WSQ	1.05	(H. Liu, Cai, et al., 2017)
	two (N3)T-Hg(II)-(N3)C base pairs (major product)	DNA	6FY6	NMR	(O. P. Schmidt et al., 2019)
(minor product)	DNA	6FY7	NMR	(O. P. Schmidt et al., 2019)	
Lead	DNA helical wire containing Hg(II)	DNA	6IUE	1.90	(Ono et al., 2019)
	DNA quadruplex	DNA	6A85	1.45	(H. Liu et al., 2018)
Terbium	DNAzyme bound to Pb(II)	Protein/ DNA	5XM8	2.55	(H. Liu, Yu, et al., 2017)
	Octameric RNA duplex soaked in terbium(III)chloride	RNA	4U47	1.95	(Schaffer et al., 2016)

^a Structures from Protein Data Bank (Berman et al., 2000) deposited since 2003. Selected structures include direct metal-nucleic acid coordination. Some lower- resolution or redundant structures excluded.

Molybdenum, Ruthenium, Rhodium, Palladium

No nucleic acid structures with directly bound Mo or Pd are found in the databases. Outer-sphere $[\text{Ru}(\text{NH}_3)_6]^{3+}$ and $[\text{Ir}(\text{NH}_3)_6]^{3+}$ interactions are observed when these exchange-inert complexes, like $[\text{Co}(\text{NH}_3)_6]^{3+}$ are used for phasing (Batey & Kieft, 2016; Ennifar et al., 2003). Another outer sphere complex of $\Delta\text{-Rh}(\text{bpy})_2(\text{chrysi})^{3+}$ (chrysi = 5,6-chrysenequinone diimine) provides an example of metalloinsertion at a mismatch site in the DNA duplex (Zeglis et al., 2009).

The anticancer Ru(III) compounds NAMI-A ($(\text{ImH})[\text{trans-RuCl}_4(\text{dmsO-S})(\text{Im})]$, Im = imidazole) and KP1019/1339 (KP1019 = $(\text{IndH})[\text{trans-RuCl}_4(\text{Ind})_2]$, Ind = indazole; KP1339 = $\text{Na}[\text{trans-RuCl}_4(\text{Ind})_2]$) undergo exchange of Cl^- and DMSO ligands to bind biomolecules, and have been subjects of many studies (Alessio & Messori, 2019; Brabec & Kasparkova, 2018). These compounds form Ru-nucleic acid complexes, predominantly through Ru-guanine N7 coordination. Studies in *S. cerevisiae* found Ru accumulation on ribosomal RNA after in-cell treatment (Hostetter et al., 2011). However, the efficacy of these compounds as anti-cancer agents may be through protein-dependent interactions (Alessio & Messori, 2019).

Silver

Ag(I) binds to N3 of cytosine and can form linear metal-mediated base pairs similar to Hg(II). Ag(I)-mediated base pairs have been shown to stabilize C:C and G:G mismatches in duplex structures (Johannsen et al., 2010; H. Liu, Shen, et al., 2017). As an example, an RNA duplex structure containing two C:C mismatches show Ag(I) centered between the two nucleobases in a linear fashion, with a distance of 2.2–2.3 Å to N3 of the two cytosines. The C–Ag(I)–C base pairing distorts the propeller angle between the nucleobases from the non-metal structure (**Figure 6.13**) (Kondo et al., 2015).

Ag(I)-mediated base pairing has been extensively studied in development of metal-DNA based sensors and nanodevices. High resolution structures of an Ag(I)-DNA nanowire consisting of a DNA dodecamer duplex (d(GGACTCGACTCC)) containing a 5' overhang showed complete Ag(I)-mediated base pairing between the duplex at each nucleotide position (PDB 5IX7). The distance between adjacent silver ions was found to be between 3.2–3.4 Å (Kondo, Tada, et al., 2017).

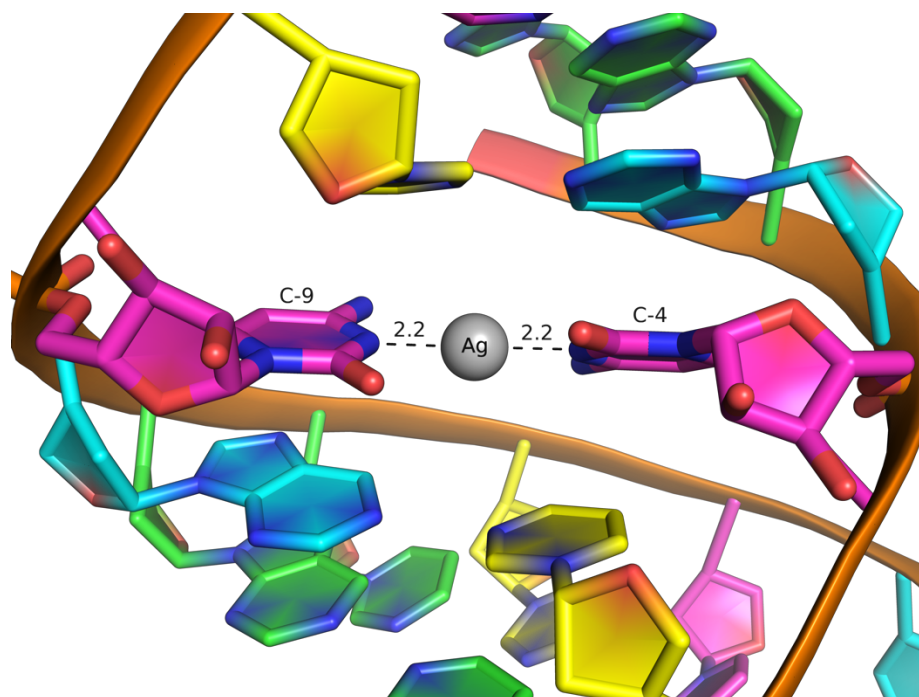


Figure 6.13. Crystal structure of RNA duplex containing C-Ag(I)-C base pair (rendered from PDB 5AY2, 1.30 Å). Ag(I) coordinates to the N3 of C-9 and C-4 and distorts the propeller twist angle along the N3-Ag-N3 bond (-29° to -27°) from the canonical Watson-Crick base pair angle of -12° in RNA duplexes.

Platinum and Palladium

Ongoing interest in Pt(II) anticancer compounds fuels frequent structure-based investigations, which have recently included polymerase-nucleic acid complexes as well as new RNA-Pt structures (**Table 6.4**). Of note, PtCl_4 (Pt(IV)) along with Os and W compounds are common reagents introduced into crystallization for heavy-metal phasing protocols and structures using those reagents are not described here.

Platinum

Several new structures of Pt(II)-bound nucleic acids have appeared that contain the products of binding anti-tumor compounds such as cisplatin, oxaliplatin, and phenanthriplatin to DNA duplexes, alone and also in complexes with several polymerases and other nucleic acid-binding proteins (**Table 6.4**). Many of the DNA structures are designed to have Pt(II) bound to the expected N7 imino ligands of G or G-G sites. New DNA structures with $[(\text{NH}_3)_2\text{Pt}]^{2+}$ (Todd & Lippard, 2010b) as well as monofunctional (Baruah et al., 2005; Komeda et al., 2006; Lovejoy et al., 2008) and non-coordinating Pt(II) compounds (Mazumdar et al., 2009; Melnikov et al., 2016) reinforce

their influence on local DNA conformation. NMR-derived structure studies also report on the influence of oxaliplatin-derived [DACH-Pt]²⁺ adducts on flexibility in particular 5' to the adduct site (Y. Wu et al., 2004).

Human polymerases η and κ are able to perform efficient translesion synthesis across platinated DNA substrates, and so their structures in complex with Pt-DNA adducts are of interest. A series of structures of Pol η with platinated DNA in the polymerase active site shows how the polymerase can accommodate and insert normal complementary bases across Pt(II)-DNA adduct sites. Structures of Pol η with DNA-Pt adducts derived from cisplatin (1,2-d(GG) (Alt et al., 2007; Ummat et al., 2012; Zhao et al., 2012) and 1,3-d(GTG) (Reißner et al., 2010) adducts), oxaliplatin (Warner et al., 2017), and the mononuclear phenanthriplatin (Gregory et al., 2014) have appeared (**Table 6.4**). Structures of platinated DNA templates complexed to archaeal polymerase Dpo4 (Wong et al., 2010), also efficient at bypass synthesis, have also appeared, as well as human Pol κ with cisplatin-derived DNA adducts (Ouzon-Shubeita et al., 2019).

While human Pol β will also perform bypass synthesis, it is far less efficient than with Pols η and κ . Crystal structures of Pol β in complex with cisplatin-platinated DNA templates provide some information about distortions of the protein active site caused by the Pt-ligand adducts (Koag et al., 2014). A newly deposited Pol β structure shows misincorporation of A across from a cisplatin-derived G-G DNA adduct (PDB 6U2O).

The 2.5 Å crystal structure of DNA Pol b complexed to a new monofunctional platinum-carbazole conjugate, carbazoleplatin, revealed both the monoplating of the N7 of a guanine (G) base and the intercalation of the carbazole ligand into neighboring G:C base pairs, causing a minor distortion of the DNA helix and remaining upstream of the bound polymerase (**Figure 6.14**) (Cheun et al., 2018). The structure also shows hydrogen bonding interactions of a Pt-aqua ligand to oxygen of a neighboring phosphodiester group.

RNA Pol II stalls at Pt(II) adducts on DNA, underlying transcription-coupled repair. Unlike other polymerases, Pol II does not appear to allow Pt-DNA adduct sites into the polymerase active site, causing translocation inhibition. This is observed in the structure of *S. cerevisiae* RNA Pol II in complex with a cisplatin-induced lesion on template DNA that is upstream of the polymerase, and the report discusses apparent inability to force the Pt-DNA adduct into the active site (Damsma et al., 2007).

The damage-recognition proteins involved in nucleotide excision repair (NER) include XPA, whose yeast homologue is Rad14. A structure of Rad24 bound to cisplatin-treated DNA shows how the protein dimer is able to induce an acute bend into the major groove of the lesion site, which in this case is towards the $(\text{NH}_3)_3\text{Pt}(\text{II})$ moiety (Koch et al., 2015).

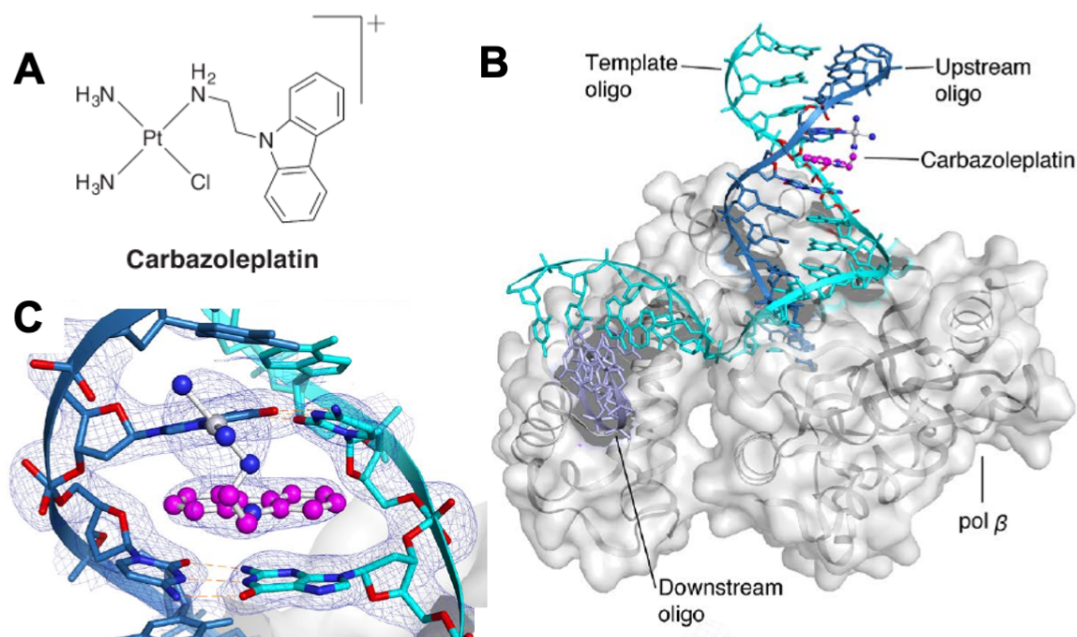


Figure 6.14. The 2.5 Å crystal structure of DNA Pol β complexed to monofunctional platinum-carbazole conjugate (PDB 5HHI). **A** | carbazoleplatin structure. **B** | DNA Pol β stalled on DNA template bound by a monofunctional carbazoleplatin showing both the monofunctional binding at G N7 and **C** | Intercalation of the carbazole ligand into neighboring G:C base pairs. Adapted with permission from (Cheun et al., 2018)

Two structures that do not contain a direct Pt-nucleic acid bond but are stabilized in DNA by their extensive Pt ligand interactions are noted here for interest. The aromatic Pt(II) ligands in the nonplanar structure of the new Pt(II) compound $[\text{Pt}(\text{H}_2\text{bapbpy})](\text{PF}_6)_2$ ($\text{H}_2\text{bapbpy} = \text{N}-(6-(6-(\text{pyridin-2-ylamino})\text{pyridin-2-yl})\text{pyridin-2-yl})\text{pyridin-2-amine}$) stabilize DNA 4-way junctions through extensive stacking interactions (van Rixel et al., 2019). Also of interest is a Pt(II)-modified etoposide-derivative, etoplatin. Etoposide inhibits human topoisomerase II through base stacking with a tetracyclic aglycone moiety and additional pendant ring, and additional interactions with the bound protein that block activity. An appended Pt(II) in etoplatin does not bind to DNA, but is instead stabilized in a conformation that supports an additional Pt-S bond with a methionine thioether in the topoisomerase active site (Wang et al., 2017).

Table 6.4. Nucleic Acid Structures containing Pt-nucleic acid adducts.

	PDB Description ^a	Type	PDB	R(Å)	Ref.
DNA/Pt	DNA octamer D (GTseGTACAC) partially crosslinked with platinum	DNA	4H5A	1.42	(—)
	DNA octamer d(GTseGTACAC) partially crosslinked with two platinums	DNA	4I1G	1.25	(—)
	The cytotoxic [Pt(H ₂ bapbpy)] platinum complex interacting with the CGTACG hexamer	DNA	6F3C	2.30	(van Rixel et al., 2019)
	High Resolution Solution NMR Structures of Oxaliplatin-DNA Adduct	DNA	2K0U	NMR	(Bhattacharyya et al., 2011)
	High Resolution Solution NMR Structures of Oxaliplatin-DNA Adduct	DNA	2K0T	NMR	(Bhattacharyya et al., 2011)
	Duplex DNA containing a cisplatin 1,2-d(GpG) intrastrand crosslink	DNA	3LPV	1.77	(Todd & Lippard, 2010b)
	Monofunctional Platinum-DNA Adduct, <i>cis</i> -{Pt(NH ₃) ₂ (pyridine)} ²⁺ Bound to Deoxyguanosine in a Dodecamer Duplex	DNA	3CO3	2.16	(Lovejoy et al., 2008)
	A Backbone binding Platinum ‘phosphate clamp’ DNA complex	DNA	2DYW	1.13	(Komeda et al., 2006)
	Solution Structure of a Platinum-Acridine Modified Octamer	DNA	1XRW	NMR	(Baruah et al., 2005)
	DNA/Pt + Pol η	Structure of the Eukaryotic DNA Polymerase η in complex with 1,2-d(GpG)-cisplatin containing DNA	Protein/ DNA	2R8K	3.30
Structure of the Eukaryotic DNA Polymerase η in complex with 1,2-d(GpG)-cisplatin containing DNA		Protein/ DNA	2R8J	3.10	(Alt et al., 2007)
DNA polymerase η in complex with the <i>cis</i> -diammineplatinum (II) 1,3- GTG intrastrand cross-link		Protein/ DNA	2WTF	2.50	(Reißner et al., 2010)
Human DNA polymerase η inserting dCMPNPP opposite the 3'G of cisplatin crosslinked Gs (Pt-GG1).		Protein/ DNA	4DL4	2.00	(Zhao et al., 2012)
Human DNA polymerase η inserting dCMPNPP opposite the 5'G of cisplatin crosslinked Gs (Pt-GG2).		Protein/ DNA	4DL5	2.92	(Zhao et al., 2012)
Human DNA polymerase η extending primer immediately after cisplatin crosslink (Pt-GG3).		Protein/ DNA	4DL6	2.50	(Zhao et al., 2012)
Human DNA polymerase η fails to extend primer 2 nucleotide after cisplatin crosslink (Pt-GG4).		Protein/ DNA	4DL7	1.97	(Zhao et al., 2012)
Crystal structure of human DNA polymerase η in ternary complex with a cisplatin DNA adduct		Protein/ DNA	4EEY	2.32	(Ummat et al., 2012)
Human DNA polymerase η inserting dCMPNPP opposite a phenanthriplatin adducted G		Protein/ DNA	4Q8E	1.55	(Gregory et al., 2014)

Table 6.4. (continued).

	PDB Description ^a	Type	PDB	R(Å)	Ref.
	Human DNA polymerase η extending primer immediately after a phenanthriplatin adducted G	Protein/ DNA	4Q8F	2.80	(Gregory et al., 2014)
	Structure of HPol η incorporating dCTP opposite the 3-prime Pt(DACH)-GG	Protein/ DNA	6MXO	2.04	(Ouzon-Shubeita et al., 2019)
DNA/Pt + Pol β	Human DNA polymerase β inserting dCMPNPP opposite the 5'G of cisplatin crosslinked Gs (Pt-GG2)	Protein/ DNA	4TUR	2.17	(Koag et al., 2014)
	Human DNA polymerase β inserting dCMPNPP opposite the 5'G of cisplatin crosslinked Gs (Pt-GG2) with manganese in the active site	Protein/ DNA	4TUS	2.42	(Koag et al., 2014)
	Structure of human DNA polymerase β Host-Guest complexed with CBZ-platinated N7-G	Protein/ DNA	5HHI	2.52	(Cheun et al., 2018)
	Structure of human DNA polymerase β misinserting dAMPNPP opposite the 5'G of the cisplatin Pt-GG intrastrand crosslink	Protein/ DNA	6U2O	2.30	(—) ^b
DNA/Pt + Dpo4	Crystal Structure of Dpo4 in complex with DNA containing the major cisplatin lesion	Protein/ DNA	3M9O	2.00	(Wong et al., 2010)
	Crystal Structure of Dpo4 in complex with DNA containing the major cisplatin lesion	Protein/ DNA	3M9M	2.90	(Wong et al., 2010)
	Crystal Structure of Dpo4 in complex with DNA containing the major cisplatin lesion	Protein/ DNA	3M9N	1.93	(Wong et al., 2010)
DNA/Pt + Pol κ	Crystal Structure of Human DNA polymerase κ in complex with DNA containing the major cisplatin lesion	Protein/ DNA	6BRX	2.80	(Jha & Ling, 2018)
	Crystal Structure of Human DNA polymerase κ in complex with DNA containing the major cisplatin lesion	Protein/ DNA	6BS1	3.15	(Jha & Ling, 2018)
DNA/Pt + Topo-II	Structure of a Human topoisomerase II β fragment in complex with DNA and E7873S	Protein/ DNA	5GWJ	2.57	(Wang et al., 2017)
	Structure of a Human topoisomerase II β fragment in complex with DNA and E7873R	Protein/ DNA	5GWI	2.74	(Wang et al., 2017)
DNA/Pt + RNA Pol II	Cisplatin lesion containing RNA polymerase II elongation complex	Protein/ DNA/ RNA	2R7Z	3.80	(Damsma et al., 2007)
DNA/Pt + Rad14	Structure of Rad14 in complex with cisplatin containing DNA	Protein/ DNA	5A39	2.80	(Koch et al., 2015)
DNA/Pt+ Nucleosome	Nucleosome core particle modified with a cisplatin 1,3- <i>cis</i> -[Pt(NH ₃) ₂] ²⁺ -d(GpTpG) intrastrand cross-link	Protein/ DNA	3O62	3.22	(Todd & Lippard, 2010a)
	2.65 Å Crystal Structure of the Nucleosome Core Particle Assembled with a 145 bp Alpha-Satellite DNA (NCP145) Derivatized with Triamminechloroplatinum(II) Chloride	Protein/ DNA	3REI	2.65	(B. Wu et al., 2011)

Table 6.4. (continued).

	PDB Description ^a	Type	PDB	R(Å)	Ref.
	2.6 Å Crystal Structure of the Nucleosome Core Particle Assembled with a 146 bp Alpha-Satellite DNA (NCP146b) Derivatized with Oxaliplatin	Protein/ DNA	3REK	2.60	(B. Wu et al., 2011)
	2.7 Å Crystal Structure of the Nucleosome Core Particle Assembled with a 146 bp Alpha-Satellite DNA (NCP146b) Derivatized with Triamminechloroplatinum(II) Chloride	Protein/ DNA	3REL	2.70	(B. Wu et al., 2011)
	Structure of trPtNAP-NCP145	Protein/ DNA	4WU8	2.45	(Chua et al., 2015)
Pt + Ribosome	Structure of cisPtNAP-NCP145	Protein/ DNA	4WU9	2.60	(Chua et al., 2015)
	Crystal structure of the <i>Thermus thermophilus</i> 70S ribosome in complex with cisplatin (co-crystallized) and bound to mRNA and A-, P- and E-site tRNAs at 2.6 Å resolution	Protein/ RNA	5J4B	2.60	(Melnikov et al., 2016)
	Crystal structure of the <i>Thermus thermophilus</i> 70S ribosome in complex with cisplatin (soaked) and bound to mRNA and A-, P- and E-site tRNAs at 2.8 Å resolution	Protein/ RNA	5J4C	2.80	(Melnikov et al., 2016)

^a Structures from Protein Data Bank (Berman et al., 2000) deposited since 2003. Selected structures include direct metal-nucleic acid coordination. Some lower- resolution or redundant structures excluded.

^b (—), No primary publication associated with structure.

Building in complexity, several structures of 140-bp DNA bound to histones, creating artificial nucleosomes, have been solved that contain Pt(II) adducts to DNA. In an early structure, a single 1,3-GTG cisplatin adduct in synthetic 146-bp DNA was complexed with histone proteins. Like with other histone complexes the DNA structure was not highly resolved in all regions, but a model was reliably built that found that the DNA-bound Pt was located internal to the nucleosome and not solvent-exposed (Todd & Lippard, 2010a). By contrast, a series of Pt-nucleosome structures formed by incubating crystallized nucleosomes in relatively high concentrations of [(NH₃)₃PtCl], cisplatin, and oxaliplatin resolved many Pt-DNA adducts that were comparable to those predicted by mapping non-nucleosome DNA treated with the same compounds (O. P. Schmidt et al., 2019). The best-resolved structure of this group included monofunctional adducts to a high number of guanine N7 positions on the nucleosome-bound DNA. A high correlation was found between accessible surface area and Pt occupancy at these positions (B. Wu et al., 2011). The latter study also found a correlation between transition metal sites and

monofunctional Pt(II) adduct locations. It was again observed that the bifunctional cisplatin-derived adduct created disorder and lack of resolution about the Pt within cisplatin-treated nucleosomes.

Finally, structures of nucleosomes containing monofunctional Pt compounds with intercalating naphthalamide ligands have been reported (Chua et al., 2015). Nucleosome crystals were incubated with the Pt compounds and a balance found between increasing occupancy and sufficient resolution. The resulting structures showed N7-G coordination of Pt(II) and intercalation of the naphthalamide rings at particularly bent regions of the nucleosome-bound DNA, along with several examples of putative hydrogen-bonding interactions between Pt-amine ligands and the DNA.

By contrast with DNA, much less is known about the interactions of Pt complexes with RNA. However, a very interesting pair of structures of Pt adducts on *T. thermophilus* ribosomes was recently reported (**Figure 6.15**) (Melnikov et al., 2016). In this study, 70S ribosomes in complex with mRNA and tRNA were co-crystallized in the presence of cisplatin. An additional structure was obtained from crystals soaked in solution with cisplatin; both cases were $>100 \mu\text{M}$ cisplatin in solution. Pt adduct formation on the >3000 nucleotides of RNA was surprisingly selective, with only 8 Pt-RNA adducts resolved in the co-crystallized structure. Interestingly, all but one of these were monofunctional adducts containing one Pt-purine N7 bond, and one remaining Cl ligand on Pt. The lack of diadduct formation may be a result of the relatively high $[\text{Cl}^-]$, or relatively short incubation times. Of the 8 Pt-RNA adducts, 3 were bound to adenine N7 positions of 5' A-G pairs, with hydrogen bonding between a Pt-ammine ligand and the neighboring G O6 position. The other 5 Pt(II) were bound to guanine N7 sites with additional hydrogen bonding to neighboring phosphodiester oxygens. The Pt-soaked crystals showed only the adenine-bound Pt(II), suggesting a kinetic preference for these sites. All but one of the Pt-RNA adducts were found in non-base paired regions of the complex RNA structure, and all were also superimposable on sites where $[\text{Mg}(\text{OH}_2)_5]^{2+}$ ions had been previously modeled bound directly to the purine N7 positions in the absence of Pt(II).

Because of the importance of exchange kinetics and competing platination targets, it is of interest to compare predicted Pt-bound sites from biomolecules treated *in vitro* and *in-cell*. Interestingly, mapping of ribosomal RNA isolated from cisplatin-treated *S. cerevisiae* shows adducts in some regions similar to those identified by *ex vivo*

crystallography, but not at the same molecular sites (Plakos & DeRose, 2017). This suggests possible in-cell effects including aquation kinetics. It is also possible that the *in vivo*-treated RNA contains more bifunctional adducts. Additional new reports regarding Pt-ribosome interactions include amino-acid derived Pt(II) compounds that influence Pt-RNA adduct location (Dremann & Chow, 2016; Rijal et al., 2014). Taken together, it is concluded that Pt(II) coordination to RNA structures occurs in noncanonical regions, in sites likely occupied by other cations, and may be affected by in-cell conditions.

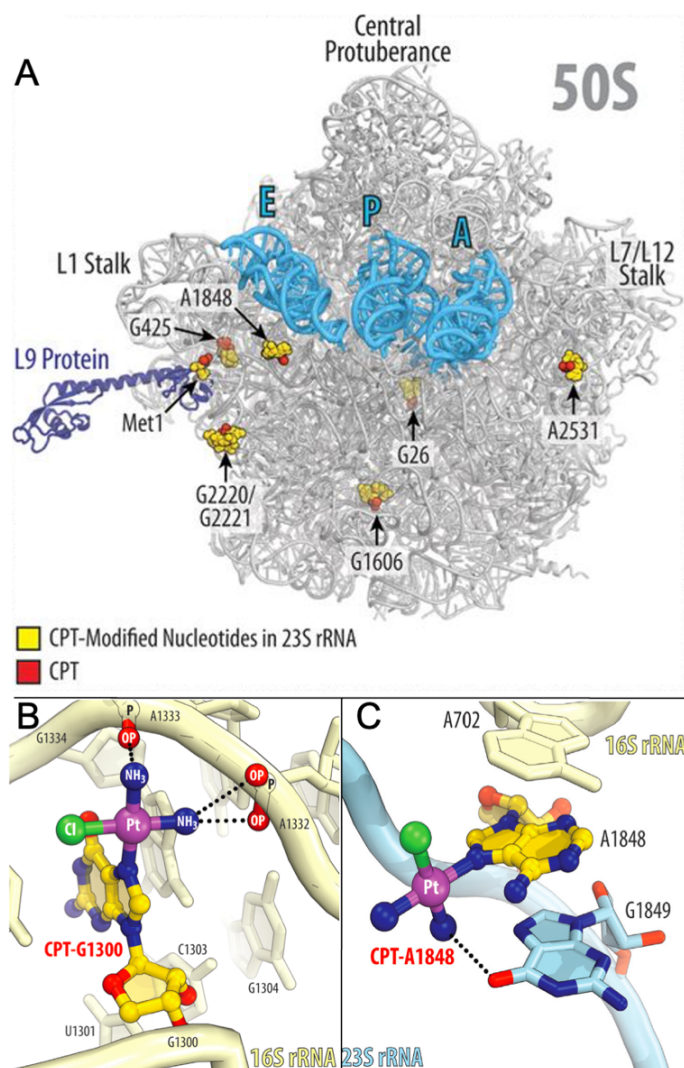


Figure 6.15. Pt-bound sites observed in 2.8 Å structure of 50S ribosome from *T. Thermophilus* in complex with mRNA and tRNAs, crystallized with exposure to cisplatin. All sites are modeled as monofunctional $[(\text{NH}_3)_2\text{PtCl}]^+$ adducts with exception of one G2220/G2221 diadduct. **A** | Modified nucleotides (yellow) bound by Pt ions (red) in 50S subunit. **B** | Characteristic monofunctional N7-G adduct with ammine ligand hydrogen bonding to backbone phosphodiester oxygens. **C** | Characteristic 5'A-G coordination motif includes ammine ligand hydrogen bonding to O6 of 3'G. Adapted with permission from (Melnikov et al., 2016)

Palladium

Palladium has similar coordination properties to those of platinum, but with faster exchange kinetics, leading to more facile ligand substitutions and isomerization.

Examples of recent work include biophysical characterization of square-planar Pd(II) compounds that associate with nucleic acids (N. Bandyopadhyay et al., 2017; Patel et al., 2014). More recent Pd-nucleic acid interactions have appeared mainly in the area of materials science, where DNA is used to template nanoparticles including Pd-oxide catalysts for Sonogashira reaction (Camacho et al., 2017) and Pd nanostructures (Satyavolu et al., 2016). A DNA aptamer selected for binding to Pd²⁺ in aqueous solution against a graphene oxide support found an aptamer-Pd²⁺ K_D of ~4 mM (20 mM Na⁺) and >2-fold binding selectivity against Mg²⁺ or Pt²⁺ (Cho et al., 2015).

Tungsten, Rhenium, Iridium, Osmium, Gold, Mercury

While these metals are not often associated with biological processes, they are of interest for sensing and materials applications and their interactions with nucleic acids have been explored (Kanellis & Dos Remedios, 2018; W. Xu et al., 2019; Zhou et al., 2017). In addition to canonical purine N7 coordination, binding to deprotonated amino ligands of pyrimidines is also observed for these larger metals (see below).

Tungsten, Rhenium, Iridium, Osmium

As noted above, [Ir(NH₃)₆]³⁺ is used for phasing purposes in nucleic acid crystallography, (Batey & Kieft, 2016) and Os(III)-ammine compounds are similarly used (Kazantsev et al., 2009; Thore, 2006; Torres-Larios et al., 2005). Although clusters of W or Re are used in protein crystallography, no nucleic acid structures have been reported.

It has previously been shown that osmium tetroxide undergoes *cis*-addition across the 5,6-double bond of thymine and uracil to form an osmate ester, and that addition of pyridine was found to greatly increase the rate of reaction possibly through formation of OsO₄ mono or bis(pyridine) intermediate (M. Schroeder, 1980). Recently, this reaction was used to map accessible uracil nucleobases in three different structured RNAs (Jing Zhang et al., 2017). Addition of osmium tetroxide (OsO₄) results in stable osmate adducts assumed to be bis(pyridine)Os(VI)O₄ that block reverse transcription, generating truncated cDNAs whose sequences identify accessible uracil in the folded RNAs.

Gold

Coordination of Au(I) to N7 of guanine was observed in an Au(I) derivative structure of the hairpin domain in the non-coding regulator RNA, 7SK. Au(I) was observed in the flexible region of the hairpin with a distance of 2.4–3.0 Å between the N7 and Au(I) ion (Martinez-Zapien et al., 2017).

One Au(III)-RNA structure has been reported from a crystallographic study comparing metal binding to HIV-1 RNA duplexes. Unexpectedly, Au(III) was observed to bind between the N3 of cytosine and deprotonated N1 of guanine in the 23-nt RNA fragment, forming a C–Au(III)–G metal-mediated base pair (Fig. 6.16), similar to Hg(II) (Ennifar et al., 2003). It should be noted that in both of these examples, occupancy around the gold ion was quite low, <40%.

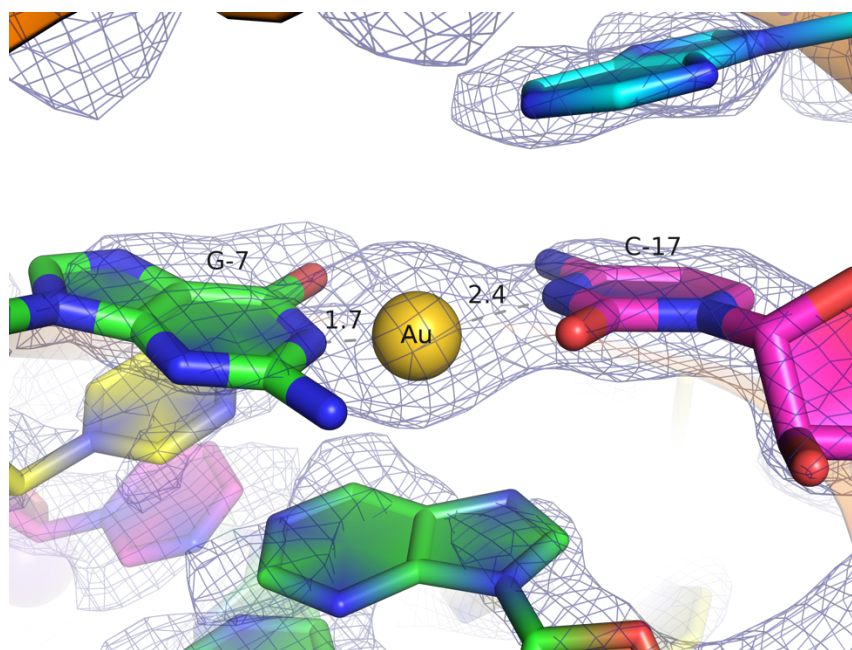


Figure 6.16. Crystal structure of HIV-1 Subtype B DNA duplex bound to Au(III) (rendered from PDB 2OIJ, 2.31 Å) with $2f_o - f_c$ density maps contoured at 1.5σ (blue). The Au(III) ion interacts with the N3 of cytosine C-17 and the N7 of deprotonated guanine G-7.

Mercury

Hg(II) shows affinity for thymine at the N3 position and can form metal-mediated base pairs in duplex structures at T:T and C:T mismatch pairs (Yamaguchi et al., 2014).

Consecutive T-Hg(II)-T base pairs were reported in DNA dodecamer d(CGCGATTTTCGCG) containing tandem T:T mismatch pairs, which adopted a B-form conformation when in complex with Hg(II). The two neighboring T-Hg(II)-T base pairs

are thought to stabilize the B-form structure through Hg(II)-Hg(II) metallophilic interactions, based on the relatively short distance (3.3 Å) between the two Hg(II) ions (Kondo et al., 2014). The pyrimidine-pyrimidine proximity in Hg-mediated base pairs has also been captured by solution NMR spectroscopy (Ono et al., 2011). In addition to DNA helices, NMR evidence for mercury-mediated U-Hg(II)-U base pairs in RNA has been reported (Johannsen et al., 2008).

In addition to N3-Hg(II)-N3, alternate binding modes for T-Hg(II)-T and C-Hg(II)-T base pairs have been observed in DNA duplex structures. In one such structure (**Figure 6.17**), Hg(II) was observed to bind to the deprotonated exocyclic N4 of cytosine and the N3 of thymine. A well-ordered water molecule, 2.7 and 2.8 Å from the O2 of C and T respectively, is thought to additionally stabilize base-pairing through H-bonding (H. Liu, Cai, et al., 2017).

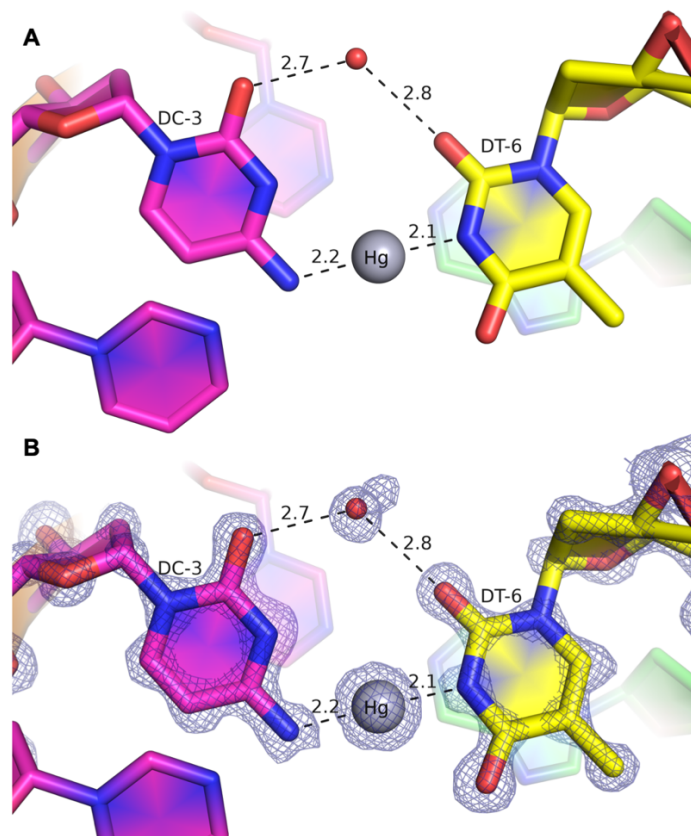


Figure 6.17. DNA duplex containing unexpected C-Hg(II)-T metallobase pairing. **A** | Crystal structure of (rendered from PDB 5WSQ, 1.05 Å) showing a water molecule (red) stabilizes the N3-Hg(II)-N3 base-pairing through H-bonding between the O2 of cytosine DC-3 and thymine DT-6. **B** | Same structure showing the $2f_c-f_c$ density maps contoured at 1.5σ (blue).

Lead

Interactions between lead and nucleic acids have been studied in particular in context of RNA- and DNA-enzyme activities, leading to Pb(II)-selective sensors. The early discovery that tRNA underwent Pb(II)-specific cleavage (by “plumbous ions”) (Werner et al., 1976) and the RNA “leadzyme” created by *in vitro* selection for cleavage in the presence of lead (Pan & Uhlenbeck, 1992) laid groundwork for further investigations of Pb(II)- specific activities, including in the well-characterized 8–17 DNAzyme where Pb(II) was found to support a 200-fold increase in the rate of RNA cleavage compared to Zn(II) and Mg(II) (H.-K. Kim et al., 2007; Mazumdar et al., 2009). This specificity forms the basis for innovative and effective nucleic acid-based Pb-sensing methods (Lake et al., 2019). A crystal structure of the Pb-bound 8–17 DNAzyme active site shows Pb(II) coordinated to the O6 of G6 guanine at a distance of 3.2 Å and to a catalytic water molecule at a distance of 2.5 Å. Their influence on the in-line arrangement of the RNA substrate suggests that Pb(II) may act indirectly, by orienting and activating the coordinated water molecule to serve as a general acid (H. Liu, Yu, et al., 2017).

In a high-resolution DNA quadruplex structures (5'-AGAGAGATGGGTGCGTT-3'), Pb(II) was found between G13- and C14-tetrads bound to the four O6 atoms of the G-tetrad and four water molecules with an octahedral geometry (**Figure 6.18**). In comparison to Na⁺, the average distance between Pb(II) ion and the four O6 atoms (2.8 Å) and the water molecules (2.5 Å) is significantly shorter, suggesting stronger binding affinity (H. Liu, Cai, et al., 2017).

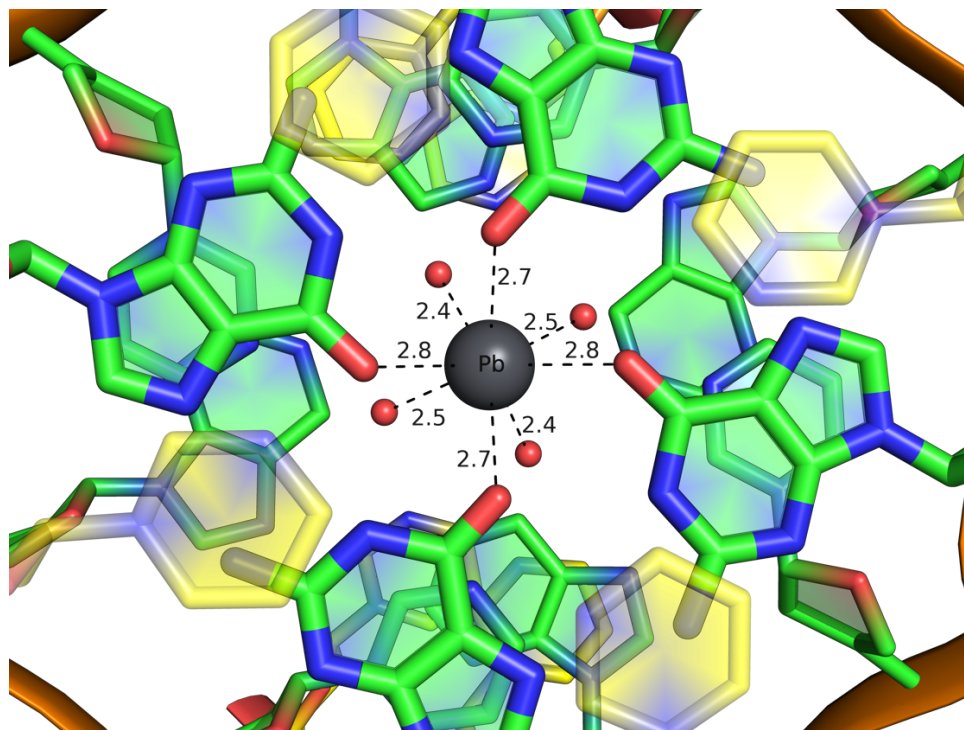


Figure 6.18. High-resolution crystal structure of Pb(II) bound to DNA quadruplex (rendered from PDB 6A85, 1.45 Å). The Pb(II) ion was found between the G13 and C14 tetrad, coordinated to the four O6 atoms of the G13 tetrad and four water molecules (red) with an octahedral geometry.

Lanthanides

Recent studies of the trivalent lanthanides with nucleic acids have focused on sensing applications and the properties of sensitized luminescence with nucleobases (Xue et al., 2018; Zhou et al., 2017). One crystal structure of a Tb(III) bound octameric RNA duplex reveals Tb(III) coordinated to the phosphate backbone within the major groove. Tb^{III} was found octahedrally coordinated to two oxygen atoms of the phosphate backbone with Tb(III)-O distances of 2.6 Å and six additional water molecules with Tb(III)-O distances between 2.3–2.9 Å (**Figure 6.19**). In comparison to structures of other divalent metal ions (Ca(II), Mn(II), Co(II), Cu(II), Sr(II)) in complex with the octameric RNA duplex, Tb(III) was found to occupy a separate site further away from the duplex center showing no coordination to nucleobases (Schaffer et al., 2016).

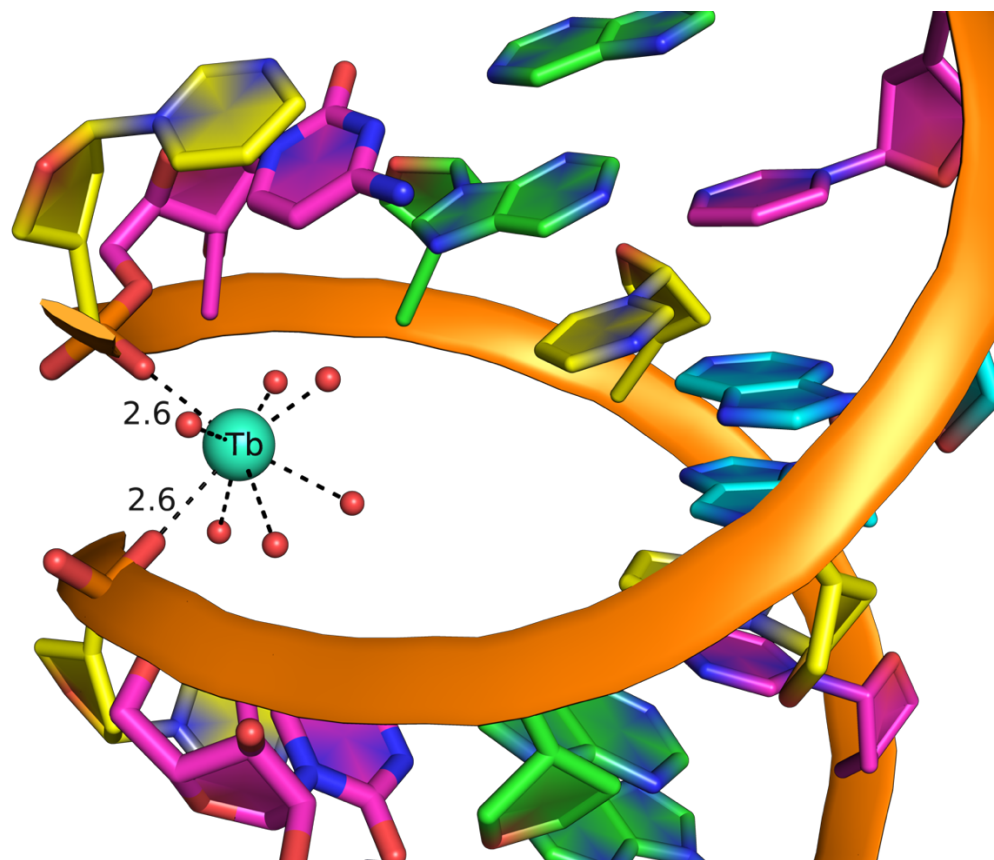


Figure 6.19. Crystal structure of octameric RNA duplex in complex with Tb(III) (rendered from PDB 4U47, 1.95 Å). The Tb(III) ion is coordinated to phosphate oxygens of the major groove and six additional water molecules (red).

Concluding Remarks

The topic of metal-nucleic acid interactions is significant to a breadth of areas including cellular biology, therapeutics, metal sensors, materials, and questions about early-earth environments. The aim of this Review has been to provide an update and extension to prior thorough reviews (V.J. DeRose et al., 2003) on metal interactions with nucleic acids. Introductory sections (and multiple additional reviews cited therein) emphasize that direct coordination of a metal ion to a nucleic acid ligand takes place in context of complex electrostatics created by RNA and DNA biopolymers. An array of cation populations with degrees of localization and hydration is expected around oligonucleotides, with evidence for these populations arising from a variety of biophysical, spectroscopic and computational sources. In that context, the main focus of this review is on metal sites in DNA and RNA that have been characterized by X-ray crystallography. Reported structures from different metal groups are provided in **Tables**

6.1–6.4, and selected examples are emphasized in the text and figures. The challenge of locating and identifying cations in large nucleic acid complexes can be appreciated, and readers are encouraged to monitor continuing improvements in technique and analysis when assessing reports for low-*Z* cations such as Mg²⁺, Na⁺ and K⁺. A number of high-resolution structures, especially with higher-*Z* transition metals, are highlighted. A particularly high number of nucleic acid structures containing Pt have been reported since 2003 and are outlined in a separate **Table 6.4**. Looking forward, exciting discoveries such as recent reports of iron-dependent riboswitches (S. Bandyopadhyay et al., 2021; J. Xu & Cotruvo, 2020) promise new horizons for this rich arena of metals and nucleic acids.

Bridge to Chapter VII

This chapter provided an updated review on metal interactions with nucleic acids, highlighting notable examples from the literature for metals with reported nucleic acid structures.

The final chapter will briefly summarize the workss and conclusions from Chapter I-VII and discuss current and future directions.

CHAPTER VII: CONCLUDING REMARKS

Summary

Platinum(II)-based chemotherapeutics represent an important classes of anti-proliferative compounds which have been influential in the advancement of our understanding and treatment of cancer and continue to play an important role in chemotherapy regimens, nearly a half century after the introduction of cisplatin. The primary aim of this work is to provide insight on the complex relationships between Pt(II)-based chemotherapeutics, and disruptions of the nucleolus and ribosome biogenesis through the development and application of analytical chemistry, chemical biology, and bioinformatics techniques.

Chapter I provides an introductory background on the significance and current understanding of Pt(II)-based chemotherapeutics, including clinical limitations and differences between currently used Pt(II) chemotherapeutics. This chapter also provides background on ribosome biogenesis and nucleolus in the context of Pt(II)-based chemotherapeutics, highlighting the potential as novel chemotherapeutic target.

Chapter II sought to investigate the finding that, unlike cisplatin, oxaliplatin induces cell death through disruption of ribosome biogenesis (Bruno et al., 2017). By investigating the structural and chemical components of Pt(II) compounds necessary for the induction of nucleolar stress—a hallmark for disruption of ribosome biogenesis—we were able to conclude that induction of nucleolar stress was highly influenced by the structure of the nonlabile ligands.

In chapter III we shifted focus to a monofunctional Pt(II) compound, phenanthriplatin, which was also identified to induce nucleolar stress and cause cell death through disruption of ribosome biogenesis (Bruno et al., 2017). Hypothesizing that fundamental differences between monofunctional Pt(II) compounds like phenanthriplatin, and canonical Pt(II) compounds such as oxaliplatin, may reveal structural or chemical properties unique to nucleolar stress, we applied our immunofluorescence-based assay to quantify relocalization of NPM1 among a subset of monofunctional Pt(II) compounds. Ultimately, we concluded that phenanthriplatin and oxaliplatin likely induce nucleolar stress through unique mechanisms.

Previous studies quantifying NPM1 relocalization induced by Pt(II) compounds revealed differences in the robustness of nucleolar stress. In Chapter IV we examined these differences in NPM1 relocalization through a time-dependent study and examined related biological effects of these compounds. We were able to conclude that significant differences in both the kinetics and degree of NPM1 relocalization existed among stress inducing Pt(II) compounds which did not correlate with broad cellular effects, such as intracellular accumulation, DNA binding, or cytotoxicity.

In Chapter V, we investigate a potential mechanism for oxaliplatin induced disruption of ribosome biogenesis, based on previous work demonstrating that nucleolar stress induced by oxaliplatin resulted from an inhibition of pre-rRNA synthesis. Hypothesizing that oxaliplatin may act as a Pol I inhibitor, we performed ChIP-seq occupancy assay on RNA Pol I machinery to determine if oxaliplatin directly perturbs RNA Pol I activity and elucidate a potential mechanism for disruption. In comparison to known Pol I inhibitors such as BMH-21, we were able to determine that oxaliplatin inhibits rRNA synthesis through a distinct mechanism, and likely does not directly perturb Pol I activity.

Lastly, Chapter VI reviews the interactions of metal coordination complexes with RNA, DNA, and nucleic acid-based enzymes focusing on structural evidence from NMR and x-ray crystal structure databases.

Future Directions

Although this work provides clear evidence on the differential cellular effects of Pt(II) compounds, a stronger understanding of their mechanism of action will be required to overcome limitations in efficacy and side-effect profiles. Additionally, a sufficient explanation for the disruption of ribosome biogenesis induced by a specific subset of Pt(II) compounds is still lacking.

More recent studies hypothesize that biophysical disruptions within the nucleolus may play a significant role in the mechanism of action for oxaliplatin. The biophysical properties which govern the structure and function of the nucleolus are poorly understood, and their biological implications even less so.

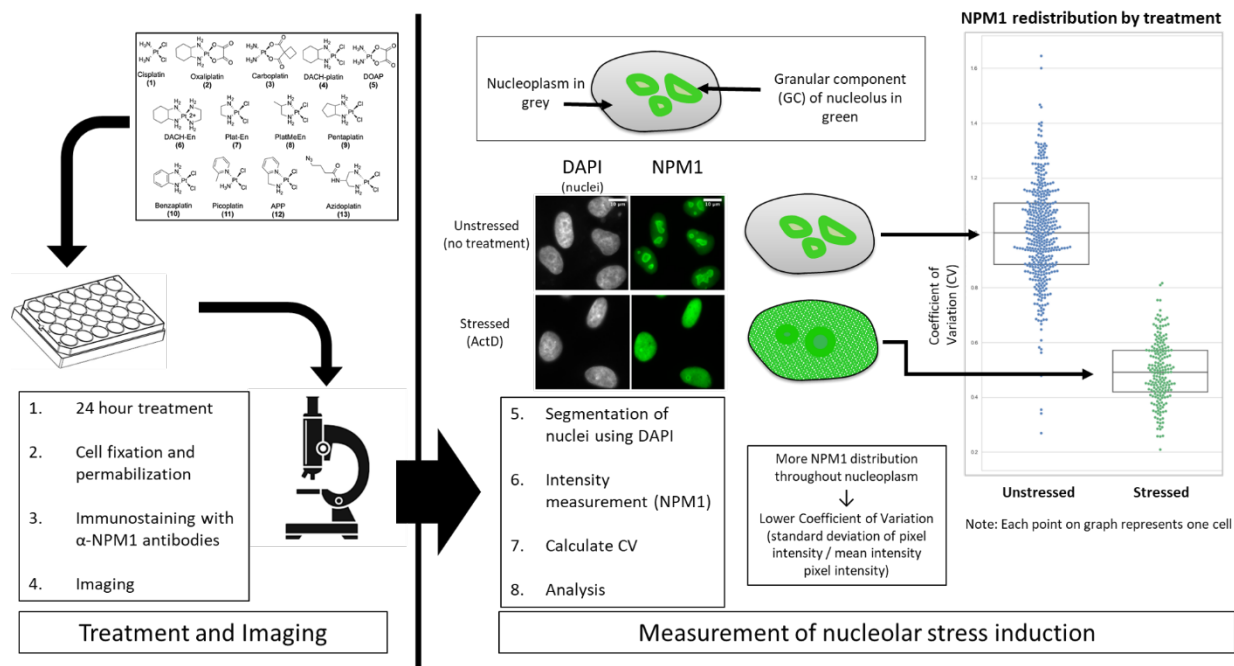
Overall, this work contributes to our understanding of the cellular effects of platinum compounds, particularly in the context of ribosome biogenesis and nucleolar

stress. Additionally, this work highlights a knowledge gap in our understanding of nucleolar structure and function, which will be necessary to overcome in order to have a stronger understand of nucleolar stress and disruption of ribosome biogenesis induced by Pt(II) compounds. Lastly, this work provides experimental tools and models which can be applied to future studies.

APPENDIX A

SUPPLEMENTARY MATERIALS FOR CHAPTER II

Supplementary Figures and Tables



Scheme A.1. NPM1 assay and quantification scheme. A549 cells were seeded on coverslips treated for 24 hours with the selected compound. Cells were fixed, permeabilized, and stained with an α -NPM1 antibody as described in Materials and Methods section. After imaging, nuclei were segmented using DAPI staining and pixel intensity from NPM1 imaging was measured. The coefficient of variation (CV, standard deviation over mean), was calculated for each nucleus, normalized to the mean CV for the no treatment control on that day, and plotted as above with each nucleus represented by one point on the plot. An average CV of 1.0 indicates no stress, whereas a lower CV (around 0.6) indicates diffusion of NPM1 throughout the nucleoplasm, a positive indicator of nucleolar stress. Treatment data sets are represented by box plots, where the center, top, and bottom lines of boxes represent the median, first and third quartile respectively.

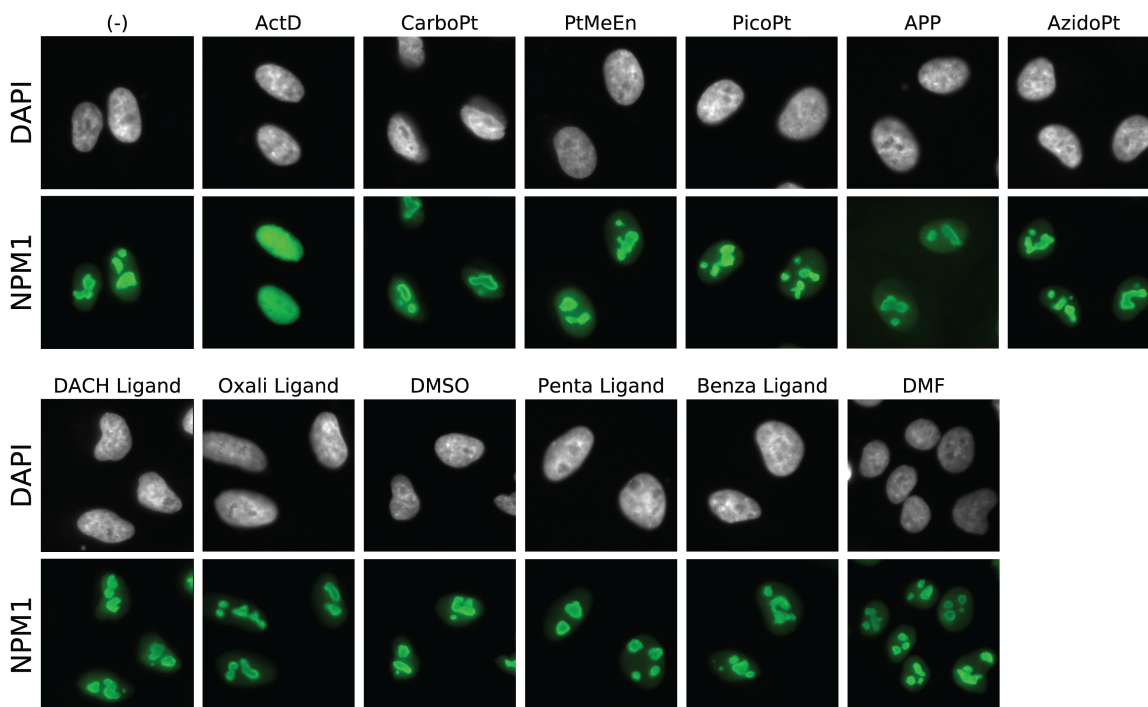


Figure A.1. Additional images for compounds tested. Top row shows negative and positive (Actinomycin D) controls, and Pt(II) compounds **3**, **8**, **11**, **12**, and **13**, — respectively CarboPt, PtMeEn, PicoPt, APP, and AzidoPt— none of which caused nucleolar stress. Bottom row shows Pt(II)-free ligands of stress-inducing Pt(II) compounds and solvents used (DMSO and DMF). Ligands alone do not induce nucleolar stress, and neither do solvents. All treatments were performed for 24 hours. Pt(II) compound and ligand treatments were conducted at 10 μM , with the exception of ActD, which was 5 nM, and **3** (CarboPt), which was 20 μM . DACP = (1*S*,2*S*)-diaminocyclopentane, *o*-PDA = *ortho*-phenylenediamine.

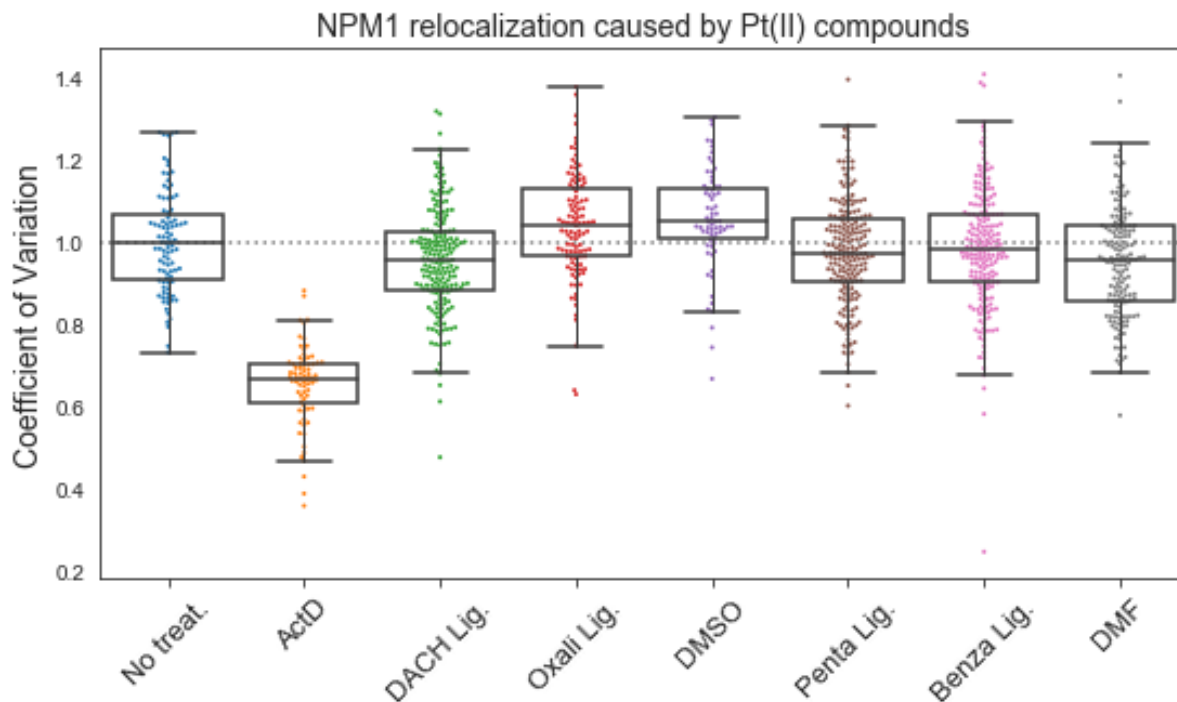


Figure A.2. Quantification of nucleolar stress induction for Pt(II)-free ligands and solvents used. CV quantification confirms that ligands alone do not induce nucleolar stress, and neither do solvents. All treatments were performed for 24 hours. Treatments were conducted at 10 μ M, with the exception of ActD, which was 5 nM. DACP = (1*S*,2*S*)-diaminocyclopentane, *o*-PDA = *ortho*-phenylenediamine. Treatment data sets are represented by standard box plots, where the center, top and bottom lines of boxes represent the median, first, and third quartile respectively. The vertical lines represent the range of data within $1.5 \times$ IQR of the lower and upper quartiles, where IQR is the interquartile range; points outside this range are considered outliers.

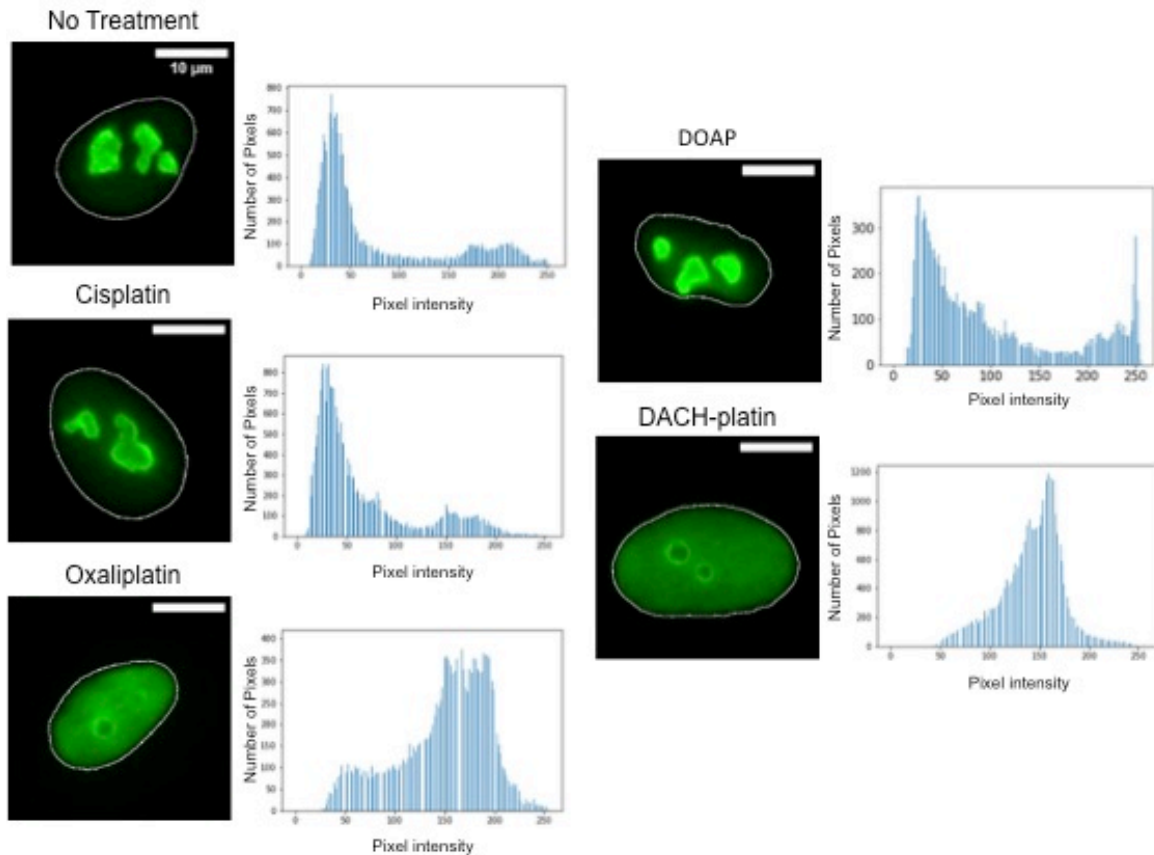


Figure A.3. Histograms showing NPM1 intensity within a single nucleus in stressed and unstressed cells. x -axis represents pixel intensity, and y -axis represents the number of pixels within a nucleus of the intensity on the x -axis. Cells not undergoing nucleolar stress have a large number of low intensity pixels and a small number of high intensity pixels, indicating NPM1 is concentrated in the granular component of the nucleolus. Cells undergoing stress have a broader distribution of pixel intensities, with the histogram skewing towards high intensity, as NPM1 has redistributed throughout the entire nucleoplasm.

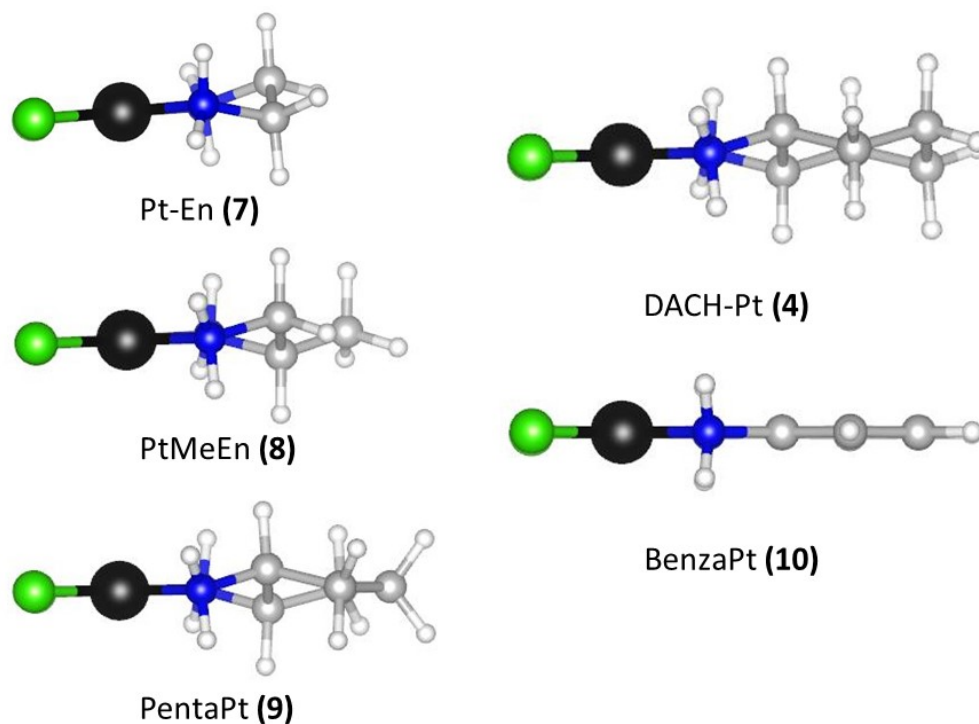


Figure A.4. DFT-optimized structures of compounds illustrating the relative size of compounds and planarity of BenzaPt, 10 relative to DACH-Pt, 4.

Table A.1. IC₅₀ values in A549 cells for selected compounds at 24 hours.

Compound	IC ₅₀ (μ M)
Oxaliplatin, 2	81.5 \pm 7.0
Cisplatin, 1	12.8 \pm 2.0
DACHplatin, 4	31.9 \pm 6.0
Pentaplatin, 9	37.5 \pm 5.0
Benzaplatin, 10	NR ^a
PlatEn, 7	46.1 \pm 6.0
PlatMeEn, 8	76.1 \pm 9.0
DOAP, 5	36.6 \pm 5.0
APP, 12	NR

^a No response, IC₅₀ value not reached at concentrations > 500 μ M

Table A.2. IC₅₀ values in A549 cells for selected compounds at 48 hours.

Compound	IC ₅₀ (μ M)
Oxaliplatin, 2	9.9 \pm 3.5
Cisplatin, 1	4.6 \pm 0.7
Benzaplatin, 10	6.9 \pm 0.7
APP, 12	36.9 \pm 4.3

Table A.3. Volume and hydrophobicity data

Compound	Volume (Å ³)	Distance (Å)	log <i>P</i>
Cisplatin, 1	19.46	3.40	-2.39 ± 0.05
PlatMeEn, 8	23.56	5.51	-1.68 ± 0.01
PlatEn, 7	21.47	4.41	-1.85 ± 0.02
APP, 12	27.66	6.21	-1.10 ± 0.06
Picoplatin, 11	27.69	6.21	(—) ^a
Pentaplatin, 9	27.85	6.21	-1.29 ± 0.03
Benzaplatin, 10	28.71	6.73	-0.92 ± 0.04
DACHplatin, 4	30.01	6.75	-0.89 ± 0.01
Carboplatin, 3	30.94	6.30	(—)
DACH-En, 6	32.41	6.72	(—)
Azidoplatin, 13	32.71	13.16	-1.20 ± 0.06
Oxaliplatin, 2	34.13	6.78	1.58 ± 0.02

^a (—), Not Measured.

Materials and Methods

Cell culture and Treatment

A549 human lung carcinoma cells (#CCL-185, American Type Culture Collection) were cultured at 37°C, 5% CO₂ in Dulbecco's Modified Eagle Medium (DMEM) supplemented with 10% Fetal Bovine Serum (FBS) and 1% antibiotic-antimycotic. Treatments were conducted on cells that had been grown for 11–25 passages to 70% confluency. Except where noted otherwise, treatments were conducted for 24 hours at 10 μM. Compounds were made into 5 mM stocks on the day of treatment in 0.9% NaCl (cisplatin), DMF (**4, 7, 8, 10, 11, 12, 13, 14**), DMSO (**5**), or water (**1, 2, 3, 6**). Stock solutions were diluted into media immediately prior to drug treatment.

Immunofluorescence

Cells to be imaged were grown on coverslips (Ted Pella product no. 260368, round glass coverslips, 10 mm diam., 0.16-0.19mm thick) as described above. After treatment, cells were washed twice with phosphate buffered saline (PBS) and fixed for 20 minutes at room temperature in 4% paraformaldehyde (PFA) in PBS. PFA was removed via aspiration and cells were then permeabilized with 0.5% Triton-X in PBS for 20 minutes at room temperature. Two 10 min blocking steps were performed with 1% bovine serum albumin (BSA) in PBST (PBS with 0.1% Tween-20). Cells were incubated for one hour in primary antibody (NPM1 Monoclonal Antibody, FC-61991, ThermoFisher, 1:200 dilution

in PBST with 1% BSA) and 1 hour in secondary antibody (Goat Anti-Mouse IgG H&L Alexa Fluor® 488, ab150113, Abcam, 1:1000 dilution in PBST with 1% BSA), with three 5 min wash steps using PBST between incubations, and were washed in the same manner again before mounting slides. Coverslips were mounted on slides with ProLong™ Diamond Antifade Mountant with DAPI (ThermoFisher) according to manufacturer's instructions.

Cytotoxicity (MTT assay)

A549 cells were seeded in 24-well plates at a density of 5×10^4 cells/mL. The following day cells were treated with 0–750 μ M of compound in DMEM supplemented with 10% FBS and antibiotic-antimycotic. 24h after treatment, compound-containing media was removed and cells washed twice with PBS. MTT in DMEM supplemented with 10% FBS and antibiotic-antimycotic was then added to cells and incubated for 3h. DMSO was used to dissolve the formazan crystals and absorbance at 595 nm was then determined using a Tecan microplate reader. Percent viability was determined by comparing to vehicle-treated control for each compound and IC₅₀ concentration calculated from triplicate measurements using the drc package in R .

Image processing and quantification

Images were taken using a HC PL Fluotar 63×/1.3 oil objective mounted on a Leica DMI8 fluorescence microscope with Leica Application Suite X software. Quantification of NPM1 relocalization was performed in an automated fashion using a Python 3 script. Images were preprocessed in ImageJ (Rueden et al., 2017; Schindelin et al., 2012) to convert the DAPI and NPM1 channels into separate 16-bit greyscale images. Between 70–225 cells were analyzed for each treatment group. Nuclei segmentation was determined with the DAPI images using Li thresholding functions in the Scikit-Image Python package (van der Walt et al., 2014). The coefficient of variation (CV) for individual nuclei, defined as the standard deviation in pixel intensity divided by the mean pixel intensity, was calculated from the NPM1 images using the SciPy Python package. All data were normalized to the no-treatment control in each experiment. NPM1 imaging results for each compound were observed on a minimum of two separate testing days. Data are represented as boxplots generated using Seaborn within Python.

Synthesis

Cisplatin used for cell treatments was purchased from Strem Chemicals. Cisplatin used as a synthetic precursor was synthesized as described below. Oxaliplatin and carboplatin were purchased from TCI. Unless otherwise noted, all other compounds were purchased from Sigma Aldrich or TCI. Picoplatin (Okada et al., 2001) and azidoplatin (Wirth et al., 2015) were synthesized as previously reported.

cis-diamminedichloroplatinum(II) (cisplatin) (1)

Cisplatin was synthesized according to previously described methods by (Dkhara, 1970) and reviewed by (J. J. Wilson & Lippard, 2014). Briefly, potassium tetrachloroplatinate (62.7 mg, 0.151 mmol, 1 eq) was dissolved in 180 μ L of water and stirred at 40°C. Potassium iodide (300 mg, 1.807 mmol, 12 eq) 250 μ L of the potassium iodide solution was added dropwise to the solution containing potassium tetrachloroplatinate. After addition of potassium iodide, the solution was warmed to 70°C. Once the solution reached 70°C it was removed from heat and cooled to room temperature. The solution was then filtered through celite. The filtrate was collected and used for the following reaction. A 2 M solution of ammonium hydroxide in water (250 μ L) was added dropwise. The solution was allowed to stand for 30 minutes, filtered, and washed with ethanol (\times 1) and ether (\times 2). The solid was collected to yield 56.2 mg *cis*-diamminediiiodoplatinum(II). Silver sulfate (37 mg, 0.119 mmol, 1eq) was added to 5 mL of water. *cis*-diamminediiiodoplatinum(II) (56.2 mg, 0.116 mmol, 1eq) was added slowly. The solution was heated to 80°C. The solution was stirred overnight. The silver iodide was filtered using celite and the filtrate collected. This solution was concentrated to 1.5 mL. Potassium chloride (174.6 mg, 2.34 mmol, 20 eq) was added to the solution and then heated to 80°C. The solution was stirred at 80°C for another 20 minutes and cooled to room temperature. The solution was filtered and washed with ethanol (\times 1) and ether (\times 2) to yield 23.5 mg (52%) *cis*-diamminedichloroplatinum(II). ^1H NMR (500 MHz, DMF- d_7 , δ): 3.99 (s, 6H).

Dichloro(*trans*-(±)-1,2-diaminocyclohexane)platinum(II) (DACH-Pt) (4)

Dichloro(*trans*-(±)-1,2-diaminocyclohexane) Platinum(II) was prepared using general methods previously described (J. J. Wilson & Lippard, 2014). Potassium tetrachloroplatinate (100.3 mg, 0.242 mmol, 1 eq) was dissolved in 4 mL of water. *trans*-(±)-1,2-diaminocyclohexane (29.1 mg, 0.255 mmol, 1eq) was added dropwise to the dark red solution and stirred for 7.5 hours. A yellow precipitate formed. The solution was filtered and washed with ice-cold methanol (×1) and acetone (×1). The yellow solid was then collected to yield 70 mg (76 %). ¹H NMR (500 MHz, DMF-d₇, δ): 5.59 (d, *J* = 7.4 Hz, 2H), 5.02 (s, 2H), 2.50 (qq, *J* = 11.2, 5.6, 3.8 Hz, 2H), 2.15–2.04 (m, 2H), 1.56 (dd, *J* = 7.7, 3.3 Hz, 2H), 1.48 (tt, *J* = 11.9, 5.6 Hz, 2H), 1.15 (qd, *J* = 11.9, 2.9 Hz, 2H). ¹⁹⁵Pt NMR (107 MHz, DMF-d₇, δ): –2270.32 (Pt).

cis-diammineoxalatoplatinum(II) (DOAP) (5)

cis-diammineoxalatoplatinum(II) was prepared using general methods previously described (J. J. Wilson & Lippard, 2014). Sodium oxalate was prepared by introducing excess sodium hydroxide to oxalic acid and filtering the resulting solid. Diiodo(*cis*-diammine)platinum(II) (92.3 mg, 0.193 mmol, 1 eq) was dissolved in 5 mL water. Silver nitrate (82mg, 0.4823 mmol, 2.5eq) was added and the reaction stirred overnight protected from light. The reaction was then filtered through celite and the filtrate collected. Sodium oxalate (26 mg, 0.194 mmol, 1 eq) was added to the filtrate and the reaction was stirred overnight and protected from light. The resulting light grey solid was filtered from the solution and washed with water (2x) and methanol (x2). Yield 33.3mg (54%). ¹H NMR (500 MHz, DMSO-d₆, δ): 4.27 (s, 6H). ¹³C NMR (126 MHz, DMSO-d₆, δ): 166.38 (2C). ¹⁹⁵Pt NMR (107 MHz, DMSO-d₆, δ): –1743.33 (Pt).

1,2-diaminocyclohexane(ethylenediamine)platinum(II) (DACH-En) (6)

(*trans*-(±)-1,2-diaminocyclohexane)dichloro platinum(II) (62 mg, 0.163 mmol, 1eq) was dissolved in 5 mL of water. 1,2-diaminoethane (32 mg, 0.533 mmol, 3.2eq) was added to the solution and refluxed for two days. The solution was then cooled room temperature over 24 hours. Solution was then evaporated to yield a yellow solid. ¹H NMR (500 MHz, D₂O, δ): 3.31 (t, *J* = 5.8 Hz, 1H), 3.05 (t, *J* = 5.8 Hz, 1H), 2.97 (s, 2H), 2.72–2.64 (m, 4H), 2.47–2.39 (m, 2H), 2.09 (dt, *J* = 12.8, 2.0 Hz, 2H), 1.67–1.60 (m, 2H), 1.41–1.28

(m, 2H), 1.20 (td, $J = 9.4, 8.9, 4.0$ Hz, 2H). ^{13}C NMR (126 MHz, D_2O , δ): 61.17 (2C), 46.83, 40.43 (2C), 32.14 (2C), 23.92 (2C). ^{195}Pt NMR (107 MHz, D_2O , δ): -3002.42 (Pt). TOF-MS ES⁺ for m/z $[\text{M}]^{2+}$ $\text{C}_8\text{H}_{21}\text{Pt}$ calculated: 368.1414 found: 368.1403 $[\text{M}]^{2+}$.

Dichloro(1,2-ethylenediamine)platinum(II) (Plat-En) (7)

Dichloro(1,2-ethylenediamine)platinum(II) was prepared using general methods previously described (J. J. Wilson & Lippard, 2014). Potassium tetrachloroplatinate (66 mg, 0.159 mmol, 1eq) was dissolved in 500 μL of water. 1,2-ethylenediamine (9.36 mg, 0.156 mmol, 1eq) was added to the dark red solution and allowed to stir at room temperature for 12 hours. A yellow precipitate formed. The solution was filtered and washed with ice-cold 0.1 M HCl ($\times 1$), ethanol ($\times 1$), and ether ($\times 1$). The yellow solid was collected to yield 27.5 mg (53%). ^1H NMR (500 MHz, DMF- d_7 , δ): 5.38 (s, 4H), 2.61 (s, 4H). ^{13}C NMR (126 MHz, DMF- d_7 , δ): 50.52 (2C). ^{195}Pt NMR (107 MHz, DMF- d_7 , δ): -2309.12 (Pt).

Dichloro(1,2-propanediamine)platinum(II) (Plat-MeEn) (8)

Dichloro(1,2-propanediamine)platinum(II) was prepared according to previously reported methods and used as a mixture of isomers (Fanizzi et al., 1987). Potassium tetrachloroplatinate (34 mg, 0.082 mmol, 1eq) was dissolved in 1 mL water and heated at 50°C. Excess potassium iodide (40 mg, 0.24 mmol, 3eq) was dissolved in 0.5 mL water and added dropwise to the platinum. The solution was stirred for 10 minutes and became black. To the stirring solution, 1,2-propanediamine (7 μL , 0.08 mmol, 1 eq) was added and the solution was stirred for 40 minutes. Yellow precipitate formed immediately. The solution was cooled to room temperature and filtered. The solid was washed with ice-cold ethanol ($\times 1$) and ether ($\times 1$). The solid was dissolved in 2 mL water and silver nitrate (28 mg, 0.16 mmol, 2eq) was added. The reaction was stirred for 2 days protected from light. The solution was filtered through celite and concentrated to 1 mL. Excess potassium chloride (120 mg, 1.61 mmol, 20 eq) was added rapidly to the concentrated solution and the mixture was stirred at 50 °C for 1 hour. The resulting yellow solid was filtered and washed with methanol ($\times 1$) and ether ($\times 1$). ^1H NMR (500 MHz, DMF- d_7 , δ): 5.74 (s, 1H), 5.55 (d, $J = 40.1$ Hz, 2H), 5.22 (s, 1H), 3.30–3.17 (m, 1H), 2.89–2.80 (m, 1H), 2.66 (td, $J = 8.2$,

6.1, 3.1 Hz, 1H), 1.53 (d, $J = 6.5$ Hz, 3H). ^{13}C NMR (126 MHz, DMSO- d_6 , δ): 56.00 (1C), 52.41 (1C), 16.38 (1CH $_3$).

Dichloro(1S,2S-diaminocyclopentane)platinum(II) (Penta-Pt) (9)

Dichloro(1S,2S-diaminocyclopentane)platinum(II) was synthesized according to previously published methods (Garbutcheon-Singh et al., 2013). Potassium tetrachloroplatinate (101 mg, 0.243 mmol, 1eq) was dissolved in 2 mL of water. (1S, 2S)-diaminocyclopentane dihydrochloride (43.1 mg, 0.249 mmol, 1eq) was added and stirring continued. 73 mg of 1,8-diazabicyclo[5.4.0]undec-7-ene (DBU) (0.482 mmol, 2eq) was added to the solution. A yellow precipitate formed. The solution was filtered and washed with ethanol ($\times 1$) and ether ($\times 2$). The yellow solid was collected to yield 50.5 mg (57%). ^1H NMR (500 MHz, DMF- d_7 , δ): 5.18 (s, 2H), 5.00 (s, 2H), 3.41–3.31 (m, 2H), 2.16 (tdd, $J = 9.6, 8.0, 5.3$ Hz, 2H), 1.78–1.64 (m, 2H), 1.63–1.48 (m, 1H). ^{13}C NMR (126 MHz, DMF- d_7 , δ): 70.21 (2C), 26.73 (2C), 23.93 (1C). ^{195}Pt NMR (107 MHz, DMF- d_7 , δ): –1987.96 (Pt).

Dichloro(*o*-phenylenediamine)platinum(II) (Benza-Pt) (10)

Dichloro(*o*-phenylenediamine)platinum(II) was prepared using general methods previously described (J. J. Wilson & Lippard, 2014). Potassium tetrachloroplatinate (103 mg, 0.248 mmol, 1eq) was dissolved in 1 mL of water. A dark red solution formed. *ortho*-phenylenediamine (26.8 mg, 0.248 mmol, 1eq) was added and stirring continued for 6 hours. The solution was filtered and washed with ice-cold ethanol ($\times 1$) and ether ($\times 2$). The dark yellow /brown solid was collected with a yield of 89.8 mg (96%). ^1H NMR (500 MHz, DMF- d_7 , δ): 7.72 (s, 2H), 7.46 (dd, $J = 5.9, 3.5$ Hz, 1H), 7.28 (dd, $J = 6.0, 3.4$ Hz, 1H). ^{13}C NMR (126 MHz, DMF- d_7 , δ): 144.76 (2C), 128.85 (2C), 127.36 (2C). ^{195}Pt NMR (107 MHz, DMF- d_7 , δ): –2199.18 (Pt).

Dichloro(2-picolylamine)platinum(II) (APP) (12)

Dichloro(2-picolylamine)platinum(II) was synthesized according to previously described methods (Brunner & Schellerer, 2003). A solution of 2-picolylamine (120 μL , 0.075 mmol, 1 eq) was made in 1.2 mL water. Potassium tetrachloroplatinate (55mg, 0.133 mmol, 2eq) was dissolved in 1.2 mL water. The platinum solution was added to the 2-picolylamine, and the pH was adjusted to pH 5 using concentrated HCl. The reaction was

stirred for 4 hours. The pH of the solution was adjusted during the reaction to be around pH 5–6 using 1 M NaOH. The resulting yellow solid was filtered and washed with water (2x) to yield 38.7 mg (89%). ^1H NMR (500 MHz, DMF- d_7 , δ): 9.43 (d, $J = 5.3$ Hz, 1H), 8.37 (t, $J = 7.7$ Hz, 1H), 7.91 (d, $J = 7.8$ Hz, 1H), 7.72 (t, $J = 6.7$ Hz, 1H), 6.42 (s, 2H), 4.55 (t, $J = 5.9$ Hz, 2H).

Measurement of partition coefficients

Water was mixed with octanol for 24 hours and left to stand for an additional 24 hours to obtain water-saturated octanol and octanol-saturated water that were used for determining partition coefficients. Measurements of the partition coefficients were performed using classical shake-flask method according to OECD guidelines (OECD, 1995). Platinum complexes were dissolved in octanol-saturated water at concentrations between 0.5 mM and 5 mM. The octanol-saturated water mixtures were mixed with water-saturated octanol in a 1:1 ratio and vortexed for 30 minutes.¹³ The mixtures were then centrifuged and 0.5 mL samples of both phases were collected and quantified using RP-HPLC as described by (Klose et al., 2018). An isocratic method was used for HPLC analysis with water and methanol. Methanol concentrations ranged from 10% to 30% with 30% being used for more hydrophobic compounds. The area of absorbance was used to calculate the ratio (P) of platinum in octanol and water as this area is proportional to the concentration according to the Lambert-Beer law. The column was washed with 95% methanol 5% water between each octanol sample and equilibrated before the next sample was introduced. The stock solution of each platinum compound was compared to the total from octanol and water samples as a check of this method. This procedure to calculate $\log P$ was performed in triplicate and standard deviations were determined.

Computations

Computations were performed as previously reported (McDevitt et al., 2019). Briefly, compounds were optimized using density functional theory (DFT) in Gaussian09 (Frisch et al., 2016). Optimizations to geometry were performed using an RMS force convergence criterion of 10^{-5} hartree. The electronic wavefunction was minimized using GGA functional PBE (Perdew et al., 1996, 1997), with the DEF2TZP basis set. We did not

explicitly include relativistic effects as these were not expected to impact the geometries of the compounds significantly (Pansini et al., 2017).

Two measures of size were used for the compounds: volume and longest vector between the platinum atom and the surface of the molecule. The vector represents the main steric component of the non-labile ligand of each compound to provide a direct comparison especially when comparing compounds that do not share the same aquation-labile ligand identity. In order to quantitatively assess the size of the molecules we used the presence of electric field, as derived from the electrostatic potential, to signify the location of the chemical system. DFT yields the electrostatic potential of the optimized, non-hydrolyzed compound structures and tools previously developed and reported were used to analyze the electrostatic potential of a chemical system (Butler et al., 2014). We used the same file format to analyze the electrostatic potential and the result was the electrostatic potentials of the optimized structures were computed by minimizing the electronic wavefunction using 500 eV planewave cutoff, a gamma only k-grid, and a PBE functional utilizing a plane-augmented wave (PAW) (Blöchl, 1994; Kresse & Joubert, 1999) basis as implemented in the Vienna Ab Initio Software Package (Kresse & Furthmüller, 1996a, 1996b; Kresse & Hafner, 1993, 1994).

All compounds were calculated in a sufficiently large computational box to minimize self-interaction. The electric field is the gradient of the electrostatic potential; therefore, the electric field includes the direction of the greatest increase in electrostatic potential. DFT calculations return electrostatic potential values on the order of 10^{-6} eV, therefore a change in less than 10^{-5} eV is considered negligible. This approach is based on previous atomic radii calculations which employ negligible change in electron density to assess the size of atoms. We used this measurement of the electric field and definition of the surface of the compound to find the total volume of the compounds as well as the longest vector from the platinum center to the farthest edge of the non-labile ligand.

APPENDIX B

SUPPLEMENTAL INFORMATION FOR CHAPTER III

Materials and methods

Reagents and synthesis

Cisplatin (Dkhara, 1970), picoplatin (Okada et al., 2001), and pyriplatin, quinoplatin, isoquinoplatin, and phenanthriplatin (Park et al., 2012) were synthesized as previously reported. Oxaliplatin was purchased from TCI America. Actinomycin D was purchased from ThermoFisher Scientific. A549 cell line was acquired from the American Type Culture Collection (ATCC).

Cell culture and treatment

A549 human lung carcinoma cells (#CCL-185, ATCC) were cultured at 37°C, 5% CO₂ in DMEM supplemented with 10% FBS and 1% antibiotic–antimycotic. A549 cells have been used previously to study nucleolar stress pathways (Bursac et al., 2014; Nicolas et al., 2016). Cells between passage 11–25 and at confluency of 70% were used in the treatments. Cells were treated for 24 h with 10 μM compound, with the exception of phenanthriplatin and phenanthridine which were administered at 0.5 μM and actinomycin D at 5 nM. The counter ion for positively charged compounds is nitrate. Stock solutions of 5 mM compound in DMF were made and used with the exception of oxaliplatin, which was made in water and actinomycin D which was made in DMSO. Immediately prior to treatment, platinum compounds were diluted into media. Final DMF and DMSO concentrations were 0.2% (*v/v*) in media. We chose to use 0.5 μM phenanthriplatin to account for the higher cellular accumulation of phenanthriplatin and to be more in line with reported 72 h IC₅₀ values which are not exhibited by the other studied compounds (Park et al., 2012).

Immunofluorescence

Cells to be imaged were grown on coverslips (Ted Pella product no. 260368, round glass coverslips, 10 mm diam., 0.16-0.19 mm thick) as described above. After treatment, cells were washed twice with phosphate buffered saline (PBS) and fixed for 20 minutes at

room temperature in 4% paraformaldehyde (PFA) in PBS. PFA was removed via aspiration and cells were then permeabilized with 0.5% Triton-X in PBS for 20 minutes at room temperature. Two 10 min blocking steps were performed with 1% bovine serum albumin (BSA) in PBST (PBS with 0.1% Tween-20). Cells were incubated for one hour in primary antibody (NPM1 Monoclonal Antibody, FC-61991, ThermoFisher, 1:200 dilution in PBST with 1% BSA) and 1 hour in secondary antibody (Goat Anti-Mouse IgG H&L Alexa Fluor 488, ab150113, Abcam, 1:1000 dilution in PBST with 1% BSA), with three 5 min wash steps using PBST between incubations, and were washed in the same manner again before mounting slides. Coverslips were mounted on slides with ProLong™ Diamond Antifade Mountant with DAPI (ThermoFisher) according to manufacturer's instructions.

Imaging and Quantification

Images were taken using a HC PL Fluotar 63×/1.3 oil objective mounted on a Leica DMI8 fluorescence microscope with Leica Application Suite X software. Quantification of NPM1 relocalization was performed in an automated fashion using a Python 3 script. Images were preprocessed in ImageJ (Rueden et al., 2017; Schindelin et al., 2012) to convert the DAPI and NPM1 channels into separate 16-bit greyscale images. Between 70 and 225 cells were analyzed for each treatment group. Nuclei segmentation was determined with the DAPI images using Li thresholding functions in the Scikit-Image Python package (van der Walt et al., 2014). The coefficient of variation (CV) for individual nuclei, defined as the standard deviation in pixel intensity divided by the mean pixel intensity, was calculated from the NPM1 images using the SciPy Python package. All data were normalized to the no-treatment control in each experiment. NPM1 imaging results for each compound were observed on a minimum of two separate testing days. Duplicates of treatments were performed and analyzed and are available upon request from the corresponding author.

Computations

Based on the experimental results, we hypothesized that the size, shape or hydrophobicity of the platinum(II) compounds may be instructive in correlating the biological activity with the chemical structure because of biological implications of these

structural components in an interaction between two biomolecules that may be disrupted. Thus, we optimized all platinum(II) compounds using density functional theory (DFT) as implemented in Gaussian09 (Frisch et al., 2016) so that we might quantitatively assess the structural differences and hydrophobicity of the compounds.

Geometry optimizations were performed with an RMS force convergence criterion of 10^{-5} hartree. The electronic wavefunction was minimized using the GGA functional PBE (Perdew et al., 1996, 1997), with the DEF2TZP basis set. Relativistic effects were not explicitly included, however, these were not expected to significantly impact the geometries of the platinum(II) complexes (Pansini et al., 2017). Solvent was implicitly included using the Solvent Model Density method (Marenich et al., 2009).

The solvent-dependent difference in Gibbs free energies ($\Delta G_{\text{water-octanol}}$) was calculated using the equation: $\Delta G_{\text{water-octanol}} = \Delta G_{\text{water}} - \Delta G_{\text{octanol}}$ where (ΔG_{water}) and ($\Delta G_{\text{octanol}}$) are the change in free energies of the system in water and *n*-octanol, respectively. (ΔG_{water}) was computed using the structure optimized in the pseudo solvent, water. This optimized structure was kept constant for all subsequent computations, including calculation of the compound in pseudo-solvent, *n*-octanol, which yielded ($\Delta G_{\text{octanol}}$). This approach minimizes the reorganizational energetic differences. Thus, ($\Delta G_{\text{water-octanol}}$) is a measure of the hydrophobicity for each compound.

Further calculations were required to assess the size and shape of the platinum(II) compounds. Two measures of size were considered, (i) volume, and (ii) the longest vector between the platinum atom and the surface of the molecule. The latter characteristic represents the main steric component of the ligand in each compound.

To quantitatively assess the volume of each compound, a definition of size is necessary. Thus, we will use the presence of electron density to signify the location of the chemical system. Since DFT yields both the electron density and electrostatic potential of the optimized, non-hydrolyzed platinum(II) compound structures and we have previously developed a tool to analyze the electrostatic potential of chemical systems (Butler et al., 2014), we will use the same file format to analyze the electrostatic potential. As a result, the electrostatic potentials of the optimized structures were computed by minimizing the electronic wavefunction using a 500 eV planewave cutoff, a gamma-only k-grid, and the PBE (Perdew et al., 1996, 1997) functional utilizing a plane-augmented wave (PAW) (Blöchl, 1994; Kresse & Joubert, 1999) basis as implemented in the Vienna

Ab initio Software Package (VASP) (Kresse & Furthmüller, 1996b, 1996a; Kresse & Hafner, 1993, 1994). All compounds were calculated within a sufficiently large computational box to minimize self-interaction.

The electric field is the gradient of the electrostatic potential; thus, the electric field embodies the direction of greatest increase in electrostatic potential. This is significant because the increased slope of the electric field enables us to more clearly define the edge of a chemical system in space. Therefore, deriving the electric field from the electrostatic potential returned by DFT allows us to assess the size of each compound by sampling the electric field. However, to achieve this, definition of a surface needs to be addressed.

We will define the edge of a chemical system as the point where the electric field magnitude no longer changes, which is intuitive considering the definition of the electrostatic potential. Since DFT calculations return electrostatic potential values on the order of 10^{-6} eV, a change in less than 10^{-5} eV is considered negligible. This approach is based on previous atomic radii calculations, which employ negligible change in electron density to assess the size of atoms (Blöchl, 1994; Kresse & Joubert, 1999).

Using the area of each compound defined by sampling the electric field, the longest vector between the platinum atom and the surface was calculated for each compound, capturing the main steric component of each ligand.

Supplemental Figures

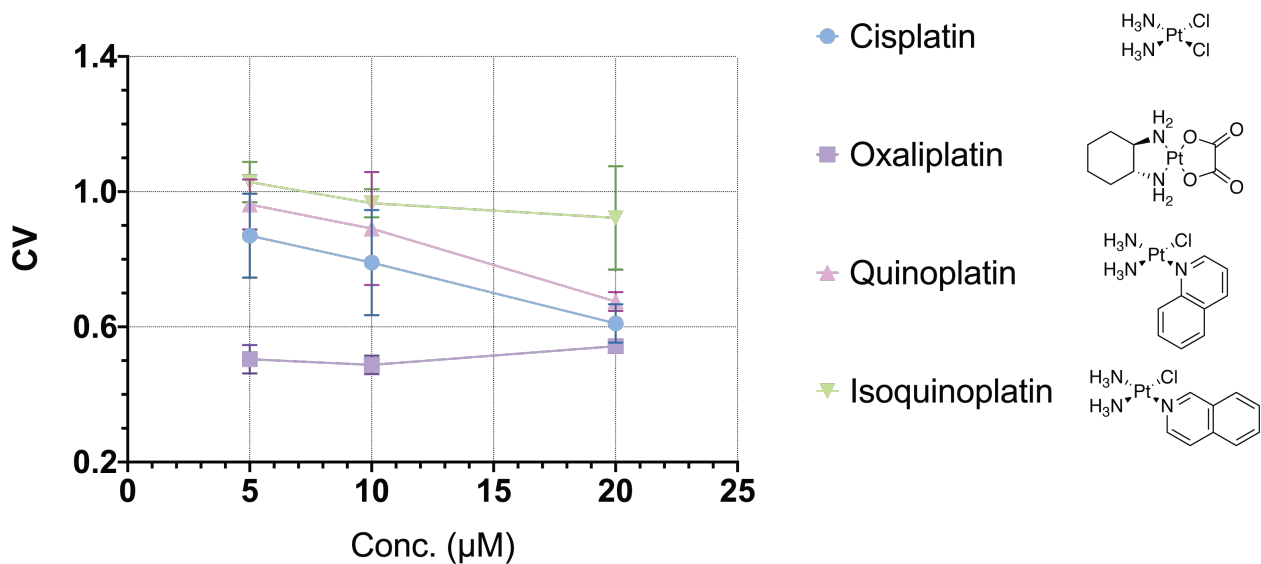


Figure B.1. Concentration dependence of nucleolar stress induced by monofunctional Pt(II) compounds at 24 h. A549 cells were treated with indicated Pt(II) compounds for 24 h. Individual CV measurements were normalized to untreated cells, plotted as mean \pm SE, $n = 3$.

APPENDIX C

SUPPORTING INFORMATION FOR CHAPTER IV

Methods

Cell Culture and Treatment

A549 human lung carcinoma cells (#CCL-185, American Type Culture Collection) were cultured at 37°C, 5% CO₂ in Dulbecco's Modified Eagle Medium (DMEM) supplemented with 10% Fetal Bovine Serum (FBS) and 1% antibiotic-antimycotic. Treatments were conducted on cells that had been grown for 11–30 passages to 70–80% confluency. Platinum compound treatments were conducted at 10 μM and Actinomycin D treatments were conducted at 5 nM unless otherwise noted. Actinomycin stocks were stored frozen in DMSO and thawed on day of use. Platinum compounds were made into 5 mM stocks on the day of treatment from solids in 0.9% NaCl (cisplatin), water (oxaliplatin), or DMF (remaining platinum compounds). Stock solutions were diluted into media immediately prior to drug treatment.

Time-Dependent NPM1 Redistribution.

Immunofluorescence Cells were grown on coverslips (Ted Pella product no. 260368, #1.5, 10 mm dia.) according to the methods previously described (Sutton, McDevitt, Prochnau, et al., 2019). After platinum drug treatment, cells were washed 2× with phosphate buffered saline (PBS) and fixed with 4% paraformaldehyde (PFA) in water at RT. PFA was then removed, and cells were permeabilized using 0.5% Triton-X in PBS for 20 min at RT. Cells were then washed with 1% bovine serum albumin (BSA) in PBST (PBS with 0.1% Tween-20) for 10 min, 2×. Following this, cells were incubated with the primary antibody (NPM1 Monoclonal Antibody, FC-61991 ThermoFisher, 1:200 dilution in PBST with 1% BSA) for 1 h. Cells were then washed with PBST for 5 min 3× and then incubated with secondary antibody (Goat Anti-Mouse IgG H&L Alexa Fluor 488, ab150113, Abcam, 1:1000 dilution in PBST with 1% BSA) for 1 h. Cells were then washed again with PBST for 5 min 3× before mounting. Coverslips were mounted on

slides with ProLong Diamond Antifade Mountant with DAPI (ThermoFisher) according to manufacturer's instructions.

Image Processing and Quantification Images were taken using a HC PL Fluotar 63×/1.3 oil objective mounted on a Leica DMI8 fluorescence microscope with Leica Application Suite X software. Quantification of NPM1 relocalization was performed in an automated fashion using a Python 3 script (Sutton, McDevitt, Prochnau, et al., 2019). Images were preprocessed in ImageJ (Rueden et al., 2017) to convert the DAPI and NPM1 channels into separate 16-bit grayscale images. Between 70 and 225 cells were analyzed for each treatment group. Nuclei segmentation was determined with the DAPI images using Li thresholding functions in the Scikit Image Python package (van der Walt et al., 2014). The coefficient of variation (CV) for individual nuclei, defined as the standard deviation in pixel intensity divided by the mean pixel intensity, was calculated from the NPM1 images using the SciPy Python package. All data were normalized to the no-treatment control in each experiment. NPM1 imaging results for each compound were observed on a minimum of three separate testing days.

rRNA Transcription Inhibition

A549 cells were grown to 70% confluency in a 6-well tissue culture plate. Drug treatment was completed for three or 5 h prior to the pulse step with the compounds indicated in DMEM supplemented with 10% FBS and 1× antibiotic–antimycotic. One hour prior to the pulse step, phosphate depletion was performed by switching regular media for phosphate-free media with 10% FBS, 1× antibiotic–antimycotic, and the drug of interest. For the pulse step, media was replaced with a solution of 15 $\mu\text{Ci}/\text{mL}$ ^{32}P orthophosphate made in phosphate-free media with FBS and antibiotic–antimycotic. After the 1 h pulse step, media was replaced with cold drug-containing DMEM with FBS and antibiotic–antimycotic for a 3 h chase. RNA was then extracted using the Zymo Quick-RNA Miniprep kit and separated by size on an agarose gel. The gel was then visualized in two ways: Total RNA was (1) visualized with an ethidium bromide stain and (2) radioactively labeled RNA produced during the pulse step was visualized. To visualize radiolabeled RNA, the gel was dried on Whatman paper using a gel dryer set for 2 h at 70°C, after which it was left on the gel dryer overnight at RT. The dried gel was exposed to a phosphor screen for 24 h, and the screen was imaged using a Storm

phosphorimager. The amount of labeled RNA was quantified by calculating the intensity of the gel bands in the images in ImageJ (Rueden et al., 2017). Prior to quantification, gel files from the Storm software were converted from square root encoding to linear encoding using the Linearize GelData ImageJ plugin (Rueden et al., 2017). Quantified radiolabeled RNA was normalized to the total 28S RNA levels for each sample, measured by EtBr. The band marked 47S includes the 47S primary transcript and 45S early pre-rRNA processing intermediate (Burger et al., 2010). RNA transcript amounts are shown on graphs as a fraction of the mean untreated control intensities for each experiment.

Cellular Platinum Accumulation

Cell Treatment and Sample Preparation A549 cells were seeded in a 10 cm culture dish and incubated for at least 24 h or until 80% confluent, prior to treatment. Cell treatments were performed following the general treatment protocol. After incubation, the treatment media were aspirated, and cells were thoroughly washed three times with warm PBS (2 mL). Cells were harvested by trypsinization using 1 mL of TrypLE Express Enzyme (ThermoFisher) and collected in 4 mL of DMEM in a 15 mL falcon tube. The cell suspension was then centrifuged (2000 rpm, 7 m), and the cell pellets were resuspended in 2 mL of cold PBS. The cell suspension was then transferred into two 1.5 mL Eppendorf tubes in separate 1 mL aliquots for acid digestion and protein concentration quantification, respectively. The samples were then centrifuged (3000 rcf, 10 m, 4°C) and the supernatant was carefully aspirated. Cell pellets for protein quantification were resuspended in 500 μ L of ice-cold RIPA buffer containing mammalian protease inhibitor cocktail (Sigma-Aldrich). Samples for acid digestion and protein quantification were stored at -20°C .

Determination of Total Protein Concentration Cell suspension for total protein analysis were lysed by vortexing on high for 15 min in 5 min increments. Total protein concentration was assayed by BCA (bicinchoninic acid) assay using a Pierce BCA Protein Assay Kit (Thermo Fisher) following the manufacturer's protocol (96-well plate). Optical density was measured on a microplate reader (Tecan Spark 20M).

Cell Fractionation Subcellular platinum quantification was performed based on previously published protocols with some modification (Dam et al., 2019; Hermann et al., 2013). After treatment, the media were aspirated, and cells were thoroughly washed three

times with warm PBS (2 mL). Cells were harvested by trypsinization using 1 mL of TrypLE Express Enzyme (Thermo Fisher) and collected in 1 mL Tris-KCl buffer (100 mM KCl, 50 mM Tris HCl, pH 7.5, 5 mM MgCl₂, 1 mM Na₂EDTA), a 200 μ L aliquot was taken for whole cell platinum accumulation analysis. The remaining sample was centrifuged (2 m, 1000 \times g, 4°C), and the supernatant was aspirated. Cell pellets were resuspended in 100 μ L of cold lysis buffer and set on ice for 15 min followed by addition of 700 μ L Tris-KCl buffer. Lysate was centrifuged (10 m, 12000 \times g, 4°C), and a 500 μ L aliquot of the supernatant (cytoplasmic fraction) was collected and stored at -20 °C until digestion. Crude nuclei pellet was resuspended in 1 mL Tris-KCl buffer and centrifuged (10 m, 12000 \times g, 4°C). Supernatant was aspirated and purified pellets were stored in 200 μ L lysis buffer at -20 °C until digestion.

Acid Digestion Nitric acid digestion was performed based on previously published protocols with some modification (Dam et al., 2019; Riisom et al., 2018). Cell pellets for acid digestion were first heated on a heat block at 65–70°C in open air until completely dry. Then, 100 μ L of concentrated nitric acid (69%, TraceSELECT, Fluka) was then added to each dry cell pellet, and the sealed samples were heated at 65–70 °C on a heat block overnight. Digested samples were then cooled to RT and diluted with 900 μ L of dH₂O to a final volume of 1 mL.

ICP-MS Total Platinum Concentration Analysis Platinum concentrations were determined by ICP-MS (Thermo Scientific, iCAP RQ ICP-MS) equipped with a CETAC ASX-500 autosampler based on published methods (Egger et al., 2009; Riisom et al., 2018) The instrument was tuned daily with an ICP-MS tuning solution (Tune B iCAP Thermo TS, Inorganic Ventures) for optimal conditions. All CPS measurement were made in kinetic energy discrimination (KED) mode. Measured platinum concentrations for each trial represent the average of three scans. Calibration standards were prepared from a platinum standard solution (1001 \pm 5 μ g/mL, Inorganic Ventures). Bismuth, indium, terbium, and yttrium from a multielement internal standard solution (10 μ g/mL, Inorganic Ventures) were used as internal standards (1 ppb) to monitor instrument drift and matrix effects. 2% (v/v) HNO₃ (TraceSELECT, Fluka) was used for dilution of standards and digested samples. Calibration standards were prepared fresh each day from the platinum standard solution to a concentration of 0.50, 1.00, 2.00, 4.00, 10.00,

20.00, 40.00, 100.00, and 200.00 ppb. Prepared digested samples diluted by a factor of 1:4 prior to measurement to a total volume of 4 mL.

Model Oligonucleotide DNA-Pt(II) Adduct Assays

Hairpin DNA sequence (5'-TATGGTATTTTATACCATA-3') (280 μ M) was folded by rapid heating to 90°C and slow cooling to 4°C in 10 mM Na₂HPO₄/NaH₂PO₄ buffer (pH 7.1), 0.1 M NaNO₃, and 10 mM Mg(NO₃)₂. The platinum compound (830 μ M) was then added, and the solution was incubated at 37°C for various time intervals. Pt(II)-bound DNA was then purified with Sephadex G-25 Medium size exclusion resin (GE Healthcare) on laboratory-prepared spin columns (BioRad) to remove unbound platinum. Purified samples were added (5.5 μ L) to 50% glycerol (9.5 μ L) and mixed. Samples were then loaded (10 μ L) on dPAGE (19:1 20% acrylamide in 8 M urea) and ran at 180 V. Gels were then stained with methylene blue for 3 min and destained in diH₂O for 30 min. Gels were then imaged using an Alpha Innotech UV Trans-illuminator and quantified using ImageJ gel quantification methods (Rueden et al., 2017).

In Cell DNA-Pt(II) Binding Assays

Cell Treatment and Sample Preparation A549 cells were seeded in a 150 mm culture dishes and incubated for at least 24 h or until at least 80% confluent, prior to treatment. Cell treatments were performed following the general treatment protocol. After incubation, the treatment media was aspirated, and cells were thoroughly washed three times with warm PBS (2 mL). Cells were harvested by trypsinization using 4 mL of TrypLE Express Enzyme (Thermo Fisher) and collected in 10 mL of DMEM in a 15 mL falcon tube. The cell suspension was then centrifuged (2000 rpm, 7 m), and the cell pellets were resuspended in 2 mL of cold PBS.

DNA Extraction and Quantification DNA was extracted from cell pellets using a ZymoBIOMICS Quick-DNA Miniprep Kit. Clean DNA was extracted from collection columns into 1.5 mL Eppendorf tubes using diH₂O at a volume of 200 μ L per centrifuge column. Once collected the DNA concentration was taken for each sample using a Nanodrop (Thermofisher NanoDrop 1000). DNA was then dried at 37°C under vacuum until all water had evaporated off.

Acid Digestion Nitric Acid digestion was performed based on previous published protocols with some modification (Dam et al., 2019; Yamada et al., 2005). For digestion, 100 μL of concentrated nitric acid (69%, TraceSELECT, Fluka) was then added to each dry DNA sample and the sealed samples were heated at 65–70 $^{\circ}\text{C}$ on a heat block overnight. Digested samples were then cooled to RT and diluted with 900 μL of dH_2O to a final volume of 1 mL. Platinum quantification was performed by ICP-MS as described above.

Molecular Modeling

Energy minimization were performed as previously reported (McDevitt et al., 2019; Sutton, McDevitt, Prochnau, et al., 2019). Briefly, compounds were optimized using density functional theory in Gaussian09 (Frisch et al., 2016). Geometry optimizations were performed using an RMS force convergence criterion of 10^{-5} hartree. The electronic wave function was minimized using GGA functional PBE with the LANL2DZ basis set (Perdew et al., 1996, 1997) and compounds were rendered in ChimeraX v1.3 (Pettersen et al., 2021) with 70% surface transparency.

Supplemental Figures

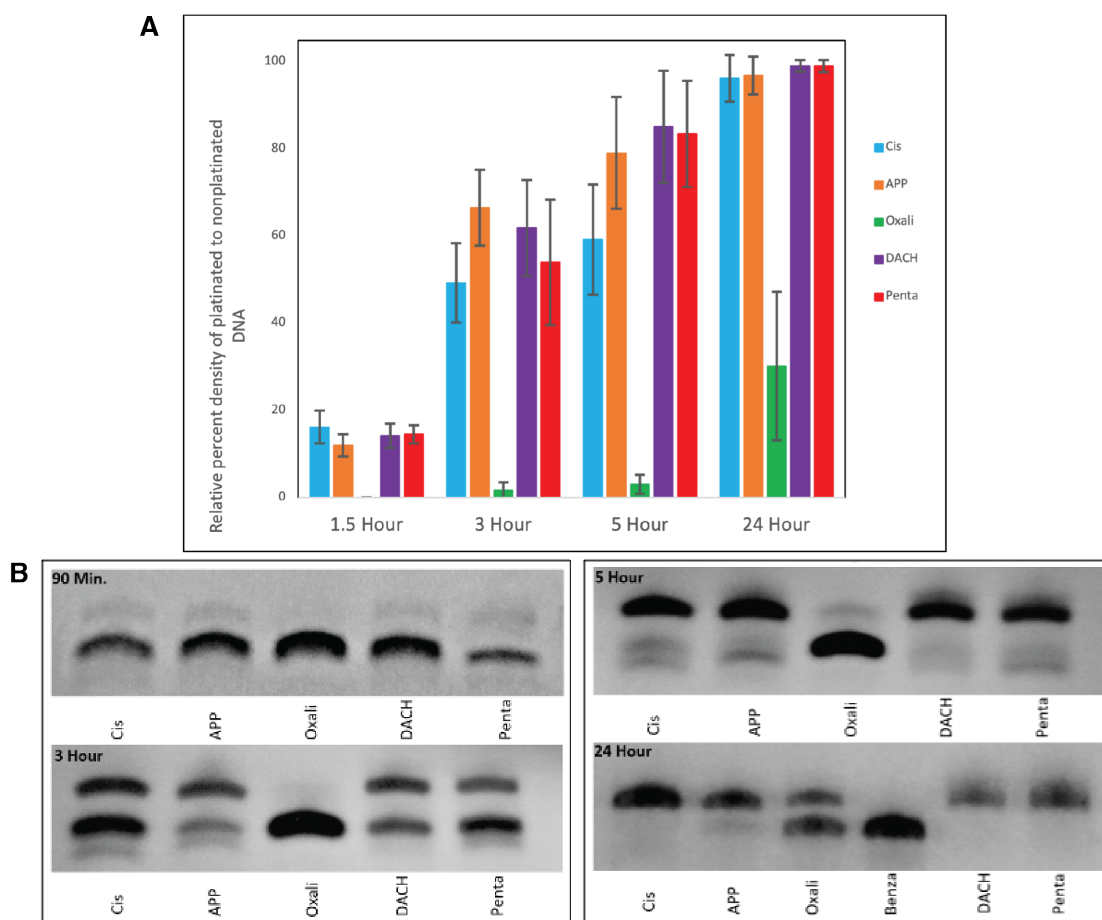


Figure C.1. Model oligonucleotide DNA-Pt(II) adduct assays. **A** | Quantification of DNA-Pt(II) binding assay. **B** | representative dPAGE gel images at various time points. Gel images were quantified using ImageJ. Binding Density is reported as the average of 3 biological replicates.

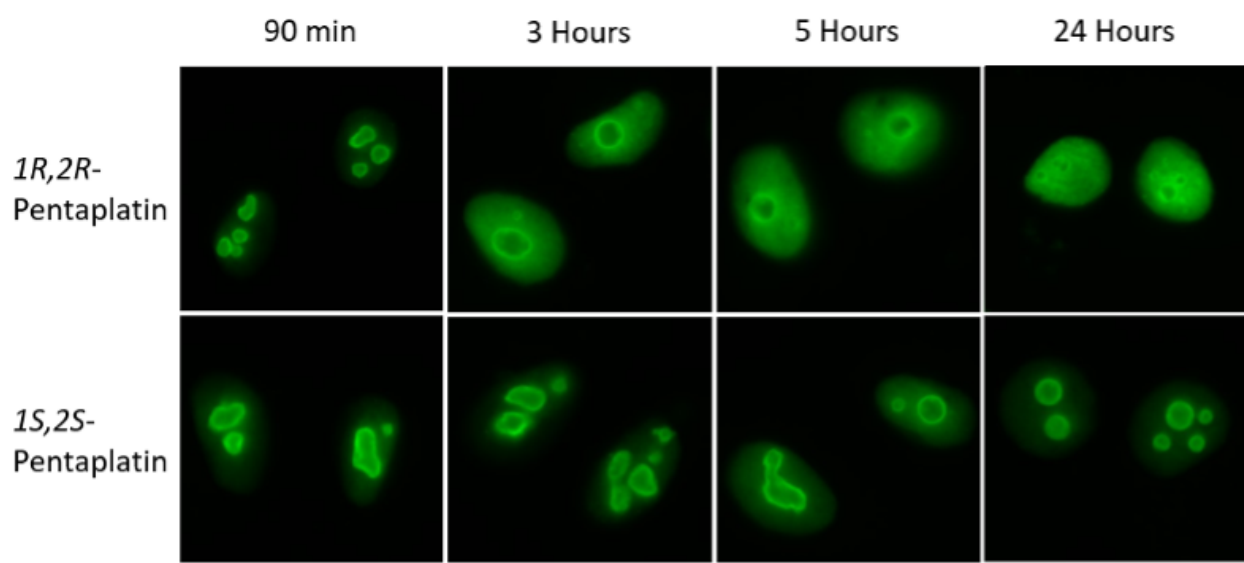


Figure C.2. Representative cell images of A549 cells treated with *1S,2S*- and *1R,2R*-pentaplatin at given treatment times.



Figure C.3. Representative cell images of A549 cells treated with *1S,2S*- and *1R,2R*-DACHplatin at given treatment times.

Synthesis of Pt(II) Compounds

Compounds **1–6** were synthesized as previously described (Sutton, McDevitt, Prochnau, et al., 2019).

Dichloro((1*S*,2*S*)-*trans*-1,2-diaminocyclopentane)platinum(II) ((1*S*, 2*S*)-pentaplatin) (**7**)

Potassium tetrachloroplatinate (101 mg, 0.243 mmol, 1eq) was dissolved in 2 mL of water. (1*S*, 2*S*)-diaminocyclopentane dihydrochloride (43.1 mg, 0.249 mmol, 1eq) was added and stirring continued. 73 mg of 1,8-diazabicyclo[5.4.0]undec-7-ene (DBU) (0.482 mmol, 2eq) was added to the solution at r.t. A yellow precipitate formed. The solution was filtered and washed with ethanol (x1) and ether (x2). ¹H NMR (500 MHz, DMF-d₇, δ): 5.18 (s, 2H), 5.00 (s, 2H), 3.41–3.31 (m, 2H), 2.16 (tdd, *J* = 9.6, 8.0, 5.3 Hz, 2H), 1.78–1.64 (m, 2H), 1.63–1.48 (m, 1H). ¹³C NMR (126 MHz, DMF-d₇, δ): 70.21 (2C), 26.73 (2C), 23.93 (1C). ¹⁹⁵Pt NMR (107 MHz, DMF-d₇, δ): –1988 (Pt).

Dichloro((1*R*,2*R*)-*trans*-1,2-diaminocyclopentane)platinum(II) ((1*R*,2*R*)-pentaplatin) (**8**)

(1*R*,2*R*)-*trans*-*N*-Boc-1,2-cyclopentanediamine (43.1 mg, 0.249 mmol, 1eq) was added to 20 mL of 4.0 M HCl in dioxane and stirring for one hour. The solution was then rotary evaporated until the solid was no longer acidic. Potassium tetrachloroplatinate (101 mg, 0.243 mmol, 1eq) was dissolved in 2 mL of water and added to the dried (1*R*,2*R*)-*trans*-cyclopentanediamine. 73 mg of 1,8-diazabicyclo[5.4.0]undec-7-ene (DBU) (0.482 mmol, 2eq) was added to the solution. A yellow precipitate formed. The solution was filtered and washed with ethanol (x1) and ether (x2). ¹H NMR (500 MHz, DMF-d₇, δ): 5.18 (s, 2H), 5.00 (s, 2H), 3.41–3.31 (m, 2H), 2.16 (tdd, *J* = 9.6, 8.0, 5.3 Hz, 2H), 1.78–1.64 (m, 2H), 1.63–1.48 (m, 1H). ¹³C NMR (126 MHz, DMF-d₇, δ): 70.21 (2C), 26.73 (2C), 23.93 (1C). ¹⁹⁵Pt NMR (107 MHz, DMF-d₇, δ): –1988 (Pt)

Dichloro((1*S*,2*S*)-*trans*-1,2-diaminocyclohexane)platinum(II) ((1*S*,2*S*)-DACHplatin) (**9**)

(1*S*,2*S*)-*trans*-*N*-Boc-1,2-cyclohexanediamine (43.1 mg, 0.249 mmol, 1eq) was added to 20 mL of 4.0 M HCl in dioxane and stirred for one hour. The solution was then rotary evaporated until the solid was no longer acidic. Potassium tetrachloroplatinate (100.3 mg, 0.242 mmol, 1 eq) was dissolved in 4 mL of water and added to the dried (1*S*,2*S*)-*trans*-cyclohexanediamine and stirred for 7.5 hours. A yellow precipitate formed. The solution was filtered and washed with ice-cold methanol (x1) and acetone (x1). ¹H NMR (500

MHz, DMF-d₇, δ): 5.59 (d, *J* = 7.4 Hz, 2H), 5.02 (s, 2H), 2.50 (qq, *J* = 11.2, 5.6, 3.8 Hz, 2H), 2.15–2.04 (m, 2H), 1.56 (dd, *J* = 7.7, 3.3 Hz, 2H), 1.48 (tt, *J* = 11.9, 5.6 Hz, 2H), 1.15 (qd, *J* = 11.9, 2.9 Hz, 2H). ¹⁹⁵Pt NMR (107 MHz, DMF-d₇, δ): –2270 (Pt).

Dichloro((1*R*,2*R*)-*trans*-1,2-diaminocyclohexane)platinum(II) ((1*R*,2*R*)-DACHplatin) (10)

(1*R*,2*R*)-*trans*-N-Boc-1,2-cyclohexdiamine (43.1 mg, 0.249 mmol, 1eq) was added to 20 mL of 4.0 M HCl in dioxane and stirred for one hour. The solution was then rotary evaporated until the solid was no longer acidic. Potassium tetrachloroplatinate (100.3 mg, 0.242 mmol, 1 eq) was dissolved in 4 mL of water and added to the dried (1*R*,2*R*)-*trans*-cyclohexdiamine and stirred for 7.5 hours. A yellow precipitate formed. The solution was filtered and washed with ice-cold methanol (x1) and acetone (x1). ¹H NMR (500 MHz, DMF-d₇, δ): 5.59 (d, *J* = 7.4 Hz, 2H), 5.02 (s, 2H), 2.50 (qq, *J* = 11.2, 5.6, 3.8 Hz, 2H), 2.15–2.04 (m, 2H), 1.56 (dd, *J* = 7.7, 3.3 Hz, 2H), 1.48 (tt, *J* = 11.9, 5.6 Hz, 2H), 1.15 (qd, *J* = 11.9, 2.9 Hz, 2H). ¹⁹⁵Pt NMR (107 MHz, DMF-d₇, δ): –2270 (Pt).

APPENDIX D

SUPPLEMENTARY MATERIALS FOR CHAPTER V

Materials and Methods

Reagents and Antibodies

Cisplatin (AvaChem Scientific, 1714), oxaliplatin (TCI Chemicals, O0372), and BMH-21 (Sigma-Aldrich, SML1183) Primary antibody: mouse monoclonal anti-UBF (F-9) (Santa Cruz, sc-13125), mouse monoclonal anti-RPA194 (C-1) (Santa Cruz, sc-13125), Mouse IgG Isotype Control (Invitrogen, 31903) Secondary antibody: Goat anti-Mouse Alexa Fluor 488 (ab150113, Abcam)

Cell culture and Treatment

A549 human lung carcinoma cells (ATCC, #CCL-185) were cultured at 37°C, 5% CO₂ in Dulbecco's Modified Eagle Medium (DMEM) supplemented with 10% Fetal Bovine Serum (FBS) and 1% antibiotic-antimycotic. U2OS human bone osteosarcoma cells (ATCC, #HTB-96) were cultured at 37°C, 5% CO₂ in McCoy's 5A medium supplemented with 10% Fetal Bovine Serum (FBS) and 1% antibiotic-antimycotic.

Stock solutions of cisplatin (5mM, 0.9% NaCl) and oxaliplatin (5mM, ddH₂O) were prepared fresh on the day of treatment. BMH-21 stock solution (500 μM, DMSO) was stored in aliquots at -20°C and thawed prior to use. Stock solutions were diluted into pre-warmed cell media immediately prior to treatment. All drug treatments were conducted on cells between passages 8–20 at 80% confluency and carried out at a final concentration of 10 μM for cisplatin and oxaliplatin, and 1 μM for BMH-21.

Immunofluorescence

Cells were grown on #1.5, 10 mm dia. coverslips (Ted Pella no. 260368) in a 24-well plate as described above. Following treatment, cells were washed twice with phosphate buffered saline (PBS) then fixed for 20 minutes at RT with 4% paraformaldehyde (PFA) in PBS and permeabilized with 0.5% Triton-X in PBS for 20 min at RT. Coverslips were then blocked with 1% bovine serum albumin (BSA) in PBST (PBS with 0.1% Tween-20) for 10

min, twice and incubated with primary antibody for 1 h. Coverslips were washed 3x with PBS for 5 min each at RT, and then incubated with secondary antibody (1:1000, in PBST with 1% BSA) for 1 h in the dark. Following three more washes with PBS for 5 min each, coverslips were mounted on slides with ProLong Diamond Antifade Mountant with DAPI (ThermoFisher, cat no. P36971) and allowed cured at RT overnight before imaging. Primary antibodies and concentrations: anti-RPA194, (1:500, in PBST with 1% BSA) and anti-UBF (1:400, in PBST with 1% BSA)

Chromatin Immunoprecipitation

Chromatin Immunoprecipitation was performed according to (Sullivan & Santos, 2020) with some modification. Following treatment, cells were washed twice with cold PBS, harvested with 2 mL of TrypLE (Gibco, cat no. 12604013), and collected in 6 mL of cell media. Cells were crosslinked with 500 μ L of 16% PFA (final concentration, 1% PFA) for 10 min at RT with rotation, which was quenched with 850 μ L of cold 1.25M glycine (final concentration, 125 mM glycine) for 5 min at RT with rotation.

Crosslinked cells were pelleted ($800 \times g$, 6 min, 4°C) and washed twice with cold PBS, then resuspended in 1 mL PBS for cell counting using a TC20 Automated Cell Counter (Bio-Rad), at 1:1 dilution with trypan blue. Approx. 5×10^6 cells were transferred to a 1.5mL protein lo-bind tube, pelleted ($800 \times g$, 6 min, 4°C), and then resuspended in 200 μ L of cold cell lysis buffer (800mM NaCl, 25 mM Tris pH 7.5, 5mM EDTA, 1% Triton X-100, 0.1% SDS, and 0.5% sodium deoxycholate) supplemented with protease / phosphatase inhibitor (Cell Signaling Technology, #5872S). Cells snap-frozen in dry ice and acetone and stored at -80°C .

On the day of experiment, cell lysate was thawed on ice and sheared using a Bioruptor sonicator (Diagenode) at 4°C for 20 cycles of 30 sec ON/OFF. Sheared chromatin was diluted with 200 μ L of cold chromatin dilution buffer (25 mM Tris pH 7.5, 5mM EDTA, 1% *v/v* Triton X-100, 0.1% *w/v* SDS) and clarified by centrifugation ($13,600 \times g$, 30 min, 4°C). A 20 μ L of diluted chromatin (5% Input) was aliquoted and stored at -20°C to serve as the CHIP Input. For each IP reaction, 100 μ L of diluted chromatin was combined with 50 μ L of preincubated Dynabeads–antibody mix in a 1.5 mL protein lo-bind tube and incubated overnight at 4°C with rotation. Dynabeads–antibody mix was prepared as followed: For each IP, 25 μ L of Dynabeads Protein G magnetic beads

(ThermoFisher, #1003D) was combined with 12.5 μL of ChIP antibody (anti-RPA194 or anti-UBF) or 1.875 μL of IgG control, and diluted chromatin dilution buffer to a final volume of 50 μL , which was incubated at RT for 2 h with rotation.

The following day, chromatin-bead mixture was set on a magnetic stand and the beads were then washed at 4°C with 500 μL of IP wash buffer—rotating for 5 min in between each of the following wash steps: *i*) “low salt” buffer (140 mM NaCl, 50 mM HEPES pH 7.9, 1mM EDTA, 1% Triton X-100, 0.1%SDS, 0.1% sodium deoxycholate) *ii*) “high salt” buffer (500 mM NaCl, 50 mM HEPES pH 7.9, 1mM EDTA, 1% Triton X-100, 0.1%SDS, 0.1% sodium deoxycholate) *iii*) LiCl buffer (20 mM Tris pH 7.5, 1mM EDTA, 250mM LiCl, 0.5% Triton X-100, 0.5% sodium deoxycholate) and *iv*) TE buffer (10 mM Tris pH 7.5, 1mM EDTA). After the final wash step the beads were incubated with 100 μL of elution buffer (10 mM Tris pH 7.5, 1mM EDTA, 1% SDS) at 65°C for 5 min on thermo shaker (VWR), followed by an additional 15 min at RT. The bead mixture was set on a magnetic stand and supernatant was collected a new centrifuge tube. The elution step was repeated to obtain 200 μL of ChIP chromatin.

To reverse crosslinking and digest contaminates, input samples were first thawed on ice and diluted with 180 μL with chromatin dilution buffer. 8 μL of 4 M NaCl (final concentration, 160 mM) and 0.5 μL of RNase A (ThermoFisher, #EN0531) (final concentration, 23 $\mu\text{g}/\text{mL}$) were added to both ChIP and Input samples, followed by incubation at 65°C for 8 h in a thermocycler (Eppendorf). Next, 2 μL of 0.5 M EDTA (final concentration, 5 mM) and 2 μL Proteinase K (New England Biolabs, #P8107S) (final concentration, 200 $\mu\text{g}/\text{mL}$) were added to each sample and incubated in a thermocycler 45°C for 2 h. ChIP and Input DNA was purified using a Zymo ChIP DNA Clean & Concentrator Kit (#D5205) and eluted into 25 μL of DNA Elution buffer (10 mM Tris pH 8.5, 0.1 mM EDTA).

DNA library for next-gen sequencing was prepared using the NEBNext Ultra II DNA Library Prep Kit, for Illumina (New England Biolabs, #E7600S) and multiplexed using NEBNext Ultra II DNA Library Prep Kit, for Illumina (New England Biolabs, #E7645S) and sequenced on an Illumina NovaSeq 6000 platform.

Data processing and rDNA mapping

A custom human genome assemble for rDNA mapping (*hs1-rDNA_genome_v1.0*), along with annotation files were obtained from publicly available GitHub repository (<https://github.com/vikramparalkar/rDNA-Mapping-Genomes>) based on published methods (George et al., 2023). The *hs1* (T2T-CHM13) reference human genome was masked for rDNA-matching loci, and a single full-length human rDNA sequence, KY962518.1 (44,838 nt) (J.-H. Kim et al., 2018) was then added as an extra chromosome (chrR).

Demultiplexed FASTQ read files were first trimmed with Trimmomatic version 0.39 (Bolger et al., 2014) with the following parameters: ILLUMINACLIP:TruSeq3-PE.fa:2:30:10:2:True LEADING:3 TRAILING:3 SLIDINGWINDOW:4:15 MINLEN:30, then mapped with Bowtie2 version 2.5.4 (Langmead & Salzberg, 2012) with the following parameters: -X 2000 -k 3 to allow for indel variations up to 2 kb, documented in rDNA repeats (Jean-Clement Mars et al., 2018), and to permit for multiple alignments for each sequence read. The resulting SAM files were filtered and into the BAM format using samtools version 1.19 (H. Li et al., 2009) with parameters: -F 4 -q 1 to retain multi-mapped read, then sorted and indexed with samtools sort and index.

Normalized coverage tracks were generated from indexed BAM files with deeptools version 3.5.3 (Ramírez et al., 2016) bamCoverage with the following parameters: -bs 1 --smoothLength 15 --maxFragmentLength 500 --minFragmentLength 30 --centerReads --extendReads --normalizeUsing CPM --ignoreForNormalization chrX chrM. Reads were normalized as total counts per million (CPM) (*# of reads per bin / total reads*) to account for differences in sequencing depth.

Averaged coverage tracks were obtained using deeptools version 3.5.3 (Ramírez et al., 2016) bigWigAverage with the following parameters: -bs 1 -r chrR. "IP Enrichment" of averaged coverage maps was calculated as the ratio of ChIP reads to Input DNA reads at each base position (*ChIP coverage / Input coverage*) using deeptools (Ramírez et al., 2016) bigwigCompare. Track visualization and sequence figures were generated with pyGenomeTracks (Lopez-Delisle et al., 2021).

Supplementary Figures

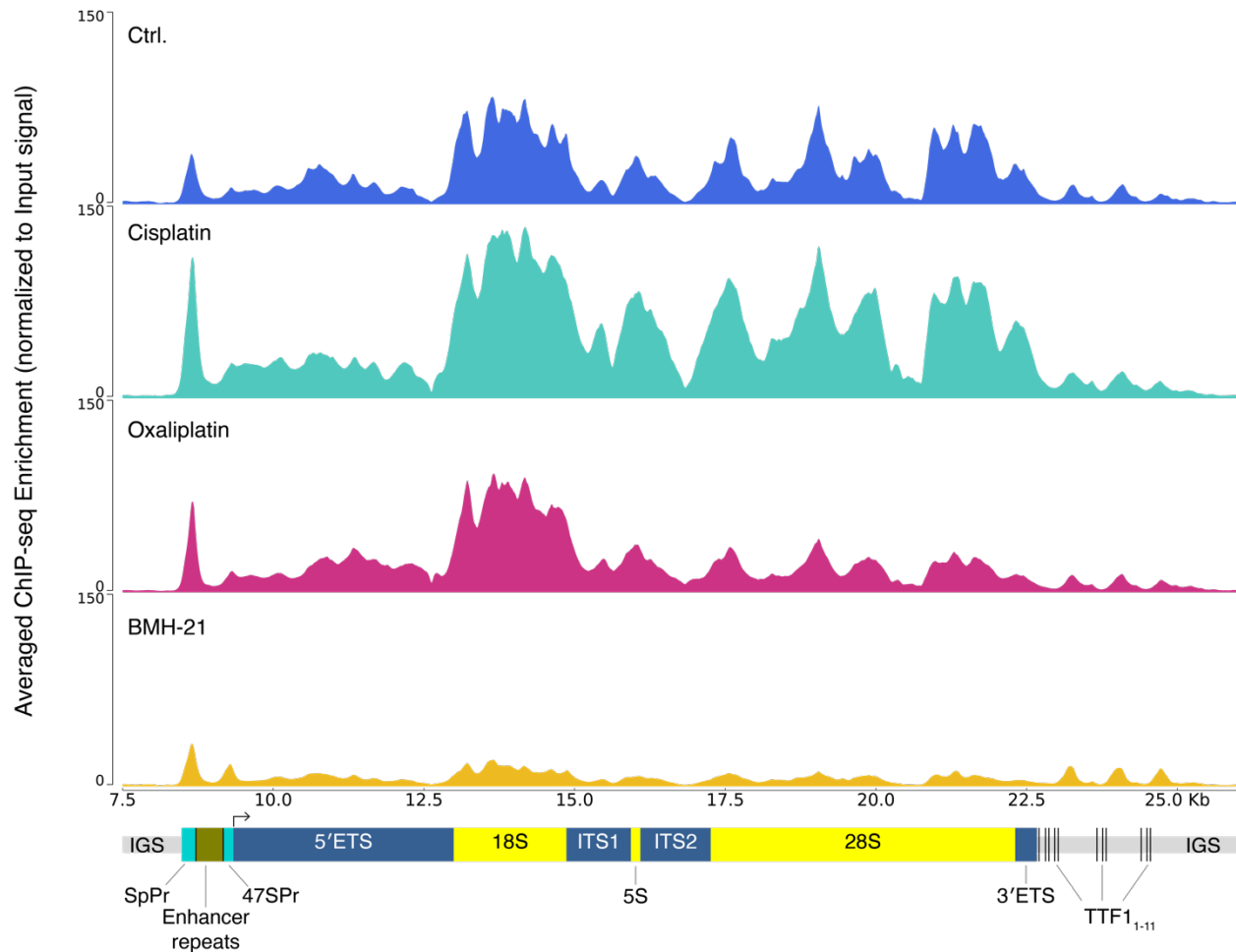


Figure D.1. ChIP-seq mapping of Pol I (RPA194) occupancy along rDNA gene in U2OS cells, following 3 h treatment with 10 μ M cisplatin or oxaliplatin, or 1 μ M BMH-21. Average sequence coverage is normalized to the read count per million reads (CPM) and shown as enrichment over the input sequence for the associated treatment. $n = 2$. Diagram of rDNA gene aligned below: intergenic spacer region (IGS), spacer and 47S promoter (SpPr, 47SPr), internal transcribed spacers (ITS1, ITS2), transcription termination factor binding sites (TTF1₁₋₁₁), external transcribed spacers (5'ETS and 3'ETS), arrow indicates transcription start site.

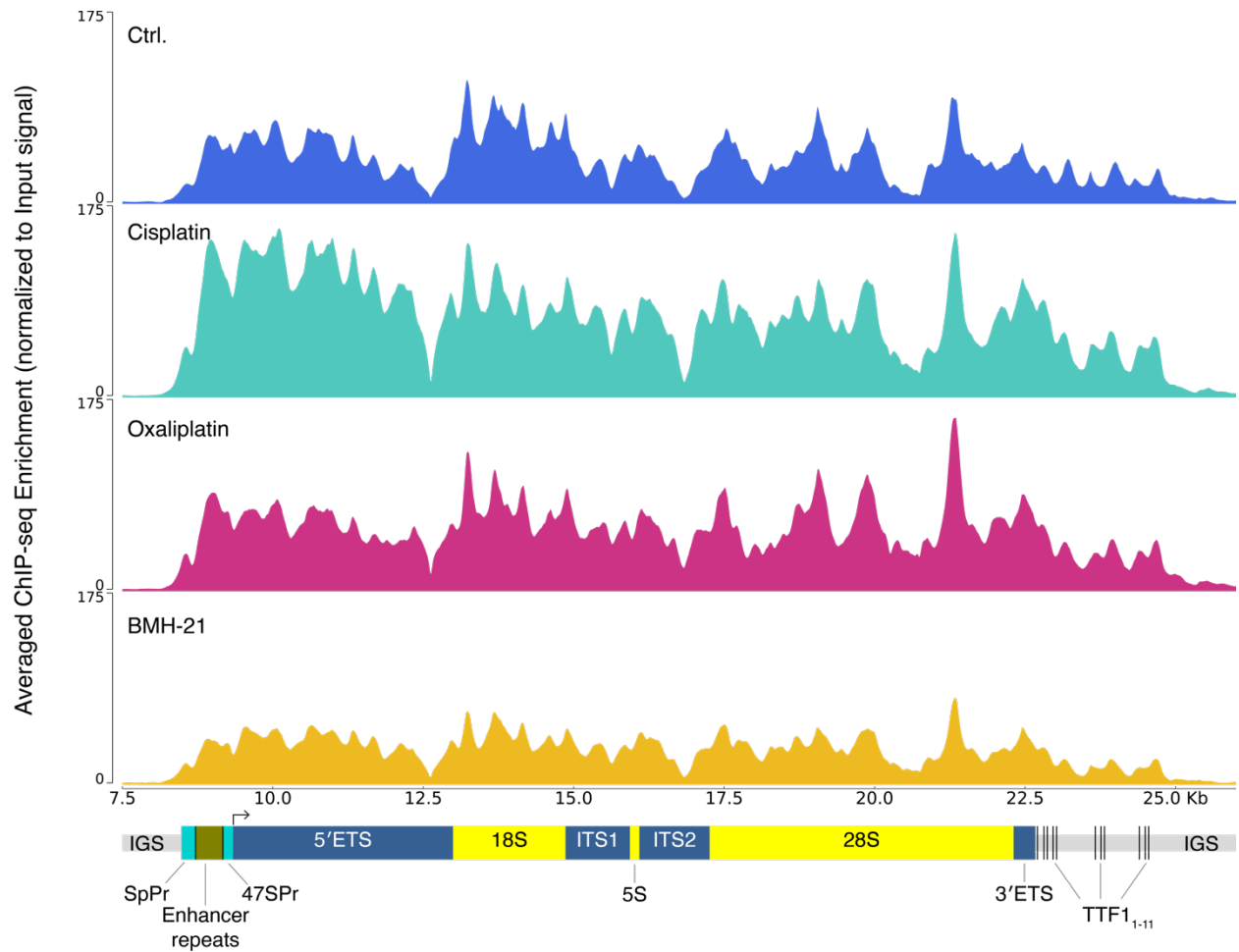


Figure D.2. ChIP-seq mapping of UBF-rDNA occupancy in U2OS cells, following 3 h treatment with 10 μ M cisplatin or oxaliplatin, or 1 μ M BMH-21. Average sequence coverage is normalized to the read count per million reads (CPM) and shown as enrichment over the input sequence for the associated treatment. $n = 2$. Diagram of rDNA gene aligned below: intergenic spacer region (IGS), spacer and 47S promoter (SpPr, 47SPr), internal transcribed spacers (ITS1, ITS2), transcription termination factor binding sites (TTF1₁₋₁₁), external transcribed spacers (5'ETS and 3'ETS), arrow indicates transcription start site.

REFERENCES CITED

- Ahmad, S. Kinetic Aspects of Platinum Anticancer Agents. *Polyhedron* **2017**, *138*, 109–124. DOI: 10.1016/j.poly.2017.09.016.
- Alessio, E.; Messori, L. NAMI-A and KP1019/1339, Two Iconic Ruthenium Anticancer Drug Candidates Face-to-Face: A Case Story in Medicinal Inorganic Chemistry. *Molecules* **2019**, *24* (10), 1995. DOI: 10.3390/molecules24101995.
- Alian, O. M.; Azmi, A. S.; Mohammad, R. M. Network Insights on Oxaliplatin Anti-cancer Mechanisms. *Clin. Transl. Med.* **2012**, *1* (1), e26. DOI: 10.1186/2001-1326-1-26.
- Almaqwashy, A. A.; Zhou, W.; Naufer, M. N.; Riddell, I. A.; Yilmaz, Ö. H.; Lippard, S. J.; Williams, M. C. DNA Intercalation Facilitates Efficient DNA-Targeted Covalent Binding of Phenanthriplatin. *J. Am. Chem. Soc.* **2019**, *141* (4), 1537–1545. DOI: 10.1021/jacs.8b10252.
- Alt, A.; Lammens, K.; Chiocchini, C.; Lammens, A.; Pieck, J. C.; Kuch, D.; Hopfner, K.-P.; Carell, T. Bypass of DNA Lesions Generated During Anticancer Treatment with Cisplatin by DNA Polymerase η . *Science* **2007**, *318* (5852), 967–970. DOI: 10.1126/science.1148242.
- Anderson, M.; Schultz, E. P.; Martick, M.; Scott, W. G. Active-Site Monovalent Cations Revealed in a 1.55-Å-Resolution Hammerhead Ribozyme Structure. *J. Mol. Biol.* **2013**, *425* (20), 3790–3798. DOI: 10.1016/j.jmb.2013.05.017.
- Antony, C.; George, S. S.; Blum, J.; Somers, P.; Thorsheim, C. L.; Wu-Corts, D. J.; Ai, Y.; Gao, L.; Lv, K.; Tremblay, M. G.; Moss, T.; Tan, K.; Wilusz, J. E.; Ganley, A. R. D.; Pimkin, M.; Paralkar, V. R. Control of Ribosomal RNA Synthesis by Hematopoietic Transcription Factors. *Mol. Cell* **2022**, *82* (20), 3826–3839.e9. DOI: 10.1016/j.molcel.2022.08.027.
- Arndt, J. W.; Gong, W.; Zhong, X.; Showalter, A. K.; Liu, J.; Dunlap, C. A.; Lin, Z.; Paxson, C.; Tsai, M.-D.; Chan, M. K. Insight into the Catalytic Mechanism of DNA Polymerase β : Structures of Intermediate Complexes. *Biochemistry* **2001**, *40* (18), 5368–5375. DOI: 10.1021/bi002176j.
- Athavale, S. S.; Petrov, A. S.; Hsiao, C.; Watkins, D.; Prickett, C. D.; Gossett, J. J.; Lie, L.; Bowman, J. C.; O'Neill, E.; Bernier, C. R.; Hud, N. V.; Wartell, R. M.; Harvey, S. C.; Williams, L. D. RNA Folding and Catalysis Mediated by Iron (II). *PloS One* **2012**, *7* (5), e38024. DOI: 10.1371/journal.pone.0038024.
- Auffinger, P.; D'Ascenzo, L.; Ennifar, E. Sodium and Potassium Interactions with Nucleic Acids. In *The Alkali Metal Ions: Their Role for Life*; Sigel, A., Sigel, H., Sigel, R. K. O., Eds.; Springer International Publishing: Cham, 2016; pp 167–201. DOI: 10.1007/978-3-319-21756-7_6.

- Auffinger, P.; Grover, N.; Westhof, E. Metal Ion Binding to RNA. *Met. Ions Life Sci.* **2011**, *9*, 1–35.
- Bachas, S. T.; Ferré-D'Amaré, A. R. Convergent Use of Heptacoordination for Cation Selectivity by RNA and Protein Metalloregulators. *Cell Chem. Biol.* **2018**, *25* (8), 962-973.e5. DOI: 10.1016/j.chembiol.2018.04.016.
- Bandyopadhyay, N.; Basu, P.; Kumar, G. S.; Guhathakurta, B.; Singh, P.; Naskar, J. P. Biophysical Studies on the Interaction of a Novel Oxime Based Palladium(II) Complex with DNA and RNA. *J. Photochem. Photobiol. B* **2017**, *173*, 560–570. DOI: 10.1016/j.jphotobiol.2017.06.044.
- Bandyopadhyay, S.; Chaudhury, S.; Mehta, D.; Ramesh, A. RETRACTED ARTICLE: Discovery of Iron-Sensing Bacterial Riboswitches. *Nat. Chem. Biol.* **2021**, *17* (8), 924. DOI: 10.1038/s41589-020-00665-7.
- Baruah, H.; Wright, M. W.; Bierbach, U. Solution Structural Study of a DNA Duplex Containing the Guanine-N7 Adduct Formed by a Cytotoxic Platinum–Acridine Hybrid Agent. *Biochemistry* **2005**, *44* (16), 6059–6070. DOI: 10.1021/bi050021b.
- Bashan, A.; Yonath, A. The Linkage between Ribosomal Crystallography, Metal Ions, Heteropolytungstates and Functional Flexibility. *J. Mol. Struct.* **2008**, *890* (1–3), 289–294. DOI: 10.1016/j.molstruc.2008.03.043.
- Batey, R. T.; Kieft, J. S. Soaking Hexammine Cations into RNA Crystals to Obtain Derivatives for Phasing Diffraction Data. In *Nucleic Acid Crystallography: Methods and Protocols*; Ennifar, E., Ed.; Springer New York: New York, NY, 2016; pp 219–232. DOI: 10.1007/978-1-4939-2763-0_14.
- Bednarski, P. J.; Trümbach, B. Use of Reversed-Phase h.p.l.c. for Determination of the Hydrolysis Rate Constants of Dichloro(1,2-Diarylethylenediamine)Platinum(II) Complexes. *Transit. Met. Chem.* **1994**, *19* (5), 513–517. DOI: 10.1007/BF00136363.
- Bensaude, O. Inhibiting Eukaryotic Transcription. Which Compound to Choose? How to Evaluate Its Activity?: Which Compound to Choose? How to Evaluate Its Activity? *Transcription* **2011**, *2* (3), 103–108. DOI: 10.4161/trns.2.3.16172.
- Berman, H. M.; Westbrook, J.; Feng, Z.; Gilliland, G.; Bhat, T. N.; Weissig, H.; Shindyalov, I. N.; Bourne, P. E. The Protein Data Bank. *Nucleic Acids Res.* **2000**, *28* (1), 235–242. DOI: 10.1093/nar/28.1.235.
- Bhattacharyya, D.; Ramachandran, S.; Sharma, S.; Pathmasiri, W.; King, C. L.; Baskerville-Abraham, I.; Boysen, G.; Swenberg, J. A.; Campbell, S. L.; Dokholyan, N. V.; Chaney, S. G. Flanking Bases Influence the Nature of DNA Distortion by Platinum 1,2-Intrastrand (GG) Cross-Links. *PLoS ONE* **2011**, *6* (8), e23582. DOI: 10.1371/journal.pone.0023582.
- Blöchl, P. E. Projector Augmented-Wave Method. *Phys. Rev. B* **1994**, *50* (24), 17953–17979. DOI: 10.1103/PhysRevB.50.17953.

- Bolger, A. M.; Lohse, M.; Usadel, B. Trimmomatic: A Flexible Trimmer for Illumina Sequence Data. *Bioinformatics* **2014**, *30* (15), 2114–2120. DOI: 10.1093/bioinformatics/btu170.
- Boukoura, S.; Larsen, D. H. Nucleolar Organization and Ribosomal DNA Stability in Response to DNA Damage. *Curr. Opin. Cell Biol.* **2024**, *89*, 102380. DOI: 10.1016/j.ceb.2024.102380.
- Boulon, S.; Westman, B. J.; Hutten, S.; Boisvert, F.-M.; Lamond, A. I. The Nucleolus under Stress. *Mol. Cell* **2010**, *40* (2), 216–227. DOI: 10.1016/j.molcel.2010.09.024.
- Bowman, J. C.; Lenz, T. K.; Hud, N. V.; Williams, L. D. Cations in Charge: Magnesium Ions in RNA Folding and Catalysis. *Curr. Opin. Struct. Biol.* **2012**, *22* (3), 262–272. DOI: 10.1016/j.sbi.2012.04.006.
- Brabec, V.; Hrabina, O.; Kasparkova, J. Cytotoxic Platinum Coordination Compounds. DNA Binding Agents. *Bioinorg. Chem. Eur. Union* **2017**, *351*, 2–31. DOI: 10.1016/j.ccr.2017.04.013.
- Brabec, V.; Kasparkova, J. Ruthenium Coordination Compounds of Biological and Biomedical Significance. DNA Binding Agents. *Coord. Chem. Rev.* **2018**, *376*, 75–94. DOI: 10.1016/j.ccr.2018.07.012.
- Brunner, H.; Schellerer, K.-M. New Porphyrin Platinum Conjugates for the Cytostatic and Photodynamic Tumor Therapy. *Inorganica Chim. Acta* **2003**, *350*, 39–48. DOI: 10.1016/S0020-1693(02)01490-1.
- Bruno, P. M.; Liu, Y.; Park, G. Y.; Murai, J.; Koch, C. E.; Eisen, T. J.; Pritchard, J. R.; Pommier, Y.; Lippard, S. J.; Hemann, M. T. A Subset of Platinum-Containing Chemotherapeutic Agents Kills Cells by Inducing Ribosome Biogenesis Stress. *Nat. Med.* **2017**, *23* (4), 461–471. DOI: 10.1038/nm.4291.
- Bruno, P. M.; Lu, M.; Dennis, K. A.; Inam, H.; Moore, C. J.; Sheehe, J.; Elledge, S. J.; Hemann, M. T.; Pritchard, J. R. The Primary Mechanism of Cytotoxicity of the Chemotherapeutic Agent CX-5461 Is Topoisomerase II Poisoning. *Proc. Natl. Acad. Sci.* **2020**, *117* (8), 4053–4060. DOI: 10.1073/pnas.1921649117.
- Burger, K.; Mühl, B.; Harasim, T.; Rohrmoser, M.; Malamoussi, A.; Orban, M.; Kellner, M.; Gruber-Eber, A.; Kremmer, E.; Hölzel, M.; Eick, D. Chemotherapeutic Drugs Inhibit Ribosome Biogenesis at Various Levels. *J. Biol. Chem.* **2010**, *285* (16), 12416–12425. DOI: 10.1074/jbc.M109.074211.
- Bursac, S.; Brdovcak, M. C.; Donati, G.; Volarevic, S. Activation of the Tumor Suppressor P53 upon Impairment of Ribosome Biogenesis. *Biochim. Biophys. Acta BBA - Mol. Basis Dis.* **2014**, *1842* (6), 817–830. DOI: 10.1016/j.bbadis.2013.08.014.
- Butcher, S. E.; Pyle, A. M. The Molecular Interactions That Stabilize RNA Tertiary Structure: RNA Motifs, Patterns, and Networks. *Acc. Chem. Res.* **2011**, *44* (12), 1302–1311. DOI: 10.1021/ar200098t.

- Butler, K. T.; Hendon, C. H.; Walsh, A. Electronic Chemical Potentials of Porous Metal–Organic Frameworks. *J. Am. Chem. Soc.* **2014**, *136* (7), 2703–2706. DOI: 10.1021/ja4110073.
- Caceres, C. A Thymine Tetrad in d(TGGGGT) Quadruplexes Stabilized with Tl⁺/Na⁺ Ions. *Nucleic Acids Res.* **2004**, *32* (3), 1097–1102. DOI: 10.1093/nar/gkh269.
- Camacho, A. S.; Martín-García, I.; Contreras-Celedón, C.; Chacón-García, L.; Alonso, F. DNA-Supported Palladium Nanoparticles as a Reusable Catalyst for the Copper- and Ligand-Free Sonogashira Reaction. *Catal. Sci. Technol.* **2017**, *7* (11), 2262–2273. DOI: 10.1039/C7CY00001D.
- Cameron, D. P.; Sornkom, J.; Alshafi, S.; Drygin, D.; Poortinga, G.; McArthur, G. A.; Hein, N.; Hannan, R.; Panov, K. I. CX-5461 Preferentially Induces Top2 α -Dependent DNA Breaks at Ribosomal DNA Loci. *Biomedicines* **2024**, *12* (7), 1514. DOI: 10.3390/biomedicines12071514.
- Cameron, I. L.; Smith, N. K. R.; Pool, T. B.; Sparks, R. L. Intracellular Concentration of Sodium and Other Elements as Related to Mitogenesis and Oncogenesis *in Vivo*. *Cancer Res.* **1980**, *40* (5), 1493.
- Canals, A.; Arribas-Bosacoma, R.; Albericio, F.; Álvarez, M.; Aymamí, J.; Coll, M. Intercalative DNA Binding of the Marine Anticancer Drug Variolin B. *Sci. Rep.* **2017**, *7* (1), 39680. DOI: 10.1038/srep39680.
- Cerretani, C.; Kanazawa, H.; Vosch, T.; Kondo, J. Crystal Structure of a NIR-Emitting DNA-Stabilized Ag₁₆ Nanocluster. *Angew. Chem. Int. Ed.* **2019**, *58* (48), 17153–17157. DOI: 10.1002/anie.201906766.
- Chaney, S. G.; Campbell, S. L.; Bassett, E.; Wu, Y. Recognition and Processing of Cisplatin- and Oxaliplatin-DNA Adducts. *Crit. Rev. Oncol. Hematol.* **2005**, *53* (1), 3–11. DOI: 10.1016/j.critrevonc.2004.08.008.
- Chen, Y.; Guo, Z.; Parsons, S.; Sadler, P. J. Stereospecific and Kinetic Control over the Hydrolysis of a Sterically Hindered Platinum Picoline Anticancer Complex. *Chem. - Eur. J.* **1998**, *4* (4), 672–676. DOI: 10.1002/(SICI)1521-3765(19980416)4:4<672::AID-CHEM672>3.0.CO;2-8.
- Cheun, Y.; Koag, M.; Naguib, Y. W.; Ouzon-Shubeita, H.; Cui, Z.; Pakotiprapha, D.; Lee, S. Synthesis, Structure, and Biological Evaluation of a Platinum-carbazole Conjugate. *Chem. Biol. Drug Des.* **2018**, *91* (1), 116–125. DOI: 10.1111/cbdd.13062.
- Cho, Y. S.; Lee, E. J.; Lee, G.-H.; Hah, S. S. Aptamer Selection for Fishing of Palladium Ion Using Graphene Oxide-Adsorbed Nanoparticles. *Bioorg. Med. Chem. Lett.* **2015**, *25* (23), 5536–5539. DOI: 10.1016/j.bmcl.2015.10.056.

- Chua, E. Y. D.; Davey, G. E.; Chin, C. F.; Droge, P.; Ang, W. H.; Davey, C. A. Stereochemical Control of Nucleosome Targeting by Platinum-Intercalator Antitumor Agents. *Nucleic Acids Res.* **2015**, *43* (11), 5284–5296. DOI: 10.1093/nar/gkv356.
- Clarke, A. M.; Engel, K. L.; Giles, K. E.; Petit, C. M.; Schneider, D. A. NETSeq Reveals Heterogeneous Nucleotide Incorporation by RNA Polymerase I. *Proc. Natl. Acad. Sci.* **2018**, *115* (50). DOI: 10.1073/pnas.1809421115.
- Colis, L.; Peltonen, K.; Sirajuddin, P.; Liu, H.; Sanders, S.; Ernst, G.; Barrow, J. C.; Laiho, M. DNA Intercalator BMH-21 Inhibits RNA Polymerase I Independent of DNA Damage Response. *Oncotarget* **2014**, *5* (12), 4361–4369. DOI: 10.18632/oncotarget.2020.
- Dairaku, T.; Furuita, K.; Sato, H.; Šebera, J.; Nakashima, K.; Kondo, J.; Yamanaka, D.; Kondo, Y.; Okamoto, I.; Ono, A.; Sychrovský, V.; Kojima, C.; Tanaka, Y. Structure Determination of an Ag^I-Mediated Cytosine-Cytosine Base Pair within DNA Duplex in Solution with ¹H/¹⁵N/¹⁰⁹Ag NMR Spectroscopy. *Chem. - Eur. J.* **2016**, *22* (37), 13028–13031. DOI: 10.1002/chem.201603048.
- Dam, C. S.; Lambert, I. H.; Gammelgaard, B.; Stürup, S. Distribution of Platinum between Nuclear and Cytosolic Fractions – Can Subcellular Fractionation Be Performed Quantitatively? *J. Pharm. Biomed. Anal.* **2019**, *165*, 82–89. DOI: 10.1016/j.jpba.2018.11.046.
- Damsma, G. E.; Alt, A.; Brueckner, F.; Carell, T.; Cramer, P. Mechanism of Transcriptional Stalling at Cisplatin-Damaged DNA. *Nat. Struct. Mol. Biol.* **2007**, *14* (12), 1127–1133. DOI: 10.1038/nsmb1314.
- Dann, C. E.; Wakeman, C. A.; Sieling, C. L.; Baker, S. C.; Irnov, I.; Winkler, W. C. Structure and Mechanism of a Metal-Sensing Regulatory RNA. *Cell* **2007**, *130* (5), 878–892. DOI: 10.1016/j.cell.2007.06.051.
- De Meester, P.; Goodgame, D. M.; Jones, T. J.; Skapski, A. C. X-Ray Evidence for Metal-N-7 Bonding in a Hydrated Manganese Derivative of Guanosine 5'-Monophosphate. *Biochem. J.* **1974**, *139* (3), 791–792. DOI: 10.1042/bj1390791.
- DeRose, Victoria J.; Yglesias, M. V. Metal Ion Interactions With DNA, RNA, and Nucleic Acid Enzymes. In *Comprehensive Coordination Chemistry III*; Elsevier, 2021; pp 968–993. DOI: 10.1016/B978-0-08-102688-5.00112-4.
- DeRose, V.J. Metal Ion Binding to Catalytic RNA Molecules. *Curr. Opin. Struct. Biol.* **2003**, *13* (3), 317–324. DOI: 10.1016/S0959-440X(03)00077-0.
- DeRose, V.J. Sensing Cellular Magnesium with RNA. *Nat. Chem. Biol.* **2007**, *3* (11), 693–694. DOI: 10.1038/nchembio1107-693.

- DeRose, V.J. Chapter 5. Characterization of Nucleic Acid–Metal Ion Binding by Spectroscopic Techniques. In *RSC Biomolecular Sciences*; Hud, N. V., Ed.; Royal Society of Chemistry: Cambridge, 2008; pp 154–179. DOI: 10.1039/9781847558763-00154.
- DeRose, V.J.; Burns, S.; Kim, N.-K.; Vogt, M. 8.29 - DNA and RNA as Ligands. In *Comprehensive Coordination Chemistry II*; McCleverty, J. A., Meyer, T. J., Eds.; Pergamon: Oxford, 2003; pp 787–813. DOI: 10.1016/B0-08-043748-6/08167-6.
- Desoize, B.; Madoulet, C. Particular Aspects of Platinum Compounds Used at Present in Cancer Treatment. *Crit. Rev. Oncol. Hematol.* **2002**, *42* (3), 317–325. DOI: 10.1016/S1040-8428(01)00219-0.
- Dkhara, S. Ch. Rapid Method for the Synthesis of *Cis*-[Pt(NH₃)₂Cl₂]. *Indian J. Chem.* **1970**, *8* (2), 193–194.
- Dodd, D. W.; Tomchick, D. R.; Corey, D. R.; Gagnon, K. T. Pathogenic C9ORF72 Antisense Repeat RNA Forms a Double Helix with Tandem C:C Mismatches. *Biochemistry* **2016**, *55* (9), 1283–1286. DOI: 10.1021/acs.biochem.6b00136.
- Dolgin, E. How COVID Unlocked the Power of RNA Vaccines. *Nature* **2021**, *589*, 189–191.
- Draper, D. E.; Grilley, D.; Soto, A. M. Ions and RNA Folding. *Annu. Rev. Biophys. Biomol. Struct.* **2005**, *34* (1), 221–243. DOI: 10.1146/annurev.biophys.34.040204.144511.
- Dremann, D. N.; Chow, C. S. The Development of Peptide Ligands That Target Helix 69 rRNA of Bacterial Ribosomes. *Bioorg. Med. Chem.* **2016**, *24* (18), 4486–4491. DOI: 10.1016/j.bmc.2016.07.050.
- Drozdal, P.; Gilski, M.; Kierzek, R.; Lomozik, L.; Jaskolski, M. Ultrahigh-Resolution Crystal Structures of Z-DNA in Complex with Mn²⁺ and Zn²⁺ Ions. *Acta Crystallogr. D Biol. Crystallogr.* **2013**, *69* (6), 1180–1190. DOI: 10.1107/S0907444913007798.
- Drozdal, P.; Gilski, M.; Kierzek, R.; Lomozik, L.; Jaskolski, M. High-Resolution Crystal Structure of Z-DNA in Complex with Cr³⁺ Cations. *JBIC J. Biol. Inorg. Chem.* **2015**, *20* (3), 595–602. DOI: 10.1007/s00775-015-1247-5.
- Drygin, D.; Lin, A.; Bliesath, J.; Ho, C. B.; O'Brien, S. E.; Proffitt, C.; Omori, M.; Haddach, M.; Schwaebe, M. K.; Siddiqui-Jain, A.; Streiner, N.; Quin, J. E.; Sanij, E.; Bywater, M. J.; Hannan, R. D.; Ryckman, D.; Anderes, K.; Rice, W. G. Targeting RNA Polymerase I with an Oral Small Molecule CX-5461 Inhibits Ribosomal RNA Synthesis and Solid Tumor Growth. *Cancer Res.* **2011**, *71* (4), 1418–1430. DOI: 10.1158/0008-5472.CAN-10-1728.

- Drygin, D.; Siddiqui-Jain, A.; O'Brien, S.; Schwaebe, M.; Lin, A.; Bliesath, J.; Ho, C. B.; Proffitt, C.; Trent, K.; Whitten, J. P.; Lim, J. K. C.; Von Hoff, D.; Anderes, K.; Rice, W. G. Anticancer Activity of CX-3543: A Direct Inhibitor of rRNA Biogenesis. *Cancer Res.* **2009**, *69* (19), 7653–7661. DOI: 10.1158/0008-5472.CAN-09-1304.
- Dunaway-Mariano, D.; Cleland, W. Investigations of Substrate Specificity and Reaction Mechanism of Several Kinases Using Chromium (III) Adenosine 5'-Triphosphate and Chromium (III) Adenosine 5'-Diphosphate. *Biochemistry* **1980**, *19* (7), 1506–1515.
- Egger, A. E.; Rappel, C.; Jakupec, M. A.; Hartinger, C. G.; Heffeter, P.; Keppler, B. K. Development of an Experimental Protocol for Uptake Studies of Metal Compounds in Adherent Tumor Cells. *J Anal Spectrom* **2009**, *24* (1), 51–61. DOI: 10.1039/B810481F.
- Englinger, B.; Pirker, C.; Heffeter, P.; Terenzi, A.; Kowol, C. R.; Keppler, B. K.; Berger, W. Metal Drugs and the Anticancer Immune Response. *Chem. Rev.* **2019**, *119* (2), 1519–1624. DOI: 10.1021/acs.chemrev.8b00396.
- Ennifar, E.; Dumas, P. Polymorphism of Bulged-out Residues in HIV-1 RNA DIS Kissing Complex and Structure Comparison with Solution Studies. *J. Mol. Biol.* **2006**, *356* (3), 771–782. DOI: 10.1016/j.jmb.2005.12.022.
- Ennifar, E.; Walter, P.; Dumas, P. A Crystallographic Study of the Binding of 13 Metal Ions to Two Related RNA Duplexes. *Nucleic Acids Res.* **2003**, *31* (10), 2671–2682. DOI: 10.1093/nar/gkg350.
- Erat, M. C.; Sigel, R. K. O. 2. Methods to Detect and Characterize Metal Ion Binding Sites in RNA. In *Metal Ions in Life Sciences*; Sigel, A., Sigel, H., Sigel, R. K. O., Eds.; Royal Society of Chemistry: Cambridge, 2011; pp 37–100. DOI: 10.1039/9781849732512-00037.
- van Eunen, K.; Bouwman, J.; Daran-Lapujade, P.; Postmus, J.; Canelas, A. B.; Mensonides, F. I. C.; Orij, R.; Tuzun, I.; van den Brink, J.; Smits, G. J.; van Gulik, W. M.; Brul, S.; Heijnen, J. J.; de Winde, J. H.; Teixeira de Mattos, M. J.; Kettner, C.; Nielsen, J.; Westerhoff, H. V.; Bakker, B. M. Measuring Enzyme Activities under Standardized in Vivo-like Conditions for Systems Biology: Standardized Enzyme Assays for Systems Biology. *FEBS J.* **2010**, *277* (3), 749–760. DOI: 10.1111/j.1742-4658.2009.07524.x.
- Facchetti, G.; Rimoldi, I. Anticancer Platinum(II) Complexes Bearing N-Heterocycle Rings. *Bioorg. Med. Chem. Lett.* **2019**, *29* (11), 1257–1263. DOI: 10.1016/j.bmcl.2019.03.045.
- Faivre, S.; Chan, D.; Salinas, R.; Woynarowska, B.; Woynarowski, J. M. DNA Strand Breaks and Apoptosis Induced by Oxaliplatin in Cancer Cells. *Biochem. Pharmacol.* **2003**, *66* (2), 225–237. DOI: 10.1016/S0006-2952(03)00260-0.

- Fanizzi, F. P.; Intini, F. P.; Maresca, L.; Natile, G.; Quaranta, R.; Coluccia, M.; Di Bari, L.; Giordano, D.; Mariglió, M. A. Biological Activity of Platinum Complexes Containing Chiral Centers on the Nitrogen or Carbon Atoms of a Chelate Diamine Ring. *Inorganica Chim. Acta* **1987**, *137* (1–2), 45–51. DOI: 10.1016/S0020-1693(00)87114-5.
- Farley-Barnes, K. I.; McCann, K. L.; Ogawa, L. M.; Merkel, J.; Surovtseva, Y. V.; Baserga, S. J. Diverse Regulators of Human Ribosome Biogenesis Discovered by Changes in Nucleolar Number. *Cell Rep.* **2018**, *22* (7), 1923–1934. DOI: 10.1016/j.celrep.2018.01.056.
- Fonseca Guerra, C.; Sanz Miguel, P. J.; Cebollada, A.; Bickelhaupt, F. M.; Lippert, B. Rationalizing the Structural Variability of the Exocyclic Amino Groups in Nucleobases and Their Metal Complexes: Cytosine and Adenine. *Chem. – Eur. J.* **2014**, *20* (31), 9494–9499. DOI: 10.1002/chem.201403066.
- Frederiksen, J. K.; Piccirilli, J. A. Identification of Catalytic Metal Ion Ligands in Ribozymes. *Methods San Diego Calif* **2009**, *49* (2), 148–166. DOI: 10.1016/j.ymeth.2009.07.005.
- Frisch, M. J.; Trucks, G. W.; Schlegel, H. B.; Scuseria, G. E.; Robb, M. A.; Cheeseman, J. R.; Scalmani, G.; Barone, V.; Petersson, G. A.; Nakatsuji, H.; Li, X.; Caricato, M.; Marenich, A.; Bloino, J.; Janesko, B. G.; Gomperts, R.; Mennucci, B.; Hratchian, H. P.; Ortiz, J. V.; Izmaylov, A. F.; Sonnenberg, J. L.; Williams-Young, D.; Ding, F.; Lipparini, F.; Egidi, F.; Goings, J.; Peng, B.; Petrone, A.; Henderson, T.; Ranasinghe, D.; Zakrzewski, V. G.; Gao, J.; Rega, N.; Zheng, G.; Liang, W.; Hada, M.; Ehara, M.; Toyota, K.; Fukuda, R.; Hasegawa, J.; Ishida, M.; Nakajima, T.; Honda, Y.; Kitao, O.; Nakai, H.; Vreven, T.; Throssell, K.; Montgomery, J. A. Gaussian 09, 2016.
- Furukawa, K.; Ramesh, A.; Zhou, Z.; Weinberg, Z.; Vallery, T.; Winkler, W. C.; Breaker, R. R. Bacterial Riboswitches Cooperatively Bind Ni²⁺ or Co²⁺ Ions and Control Expression of Heavy Metal Transporters. *Mol. Cell* **2015**, *57* (6), 1088–1098. DOI: 10.1016/j.molcel.2015.02.009.
- Fyfe, A. C.; Dunten, P. W.; Martick, M. M.; Scott, W. G. Structural Variations and Solvent Structure of r(UGGGGU) Quadruplexes Stabilized by Sr²⁺ Ions. *J. Mol. Biol.* **2015**, *427* (12), 2205–2219. DOI: 10.1016/j.jmb.2015.03.022.
- Garbutcheon-Singh, K. B.; Leverett, P.; Myers, S.; Aldrich-Wright, J. R. Cytotoxic Platinum(II) Intercalators That Incorporate 1R,2R-Diaminocyclopentane. *Dalton Trans* **2013**, *42* (4), 918–926. DOI: 10.1039/C2DT31323E.
- Gebala, M.; Herschlag, D. Quantitative Studies of an RNA Duplex Electrostatics by Ion Counting. *Biophys. J.* **2019**, *117* (6), 1116–1124. DOI: 10.1016/j.bpj.2019.08.007.
- George, S. S.; Pimkin, M.; Paralkar, V. R. Construction and Validation of Customized Genomes for Human and Mouse Ribosomal DNA Mapping. *J. Biol. Chem.* **2023**, *299* (6), 104766. DOI: 10.1016/j.jbc.2023.104766.

- Ghezzi, A.; Aceto, M.; Cassino, C.; Gabano, E.; Osella, D. Uptake of Antitumor Platinum(II)-Complexes by Cancer Cells, Assayed by Inductively Coupled Plasma Mass Spectrometry (ICP-MS). *J. Inorg. Biochem.* **2004**, *98* (1), 73–78. DOI: 10.1016/j.jinorgbio.2003.08.014.
- Ghosh, S. Cisplatin: The First Metal Based Anticancer Drug. *Bioorganic Chem.* **2019**, *88*, 102925. DOI: 10.1016/j.bioorg.2019.102925.
- Gilbert, S. D.; Rambo, R. P.; Van Tyne, D.; Batey, R. T. Structure of the SAM-II Riboswitch Bound to S-Adenosylmethionine. *Nat. Struct. Mol. Biol.* **2008**, *15* (2), 177–182. DOI: 10.1038/nsmb.1371.
- Gill, M. L.; Strobel, S. A.; Loria, J. P. Crystallization and Characterization of the Thallium Form of the Oxytricha Nova G-Quadruplex. *Nucleic Acids Res.* **2006**, *34* (16), 4506–4514. DOI: 10.1093/nar/gkl616.
- González-Arzola, K. The Nucleolus: Coordinating Stress Response and Genomic Stability. *Biochim. Biophys. Acta BBA - Gene Regul. Mech.* **2024**, *1867* (2), 195029. DOI: 10.1016/j.bbagr.2024.195029.
- Goodisman, J.; Rehfuss, R.; Ward, B.; Dabrowiak, J. C. Site-Specific Binding Constants for Actinomycin D on DNA Determined from Footprinting Studies. *Biochemistry* **1992**, *31* (4), 1046–1058. DOI: 10.1021/bi00119a013.
- Greenfeld, M.; Herschlag, D. Chapter 18 - Probing Nucleic Acid–Ion Interactions with Buffer Exchange-Atomic Emission Spectroscopy. In *Methods in Enzymology*; Academic Press, 2009; Vol. 469, pp 375–389. DOI: 10.1016/S0076-6879(09)69018-2.
- Gregory, M. T.; Park, G. Y.; Johnstone, T. C.; Lee, Y.-S.; Yang, W.; Lippard, S. J. Structural and Mechanistic Studies of Polymerase η Bypass of Phenanthriplatin DNA Damage. *Proc. Natl. Acad. Sci.* **2014**, *111* (25), 9133–9138. DOI: 10.1073/pnas.1405739111.
- Hadjiliadis, N. D.; Sletten, E. *Metal Complex-DNA Interactions*; Wiley: Chichester, West Sussex, U.K., 2009.
- Hah, S. S.; Sumbad, R. A.; De Vere White, R. W.; Turteltaub, K. W.; Henderson, P. T. Characterization of Oxaliplatin–DNA Adduct Formation in DNA and Differentiation of Cancer Cell Drug Sensitivity at Microdose Concentrations. *Chem. Res. Toxicol.* **2007**, *20* (12), 1745–1751. DOI: 10.1021/tx700376a.
- Hall, M. D.; Okabe, M.; Shen, D.-W.; Liang, X.-J.; Gottesman, M. M. The Role of Cellular Accumulation in Determining Sensitivity to Platinum-Based Chemotherapy. *Annu. Rev. Pharmacol. Toxicol.* **2008**, *48* (1), 495–535. DOI: 10.1146/annurev.pharmtox.48.080907.180426.

- Hamdane, N.; Herdman, C.; Mars, J.-C.; Stefanovsky, V.; Tremblay, M. G.; Moss, T. Depletion of the Cisplatin Targeted HMGB-Box Factor UBF Selectively Induces P53-Independent Apoptotic Death in Transformed Cells. *Oncotarget* **2015**, *6* (29), 27519–27536. DOI: 10.18632/oncotarget.4823.
- Hamdane, N.; Stefanovsky, V. Y.; Tremblay, M. G.; Németh, A.; Paquet, E.; Lessard, F.; Sanij, E.; Hannan, R.; Moss, T. Conditional Inactivation of Upstream Binding Factor Reveals Its Epigenetic Functions and the Existence of a Somatic Nucleolar Precursor Body. *PLoS Genet.* **2014**, *10* (8), e1004505. DOI: 10.1371/journal.pgen.1004505.
- Hannon, M. J.; Reedijk, J. Metal Interactions with Nucleic Acids. *Dalton Trans.* **2015**, *44* (8), 3503–3504. DOI: 10.1039/C5DT90025E.
- Hayes, R. L.; Noel, J. K.; Mohanty, U.; Whitford, P. C.; Hennelly, S. P.; Onuchic, J. N.; Sanbonmatsu, K. Y. Magnesium Fluctuations Modulate RNA Dynamics in the SAM-I Riboswitch. *J. Am. Chem. Soc.* **2012**, *134* (29), 12043–12053. DOI: 10.1021/ja301454u.
- Hermann, G.; Heffeter, P.; Falta, T.; Berger, W.; Hann, S.; Koellensperger, G. In Vitro Studies on Cisplatin Focusing on Kinetic Aspects of Intracellular Chemistry by LC-ICP-MS. *Metallomics* **2013**, *5* (6), 636. DOI: 10.1039/c3mt20251h.
- Ho, P. S.; Mooers, B. H. M. Z-DNA Crystallography. *Biopolymers* **1997**, *44* (1), 65–90. DOI: 10.1002/(SICI)1097-0282(1997)44:1<65::AID-BIP5>3.0.CO;2-Y.
- Hoogstraten, C. G.; Grant, C. V.; Horton, T. E.; DeRose, V. J.; Britt, R. D. Structural Analysis of Metal Ion Ligation to Nucleotides and Nucleic Acids Using Pulsed EPR Spectroscopy. *J. Am. Chem. Soc.* **2002**, *124* (5), 834–842. DOI: 10.1021/ja0112238.
- Hori, Y.; Engel, C.; Kobayashi, T. Regulation of Ribosomal RNA Gene Copy Number, Transcription and Nucleolus Organization in Eukaryotes. *Nat. Rev. Mol. Cell Biol.* **2023**, *24* (6), 414–429. DOI: 10.1038/s41580-022-00573-9.
- Hostetter, A. A.; Miranda, M. L.; DeRose, V. J.; McFarlane Holman, K. L. Ru Binding to RNA Following Treatment with the Antimetastatic Prodrug NAMI-A in *Saccharomyces Cerevisiae* and in Vitro. *JBIC J. Biol. Inorg. Chem.* **2011**, *16* (8), 1177–1185. DOI: 10.1007/s00775-011-0806-7.
- Hostetter, A. A.; Osborn, M. F.; DeRose, V. J. RNA-Pt Adducts Following Cisplatin Treatment of *Saccharomyces Cerevisiae*. *ACS Chem. Biol.* **2012**, *7* (1), 218–225. DOI: 10.1021/cb200279p.
- Hou, C.; Tsodikov, O. V. Utilizing Guanine-Coordinated Zn²⁺ Ions to Determine DNA Crystal Structures by Single-Wavelength Anomalous Diffraction. *Acta Crystallogr. Sect. Struct. Biol.* **2019**, *75* (1), 32–40. DOI: 10.1107/S205979831801553X.

- Hou, C.; Weidenbach, S.; Cano, K. E.; Wang, Z.; Mitra, P.; Ivanov, D. N.; Rohr, J.; Tsodikov, O. V. Structures of Mithramycin Analogues Bound to DNA and Implications for Targeting Transcription Factor FLII. *Nucleic Acids Res.* **2016**, *44* (18), 8990–9004. DOI: 10.1093/nar/gkw761.
- Huang, L.; Serganov, A.; Patel, D. J. Structural Insights into Ligand Recognition by a Sensing Domain of the Cooperative Glycine Riboswitch. *Mol. Cell* **2010**, *40* (5), 774–786. DOI: 10.1016/j.molcel.2010.11.026.
- Huang, T.-Y.; Chang, C.; Kao, Y.-F.; Chin, C.-H.; Ni, C.-W.; Hsu, H.-Y.; Hu, N.-J.; Hsieh, L.-C.; Chou, S.-H.; Lee, I.-R.; Hou, M.-H. Parity-Dependent Hairpin Configurations of Repetitive DNA Sequence Promote Slippage Associated with DNA Expansion. *Proc. Natl. Acad. Sci.* **2017**, *114* (36), 9535–9540. DOI: 10.1073/pnas.1708691114.
- Huard, D. J. E.; Demissie, A.; Kim, D.; Lewis, D.; Dickson, R. M.; Petty, J. T.; Lieberman, R. L. Atomic Structure of a Fluorescent Ag₈ Cluster Templated by a Multistranded DNA Scaffold. *J. Am. Chem. Soc.* **2019**, *141* (29), 11465–11470. DOI: 10.1021/jacs.8b12203.
- Hud, N. V. *Nucleic Acid-Metal Ion Interactions*; RSC Biomolecular Sciences; The Royal Society of Chemistry, 2008; p P433. DOI: 10.1039/9781847558763.
- Huffines, A. K.; Edwards, Y. J. K.; Schneider, D. A. Spt4 Promotes Pol I Processivity and Transcription Elongation. *Genes* **2021**, *12* (3), 413. DOI: 10.3390/genes12030413.
- Huffines, A. K.; Engel, K. L.; French, S. L.; Zhang, Y.; Viktorovskaya, O. V.; Schneider, D. A. Rate of Transcription Elongation and Sequence-Specific Pausing by RNA Polymerase I Directly Influence rRNA Processing. *J. Biol. Chem.* **2022**, *298* (12), 102730. DOI: 10.1016/j.jbc.2022.102730.
- Hunsicker-Wang, L.; Vogt, M.; DeRose, V. J. EPR Methods to Study Specific Metal-Ion Binding Sites in RNA. In *Methods in Enzymology*; Elsevier, 2009; Vol. 468, pp 335–367. DOI: 10.1016/S0076-6879(09)68016-2.
- Hwang, S.-P.; Denicourt, C. The Impact of Ribosome Biogenesis in Cancer: From Proliferation to Metastasis. *NAR Cancer* **2024**, *6* (2), zcae017. DOI: 10.1093/narcan/zcae017.
- Jacobs, R. Q.; Fuller, K. B.; Cooper, S. L.; Carter, Z. I.; Laiho, M.; Lucius, A. L.; Schneider, D. A. RNA Polymerase I Is Uniquely Vulnerable to the Small-Molecule Inhibitor BMH-21. *Cancers* **2022**, *14* (22), 5544. DOI: 10.3390/cancers14225544.
- Jacobs, R. Q.; Huffines, A. K.; Laiho, M.; Schneider, D. A. The Small-Molecule BMH-21 Directly Inhibits Transcription Elongation and DNA Occupancy of RNA Polymerase I in Vivo and in Vitro. *J. Biol. Chem.* **2022**, *298* (1), 101450. DOI: 10.1016/j.jbc.2021.101450.

- Jamieson, E. R.; Lippard, S. J. Structure, Recognition, and Processing of Cisplatin–DNA Adducts. *Chem. Rev.* **1999**, *99* (9), 2467–2498. DOI: 10.1021/cr980421n.
- Jayarathna, D. R.; Stout, H. D.; Achim, C. Metal Coordination to Ligand-Modified Peptide Nucleic Acid Triplexes. *Inorg. Chem.* **2018**, *57* (12), 6865–6872. DOI: 10.1021/acs.inorgchem.8b00442.
- Jerremalm, E.; Videhult, P.; Alvelius, G.; Griffiths, W. J.; Bergman, T.; Eksborg, S.; Ehrsson, H. Alkaline Hydrolysis of Oxaliplatin—Isolation and Identification of the Oxalato Monodentate Intermediate. *J. Pharm. Sci.* **2002**, *91* (10), 2116–2121. DOI: 10.1002/jps.10201.
- Jha, V.; Ling, H. Structural Basis for Human DNA Polymerase Kappa to Bypass Cisplatin Intrastrand Cross-Link (Pt-GG) Lesion as an Efficient and Accurate Extender. *J. Mol. Biol.* **2018**, *430* (11), 1577–1589. DOI: 10.1016/j.jmb.2018.04.023.
- Jia, S.; Wang, J.; Xie, M.; Sun, J.; Liu, H.; Zhang, Y.; Chao, J.; Li, J.; Wang, L.; Lin, J.; Gothelf, K. V.; Fan, C. Programming DNA Origami Patterning with Non-Canonical DNA-Based Metallization Reactions. *Nat. Commun.* **2019**, *10* (1), 5597. DOI: 10.1038/s41467-019-13507-5.
- Jiang, F.; Doudna, J. A. CRISPR–Cas9 Structures and Mechanisms. *Annu. Rev. Biophys.* **2017**, *46* (1), 505–529. DOI: 10.1146/annurev-biophys-062215-010822.
- Johannsen, S.; Megger, N.; Böhme, D.; Sigel, R. K. O.; Müller, J. Solution Structure of a DNA Double Helix with Consecutive Metal-Mediated Base Pairs. *Nat. Chem.* **2010**, *2* (3), 229–234. DOI: 10.1038/nchem.512.
- Johannsen, S.; Paulus, S.; Düpre, N.; Müller, J.; Sigel, R. K. O. Using in Vitro Transcription to Construct Scaffolds for One-Dimensional Arrays of Mercuric Ions. *J. Inorg. Biochem.* **2008**, *102* (5–6), 1141–1151. DOI: 10.1016/j.jinorgbio.2007.12.023.
- Johnson, B. W.; Burgess, M. W.; Murray, V.; Aldrich-Wright, J. R.; Temple, M. D. The Interactions of Novel Mononuclear Platinum-Based Complexes with DNA. *BMC Cancer* **2018**, *18* (1), 1284. DOI: 10.1186/s12885-018-5194-8.
- Johnstone, T. C.; Lippard, S. J. The Chiral Potential of Phenanthriplatin and Its Influence on Guanine Binding. *J. Am. Chem. Soc.* **2014**, *136* (5), 2126–2134. DOI: 10.1021/ja4125115.
- Johnstone, T. C.; Park, G. Y.; Lippard, S. J. Understanding and Improving Platinum Anticancer Drugs--Phenanthriplatin. *Anticancer Res.* **2014**, *34* (1), 471–476.
- Johnstone, T. C.; Suntharalingam, K.; Lippard, S. J. The Next Generation of Platinum Drugs: Targeted Pt(II) Agents, Nanoparticle Delivery, and Pt(IV) Prodrugs. *Chem. Rev.* **2016**, *116* (5), 3436–3486. DOI: 10.1021/acs.chemrev.5b00597.

- Jordan, P.; Carmo-Fonseca, M. Cisplatin Inhibits Synthesis of Ribosomal RNA in Vivo. *Nucleic Acids Res.* **1998**, *26* (12), 2831–2836. DOI: 10.1093/nar/26.12.2831.
- Kanellis, V. G.; Dos Remedios, C. G. A Review of Heavy Metal Cation Binding to Deoxyribonucleic Acids for the Creation of Chemical Sensors. *Biophys. Rev.* **2018**, *10* (5), 1401–1414. DOI: 10.1007/s12551-018-0455-y.
- Kapinos, L. E.; Operschall, B. P.; Larsen, E.; Sigel, H. Understanding the Acid–Base Properties of Adenosine: The Intrinsic Basicities of N1, N3 and N7. *Chem. Eur. J.* **2011**, *17* (29), 8156–8164.
- Karthik, S.; Thirugnanasambandam, A.; Mandal, P. K.; Gautham, N. Comparison of X-Ray Crystal Structures of a Tetradecamer Sequence d(CCCGGGTACCCGGG)₂ at 1.7 Å Resolution. *Nucleosides Nucleotides Nucleic Acids* **2017**, 1–12. DOI: 10.1080/15257770.2017.1287378.
- Kaul, C.; Müller, M.; Wagner, M.; Schneider, S.; Carell, T. Reversible Bond Formation Enables the Replication and Amplification of a Crosslinking Salen Complex as an Orthogonal Base Pair. *Nat. Chem.* **2011**, *3* (10), 794–800. DOI: 10.1038/nchem.1117.
- Kazantsev, A. V.; Krivenko, A. A.; Pace, N. R. Mapping Metal-Binding Sites in the Catalytic Domain of Bacterial RNase P RNA. *RNA N. Y. N* **2009**, *15* (2), 266–276. DOI: 10.1261/rna.1331809.
- Ke, A.; Ding, F.; Batchelor, J. D.; Doudna, J. A. Structural Roles of Monovalent Cations in the HDV Ribozyme. *Structure* **2007**, *15* (3), 281–287. DOI: 10.1016/j.str.2007.01.017.
- Keck, M. V.; Lippard, S. J. Unwinding of Supercoiled DNA by Platinum-Ethidium and Related Complexes. *J. Am. Chem. Soc.* **1992**, *114* (9), 3386–3390. DOI: 10.1021/ja00035a033.
- Kelland, L. The Resurgence of Platinum-Based Cancer Chemotherapy. *Nat. Rev. Cancer* **2007**, *7* (8), 573–584. DOI: 10.1038/nrc2167.
- Kellinger, M. W.; Park, G. Y.; Chong, J.; Lippard, S. J.; Wang, D. Effect of a Monofunctional Phenanthriplatin-DNA Adduct on RNA Polymerase II Transcriptional Fidelity and Translesion Synthesis. *J. Am. Chem. Soc.* **2013**, *135* (35), 13054–13061. DOI: 10.1021/ja405475y.
- Kim, H.-K.; Liu, J.; Li, J.; Nagraj, N.; Li, M.; Pavot, C. M.-B.; Lu, Y. Metal-Dependent Global Folding and Activity of the 8-17 DNAzyme Studied by Fluorescence Resonance Energy Transfer. *J. Am. Chem. Soc.* **2007**, *129* (21), 6896–6902. DOI: 10.1021/ja0712625.

- Kim, J.-H.; Dilthey, A. T.; Nagaraja, R.; Lee, H.-S.; Koren, S.; Dudekula, D.; Wood III, W. H.; Piao, Y.; Ogurtsov, A. Y.; Utani, K.; Noskov, V. N.; Shabalina, S. A.; Schlessinger, D.; Phillippy, A. M.; Larionov, V. Variation in Human Chromosome 21 Ribosomal RNA Genes Characterized by TAR Cloning and Long-Read Sequencing. *Nucleic Acids Res.* **2018**, *46* (13), 6712–6725. DOI: 10.1093/nar/gky442.
- Klein, D. J.; Moore, P. B.; Steitz, T. A. The Contribution of Metal Ions to the Structural Stability of the Large Ribosomal Subunit. *RNA N. Y. N* **2004**, *10* (9), 1366–1379. DOI: 10.1261/rna.7390804.
- Klose, M.; Theiner, S.; Varbanov, H.; Hoefler, D.; Pichler, V.; Galanski, M. S.; Meier-Menches, S.; Keppler, B. Development and Validation of Liquid Chromatography-Based Methods to Assess the Lipophilicity of Cytotoxic Platinum(IV) Complexes. *Inorganics* **2018**, *6* (4), 130. DOI: 10.3390/inorganics6040130.
- Koag, M.-C.; Lai, L.; Lee, S. Structural Basis for the Inefficient Nucleotide Incorporation Opposite Cisplatin-DNA Lesion by Human DNA Polymerase β . *J. Biol. Chem.* **2014**, *289* (45), 31341–31348. DOI: 10.1074/jbc.M114.605451.
- Koch, S. C.; Kuper, J.; Gasteiger, K. L.; Simon, N.; Strasser, R.; Eisen, D.; Geiger, S.; Schneider, S.; Kisker, C.; Carell, T. Structural Insights into the Recognition of Cisplatin and AAF-dG Lesion by Rad14 (XPA). *Proc. Natl. Acad. Sci.* **2015**, *112* (27), 8272–8277. DOI: 10.1073/pnas.1508509112.
- Kolev, S. K.; Petkov, P. St.; Rangelov, M. A.; Trifonov, D. V.; Milenov, T. I.; Vayssilov, G. N. Interaction of Na^+ , K^+ , Mg^{2+} and Ca^{2+} Counter Cations with RNA. *Metallomics* **2018**, *10* (5), 659–678. DOI: 10.1039/C8MT00043C.
- Komeda, S.; Moulaei, T.; Woods, K. K.; Chikuma, M.; Farrell, N. P.; Williams, L. D. A Third Mode of DNA Binding: Phosphate Clamps by a Polynuclear Platinum Complex. *J. Am. Chem. Soc.* **2006**, *128* (50), 16092–16103. DOI: 10.1021/ja062851y.
- Kondo, J.; Sugawara, T.; Saneyoshi, H.; Ono, A. Crystal Structure of a DNA Duplex Containing Four Ag(I) Ions in Consecutive Dinuclear Ag(I)-Mediated Base Pairs: 4-Thiothymine–2Ag(I)–4-Thiothymine. *Chem Commun* **2017**, *53* (86), 11747–11750. DOI: 10.1039/C7CC06153F.
- Kondo, J.; Tada, Y.; Dairaku, T.; Hattori, Y.; Saneyoshi, H.; Ono, A.; Tanaka, Y. A Metallo-DNA Nanowire with Uninterrupted One-Dimensional Silver Array. *Nat. Chem.* **2017**, *9* (10), 956–960. DOI: 10.1038/nchem.2808.
- Kondo, J.; Tada, Y.; Dairaku, T.; Saneyoshi, H.; Okamoto, I.; Tanaka, Y.; Ono, A. High-Resolution Crystal Structure of a Silver(I)–RNA Hybrid Duplex Containing Watson–Crick-like C–Silver(I)–C Metallo-Base Pairs. *Angew. Chem. Int. Ed.* **2015**, *54* (45), 13323–13326. DOI: 10.1002/anie.201507894.

- Kondo, J.; Yamada, T.; Hirose, C.; Okamoto, I.; Tanaka, Y.; Ono, A. Crystal Structure of Metallo DNA Duplex Containing Consecutive Watson-Crick-like T-Hg^{II}-T Base Pairs. *Angew. Chem. Int. Ed.* **2014**, *53* (9), 2385–2388. DOI: 10.1002/anie.201309066.
- Kraemer-Chant, C. M.; Heckman, J. E.; Lambert, D.; Burke, J. M. Cobalt(III)Hexaammine-Dependent Photocrosslinks in the Hairpin Ribozyme. *J. Inorg. Biochem.* **2014**, *131*, 87–98. DOI: 10.1016/j.jinorgbio.2013.11.001.
- Kresse, G.; Furthmüller, J. Efficiency of Ab-Initio Total Energy Calculations for Metals and Semiconductors Using a Plane-Wave Basis Set. *Comput. Mater. Sci.* **1996**, *6* (1), 15–50. DOI: 10.1016/0927-0256(96)00008-0.
- Kresse, G.; Furthmüller, J. Efficient Iterative Schemes for *Ab Initio* Total-Energy Calculations Using a Plane-Wave Basis Set. *Phys. Rev. B* **1996**, *54* (16), 11169–11186. DOI: 10.1103/PhysRevB.54.11169.
- Kresse, G.; Hafner, J. *Ab Initio* Molecular Dynamics for Liquid Metals. *Phys. Rev. B* **1993**, *47* (1), 558–561. DOI: 10.1103/PhysRevB.47.558.
- Kresse, G.; Hafner, J. *Ab Initio* Molecular-Dynamics Simulation of the Liquid-Metal–Amorphous-Semiconductor Transition in Germanium. *Phys. Rev. B* **1994**, *49* (20), 14251–14269. DOI: 10.1103/PhysRevB.49.14251.
- Kresse, G.; Joubert, D. From Ultrasoft Pseudopotentials to the Projector Augmented-Wave Method. *Phys. Rev. B* **1999**, *59* (3), 1758–1775. DOI: 10.1103/PhysRevB.59.1758.
- Kumbhar, S.; Johannsen, S.; Sigel, R. K. O.; Waller, M. P.; Müller, J. A QM/MM Refinement of an Experimental DNA Structure with Metal-Mediated Base Pairs. *J. Inorg. Biochem.* **2013**, *127*, 203–210. DOI: 10.1016/j.jinorgbio.2013.03.009.
- Kuzuya, A.; Ohya, Y. Nanomechanical Molecular Devices Made of DNA Origami. *Acc. Chem. Res.* **2014**, *47* (6), 1742–1749. DOI: 10.1021/ar400328v.
- Labiuk, S. L.; Delbaere, L. T. J.; Lee, J. S. Cobalt(II), Nickel(II) and Zinc(II) Do Not Bind to Intra-Helical N(7) Guanine Positions in the B-Form Crystal Structure of d(GGCGCC). *JBIC J. Biol. Inorg. Chem.* **2003**, *8* (7), 715–720. DOI: 10.1007/s00775-003-0473-4.
- Lafontaine, D. L. J.; Riback, J. A.; Bascetin, R.; Brangwynne, C. P. The Nucleolus as a Multiphase Liquid Condensate. *Nat. Rev. Mol. Cell Biol.* **2021**, *22* (3), 165–182. DOI: 10.1038/s41580-020-0272-6.
- Lake, R. J.; Yang, Z.; Zhang, J.; Lu, Y. DNAzymes as Activity-Based Sensors for Metal Ions: Recent Applications, Demonstrated Advantages, Current Challenges, and Future Directions. *Acc. Chem. Res.* **2019**, *52* (12), 3275–3286. DOI: 10.1021/acs.accounts.9b00419.

- Langmead, B.; Salzberg, S. L. Fast Gapped-Read Alignment with Bowtie 2. *Nat. Methods* **2012**, *9* (4), 357–359. DOI: 10.1038/nmeth.1923.
- Leonarski, F.; D'Ascenzo, L.; Auffinger, P. Nucleobase Carbonyl Groups Are Poor Mg²⁺ Inner-Sphere Binders but Excellent Monovalent Ion Binders—a Critical PDB Survey. *RNA* **2019**, *25* (2), 173–192. DOI: 10.1261/rna.068437.118.
- Leontis, N. B.; Westhof, E. Analysis of RNA Motifs. *Curr. Opin. Struct. Biol.* **2003**, *13* (3), 300–308. DOI: 10.1016/S0959-440X(03)00076-9.
- Levina, A.; Crans, D. C.; Lay, P. A. Speciation of Metal Drugs, Supplements and Toxins in Media and Bodily Fluids Controls in Vitro Activities. *Coord. Chem. Rev.* **2017**, *352*, 473–498. DOI: 10.1016/j.ccr.2017.01.002.
- Li, H.; Handsaker, B.; Wysoker, A.; Fennell, T.; Ruan, J.; Homer, N.; Marth, G.; Abecasis, G.; Durbin, R.; 1000 Genome Project Data Processing Subgroup. The Sequence Alignment/Map Format and SAMtools. *Bioinformatics* **2009**, *25* (16), 2078–2079. DOI: 10.1093/bioinformatics/btp352.
- Li, S.; Su, Z.; Lehmann, J.; Stamatopoulou, V.; Giarimoglou, N.; Henderson, F. E.; Fan, L.; Pintilie, G. D.; Zhang, K.; Chen, M.; Ludtke, S. J.; Wang, Y.-X.; Stathopoulos, C.; Chiu, W.; Zhang, J. Structural Basis of Amino Acid Surveillance by Higher-Order tRNA-mRNA Interactions. *Nat. Struct. Mol. Biol.* **2019**, *26* (12), 1094–1105. DOI: 10.1038/s41594-019-0326-7.
- Liberman, J. A.; Salim, M.; Krucinska, J.; Wedekind, J. E. Structure of a Class II preQ₁ Riboswitch Reveals Ligand Recognition by a New Fold. *Nat. Chem. Biol.* **2013**, *9* (6), 353–355. DOI: 10.1038/nchembio.1231.
- Lipfert, J.; Doniach, S.; Das, R.; Herschlag, D. Understanding Nucleic Acid–Ion Interactions. *Annu. Rev. Biochem.* **2014**, *83* (1), 813–841. DOI: 10.1146/annurev-biochem-060409-092720.
- Lippert, B. Ligand-pK_a Shifts through Metals: Potential Relevance to Ribozyme Chemistry. *Chem. Biodivers.* **2008**, *5* (8), 1455–1474. DOI: 10.1002/cbdv.200890135.
- Liu, H.; Cai, C.; Haruehanroengra, P.; Yao, Q.; Chen, Y.; Yang, C.; Luo, Q.; Wu, B.; Li, J.; Ma, J.; Sheng, J.; Gan, J. Flexibility and Stabilization of Hg^{II}-Mediated C:T and T:T Base Pairs in DNA Duplex. *Nucleic Acids Res.* **2017**, *45* (5), 2910–2918. DOI: 10.1093/nar/gkw1296.
- Liu, H.; Shen, F.; Haruehanroengra, P.; Yao, Q.; Cheng, Y.; Chen, Y.; Yang, C.; Zhang, J.; Wu, B.; Luo, Q.; Cui, R.; Li, J.; Ma, J.; Sheng, J.; Gan, J. A DNA Structure Containing Ag^I-Mediated G:G and C:C Base Pairs. *Angew. Chem. Int. Ed.* **2017**, *56* (32), 9430–9434. DOI: 10.1002/anie.201704891.

- Liu, H.; Wang, R.; Yu, X.; Shen, F.; Lan, W.; Haruehanroengra, P.; Yao, Q.; Zhang, J.; Chen, Y.; Li, S.; Wu, B.; Zheng, L.; Ma, J.; Lin, J.; Cao, C.; Li, J.; Sheng, J.; Gan, J. High-Resolution DNA Quadruplex Structure Containing All the A-, G-, C-, T-Tetrads. *Nucleic Acids Res.* **2018**, *46* (21), 11627–11638. DOI: 10.1093/nar/gky902.
- Liu, H.; Yu, X.; Chen, Y.; Zhang, J.; Wu, B.; Zheng, L.; Haruehanroengra, P.; Wang, R.; Li, S.; Lin, J.; Li, J.; Sheng, J.; Huang, Z.; Ma, J.; Gan, J. Crystal Structure of an RNA-Cleaving DNAzyme. *Nat. Commun.* **2017**, *8* (1). DOI: 10.1038/s41467-017-02203-x.
- Liu, Y.; Freeman, A. D. J.; Déclais, A.-C.; Lilley, D. M. J. A Monovalent Ion in the DNA Binding Interface of the Eukaryotic Junction-Resolving Enzyme GEN1. *Nucleic Acids Res.* **2018**, *46*, 11089–11098. DOI: 10.1093/nar/gky863.
- Lopez-Delisle, L.; Rabbani, L.; Wolff, J.; Bhardwaj, V.; Backofen, R.; Grüning, B.; Ramírez, F.; Manke, T. pyGenomeTracks: Reproducible Plots for Multivariate Genomic Datasets. *Bioinformatics* **2021**, *37* (3), 422–423. DOI: 10.1093/bioinformatics/btaa692.
- Lovejoy, K. S.; Todd, R. C.; Zhang, S.; McCormick, M. S.; D'Aquino, J. A.; Reardon, J. T.; Sancar, A.; Giacomini, K. M.; Lippard, S. J. *Cis*-Diammine(Pyridine)Chloroplatinum(II), a Monofunctional Platinum(II) Antitumor Agent: Uptake, Structure, Function, and Prospects. *Proc. Natl. Acad. Sci.* **2008**, *105* (26), 8902–8907. DOI: 10.1073/pnas.0803441105.
- Lu, L.; Yi, H.; Chen, C.; Yan, S.; Yao, H.; He, G.; Li, G.; Jiang, Y.; Deng, T.; Deng, X. Nucleolar Stress: Is There a Reverse Version? *J. Cancer* **2018**, *9* (20), 3723–3727. DOI: 10.7150/jca.27660.
- Malina, J.; Novakova, O.; Vojtiskova, M.; Natile, G.; Brabec, V. Conformation of DNA GG Intrastrand Cross-Link of Antitumor Oxaliplatin and Its Enantiomeric Analog. *Biophys. J.* **2007**, *93* (11), 3950–3962. DOI: 10.1529/biophysj.107.116996.
- Mandal, P. K.; Collie, G. W.; Kauffmann, B.; Huc, I. Racemic DNA Crystallography. *Angew. Chem. Int. Ed.* **2014**, *53* (52), 14424–14427. DOI: 10.1002/anie.201409014.
- Mandal, P. K.; Collie, G. W.; Srivastava, S. C.; Kauffmann, B.; Huc, I. Structure Elucidation of the Pribnow Box Consensus Promoter Sequence by Racemic DNA Crystallography. *Nucleic Acids Res.* **2016**, *44* (12), 5936–5943. DOI: 10.1093/nar/gkw367.
- Mandal, P. K.; Venkadesh, S.; Gautham, N. Interactions of Mn²⁺ with a Non-Self-Complementary Z-Type DNA Duplex. *Acta Crystallograph. Sect. F Struct. Biol. Cryst. Commun.* **2012**, *68* (12), 1420–1426. DOI: 10.1107/S1744309112041759.
- Mandal, P. K.; Venkadesh, S.; Gautham, N. Structure of the Tetradecanucleotide d(CCCCGGTACCGGG)₂ as an A-DNA Duplex. *Acta Crystallograph. Sect. F Struct. Biol. Cryst. Commun.* **2012**, *68* (4), 393–399. DOI: 10.1107/S174430911200869X.

- Marcia, M.; Pyle, A. M. Visualizing Group II Intron Catalysis through the Stages of Splicing. *Cell* **2012**, *151* (3), 497–507. DOI: 10.1016/j.cell.2012.09.033.
- Marenich, A. V.; Cramer, C. J.; Truhlar, D. G. Universal Solvation Model Based on Solute Electron Density and on a Continuum Model of the Solvent Defined by the Bulk Dielectric Constant and Atomic Surface Tensions. *J. Phys. Chem. B* **2009**, *113* (18), 6378–6396. DOI: 10.1021/jp810292n.
- Mars, Jean-Clement; Sabourin-Felix, M.; Tremblay, M. G.; Moss, T. A Deconvolution Protocol for ChIP-Seq Reveals Analogous Enhancer Structures on the Mouse and Human Ribosomal RNA Genes. *G3 GenesGenomesGenetics* **2018**, *8* (1), 303–314. DOI: 10.1534/g3.117.300225.
- Mars, Jean-Clément; Tremblay, M. G.; Valere, M.; Sibai, D. S.; Sabourin-Felix, M.; Lessard, F.; Moss, T. The Chemotherapeutic Agent CX-5461 Irreversibly Blocks RNA Polymerase I Initiation and Promoter Release to Cause Nucleolar Disruption, DNA Damage and Cell Inviability. *NAR Cancer* **2020**, *2* (4), zcaa032. DOI: 10.1093/narcan/zcaa032.
- Martick, M.; Lee, T.-S.; York, D. M.; Scott, W. G. Solvent Structure and Hammerhead Ribozyme Catalysis. *Chem. Biol.* **2008**, *15* (4), 332–342. DOI: 10.1016/j.chembiol.2008.03.010.
- Martinez-Zapien, D.; Legrand, P.; McEwen, A. G.; Proux, F.; Cragnolini, T.; Pasquali, S.; Dock-Bregeon, A.-C. The Crystal Structure of the 5' Functional Domain of the Transcription Riboregulator 7SK. *Nucleic Acids Res.* **2017**, gkw1351. DOI: 10.1093/nar/gkw1351.
- Mazumdar, D.; Nagraj, N.; Kim, H.-K.; Meng, X.; Brown, A. K.; Sun, Q.; Li, W.; Lu, Y. Activity, Folding and Z-DNA Formation of the 8-17 DNAzyme in the Presence of Monovalent Ions. *J. Am. Chem. Soc.* **2009**, *131* (15), 5506–5515. DOI: 10.1021/ja8082939.
- McDevitt, C. E.; Guerrero, A. S.; Smith, H. M.; DeRose, V. J. Influence of Ring Modifications on Nucleolar Stress Caused by Oxaliplatin-Like Compounds**. *ChemBioChem* **2022**, *23* (14), e202200130. DOI: 10.1002/cbic.202200130.
- McDevitt, C. E.; Yglesias, M. V.; Mroz, A. M.; Sutton, E. C.; Yang, M. C.; Hendon, C. H.; DeRose, V. J. Monofunctional Platinum(II) Compounds and Nucleolar Stress: Is Phenanthriplatin Unique? *JBIC J. Biol. Inorg. Chem.* **2019**, *24* (6), 899–908. DOI: 10.1007/s00775-019-01707-9.
- McKeage, M. J.; Hsu, T.; Screnci, D.; Haddad, G.; Baguley, B. C. Nucleolar Damage Correlates with Neurotoxicity Induced by Different Platinum Drugs. *Br. J. Cancer* **2001**, *85* (8), 1219–1225. DOI: 10.1054/bjoc.2001.2024.
- Medina-Molner, A.; Spingler, B. When Two Metal Centres Are Needed Instead of One: Exclusive Induction of Z-DNA by Dinuclear Metal Complexes. *Chem. Commun.* **2012**, *48* (14), 1961–1963. DOI: 10.1039/C2CC16483C.

- Meisburger, S. P.; Pabit, S. A.; Pollack, L. Determining the Locations of Ions and Water around DNA from X-Ray Scattering Measurements. *Biophys. J.* **2015**, *108* (12), 2886–2895. DOI: 10.1016/j.bpj.2015.05.006.
- Melnikov, S. V.; Söll, D.; Steitz, T. A.; Polikanov, Y. S. Insights into RNA Binding by the Anticancer Drug Cisplatin from the Crystal Structure of Cisplatin-Modified Ribosome. *Nucleic Acids Res.* **2016**, *44* (10), 4978–4987. DOI: 10.1093/nar/gkw246.
- Millonig, H.; Pous, J.; Gouyette, C.; Subirana, J. A.; Campos, J. L. The Interaction of Manganese Ions with DNA. *J. Inorg. Biochem.* **2009**, *103* (6), 876–880. DOI: 10.1016/j.jinorgbio.2009.03.004.
- Milo, R.; Phillips, R.; Orme, N. *Cell Biology by the Numbers*; Garland Science, 2016.
- Mir, A.; Chen, J.; Robinson, K.; Lendy, E.; Goodman, J.; Neau, D.; Golden, B. L. Two Divalent Metal Ions and Conformational Changes Play Roles in the Hammerhead Ribozyme Cleavage Reaction. *Biochemistry* **2015**, *54* (41), 6369–6381. DOI: 10.1021/acs.biochem.5b00824.
- Mohideen, K.; Muhammad, R.; Davey, C. A. Perturbations in Nucleosome Structure from Heavy Metal Association. *Nucleic Acids Res.* **2010**, *38* (18), 6301–6311. DOI: 10.1093/nar/gkq420.
- Mooers, B. H. M.; Singh, A. The Crystal Structure of an Oligo(U):Pre-mRNA Duplex from a Trypanosome RNA Editing Substrate. *RNA* **2011**, *17* (10), 1870–1883. DOI: 10.1261/rna.2880311.
- Moon, W. J.; Liu, J. Replacing Mg²⁺ by Fe²⁺ for RNA-Cleaving DNazymes. *ChemBioChem* **2020**, *21* (3), 401–407. DOI: 10.1002/cbic.201900344.
- Morris, D. L. DNA-Bound Metal Ions: Recent Developments. *Biomol. Concepts* **2014**, *5* (5), 397–407. DOI: 10.1515/bmc-2014-0021.
- Moulaei, T.; Maehigashi, T.; Lountos, G. T.; Komeda, S.; Watkins, D.; Stone, M. P.; Marky, L. A.; Li, J.; Gold, B.; Williams, L. D. Structure of B-DNA with Cations Tethered in the Major Groove[†]. *Biochemistry* **2005**, *44* (20), 7458–7468. DOI: 10.1021/bi050128z.
- Müller, J. Nucleic Acid Duplexes with Metal-Mediated Base Pairs and Their Structures. *Coord. Chem. Rev.* **2019**, *393*, 37–47. DOI: 10.1016/j.ccr.2019.05.007.
- del Mundo, I. M. A.; Sitters, K. E.; Fountain, M. A.; Morrow, J. R. Structural Basis for Bifunctional Zinc(II) Macrocyclic Complex Recognition of Thymine Bulges in DNA. *Inorg. Chem.* **2012**, *51* (9), 5444–5457. DOI: 10.1021/ic3004245.
- Nechay, M.; Wang, D.; Kleiner, R. E. Inhibition of Nucleolar Transcription by Oxaliplatin Involves ATM/ATR Kinase Signaling. *Cell Chem. Biol.* **2023**, *30* (8), 906–919.e4. DOI: 10.1016/j.chembiol.2023.06.010.

- Negi, S. S.; Brown, P. rRNA Synthesis Inhibitor, CX-5461, Activates ATM/ATR Pathway in Acute Lymphoblastic Leukemia, Arrests Cells in G2 Phase and Induces Apoptosis. *Oncotarget* **2015**, *6* (20), 18094–18104. DOI: 10.18632/oncotarget.4093.
- Németh, A.; Guibert, S.; Tiwari, V. K.; Ohlsson, R.; Längst, G. Epigenetic Regulation of TTF-I-Mediated Promoter–Terminator Interactions of rRNA Genes. *EMBO J.* **2008**, *27* (8), 1255–1265. DOI: 10.1038/emboj.2008.57.
- Nguyen, D.; Zandarashvili, L.; White, M. A.; Iwahara, J. Stereospecific Effects of Oxygen-to-Sulfur Substitution in DNA Phosphate on Ion Pair Dynamics and Protein-DNA Affinity. *ChemBioChem* **2016**, *17* (17), 1636–1642. DOI: 10.1002/cbic.201600265.
- Nicolas, E.; Parisot, P.; Pinto-Monteiro, C.; De Walque, R.; De Vleeschouwer, C.; Lafontaine, D. L. J. Involvement of Human Ribosomal Proteins in Nucleolar Structure and P53-Dependent Nucleolar Stress. *Nat. Commun.* **2016**, *7* (1), 11390. DOI: 10.1038/ncomms11390.
- Novikova, I. V.; Hennelly, S. P.; Tung, C.-S.; Sanbonmatsu, K. Y. Rise of the RNA Machines: Exploring the Structure of Long Non-Coding RNAs. *J. Mol. Biol.* **2013**, *425* (19), 3731–3746.
- Nurk, S.; Koren, S.; Rhie, A.; Rautiainen, M.; Bzikadze, A. V.; Mikheenko, A.; Vollger, M. R.; Altemose, N.; Uralsky, L.; Gershman, A.; Aganezov, S.; Hoyt, S. J.; Diekhans, M.; Logsdon, G. A.; Alonge, M.; Antonarakis, S. E.; Borchers, M.; Bouffard, G. G.; Brooks, S. Y.; Caldas, G. V.; Chen, N.-C.; Cheng, H.; Chin, C.-S.; Chow, W.; de Lima, L. G.; Dishuck, P. C.; Durbin, R.; Dvorkina, T.; Fiddes, I. T.; Formenti, G.; Fulton, R. S.; Fungtammasan, A.; Garrison, E.; Grady, P. G. S.; Graves-Lindsay, T. A.; Hall, I. M.; Hansen, N. F.; Hartley, G. A.; Haukness, M.; Howe, K.; Hunkapiller, M. W.; Jain, C.; Jain, M.; Jarvis, E. D.; Kerpedjiev, P.; Kirsche, M.; Kolmogorov, M.; Korlach, J.; Kremitzki, M.; Li, H.; Maduro, V. V.; Marschall, T.; McCartney, A. M.; McDaniel, J.; Miller, D. E.; Mullikin, J. C.; Myers, E. W.; Olson, N. D.; Paten, B.; Peluso, P.; Pevzner, P. A.; Porubsky, D.; Potapova, T.; Rogaev, E. I.; Rosenfeld, J. A.; Salzberg, S. L.; Schneider, V. A.; Sedlazeck, F. J.; Shafin, K.; Shew, C. J.; Shumate, A.; Sims, Y.; Smit, A. F. A.; Soto, D. C.; Sović, I.; Storer, J. M.; Streets, A.; Sullivan, B. A.; Thibaud-Nissen, F.; Torrance, J.; Wagner, J.; Walenz, B. P.; Wenger, A.; Wood, J. M. D.; Xiao, C.; Yan, S. M.; Young, A. C.; Zarate, S.; Surti, U.; McCoy, R. C.; Dennis, M. Y.; Alexandrov, I. A.; Gerton, J. L.; O'Neill, R. J.; Timp, W.; Zook, J. M.; Schatz, M. C.; Eichler, E. E.; Miga, K. H.; Phillippy, A. M. The Complete Sequence of a Human Genome. *Science* **2022**, *376* (6588), 44–53. DOI: 10.1126/science.abj6987.
- O'Dowd, P. D.; Sutcliffe, D. F.; Griffith, D. M. Oxaliplatin and Its Derivatives – An Overview. *Coord. Chem. Rev.* **2023**, *497*, 215439. DOI: 10.1016/j.ccr.2023.215439.

- OECD. *Test No. 107: Partition Coefficient (n-Octanol/Water): Shake Flask Method*; OECD Guidelines for the Testing of Chemicals, Section 1; OECD, 1995. DOI: 10.1787/9789264069626-en.
- Okada, T.; El-Mehasseb, I. M.; Kodaka, M.; Tomohiro, T.; Okamoto, K.; Okuno, H. Mononuclear Platinum(II) Complex with 2-Phenylpyridine Ligands Showing High Cytotoxicity against Mouse Sarcoma 180 Cells Acquiring High Cisplatin Resistance. *J. Med. Chem.* **2001**, *44* (26), 4661–4667. DOI: 10.1021/jm010203d.
- Ono, A.; Kanazawa, H.; Ito, H.; Goto, M.; Nakamura, K.; Saneyoshi, H.; Kondo, J. A Novel DNA Helical Wire Containing Hg^{II}-Mediated T:T and T:G Pairs. *Angew. Chem. Int. Ed.* **2019**, *58* (47), 16835–16838. DOI: 10.1002/anie.201910029.
- Ono, A.; Torigoe, H.; Tanaka, Y.; Okamoto, I. Binding of Metal Ions by Pyrimidine Base Pairs in DNA Duplexes. *Chem. Soc. Rev.* **2011**, *40* (12), 5855–5866.
- Osborn, M. F.; White, J. D.; Haley, M. M.; DeRose, V. J. Platinum-RNA Modifications Following Drug Treatment in *S. Cerevisiae* Identified by Click Chemistry and Enzymatic Mapping. *ACS Chem. Biol.* **2014**, *9* (10), 2404–2411. DOI: 10.1021/cb500395z.
- Ouzon-Shubeita, H.; Baker, M.; Koag, M.-C.; Lee, S. Structural Basis for the Bypass of the Major Oxaliplatin–DNA Adducts by Human DNA Polymerase η . *Biochem. J.* **2019**, *476* (4), 747–758. DOI: 10.1042/BCJ20180848.
- Pages, B. J.; Ang, D. L.; Wright, E. P.; Aldrich-Wright, J. R. Metal Complex Interactions with DNA. *Dalton Trans.* **2015**, *44* (8), 3505–3526. DOI: 10.1039/C4DT02700K.
- Palmer, B. F. Regulation of Potassium Homeostasis. *Clin. J. Am. Soc. Nephrol.* **2015**, *10* (6), 1050–1060. DOI: 10.2215/CJN.08580813.
- Pan, T.; Uhlenbeck, O. C. In Vitro Selection of RNAs That Undergo Autolytic Cleavage with Lead(2+). *Biochemistry* **1992**, *31* (16), 3887–3895. DOI: 10.1021/bi00131a001.
- Pansini, F. N. N.; Neto, A. C.; De Campos, M.; De Aquino, R. M. Effects of All-Electron Basis Sets and the Scalar Relativistic Corrections in the Structure and Electronic Properties of Niobium Clusters. *J. Phys. Chem. A* **2017**, *121* (30), 5728–5734. DOI: 10.1021/acs.jpca.7b04600.
- Park, G. Y.; Wilson, J. J.; Song, Y.; Lippard, S. J. Phenanthriplatin, a Monofunctional DNA-Binding Platinum Anticancer Drug Candidate with Unusual Potency and Cellular Activity Profile. *Proc. Natl. Acad. Sci.* **2012**, *109* (30), 11987–11992. DOI: 10.1073/pnas.1207670109.
- Patel, M. N.; Patidar, A. P.; Karia, P. S.; Vekariya, P. A. Cytotoxic, Antibacterial and Nucleic Acid Interaction Studies of Square Planar Palladium(II) Complexes. *Inorganica Chim. Acta* **2014**, *419*, 45–54. DOI: 10.1016/j.ica.2014.04.037.

- Pechlaner, M.; Sigel, R. K. O. Characterization of Metal Ion-Nucleic Acid Interactions in Solution. In *Interplay between Metal Ions and Nucleic Acids*; Sigel, A., Sigel, H., Sigel, R. K. O., Eds.; Metal Ions in Life Sciences; Springer Netherlands: Dordrecht, 2012; Vol. 10, pp 1–42. DOI: 10.1007/978-94-007-2172-2_1.
- Peltonen, K.; Colis, L.; Liu, H.; Trivedi, R.; Moubarek, M. S.; Moore, H. M.; Bai, B.; Rudek, M. A.; Bieberich, C. J.; Laiho, M. A Targeting Modality for Destruction of RNA Polymerase I That Possesses Anticancer Activity. *Cancer Cell* **2014**, 25 (1), 77–90. DOI: 10.1016/j.ccr.2013.12.009.
- Peña, C.; Hurt, E.; Panse, V. G. Eukaryotic Ribosome Assembly, Transport and Quality Control. *Nat. Struct. Mol. Biol.* **2017**, 24 (9), 689–699. DOI: 10.1038/nsmb.3454.
- Penzo, M.; Montanaro, L.; Treré, D.; Derenzini, M. The Ribosome Biogenesis—Cancer Connection. *Cells* **2019**, 8 (1), 55. DOI: 10.3390/cells8010055.
- Perdew, J. P.; Burke, K.; Ernzerhof, M. Generalized Gradient Approximation Made Simple. *Phys. Rev. Lett.* **1996**, 77 (18), 3865–3868. DOI: 10.1103/PhysRevLett.77.3865.
- Perdew, J. P.; Burke, K.; Ernzerhof, M. Generalized Gradient Approximation Made Simple [Phys. Rev. Lett. 77, 3865 (1996)]. *Phys. Rev. Lett.* **1997**, 78 (7), 1396–1396. DOI: 10.1103/PhysRevLett.78.1396.
- Peselis, A.; Serganov, A. *ykkC* Riboswitches Employ an Add-on Helix to Adjust Specificity for Polyanionic Ligands. *Nat. Chem. Biol.* **2018**, 14 (9), 887–894. DOI: 10.1038/s41589-018-0114-4.
- Peterson, E. J.; Menon, V. R.; Gatti, L.; Kipping, R.; Dewasinghe, D.; Perego, P.; Povirk, L. F.; Farrell, N. P. Nucleolar Targeting by Platinum: P53-Independent Apoptosis Follows rRNA Inhibition, Cell-Cycle Arrest, and DNA Compaction. *Mol. Pharm.* **2015**, 12 (1), 287–297. DOI: 10.1021/mp5006867.
- Petrou, A. L. Interactions of Aluminum(III) with the Biologically Relevant Ligand d-Ribose. *Coord. Chem. Rev.* **2002**, 228 (2), 153–162. DOI: 10.1016/S0010-8545(01)00466-0.
- Petterson, E. F.; Goddard, T. D.; Huang, C. C.; Meng, E. C.; Couch, G. S.; Croll, T. I.; Morris, J. H.; Ferrin, T. E. UCSF CHIMERAX: Structure Visualization for Researchers, Educators, and Developers. *Protein Sci.* **2021**, 30 (1), 70–82. DOI: 10.1002/pro.3943.
- Pickard, A. J.; Bierbach, U. The Cell's Nucleolus: An Emerging Target for Chemotherapeutic Intervention. *ChemMedChem* **2013**, 8 (9), 1441–1449. DOI: 10.1002/cmdc.201300262.
- Pierre, V. C.; Kaiser, J. T.; Barton, J. K. Insights into Finding a Mismatch through the Structure of a Mismatched DNA Bound by a Rhodium Intercalator. *Proc. Natl. Acad. Sci.* **2007**, 104 (2), 429–434. DOI: 10.1073/pnas.0610170104.

- Pigg, H. C.; Alley, K. R.; Griffin, C. R.; Moon, C. H.; Kraske, S. J.; DeRose, V. J. The Unique Pt(II)-Induced Nucleolar Stress Response and Its Deviation from DNA Damage Response Pathways. *J. Biol. Chem.* **2024**, 107858. DOI: 10.1016/j.jbc.2024.107858.
- Pigg, H. C.; Yglesias, M. V.; Sutton, E. C.; McDevitt, C. E.; Shaw, M.; DeRose, V. J. Time-Dependent Studies of Oxaliplatin and Other Nucleolar Stress-Inducing Pt(II) Derivatives. *ACS Chem. Biol.* **2022**, 17 (8), 2262–2271. DOI: 10.1021/acscchembio.2c00399.
- Pikovskaya, O.; Polonskaia, A.; Patel, D. J.; Serganov, A. Structural Principles of Nucleoside Selectivity in a 2'-Deoxyguanosine Riboswitch. *Nat. Chem. Biol.* **2011**, 7 (10), 748–755. DOI: 10.1038/nchembio.631.
- Pitts, S.; Laiho, M. Regulation of RNA Polymerase I Stability and Function. *Cancers* **2022**, 14 (23), 5776. DOI: 10.3390/cancers14235776.
- Pizarro, A. M.; Sadler, P. J. Chapter 10 Metal Ion–Nucleic Acid Interactions in Disease and Medicine. In *Nucleic Acid-Metal Ion Interactions*; The Royal Society of Chemistry, 2009; pp 350–416. DOI: 10.1039/9781847558763-00350.
- Plakos, K.; DeRose, V. J. Mapping Platinum Adducts on Yeast Ribosomal RNA Using High-Throughput Sequencing. *Chem. Commun.* **2017**, 53 (95), 12746–12749. DOI: 10.1039/C7CC06708A.
- Ponce-Salvatierra, A.; Wawrzyniak-Turek, K.; Steuerwald, U.; Höbartner, C.; Pena, V. Crystal Structure of a DNA Catalyst. *Nature* **2016**, 529 (7585), 231–234. DOI: 10.1038/nature16471.
- Popović, M.; Fliss, P. S.; Ditzler, M. A. *In Vitro* Evolution of Distinct Self-Cleaving Ribozymes in Diverse Environments. *Nucleic Acids Res.* **2015**, 43 (14), 7070–7082. DOI: 10.1093/nar/gkv648.
- Price, I. R.; Gaballa, A.; Ding, F.; Helmann, J. D.; Ke, A. Mn²⁺-Sensing Mechanisms of *yybP-ykoY* Orphan Riboswitches. *Mol. Cell* **2015**, 57 (6), 1110–1123. DOI: 10.1016/j.molcel.2015.02.016.
- Quin, J.; Chan, K. T.; Devlin, J. R.; Cameron, D. P.; Diesch, J.; Cullinane, C.; Ahern, J.; Khot, A.; Hein, N.; George, A. J.; Hannan, K. M.; Poortinga, G.; Sheppard, K. E.; Khanna, K. K.; Johnstone, R. W.; Drygin, D.; McArthur, G. A.; Pearson, R. B.; Sanij, E.; Hannan, R. D. Inhibition of RNA Polymerase I Transcription Initiation by CX-5461 Activates Non-Canonical ATM/ATR Signaling. *Oncotarget* **2016**, 7 (31), 49800–49818. DOI: 10.18632/oncotarget.10452.
- Ramesh, A.; Wakeman, C. A.; Winkler, W. C. Insights into Metalloregulation by M-Box Riboswitch RNAs via Structural Analysis of Manganese-Bound Complexes. *J. Mol. Biol.* **2011**, 407 (4), 556–570. DOI: 10.1016/j.jmb.2011.01.049.

- Ramezani, H.; Dietz, H. Building Machines with DNA Molecules. *Nat. Rev. Genet.* **2020**, *21* (1), 5–26. DOI: 10.1038/s41576-019-0175-6.
- Ramírez, F.; Ryan, D. P.; Grüning, B.; Bhardwaj, V.; Kilpert, F.; Richter, A. S.; Heyne, S.; Dündar, F.; Manke, T. deepTools2: A next Generation Web Server for Deep-Sequencing Data Analysis. *Nucleic Acids Res.* **2016**, *44* (W1), W160–W165. DOI: 10.1093/nar/gkw257.
- Rausch, C.; Hastert, F. D.; Cardoso, M. C. DNA Modification Readers and Writers and Their Interplay. *Read. DNA Modif.* **2020**, *432* (6), 1731–1746. DOI: 10.1016/j.jmb.2019.12.018.
- Raymond, E.; Faivre, S.; Chaney, S.; Woynarowski, J.; Cvitkovic, E. Cellular and Molecular Pharmacology of Oxaliplatin. *Mol. Cancer Ther.* **2002**, *1* (3), 227–235.
- Reißner, T.; Schneider, S.; Schorr, S.; Carell, T. Crystal Structure of a Cisplatin–(1,3-GTG) Cross-Link within DNA Polymerase η . *Angew. Chem. Int. Ed.* **2010**, *49* (17), 3077–3080. DOI: 10.1002/anie.201000414.
- Ren, A.; Rajashankar, K. R.; Patel, D. J. Fluoride Ion Encapsulation by Mg^{2+} Ions and Phosphates in a Fluoride Riboswitch. *Nature* **2012**, *486* (7401), 85–89. DOI: 10.1038/nature11152.
- Ren, A.; Xue, Y.; Peselis, A.; Serganov, A.; Al-Hashimi, H. M.; Patel, D. J. Structural and Dynamic Basis for Low-Affinity, High-Selectivity Binding of L-Glutamine by the Glutamine Riboswitch. *Cell Rep.* **2015**, *13* (9), 1800–1813. DOI: 10.1016/j.celrep.2015.10.062.
- Rhodes, D.; Lipps, H. J. G-Quadruplexes and Their Regulatory Roles in Biology. *Nucleic Acids Res.* **2015**, *43* (18), 8627–8637. DOI: 10.1093/nar/gkv862.
- Riddell, I. A.; Agama, K.; Park, G. Y.; Pommier, Y.; Lippard, S. J. Phenanthriplatin Acts As a Covalent Poison of Topoisomerase II Cleavage Complexes. *ACS Chem. Biol.* **2016**, *11* (11), 2996–3001. DOI: 10.1021/acschembio.6b00565.
- Riddell, I. A.; Lippard, S. J. 1. Cisplatin and Oxaliplatin: Our Current Understanding of Their Actions. In *Metallo-Drugs: Development and Action of Anticancer Agents*; Sigel, A., Sigel, H., Freisinger, E., Sigel, R. K. O., Eds.; De Gruyter, 2018; pp 1–42. DOI: 10.1515/9783110470734-001.
- Riisom, M.; Gammelgaard, B.; Lambert, I. H.; Stürup, S. Development and Validation of an ICP-MS Method for Quantification of Total Carbon and Platinum in Cell Samples and Comparison of Open-Vessel and Microwave-Assisted Acid Digestion Methods. *J. Pharm. Biomed. Anal.* **2018**, *158*, 144–150. DOI: 10.1016/j.jpba.2018.05.038.
- Rijal, K.; Bao, X.; Chow, C. S. Amino Acid-Linked Platinum(Ii) Analogues Have Altered Specificity for RNA Compared to Cisplatin. *Chem. Commun.* **2014**, *50* (30), 3918–3920. DOI: 10.1039/C3CC49035A.

- Rijal, K.; Chow, C. S. A New Role for Cisplatin: Probing Ribosomal RNA Structure. *Chem Commun* **2008**, No. 1, 107–109. DOI: 10.1039/B816633A.
- van Rixel, V. H. S.; Busemann, A.; Wissingh, M. F.; Hopkins, S. L.; Siewert, B.; van de Griend, C.; Siegler, M. A.; Marzo, T.; Papi, F.; Ferraroni, M.; Gratteri, P.; Bazzicalupi, C.; Messori, L.; Bonnet, S. Induction of a Four-Way Junction Structure in the DNA Palindromic Hexanucleotide 5'-d(CGTACG)-3' by a Mononuclear Platinum Complex. *Angew. Chem. Int. Ed.* **2019**, *58* (28), 9378–9382. DOI: 10.1002/anie.201814532.
- Rohner, M.; Medina-Molner, A.; Spingler, B. N,N,O and N,O,N Meridional Cis Coordination of Two Guanines to Copper(II) by d(CGCGCG)₂. *Inorg. Chem.* **2016**, *55* (12), 6130–6140. DOI: 10.1021/acs.inorgchem.6b00672.
- Romani, A. M. P. Cellular Magnesium Homeostasis. *Arch. Biochem. Biophys.* **2011**, *512* (1), 1–23. DOI: 10.1016/j.abb.2011.05.010.
- de Rosa, M.; de Sanctis, D.; Rosario, A. L.; Archer, M.; Rich, A.; Athanasiadis, A.; Carrondo, M. A. Crystal Structure of a Junction between Two Z-DNA Helices. *Proc. Natl. Acad. Sci.* **2010**, *107* (20), 9088. DOI: 10.1073/pnas.1003182107.
- Rose, P. K.; Watkins, N. H.; Yao, X.; Zhang, S.; Mancera-Ortiz, I. Y.; Sloop, J. T.; Donati, G. L.; Day, C. S.; Bierbach, U. Effect of the Nonleaving Groups on the Cellular Uptake and Cytotoxicity of Platinum-Acridine Anticancer Agents. *Inorganica Chim. Acta* **2019**, *492*, 150–155. DOI: 10.1016/j.ica.2019.04.030.
- Rosenberg, B.; Van Camp, L.; Krigas, T. Inhibition of Cell Division in Escherichia Coli by Electrolysis Products from a Platinum Electrode. *Nature* **1965**, *205* (4972), 698–699. DOI: 10.1038/205698a0.
- Rosenberg, B.; Van Camp, L.; Trosko, J. E.; Mansour, V. H. Platinum Compounds: A New Class of Potent Antitumour Agents. *Nature* **1969**, *222* (5191), 385–386. DOI: 10.1038/222385a0.
- Rottenberg, S.; Disler, C.; Perego, P. The Rediscovery of Platinum-Based Cancer Therapy. *Nat. Rev. Cancer* **2021**, *21* (1), 37–50. DOI: 10.1038/s41568-020-00308-y.
- Roundtree, I. A.; He, C. RNA Epigenetics—Chemical Messages for Posttranscriptional Gene Regulation. *Curr. Opin. Chem. Biol.* **2016**, *30*, 46–51.
- Roy, S.; Onuchic, J. N.; Sanbonmatsu, K. Y. Cooperation between Magnesium and Metabolite Controls Collapse of the SAM-I Riboswitch. *Biophys. J.* **2017**, *113* (2), 348–359. DOI: 10.1016/j.bpj.2017.06.044.
- Rozov, A.; Khusainov, I.; El Omari, K.; Duman, R.; Mykhaylyk, V.; Yusupov, M.; Westhof, E.; Wagner, A.; Yusupova, G. Importance of Potassium Ions for Ribosome Structure and Function Revealed by Long-Wavelength X-Ray Diffraction. *Nat. Commun.* **2019**, *10* (1), 2519. DOI: 10.1038/s41467-019-10409-4.

- Rubbi, C. P.; Milner, J. Disruption of the Nucleolus Mediates Stabilization of P53 in Response to DNA Damage and Other Stresses. *EMBO J.* **2003**, *22* (22), 6068–6077. DOI: 10.1093/emboj/cdg579.
- Rueden, C. T.; Schindelin, J.; Hiner, M. C.; DeZonia, B. E.; Walter, A. E.; Arena, E. T.; Eliceiri, K. W. ImageJ2: ImageJ for the next Generation of Scientific Image Data. *BMC Bioinformatics* **2017**, *18* (1), 529. DOI: 10.1186/s12859-017-1934-z.
- Russell, J.; Zomerdijk, J. C. B. M. RNA-Polymerase-I-Directed rDNA Transcription, Life and Works. *Trends Biochem. Sci.* **2005**, *30* (2), 87–96. DOI: 10.1016/j.tibs.2004.12.008.
- Samara, N. L.; Yang, W. Cation Trafficking Propels RNA Hydrolysis. *Nat. Struct. Mol. Biol.* **2018**, *25* (8), 715–721. DOI: 10.1038/s41594-018-0099-4.
- Sani, E.; Poortinga, G.; Sharkey, K.; Hung, S.; Holloway, T. P.; Quin, J.; Robb, E.; Wong, L. H.; Thomas, W. G.; Stefanovsky, V.; Moss, T.; Rothblum, L.; Hannan, K. M.; McArthur, G. A.; Pearson, R. B.; Hannan, R. D. UBF Levels Determine the Number of Active Ribosomal RNA Genes in Mammals. *J. Cell Biol.* **2008**, *183* (7), 1259–1274. DOI: 10.1083/jcb.200805146.
- Saris, C. P.; Van De Vaart, P. J. M.; Rietbroek, R. C.; Bloramaert, F. *In Vitro* Formation of DNA Adducts by Cisplatin, Lobaplatin and Oxaliplatin in Calf Thymus DNA in Solution and in Cultured Human Cells. *Carcinogenesis* **1996**, *17* (12), 2763–2769. DOI: 10.1093/carcin/17.12.2763.
- Satange, R.; Chuang, C.-Y.; Neidle, S.; Hou, M.-H. Polymorphic G:G Mismatches Act as Hotspots for Inducing Right-Handed Z-DNA by DNA Intercalation. *Nucleic Acids Res.* **2019**, *47* (16), 8899–8912. DOI: 10.1093/nar/gkz653.
- Satyavolu, N. S. R.; Tan, L. H.; Lu, Y. DNA-Mediated Morphological Control of Pd–Au Bimetallic Nanoparticles. *J. Am. Chem. Soc.* **2016**, *138* (50), 16542–16548. DOI: 10.1021/jacs.6b10983.
- Saunders, A. M.; DeRose, V. J. Beyond Mg²⁺: Functional Interactions between RNA and Transition Metals. *Curr. Opin. Chem. Biol.* **2016**, *31*, 153–159. DOI: 10.1016/j.cbpa.2016.02.015.
- Schaffer, M. F.; Peng, G.; Spingler, B.; Schnabl, J.; Wang, M.; Olieric, V.; Sigel, R. K. O. The X-Ray Structures of Six Octameric RNA Duplexes in the Presence of Different Di- and Trivalent Cations. *Int. J. Mol. Sci.* **2016**, *17* (7). DOI: 10.3390/ijms17070988.
- Schindelin, J.; Arganda-Carreras, I.; Frise, E.; Kaynig, V.; Longair, M.; Pietzsch, T.; Preibisch, S.; Rueden, C.; Saalfeld, S.; Schmid, B.; Tinevez, J.-Y.; White, D. J.; Hartenstein, V.; Eliceiri, K.; Tomancak, P.; Cardona, A. Fiji: An Open-Source Platform for Biological-Image Analysis. *Nat. Methods* **2012**, *9* (7), 676–682. DOI: 10.1038/nmeth.2019.

- Schlegel, M. K.; Essen, L.-O.; Meggers, E. Duplex Structure of a Minimal Nucleic Acid. *J. Am. Chem. Soc.* **2008**, *130* (26), 8158–8159. DOI: 10.1021/ja802788g.
- Schmidt, H. B.; Jaafar, Z. A.; Wulff, B. E.; Rodencal, J. J.; Hong, K.; Aziz-Zanjani, M. O.; Jackson, P. K.; Leonetti, M. D.; Dixon, S. J.; Rohatgi, R.; Brandman, O. Oxaliplatin Disrupts Nucleolar Function through Biophysical Disintegration. *Cell Rep.* **2022**, *41* (6), 111629. DOI: 10.1016/j.celrep.2022.111629.
- Schmidt, O. P.; Jurt, S.; Johannsen, S.; Karimi, A.; Sigel, R. K. O.; Luedtke, N. W. Concerted Dynamics of Metallo-Base Pairs in an A/B-Form Helical Transition. *Nat. Commun.* **2019**, *10* (1), 4818. DOI: 10.1038/s41467-019-12440-x.
- Schmitz, S. U.; Grote, P.; Herrmann, B. G. Mechanisms of Long Noncoding RNA Function in Development and Disease. *Cell. Mol. Life Sci.* **2016**, *73* (13), 2491–2509. DOI: 10.1007/s00018-016-2174-5.
- Schnabl, J.; Sigel, R. K. Controlling Ribozyme Activity by Metal Ions. *Curr. Opin. Chem. Biol.* **2010**, *14* (2), 269–275. DOI: 10.1016/j.cbpa.2009.11.024.
- Schoch, S.; Gajewski, S.; Rothfuß, J.; Hartwig, A.; Köberle, B. Comparative Study of the Mode of Action of Clinically Approved Platinum-Based Chemotherapeutics. *Int. J. Mol. Sci.* **2020**, *21* (18), 6928. DOI: 10.3390/ijms21186928.
- Schroeder, G. M.; Dutta, D.; Cavender, C. E.; Jenkins, J. L.; Pritchett, E. M.; Baker, C. D.; Ashton, J. M.; Mathews, D. H.; Wedekind, J. E. Analysis of a preQ₁-I Riboswitch in Effector-Free and Bound States Reveals a Metabolite-Programmed Nucleobase-Stacking Spine That Controls Gene Regulation. *Nucleic Acids Res.* **2020**, *48* (14), 8146–8164. DOI: 10.1093/nar/gkaa546.
- Schroeder, M. Osmium Tetraoxide Cis Hydroxylation of Unsaturated Substrates. *Chem. Rev.* **1980**, *80* (2), 187–213.
- Serganov, A.; Huang, L.; Patel, D. J. Structural Insights into Amino Acid Binding and Gene Control by a Lysine Riboswitch. *Nature* **2008**, *455* (7217), 1263–1267. DOI: 10.1038/nature07326.
- Serganov, A.; Huang, L.; Patel, D. J. Coenzyme Recognition and Gene Regulation by a Flavin Mononucleotide Riboswitch. *Nature* **2009**, *458* (7235), 233–237. DOI: 10.1038/nature07642.
- Shi, H.; Moore, P. B. The Crystal Structure of Yeast Phenylalanine tRNA at 1.93 Å Resolution: A Classic Structure Revisited. *RNA* **2000**, *6* (8), 1091–1105.
- Shu, X.; Xiong, X.; Song, J.; He, C.; Yi, C. Base-Resolution Analysis of Cisplatin–DNA Adducts at the Genome Scale. *Angew. Chem. Int. Ed.* **2016**, *55* (46), 14246–14249. DOI: 10.1002/anie.201607380.

- Siew, Y.-Y.; Neo, S.-Y.; Yew, H.-C.; Lim, S.-W.; Ng, Y.-C.; Lew, S.-M.; Seetoh, W.-G.; Seow, S.-V.; Koh, H.-L. Oxaliplatin Regulates Expression of Stress Ligands in Ovarian Cancer Cells and Modulates Their Susceptibility to Natural Killer Cell-Mediated Cytotoxicity. *Int. Immunol.* **2015**, *27* (12), 621–632. DOI: 10.1093/intimm/dxv041.
- Sigel, R. K. O.; Sigel, H. A Stability Concept for Metal Ion Coordination to Single-Stranded Nucleic Acids and Affinities of Individual Sites. *Acc. Chem. Res.* **2010**, *43* (7), 974–984. DOI: 10.1021/ar900197y.
- Sjekloća, L.; Ferré-D'Amaré, A. R. Binding between G-Quadruplexes at the Homodimer Interface of the Corn RNA Aptamer Strongly Activates Thioflavin T Fluorescence. *Cell Chem. Biol.* **2019**, *26* (8), 1159–1168.e4. DOI: 10.1016/j.chembiol.2019.04.012.
- Suchánková, T.; Kubíček, K.; Kašpárková, J.; Brabec, V.; Kozelka, J. Platinum–DNA Interstrand Crosslinks: Molecular Determinants of Bending and Unwinding of the Double Helix. *J. Inorg. Biochem.* **2012**, *108*, 69–79. DOI: 10.1016/j.jinorgbio.2011.09.025.
- Suddala, K. C.; Price, I. R.; Dandpat, S. S.; Janeček, M.; Kührová, P.; Šponer, J.; Banáš, P.; Ke, A.; Walter, N. G. Local-to-Global Signal Transduction at the Core of a Mn²⁺ Sensing Riboswitch. *Nat. Commun.* **2019**, *10* (1), 4304. DOI: 10.1038/s41467-019-12230-5.
- Sullivan, A. E.; Santos, S. D. M. An Optimized Protocol for ChIP-Seq from Human Embryonic Stem Cell Cultures. *STAR Protoc.* **2020**, *1* (2), 100062. DOI: 10.1016/j.xpro.2020.100062.
- Sun, A.; Gasser, C.; Li, F.; Chen, H.; Mair, S.; Krasheninina, O.; Micura, R.; Ren, A. SAM-VI Riboswitch Structure and Signature for Ligand Discrimination. *Nat. Commun.* **2019**, *10* (1), 5728. DOI: 10.1038/s41467-019-13600-9.
- Sutton, E. C.; DeRose, V. J. Early Nucleolar Responses Differentiate Mechanisms of Cell Death Induced by Oxaliplatin and Cisplatin. *J. Biol. Chem.* **2021**, *296*, 100633. DOI: 10.1016/j.jbc.2021.100633.
- Sutton, E. C.; McDevitt, C. E.; Prochnau, J. Y.; Yglesias, M. V.; Mroz, A. M.; Yang, M. C.; Cunningham, R. M.; Hendon, C. H.; DeRose, V. J. Nucleolar Stress Induction by Oxaliplatin and Derivatives. *J. Am. Chem. Soc.* **2019**, *141* (46), 18411–18415. DOI: 10.1021/jacs.9b10319.
- Sutton, E. C.; McDevitt, C. E.; Yglesias, M. V.; Cunningham, R. M.; DeRose, V. J. Tracking the Cellular Targets of Platinum Anticancer Drugs: Current Tools and Emergent Methods. *Inorganica Chim. Acta* **2019**, *498*, 118984. DOI: 10.1016/j.ica.2019.118984.

- Takezawa, Y.; Shionoya, M. Metal-Mediated DNA Base Pairing: Alternatives to Hydrogen-Bonded Watson-Crick Base Pairs. *Acc. Chem. Res.* **2012**, *45* (12), 2066–2076. DOI: 10.1021/ar200313h.
- Terenzi, A.; Pirker, C.; Keppler, B. K.; Berger, W. Anticancer Metal Drugs and Immunogenic Cell Death. *J. Inorg. Biochem.* **2016**, *165*, 71–79. DOI: 10.1016/j.jinorgbio.2016.06.021.
- Textor, L. C.; Wilmanns, M.; Holton, S. J. Expression, Purification, Crystallization and Preliminary Crystallographic Analysis of the Mouse Transcription Factor MafB in Complex with Its DNA-Recognition Motif Cmare. *Acta Crystallograph. Sect. F Struct. Biol. Cryst. Commun.* **2007**, *63* (8), 657–661. DOI: 10.1107/S1744309107031260.
- Thaplyal, P.; Bevilacqua, P. Experimental Approaches for Measuring pKa's in RNA and DNA. *Methods Enzymol.* **2014**, *549*, 189–219. DOI: 10.1016/B978-0-12-801122-5.00009-X.
- Theophanous, A.; Christodoulou, A.; Mattheou, C.; Sibai, D. S.; Moss, T.; Santama, N. Transcription Factor UBF Depletion in Mouse Cells Results in Downregulation of Both Downstream and Upstream Elements of the rRNA Transcription Network. *J. Biol. Chem.* **2023**, *299* (10), 105203. DOI: 10.1016/j.jbc.2023.105203.
- Thore, S. Structure of the Eukaryotic Thiamine Pyrophosphate Riboswitch with Its Regulatory Ligand. *Science* **2006**, *312* (5777), 1208–1211. DOI: 10.1126/science.1128451.
- Todd, R. C.; Lippard, S. J. Consequences of Cisplatin Binding on Nucleosome Structure and Dynamics. *Chem. Biol.* **2010**, *17* (12), 1334–1343. DOI: 10.1016/j.chembiol.2010.10.018.
- Todd, R. C.; Lippard, S. J. Structure of Duplex DNA Containing the Cisplatin 1,2- $\{Pt(NH_3)_2\}^{2+}$ -d (GpG) Cross-Link at 1.77 Å Resolution. *J. Inorg. Biochem.* **2010**, *104* (9), 902–908. DOI: 10.1016/j.jinorgbio.2010.04.005.
- Torres-Larios, A.; Swinger, K. K.; Krasilnikov, A. S.; Pan, T.; Mondragón, A. Crystal Structure of the RNA Component of Bacterial Ribonuclease P. *Nature* **2005**, *437* (7058), 584–587. DOI: 10.1038/nature04074.
- Toscano, F.; Parmentier, B.; Fajoui, Z. E.; Estornes, Y.; Chayvialle, J.-A.; Saurin, J.-C.; Abello, J. P53 Dependent and Independent Sensitivity to Oxaliplatin of Colon Cancer Cells. *Biochem. Pharmacol.* **2007**, *74* (3), 392–406. DOI: 10.1016/j.bcp.2007.05.001.
- Trachman, R. J.; Demeshkina, N. A.; Lau, M. W. L.; Panchapakesan, S. S. S.; Jeng, S. C. Y.; Unrau, P. J.; Ferré-D'Amaré, A. R. Structural Basis for High-Affinity Fluorophore Binding and Activation by RNA Mango. *Nat. Chem. Biol.* **2017**, *13* (7), 807–813. DOI: 10.1038/nchembio.2392.

- Tsai, R. Y. L.; Pederson, T. Connecting the Nucleolus to the Cell Cycle and Human Disease. *FASEB J.* **2014**, *28* (8), 3290–3296. DOI: 10.1096/fj.14-254680.
- Tseng, W.-H.; Chang, C.; Wu, P.-C.; Hu, N.-J.; Lee, G.-H.; Tzeng, C.-C.; Neidle, S.; Hou, M.-H. Induced-Fit Recognition of CCG Trinucleotide Repeats by a Nickel-Chromomycin Complex Resulting in Large-Scale DNA Deformation. *Angew. Chem. Int. Ed.* **2017**, *56* (30), 8761–8765. DOI: 10.1002/anie.201703989.
- Ummat, A.; Rechkoblit, O.; Jain, R.; Roy Choudhury, J.; Johnson, R. E.; Silverstein, T. D.; Buku, A.; Lone, S.; Prakash, L.; Prakash, S.; Aggarwal, A. K. Structural Basis for Cisplatin DNA Damage Tolerance by Human Polymerase η during Cancer Chemotherapy. *Nat. Struct. Mol. Biol.* **2012**, *19* (6), 628–632. DOI: 10.1038/nsmb.2295.
- Valls, N.; Steiner, R. A.; Wright, G.; Murshudov, G. N.; Subirana, J. A. Variable Role of Ions in Two Drug Intercalation Complexes of DNA. *JBIC J. Biol. Inorg. Chem.* **2005**, *10* (5), 476–482. DOI: 10.1007/s00775-005-0655-3.
- Valls, N.; Usón, I.; Gouyette, C.; Subirana, J. A. A Cubic Arrangement of DNA Double Helices Based on Nickel–Guanine Interactions. *J. Am. Chem. Soc.* **2004**, *126* (25), 7812–7816. DOI: 10.1021/ja049393i.
- Vasilyev, N.; Polonskaia, A.; Darnell, J. C.; Darnell, R. B.; Patel, D. J.; Serganov, A. Crystal Structure Reveals Specific Recognition of a G-Quadruplex RNA by a β -Turn in the RGG Motif of FMRP. *Proc. Natl. Acad. Sci.* **2015**, *112* (39), E5391–E5400. DOI: 10.1073/pnas.1515737112.
- Vekris, A.; Meynard, D.; Haaz, M.-C.; Bayssas, M.; Bonnet, J.; Robert, J. Molecular Determinants of the Cytotoxicity of Platinum Compounds. *Cancer Res.* **2004**, *64* (1), 356–362. DOI: 10.1158/0008-5472.CAN-03-2258.
- Vogt, M.; Lahiri, S.; Hoogstraten, C. G.; Britt, R. D.; DeRose, V. J. Coordination Environment of a Site-Bound Metal Ion in the Hammerhead Ribozyme Determined by ^{15}N and ^2H ESEEM Spectroscopy. *J. Am. Chem. Soc.* **2006**, *128* (51), 16764–16770. DOI: 10.1021/ja057035p.
- van der Walt, S.; Schönberger, J. L.; Nunez-Iglesias, J.; Boulogne, F.; Warner, J. D.; Yager, N.; Gouillart, E.; Yu, T. Scikit-Image: Image Processing in Python. *PeerJ* **2014**, *2*, e453. DOI: 10.7717/peerj.453.
- Wang, Y.-R.; Chen, S.-F.; Wu, C.-C.; Liao, Y.-W.; Lin, T.-S.; Liu, K.-T.; Chen, Y.-S.; Li, T.-K.; Chien, T.-C.; Chan, N.-L. Producing Irreversible Topoisomerase II-Mediated DNA Breaks by Site-Specific Pt(II)-Methionine Coordination Chemistry. *Nucleic Acids Res.* **2017**, *45* (18), 10861–10871. DOI: 10.1093/nar/gkx742.
- Ward, W. L.; Plakos, K.; DeRose, V. J. Nucleic Acid Catalysis: Metals, Nucleobases, and Other Cofactors. *Chem. Rev.* **2014**, *114* (8), 4318–4342. DOI: 10.1021/cr400476k.

- Warner, K. D.; Homan, P.; Weeks, K. M.; Smith, A. G.; Abell, C.; Ferré-D'Amaré, A. R. Validating Fragment-Based Drug Discovery for Biological RNAs: Lead Fragments Bind and Remodel the TPP Riboswitch Specifically. *Chem. Biol.* **2014**, *21* (5), 591–595. DOI: 10.1016/j.chembiol.2014.03.007.
- Warner, K. D.; Sjekloća, L.; Song, W.; Filonov, G. S.; Jaffrey, S. R.; Ferré-D'Amaré, A. R. A Homodimer Interface without Base Pairs in an RNA Mimic of Red Fluorescent Protein. *Nat. Chem. Biol.* **2017**, *13* (11), 1195–1201. DOI: 10.1038/nchembio.2475.
- Watkins, D.; Mohan, S.; Koudelka, G. B.; Williams, L. D. Sequence Recognition of DNA by Protein-Induced Conformational Transitions. *J. Mol. Biol.* **2010**, *396* (4), 1145–1164. DOI: 10.1016/j.jmb.2009.12.050.
- Wedekind, J. E.; Dutta, D.; Belashov, I. A.; Jenkins, J. L. Metalloriboswitches: RNA-Based Inorganic Ion Sensors That Regulate Genes. *J. Biol. Chem.* **2017**, *292* (23), 9441–9450. DOI: 10.1074/jbc.R117.787713.
- Weeks, S. E.; Metge, B. J.; Samant, R. S. The Nucleolus: A Central Response Hub for the Stressors That Drive Cancer Progression. *Cell. Mol. Life Sci.* **2019**, *76* (22), 4511–4524. DOI: 10.1007/s00018-019-03231-0.
- Wei, T.; Najmi, S. M.; Liu, H.; Peltonen, K.; Kucerova, A.; Schneider, D. A.; Laiho, M. Small-Molecule Targeting of RNA Polymerase I Activates a Conserved Transcription Elongation Checkpoint. *Cell Rep.* **2018**, *23* (2), 404–414. DOI: 10.1016/j.celrep.2018.03.066.
- Werner, C.; Krebs, B.; Keith, G.; Dirheimer, G. Specific Cleavages of Pure tRNAs by Plumbous Ions. *Biochim. Biophys. Acta BBA - Nucleic Acids Protein Synth.* **1976**, *432* (2), 161–175. DOI: 10.1016/0005-2787(76)90158-1.
- Wexselblatt, E.; Yavin, E.; Gibson, D. Cellular Interactions of Platinum Drugs. *Inorganica Chim. Acta* **2012**, *393*, 75–83. DOI: 10.1016/j.ica.2012.07.013.
- Wilson, J. J.; Lippard, S. J. Synthetic Methods for the Preparation of Platinum Anticancer Complexes. *Chem. Rev.* **2014**, *114* (8), 4470–4495. DOI: 10.1021/cr4004314.
- Wilson, R. C.; Doudna, J. A. Molecular Mechanisms of RNA Interference. *Annu. Rev. Biophys.* **2013**, *42* (1), 217–239. DOI: 10.1146/annurev-biophys-083012-130404.
- Wirth, R.; White, J. D.; Moghaddam, A. D.; Ginzburg, A. L.; Zakharov, L. N.; Haley, M. M.; DeRose, V. J. Azide vs Alkyne Functionalization in Pt(II) Complexes for Post-Treatment Click Modification: Solid-State Structure, Fluorescent Labeling, and Cellular Fate. *J. Am. Chem. Soc.* **2015**, *137* (48), 15169–15175. DOI: 10.1021/jacs.5b09108.
- Wise, S. S.; Wise, J. P., Sr. Chromium and Genomic Stability. *Mutat. Res.* **2012**, *733* (1–2), 78–82. DOI: 10.1016/j.mrfmmm.2011.12.002.

- Wong, J. H.; Brown, J. A.; Suo, Z.; Blum, P.; Nohmi, T.; Ling, H. Structural Insight into Dynamic Bypass of the Major Cisplatin-DNA Adduct by Y-Family Polymerase Dpo4. *EMBO J.* **2010**, *29* (12), 2059–2069. DOI: 10.1038/emboj.2010.101.
- Woods, S. J.; Hannan, K. M.; Pearson, R. B.; Hannan, R. D. The Nucleolus as a Fundamental Regulator of the P53 Response and a New Target for Cancer Therapy. *Biochim. Biophys. Acta BBA - Gene Regul. Mech.* **2015**, *1849* (7), 821–829. DOI: 10.1016/j.bbagr.2014.10.007.
- Woynarowski, J. M.; Chapman, W. G.; Napier, C.; Herzig, M. C. S.; Juniewicz, P. Sequence- and Region-Specificity of Oxaliplatin Adducts in Naked and Cellular DNA. *Mol. Pharmacol.* **1998**, *54* (5), 770–777. DOI: 10.1124/mol.54.5.770.
- Woynarowski, J. M.; Faivre, S.; Herzig, M. C. S.; Arnett, B.; Chapman, W. G.; Trevino, A. V.; Raymond, E.; Chaney, S. G.; Vaisman, A.; Varchenko, M.; Juniewicz, P. E. Oxaliplatin-Induced Damage of Cellular DNA. *Mol. Pharmacol.* **2000**, *58* (5), 920–927. DOI: 10.1124/mol.58.5.920.
- Wu, B.; Davey, G. E.; Nazarov, A. A.; Dyson, P. J.; Davey, C. A. Specific DNA Structural Attributes Modulate Platinum Anticancer Drug Site Selection and Cross-Link Generation. *Nucleic Acids Res.* **2011**, *39* (18), 8200–8212. DOI: 10.1093/nar/gkr491.
- Wu, Y.; Pradhan, P.; Havener, J.; Boysen, G.; Swenberg, J. A.; Campbell, S. L.; Chaney, S. G. NMR Solution Structure of an Oxaliplatin 1,2-d(GG) Intrastrand Cross-Link in a DNA Dodecamer Duplex. *J. Mol. Biol.* **2004**, *341* (5), 1251–1269. DOI: 10.1016/j.jmb.2004.06.066.
- Xu, J.; Cotruvo, J. A. The *czcD* (NiCo) Riboswitch Responds to Iron(II). *Biochemistry* **2020**, *59* (15), 1508–1516. DOI: 10.1021/acs.biochem.0c00074.
- Xu, W.; He, W.; Du, Z.; Zhu, L.; Huang, K.; Lu, Y.; Luo, Y. Functional Nucleic Acid Nanomaterials: Development, Properties, and Applications. *Angew. Chem. Int. Ed.* **2019**, *59* (n/a), 2–31. DOI: 10.1002/anie.201909927.
- Xuan, J.; Gitareja, K.; Brajanovski, N.; Sanij, E. Harnessing the Nucleolar DNA Damage Response in Cancer Therapy. *Genes* **2021**, *12* (8), 1156. DOI: 10.3390/genes12081156.
- Xue, S.-F.; Chen, Z.-H.; Han, X.-Y.; Lin, Z.-Y.; Wang, Q.-X.; Zhang, M.; Shi, G. DNA Encountering Terbium(III): A Smart “Chemical Nose/Tongue” for Large-Scale Time-Gated Luminescent and Lifetime-Based Sensing. *Anal. Chem.* **2018**, *90* (5), 3443–3451. DOI: 10.1021/acs.analchem.7b05167.
- Yamada, K.; Kato, N.; Takagi, A.; Koi, M.; Hemmi, H. One-Milliliter Wet-Digestion for Inductively Coupled Plasma Mass Spectrometry (ICP-MS): Determination of Platinum-DNA Adducts in Cells Treated with Platinum(II) Complexes. *Anal. Bioanal. Chem.* **2005**, *382* (7), 1702–1707. DOI: 10.1007/s00216-005-3339-5.

- Yamaguchi, H.; Šebera, J.; Kondo, J.; Oda, S.; Komuro, T.; Kawamura, T.; Dairaku, T.; Kondo, Y.; Okamoto, I.; Ono, A.; Burda, J. V.; Kojima, C.; Sychrovský, V.; Tanaka, Y. The Structure of Metallo-DNA with Consecutive Thymine–HgII–Thymine Base Pairs Explains Positive Entropy for the Metallo Base Pair Formation. *Nucleic Acids Res.* **2014**, *42* (6), 4094–4099. DOI: 10.1093/nar/gkt1344.
- Yang, K.; Wang, M.; Zhao, Y.; Sun, X.; Yang, Y.; Li, X.; Zhou, A.; Chu, H.; Zhou, H.; Xu, J.; Wu, M.; Yang, J.; Yi, J. A Redox Mechanism Underlying Nucleolar Stress Sensing by Nucleophosmin. *Nat. Commun.* **2016**, *7* (1), 13599. DOI: 10.1038/ncomms13599.
- Yang, K.; Yang, J.; Yi, J. Nucleolar Stress: Hallmarks, Sensing Mechanism and Diseases. *Cell Stress* **2018**, *2* (6), 125–140. DOI: 10.15698/cst2018.06.139.
- Yeh, J. I.; Shivachev, B.; Rapireddy, S.; Crawford, M. J.; Gil, R. R.; Du, S.; Madrid, M.; Ly, D. H. Crystal Structure of Chiral γ PNA with Complementary DNA Strand: Insights into the Stability and Specificity of Recognition and Conformational Preorganization. *J. Am. Chem. Soc.* **2010**, *132* (31), 10717–10727. DOI: 10.1021/ja907225d.
- Yung, B. Y.-M.; Busch, R. K.; Busch, H.; Mauger, A. B.; Chan, P.-K. Effects of Actinomycin D Analogs on Nucleolar Phosphoprotein B23 (37,000 Daltons/pI 5.1). *Biochem. Pharmacol.* **1985**, *34* (22), 4059–4063. DOI: 10.1016/0006-2952(85)90387-9.
- Zeglis, B. M.; Pierre, V. C.; Kaiser, J. T.; Barton, J. K. A Bulky Rhodium Complex Bound to an Adenosine-Adenosine DNA Mismatch: General Architecture of the Metalloinsertion Binding Mode. *Biochemistry* **2009**, *48* (20), 4247–4253. DOI: 10.1021/bi900194e.
- Zhai, X.; Beckmann, H.; Jantzen, H.-M.; Essigmann, J. M. Cisplatin–DNA Adducts Inhibit Ribosomal RNA Synthesis by Hijacking the Transcription Factor Human Upstream Binding Factor. *Biochemistry* **1998**, *37* (46), 16307–16315. DOI: 10.1021/bi981708h.
- Zhang, H.-Y.; Liu, Y.-R.; Ji, C.; Li, W.; Dou, S.-X.; Xie, P.; Wang, W.-C.; Zhang, L.-Y.; Wang, P.-Y. Oxaliplatin and Its Enantiomer Induce Different Condensation Dynamics of Single DNA Molecules. *PLoS ONE* **2013**, *8* (8), e71556. DOI: 10.1371/journal.pone.0071556.
- Zhang, Jing; Li, D.; Zhang, J.; Chen, D.; Murchie, A. I. H. Osmium Tetroxide as a Probe of RNA Structure. *RNA* **2017**, *23* (4), 483–492. DOI: 10.1261/rna.057539.116.
- Zhang, Jinwei; Ferré-D'Amaré, A. R. Dramatic Improvement of Crystals of Large RNAs by Cation Replacement and Dehydration. *Structure* **2014**, *22* (9), 1363–1371. DOI: 10.1016/j.str.2014.07.011.

- Zhao, Y.; Biertümpfel, C.; Gregory, M. T.; Hua, Y.-J.; Hanaoka, F.; Yang, W. Structural Basis of Human DNA Polymerase η -Mediated Chemoresistance to Cisplatin. *Proc. Natl. Acad. Sci.* **2012**, *109* (19), 7269–7274. DOI: 10.1073/pnas.1202681109.
- Zheng, L.; Mairhofer, E.; Teplova, M.; Zhang, Y.; Ma, J.; Patel, D. J.; Micura, R.; Ren, A. Structure-Based Insights into Self-Cleavage by a Four-Way Junctional Twister-Sister Ribozyme. *Nat. Commun.* **2017**, *8* (1). DOI: 10.1038/s41467-017-01276-y.
- Zhou, W.; Saran, R.; Liu, J. Metal Sensing by DNA. *Chem. Rev.* **2017**, *117* (12), 8272–8325. DOI: 10.1021/acs.chemrev.7b00063.
- Zisi, A.; Bartek, J.; Lindström, M. S. Targeting Ribosome Biogenesis in Cancer: Lessons Learned and Way Forward. *Cancers* **2022**, *14* (9), 2126. DOI: 10.3390/cancers14092126.